



UNIVERSITY OF LEEDS

Topological Hall Effect due to Skyrmions in Magnetic Multilayers



Alexandra Jane Stacey

University of Leeds

School of Physics and Astronomy

Submitted in accordance with the requirements for the degree of

Doctor of Philosophy

July, 2023

In memoriam
*soceri mei **Simonis Stacii.***
Requiem aeternam dona ei, Domine, et lux perpetua luceat ei.
Requiescat in pace.

*And for my parents, **Dawn and Nigel Huxtable;***
*my mother-in-law, **Carmel Stacey;***
*and my husband, **Dr Gregory Stacey.***

Thank you for loving and supporting me unconditionally.

Intellectual Property Statement

The candidate confirms that the work submitted is her own and that appropriate credit has been given where reference has been made to the work of others.

This copy has been supplied on the understanding that it is copyright material and that no quotation from the thesis may be published without proper acknowledgement.

The right of Alexandra Jane Stacey to be identified as Author of this work has been asserted by her in accordance with the Copyright, Designs and Patents Act 1988.

© 2023The University of Leeds and Alexandra Jane Stacey .

The experimental set-up for collection of temperature dependent electrical transport data and subsequent measurements were performed by a team which has included Alexandra Stacey, Dr Nathan Satchell, Dr Gavin Burnell, and Prof. Chris Marrows. The findings in chapters 6 and 7 are the result of this work.

My own contributions, fully and explicitly indicated in the thesis, are as follows: All sample preparation, material deposition (choice of number of multilayer repeats), characterisation, and decisions regarding the temperatures and magnetic fields at which to measure samples. Additionally, all sample wirebonding and loading into experimental apparatus (cryostat for transport measurements and SQUID-VSM) performed during office-hours was done by the candidate ($\geq 80\%$ of the total loading and unloading of the cryostat). All data analysis was carried out by the author, as well as all figure production and choices regarding data presentation. The author was involved in all calibration measurements, experimental set-up, and data collection (including some remote supervision of data collection outside of office hours), and is capable of explaining and replicating the apparatus configuration for the electrical transport measurements.

The other members of the group and their contributions have been as follows: Dr Gavin Burnell: configuration and arrangement of the Keithley 6221 and 2182 measurement apparatus ensuring the simultaneous measurement of transverse and longitudinal resistance during transport measurements. Authorship of the in-house NI LabVIEW™ code that enables the user interface for controlling and automation of cryostat transport measurements. Support in initial training and configuration of transport measurements.

Dr Nathan Satchell: provision of support and guidance to the author when carrying out experimental transport measurements and superconducting magnet calibration, loading and unloading of samples when this was required outside of office hours ($\leq 20\%$ of total loading and unloading of the cryostat), remote supervision of measurements carried out outside of office hours, and assistance in interpretation of analysed data.

Prof. Chris Marrows: supervision of the candidate, management guidance during sample growth and structure choice, and discussion and assistance in interpretation of analysed data.

Acknowledgements

These acknowledgements are rather long, however, I hope that you will bear with me in thanking the large number of people who have contributed to this work, my wellbeing, and to my growth as a person. This thesis is the product of four and a half years of work on my part and, to change the saying a little, it took a metaphorical village (and about the same number of people as making a literal one!).

First thanks must go to my supervisor, Prof. Chris Marrows, for giving me the opportunity to pursue this research project. Throughout he has been supportive, knowledgeable, and unceasingly calm. I left every supervision meeting with my ideas clearer and more motivated to take the next necessary steps. Your belief in my ability to take ownership of this work, even at the very beginning, gave me the confidence to do so. Likewise, Prof. Bryan Hickey - head of the condensed matter group and my second supervisor, is due my gratitude for his support and guidance throughout the project. I appreciate the help you have both given me very much.

Dr Mark Rosamond, deserves my sincere thanks for his help throughout my attempts at photo and electron lithography over two to three years of my research. I greatly enjoyed working with you and learning from you.

Special thanks must be given to Dr Mannan Ali, without whom the experimental apparatus would likely all spontaneously cease to function. He has provided invaluable training and support throughout the experimental work that I have undertaken and his aid is greatly appreciated.

I owe a great deal to the help and support of Dr Gavin Burnell. You are the reason that I understand how to set-up and perform electrical transport measurements. I greatly appreciate the time that you have so willingly given to helping me work through ideas for experimental set-ups and going above and beyond to adapt the in-house software to support the new combinations of apparatus that I was after. Your contributions to the CM group in Leeds are immeasurable and generously given.

My thanks must also be extended to all the other members of the CM group. In particular, to Emily Darwin who endured extremely long hours of work on beamtimes with me. You helped make the lack of sleep and stress bearable! My office-mates, Dr Josh Gretton and Dr Matt Rogers, were welcoming and full of useful pieces of information that made my arrival to Leeds easy and fun. Sharing an office with you was both fun and productive, thank you. Sean Stansill, Alistair Walton, and Kathryn Moran have all been good friends and contributed to my enjoyment of the time as a PhD student in Leeds. Dr Philippa Shepley is also due particular thanks for the practical support she provided during experimental work and her friendship.

I am forever indebted to Dr Nathan Satchell for his guidance and support throughout the time that we have both been in Leeds. Your contribution to my research throughout

the final year of my PhD has been profound. When I couldn't see the wood for the trees, trying to determine the magnetic field felt by the samples in two different superconducting magnets, and realising that I needed to redo the majority of my electrical measurements, you helped me to gain perspective, find the next steps, and motivated me to keep going when it felt like giving up might be a much better idea. I was seriously close to calling it quits after nearly four years of work when you stepped up and provided the practical and moral support that I needed. I am also grateful for our friendship that I hope will last far beyond my time in academia.

Dr Katharina Zeissler was responsible for a great deal of my initial training when I arrived in Leeds. She is a great teacher and scientist, and helped me to transition from undergraduate study to independent graduate level research with relative ease. The number of hours that we have since spent discussing physics and that you have patiently and sympathetically listened to me lament the difficulties experiments are uncountable. The fact that you were willing to give so much of your time to discussing this project with me, even after you moved on from Leeds, is nigh on incomprehensible. Thank you for your friendship and support - I am grateful that our friendship has continued beyond our short time working together.

The support that I have received from my study skills tutor, Carol Kearney, and mentor, Kathryn Boardman, has been instrumental throughout the PhD. You have provided me with the writing skills that I was lacking and helped me to be kind to myself when I set myself standards that weren't practical or healthy. I cannot express my gratitude to you both enough. The fact that I can now consistently produce written work that I am happy with, hopefully, tells you both how much you have given me. My future is immeasurably brighter because of you.

My parents, Dawn and Nigel Huxtable, have always supported me no matter what it is that I tell them I've decided to do next - even when that was embarking on a doctorate while writing was still a painful and dreaded task for me (see - I told you writing a thesis would fix it!). Thank you for spending some of your holiday decluttering and doing chores that had fallen by the wayside while I wrote this thesis. I love you both very much and appreciate you being there for me whenever I need you, despite the time difference down-under in NZ. I promise not to be writing a thesis next time you come all the way around the world to visit.

My heartfelt thanks and appreciation go to my husband, Gregory Stacey. You make me laugh when I am sad and calm when I am stressed. You are willing to hold me accountable if I'm procrastinating or not putting in the effort, even when I *really* don't want to hear it. And you cook dinner far more often than I even attempt to feed us. Thank you for the last four and a half years, I love you, and I look forward to the

years to come.

Finally, but by no means least, my mother-in-law, Carmel Stacey, is due my sincere gratitude for letting me 'keep her company' - she fed me and gave great encouragement to me as I struggled through analysis - while Greg was away at a theology conference for a week. She also kept me company and provided support through the last moments before submission of this thesis - thank you.

Abstract

Possible contributions to the Hall effect, anomalous and topological, in $[\text{CoB|Ir|Pt}]_{\times n}$ multilayers are determined and the temperature and repeat layer, n , dependent behaviour characterised. Understanding the relationship between skyrmions and the behaviour of the Hall effect is essential to realise skyrmionic data storage.

Excess Hall resistivity remaining after the ordinary and anomalous Hall effects are subtracted from the Hall resistivity is measured in Pt/CoB/Ir multilayers and shown to depend on the temperature and n . The number, and variation in number, of peak and trough-like features in $\rho_{\text{xy,excess}}$ as the magnetic field is varied is inversely proportional to the temperature and n . Correlation between the temperature dependence of maximum $\rho_{\text{xy,excess}}$ signal and anomalous contribution, ρ_{A} , is observed possibly suggesting shared physical origins between $\rho_{\text{xy,excess}}$ and ρ_{A} . The observations reported suggest that $\rho_{\text{xy,excess}}$ is, at least partially, topological in nature. This is supported by the dependence of maximum $\rho_{\text{xy,excess}}$ on n in agreement with previous reports of skyrmion presence in similar multilayer samples with $2 \leq n \leq 10$.

The temperature dependence of the anomalous Hall effect in $[\text{CoB|Ir|Pt}]_{\times n}$ is accounted for by the temperature dependence of the saturation magnetisation, $M_{\text{S}}(T)$. Extrinsic (skew scattering, α , and side-jump, β) and intrinsic (b) contributions to the anomalous Hall effect are determined by scaling with longitudinal resistivity, ρ_{xx} , to be $\alpha = -0.02$, $\beta = 1710$ S/cm, and $b = 520$ S/cm. The AHE is described well in these samples by $\rho_{\text{A}}M_0/M_{\text{S}} = (\alpha\rho_{\text{xx}0} + \beta\rho_{\text{xx}0}^2 + b\rho_{\text{xx}}^2)$, where $\rho_{\text{xx}0}$ is from impurity scattering, and ρ_{xx} is from phonon-lattice interactions. α , β , and b are like those found in literature for single-layered ferromagnetic materials. Side-jump scattering is the largest contribution to the anomalous Hall resistivity in $[\text{CoB|Ir|Pt}]_{\times n}$ multilayers suggesting that the large side-jump coefficient observed could be contributing to the temperature dependence of $\rho_{\text{xy,excess}}$.

CONTENTS

1	Introduction	1
1.1	Thesis Outline	2
2	Literature Review	4
2.1	Introduction	5
2.2	Interactions in Magnetism	5
2.2.1	Anisotropies in Magnetism	7
2.3	Dzyaloshinskii-Moriya Interaction (DMI)	11
2.4	Magnetisation Processes in Ferromagnets	15
2.5	Magnetic Skyrmions	18
2.5.1	Skyrmion Definition	19
2.5.2	Topological Considerations	20
2.5.3	Types of Skyrmions	20
2.5.4	Materials Hosting Skyrmions	21
2.5.5	Magnetic Multilayer Design Strategies	22
2.6	Advances in Skyrmion Research	23
2.6.1	Skyrmion Dynamics	24
2.6.2	Potential Applications	25
2.6.3	The Hall Effect	26
2.6.4	Hall Transport Measurements	30
2.7	Conclusion	31
3	Experimental Methods	32
3.1	Introduction	33
3.1.1	DC Magnetron Sputtering	33
3.2	Characterisation	36
3.2.1	X-Ray Reflectometry (XRR)	36
3.2.2	GenX XRR Fitting & Interface Roughness	38

3.2.3	LASER MOKE Magnetometry	43
3.2.4	Superconducting Quantum Interference Device (SQUID) Magnetometry	44
3.2.5	Instrument Precision, Systematic Errors, and Random Errors	47
3.3	Electrical Transport Measurements	49
3.3.1	Cryostat Hall Resistance Measurements	50
3.3.2	Instrument Precision, Systematic Errors, and Random Errors	55
4	Preliminary Work	57
4.1	Introduction	58
4.2	Device Fabrication & Lithography Design Evolution	59
4.2.1	Lithography Process Summary	59
4.2.2	Optical Lithography (OL) and Electron Beam Lithography (EBL)	61
4.2.3	Ion Mill Etching	63
4.2.4	Electron Beam Evaporation	65
4.2.5	Device Fabrication Challenges	65
4.2.6	Testing the Effects of Lithography Techniques on Contact Resistance	66
4.2.7	X-Ray Magnetic Circular Dichroism - Scanning Transmission X-Ray Microscopy (XMCD-STXM)	68
4.3	XMCD-STXM Room Temperature Transport Measurements	69
5	Field Corrections and Data Analysis	75
5.1	Introduction	76
5.2	Calibration of Superconducting Magnets	76
5.2.1	SQUID-VSM Magnet	78
5.2.2	Cryostat Transport Magnet	79
5.2.3	Additive Effect of the Field Corrections	80
5.3	Data Analysis	82
5.3.1	Transport Measurements	82
5.3.2	SQUID Magnetometry	84
5.3.3	Subtraction of Hysteresis Loops	85
5.3.4	Critical Analysis of Subtraction Result	85
5.4	Features or artefacts?	91
5.4.1	FWHM as a Measure of Feature Size	91
5.4.2	Defining the Size of a ‘Real’ Feature	93
5.5	Error Estimation and Propagation	95
5.6	Conclusion	96

6	Topological Hall Effect in CoB Ir Pt Multilayers	98
6.1	Introduction	99
6.2	Sample Growth and Characterisation	99
6.2.1	Growth Conditions	100
6.2.2	Characterisation Parameters	101
6.2.3	Excess Hall Resistivity	101
6.3	Temperature Dependence	106
6.4	Multilayer Repeat, n , Dependence	115
6.5	Conclusion	117
7	Anomalous Hall Effect in [CoB Ir Pt]$_{\times n}$ Multilayers	118
7.1	Introduction	119
7.2	Temperature Dependence of the AHE	119
7.3	AHE and Longitudinal Resistivity	121
7.4	Conclusion	126
8	Conclusion	128
8.1	Conclusion	129
8.1.1	Excess Hall Resistivity	130
8.1.2	Anomalous Hall Effect	130
8.2	Further Work	131
	References	133

Abbreviations

AC	Alternating Current
AHE	Anomalous Hall Effect
DC	Direct Current
DMI	Dzyaloshinskii-Moriya Interaction
EBL	Electron Beam Lithography
FIB	Focused Ion Beam
FM	Ferromagnet(ic)
FWHM	Full Width Half Maximum
IP	In-Plane (parallel to sample surface)
JJ	Josephson Junction
LTEM	Lorentz Transmission Electron Microscopy
MFM	Magnetic Force Microscopy
MOKE	Magneto-Optical Kerr Effect
OHE	Ordinary Hall Effect
OOP	Out-of-Plane (perpendicular to sample surface)
OL	Optical Lithography/Photolithography
PMA	Perpendicular Magnetic Anisotropy
SEM	Scanning Electron Microscope/Microscopy
SkHE	Skyrmion Hall Effect
STXM	Scanning Transmission X-Ray Microscopy
SQUID	Superconducting Quantum Interference Device
TEM	Transmission Electron Microscopy
THE	Topological Hall Effect
UHV	Ultra High Vacuum
VSM	Vibrating Sample Magnetometry
VTI	Variable Temperature Insert
XMCD	X-ray Magnetic Circular Dichroism
XRR	X-Ray Reflectometry

CHAPTER 1

Introduction

INTRODUCTION

The effect of climate change is one of the most pressing issues of the modern day. One month before I began my PhD research in June 2018, Forbes magazine reported that every day we are generating 2.5 quintillion bytes of data [1]. The electricity required both to store and recall that data has become a significant proportion of the total used each year with the Independent reporting that in 2016 the electricity used globally for data storage was 1.5 times the total amount used by the UK [2].

Application of magnetic skyrmions in magnetic data storage has been proposed as an alternative, lower energy, method of data storage due the potential ease of writing and deleting them compared to conventional magnetic domains. In particular, the ability to nucleate (‘write’) and manipulate skyrmions with small current densities is promising and their potential for use in logic gates has already been demonstrated [3].

The direct writing of room temperature skyrmion lattices was realised in 2018 by Zhang et. al. in Pt/Co/Ta multilayers using Scanning Magnetic Force Microscopy [4]. Writing of individual skyrmions at room temperature using only electrical current has also been demonstrated recently [5]. Racetrack memory devices using conventional magnetic domains have been suggested for energy efficient data storage [6] and a strategy for such a device employing Néel skyrmions was suggested in 2014 [7].

In order to progress towards the realisation of such technologies, it is necessary to fully understand the material properties which have an effect on the electrical transport behaviour of skyrmions. The Hall effect is particularly important in this regard because the non-trivial topology of skyrmions has been shown to cause an additional contribution to the Hall effect that could be used to electronically detect the presence of skyrmions [8; 9]. A complete understanding of the topological and anomalous Hall effects within materials proposed for technical applications is necessary in order to read data stored using skyrmions by electrical Hall measurement rather than by use of magnetic tunnel junctions that require more extensive and delicate fabrication than the production of contacts in a Hall geometry configuration.

1.1 Thesis Outline

This thesis aims to determine the topological Hall effect due to magnetic skyrmions in $[\text{CoB}|\text{Ir}|\text{Pt}]_{\times n}$ multilayers, and any temperature or n dependent behaviour exhibited, as well as investigating the extrinsic and intrinsic contributions to the anomalous Hall effect. Previous measurements and reports of the magnitude of the topological Hall effect in materials hosting skyrmions have been inconsistent, both with each other and with the magnitude predicted by existing Berry phase theory [8; 10]. Further motivation for this research topic, relevant background condensed matter theory, and pertinent existing literature are discussed in detail in chapter 2.

Understanding the relationship between the number of skyrmions present and their individual

contribution to the Hall effect is essential for any future application of skyrmions in magnetic data storage devices. To this end, hysteresis loops in Hall resistivity were measured in $[\text{CoB|Ir|Pt}]_{\times n}$ samples, with $n = 1, 4, 6, 10, 15,$ and 18 ; at temperatures ranging from ~ 290 K down to ~ 5 K. The experimental equipment and methods used to perform these measurements are presented in chapter 3.

The analysis methods used to apply field corrections and carefully remove the ordinary and anomalous Hall effects from the Hall measurements to determine the excess resistivity, $\rho_{\text{xy,excess}}$, are described in detail in chapter 5.

Chapter 6 examines the behaviour of $\rho_{\text{xy,excess}}$ in relation to the temperature, sample structure, and corresponding anomalous Hall contribution. The $\rho_{\text{xy,excess}}$ signal measured in Pt/CoB/Ir multilayers is shown to change shape depending on the temperature and number of repeats in multilayer. Lowering the temperature increases the number of peak or trough like features present in the signal and lowering the number of multilayer repeats increases the variation in the number of features present at different temperatures. A potential correlation between the temperature dependence of the maximum $\rho_{\text{xy,excess}}$ signal and ρ_{A} is observed.

In chapter 7, the behaviour of the anomalous Hall resistivity in the same $[\text{CoB|Ir|Pt}]_{\times n}$ multilayers, and at the same temperatures, is investigated. In particular, the different extrinsic (skew scattering, α , and side-jump, β) and intrinsic (b) contributions to the anomalous Hall effect were determined from the scaling of the anomalous Hall resistivity, ρ_{A} , with the longitudinal resistivity, ρ_{xx} . The different contributions were found to be $\alpha = -0.02$, $\beta = 1710$ S/cm, and $b = 520$ S/cm. The AHE is shown to be described well, in samples with $n = 1, 4, 6,$ and 15 , by the expression $\rho_{\text{A}}M_0/M_S = (\alpha\rho_{\text{xx}0} + \beta\rho_{\text{xx}0}^2 + b\rho_{\text{xx}}^2)$, where $\rho_{\text{xx}0}$ is the residual longitudinal resistivity due to impurity scattering, ρ_{xx} is the temperature dependent longitudinal resistivity.

A summary of all results presented in this thesis and several suggestions for areas of further work are laid out in chapter 8. Here, in addition to suggestions for further investigation into the origins of the AHE and THE in $[\text{CoB|Ir|Pt}]_{\times n}$ multilayers, a summary of preliminary experimental work that was hindered by the COVID-19 pandemic and subsequent university building work is presented in section 8.2. In particular, an experimental set-up where Hall transport measurements and Kerr microscopy are combined provided solid preliminary results that indicate a potentially fruitful method for future work.

CHAPTER 2

Literature Review

2.1 Introduction

In this section a summary of the major advances in skyrmion research is given, as well as the beginnings of the essential theory describing magnetic skyrmions.

Section 2.2 introduces the interactions which govern the stability of skyrmions in different materials and allow us to tailor materials to produce environments where skyrmions are stable in the temperature and magnetic field ranges required for potential industrial application. The physical origin of the different types of anisotropies that occur in magnetism are discussed in n 2.2.1 and a separate section, 2.3, is dedicated to the Dzyaloshinskii-Moriya interaction, without which magnetic skyrmions would not be present in the CoB|Ir|Pt multilayers used throughout this project.

Section 2.5 introduces the concept of a skyrmion, beginning with its conception as a solution in particle physics through to its significance in condensed matter physics - pertinent to the subject matter of this thesis. The mathematical and topological properties of magnetic skyrmions are defined in Sections 2.5.1 and 2.5.2. The types of skyrmions which exist and their fundamental differences and similarities are covered in Section 2.5.3, followed by a discussion of the types of materials in which these different types are found in Section 2.5.4. These materials are roughly divided between the bulk materials which produce skyrmion lattices, and thin films or multilayers which can host individual skyrmions.

Section 2.6 concludes the literature review with some of the most significant recent advances including methods for nucleation of skyrmions, the dynamics of skyrmions and the environments necessary for their motion, the Skyrmion Hall Effect, and the potential applications of skyrmions in technology (2.6.2). The contributions to the Hall effect are discussed in Section 2.6.3. The physical origin of the ordinary Hall effect is explained, the behaviour of the anomalous Hall effect and its relationship to the scattering mechanisms in materials is discussed, and the current theoretical description of the topological Hall effect is laid out.

2.2 Interactions in Magnetism

There are multiple interactions which are required to permit the formation and stabilisation of magnetic skyrmions. Two of the most important interactions discussed in this section are the basic magnetostatic considerations of magnetic dipole-dipole interactions and the Heisenberg exchange interaction (Section 2.2) which has its basis in quantum mechanics. The Dzyaloshinskii-Moriya (Section 2.3) interaction is central to the mechanism allowing skyrmions to exist in the materials used in this project and as such is discussed in its own section.

Dipole-Dipole Interaction

The magnetic dipole-dipole interaction emerges from the potential energy of two magnetic dipoles μ_1 and μ_2 , which may be macroscopic, separated by a distance r ,

$$E_{\text{dipole}} = \frac{\mu_0}{4\pi r^3} \left[\boldsymbol{\mu}_1 \cdot \boldsymbol{\mu}_2 - \frac{3}{r^2} (\boldsymbol{\mu}_1 \cdot \mathbf{r})(\boldsymbol{\mu}_2 \cdot \mathbf{r}) \right], \quad (2.1)$$

where μ_0 is the permeability of free space. The interaction energy between the two can also be defined as the potential energy that each experiences due to the magnetic field from the other magnetic dipole,

$$E_{\text{dipole}} = -\boldsymbol{\mu}_1 \cdot \mathbf{B}_2(\mathbf{r}_1) = -\boldsymbol{\mu}_2 \cdot \mathbf{B}_1(\mathbf{r}_2), \quad (2.2)$$

where $\mathbf{B}_2(\mathbf{r}_1)$ is the magnetic field at the point \mathbf{r}_1 due to $\boldsymbol{\mu}_2$,

$$\mathbf{B}_2(\mathbf{r}_1) = -\mu_0 \nabla \left(\frac{\boldsymbol{\mu}_2 \cdot (\mathbf{r}_1 - \mathbf{r}_2)}{4\pi |\mathbf{r}_1 - \mathbf{r}_2|^3} \right) \quad (2.3)$$

and vice versa [11]. The magnetic dipole-dipole interaction is described using classical electromagnetism and allows us to describe the potential energy of magnetic materials in the presence of the magnetic field due to other magnetic materials. Dipole-dipole interactions are usually small and vanish in bulk cubic crystals; even in thin films, it is not strong enough to cause magnetic ordering. However, it leads to stray fields in ferromagnetic materials which contributes to important demagnetising effects and magnetic domain formation.

Heisenberg Exchange Interaction

The Heisenberg exchange interaction is a quantum-mechanical phenomenon, which occurs between two identical particles - e.g. two electrons - and determines the form that the Coulomb interaction takes when including the effect of the Pauli exclusion principle. The quantum mechanical wave function of identical particles exhibits an exchange symmetry. When two particles are swapped, this symmetry means that the wavefunction either remains unchanged if it is symmetric under exchange or changes sign in the case of an antisymmetric wavefunction. Fermions and bosons both have wave functions which are subject to this symmetry. For bosons, particles with integer spin, the overall wavefunction is symmetric whereas fermions, like electrons with spin- $\frac{1}{2}$, have antisymmetric overall wavefunctions that results in the Pauli exclusion principle. In order for the overall wavefunction to be antisymmetric one or other of the spatial and spin states must be antisymmetric while the other is symmetric. This means that the form of the spin state determines the spatial state. The Coulomb interaction energy is described by the spatial states of the wavefunction; therefore, the form of the spin wavefunction also affects this energy via antisymmetric requirement on the overall wavefunction. The Hamiltonian that describes the energy associated with this extra term in the Coulomb interaction for indistinguishable particles is given by

$$\mathcal{H}_{\text{Ex}} = - \sum_{i,j} \mathcal{J}_{ij} \mathbf{s}_i \cdot \mathbf{s}_j \quad (2.4)$$

where i, j denote atomic sites, J_{ij} is the strength of the exchange interaction between sites i and j , and $\mathbf{s}_i = \boldsymbol{\mu}_i/|\boldsymbol{\mu}_i|$ is the classical spin vector associated with the magnetic moment $\boldsymbol{\mu}_i$ at site i . The strength of exchange interactions at the atomic level (J_{ij}) influences the critical temperature of ferromagnets. Mean-field models predict that the Curie temperature of a simple ferromagnet with one nearest neighbour exchange interaction J_0 is

$$T_c = \frac{zJ_0}{k_B}, \quad (2.5)$$

where z is the number of nearest neighbours ($z = 6$ for simple cubic and face centered cubic), and k_B is Boltzmann's constant[12]. When considering real materials, there are many factors which affect the values of these idealised exchange interactions including: boundary conditions at the surface of a thin film which introduces frustration, strain and defects which change the electron wavefunctions[13], etc. These effects vary between samples, even when grown in similar conditions which can inhibit or enhance the ability to stabilise skyrmions[14]. Considering equation 2.4, one can see that the exchange energy will depend on the crystal structure of the material in question because different crystal structures have different numbers of nearest neighbours for which J_{ij} is non-zero.

2.2.1 Anisotropies in Magnetism

Anisotropies are asymmetries which cause states where the magnetisation points in certain directions to be more energetically favourable than others and must be taken into account in order to understand how non-collinear magnetic structures, for example skyrmions, can be supported in a material. Anisotropy is the general name given to the preference of a ferromagnetic material to maintain its magnetisation in a particular direction or plane relative to the sample as a whole. This occurs due to an energy cost associated with the rotation of the magnetisation into certain axes. The energy cost is related to multiple sources including: shape anisotropy which arises due to the shape of the magnet and the effects of dipole-dipole interactions including stray fields and demagnetising effects; magnetocrystalline anisotropy which is due to the spin-orbit interaction between the electrons in the lattice and the crystal lattice as a whole [15]; and surface anisotropy which occurs at surfaces and interfaces due to the loss of symmetry at the boundaries of a material. Understanding the interplay between anisotropies and the interactions discussed in Section 2.2 allows the materials used for device fabrication to be tailored in order to achieve the best environment in which to create and measure skyrmions.

Shape Anisotropy & Demagnetising Effects

Shape anisotropy occurs due to the long-range magnetostatic interactions—dipole-dipole interactions—this means that the magnetic energy depends on the macroscopic orientation of the magnetisation

with respect to the shape of the magnet. The total magnetostatic energy is given by the sum of discrete dipole-dipole interactions in the ferromagnet:

$$E_{\text{ms}} = \frac{\mu_0}{4\pi} \sum_{i,j} = \frac{1}{2|\mathbf{r}_{ij}|^3} \left[\boldsymbol{\mu}_i \cdot \boldsymbol{\mu}_j - \frac{3}{|\mathbf{r}_{ij}|^2} (\boldsymbol{\mu}_i \cdot \mathbf{r}_{ij})(\boldsymbol{\mu}_j \cdot \mathbf{r}_{ij}) \right], \quad (2.6)$$

where the summation is over all spins i, j , the factor $1/2$ accounts for double counting of interactions, $\mathbf{r}_{ij} = \mathbf{r}_j - \mathbf{r}_i$ is the displacement vector between sites i and j . In practice, this can be approximated as an integral over a continuous magnetisation field,

$$E_{\text{ms}} = -\frac{\mu_0}{2} \int_V \mathbf{M}(\mathbf{r}) \cdot \mathbf{H}_D(\mathbf{r}) d\mathbf{r}^3, \quad (2.7)$$

where E_{ms} is the magnetostatic energy, the integral is over the volume V of the sample, $\mathbf{M}(\mathbf{r})$ is the magnetisation field at the point \mathbf{r} , \mathbf{H}_D is the demagnetising (self-interaction) field. In most cases there isn't a simple expression for E_{ms} . But, assuming the ferromagnet is homogeneously magnetised, the magnetostatic energy becomes

$$E_{\text{ms}} = \frac{\mu_0}{2} M_S^2 (D_x m_x^2 + D_y m_y^2 + D_z m_z^2) V, \quad (2.8)$$

where x, y , and z refer to the Cartesian axes of the sample, M_S is the saturation magnetisation, $D_{x,y,z}$ are the demagnetising factors in each direction, $m_{x,y,z}$ are the components of the magnetisation unit vector, and V is the volume of the sample [12]. In this special case the demagnetising field is proportional to the magnetisation of the sample,

$$\mathbf{H}_{D,i} = -D_i \mathbf{M}_i, \quad (2.9)$$

where $i = x, y, z$ and denote the principle axes of the sample, D_i are the demagnetising factors, and M_i is the component of saturation magnetisation [12]. From this we can see that the magnetostatic energy will be higher when the magnetisation is oriented in the sample to increase the demagnetising factor. The aim of minimising this energy promotes either single domain ferromagnets or domain orientations which minimise the overall energy due to the demagnetising, or stray, field of a magnet. By considering a plate, where $D_x = D_y$, and $|\mathbf{D}| = 1$, it is possible to write the magnetostatic contribution as an effective easy plane anisotropy with anisotropy energy density, K_{ms} , which is given by

$$K_{\text{ms}} = \frac{\mu_0}{4} (1 - 3D_z) M_S^2, \quad (2.10)$$

where D_z is the demagnetising factor in the out-of-plane direction, M_S is the saturation magnetisation, and μ_0 is the permeability of free space [12]. For thin films $D_z \approx 1$,

$$K_{\text{ms,thin-film}} = -\frac{\mu_0}{2} M_S^2, \quad (2.11)$$

where M_S is the saturation magnetisation and μ_0 is the permeability of free space. This means that thin films will magnetise in-plane and other anisotropies must come into play in order to produce an out-of-plane remanence.

Magnetocrystalline Anisotropy

Magnetocrystalline anisotropy is an intrinsic property of ferromagnetic materials. To first order it occurs due to spin-orbit interaction between each individual orbital electron's spin and the potential of the crystalline lattice. Spin-orbit coupling couples the spin of an electron with the magnetic field produced by its motion, and it can be described by the Hamiltonian of an effective spin-orbit field which acts on the individual orbital moments,

$$\mathcal{H}_{\text{SO}} = -\mathbf{m}_l \cdot \mathbf{H}_{\text{eff SO}}, \quad (2.12)$$

where \mathbf{m}_l is the orbital moment and $\mathbf{H}_{\text{eff SO}}$, is the effective spin-orbit field given by

$$\mathbf{H}_{\text{eff SO}} = \frac{-e\hbar^2 \mathbf{S}}{4m_e^2 c^2 r \mu_B}. \quad (2.13)$$

In equation 2.13, \mathbf{S} is the spin unit vector, \hbar is the reduced Planck constant, e is the magnitude of the charge of the electron, m_e is the mass of the electron, c is the speed of light, r is the orbital radius of the electron with the spin vector \mathbf{S} , and μ_B is the Bohr magneton. The main point to take away from this is that due to spin-orbit interaction between individual orbital moments and the overall crystalline lattice there will be energetically preferred crystalline axes. These are referred to as 'easy' axes, the opposite of these, which are energetically undesirable, are called 'hard' axes. The easy axis anisotropy field, H_a^z , has the same magnitude as the field required to saturate the magnetisation of a crystal along its hard axis [16], and for a first order uniaxial anisotropy, this is given by

$$H_a^z = \frac{2K_1}{\mu_0 M_S}, \quad (2.14)$$

where K_1 is the first order uniaxial anisotropy constant.

Surface and Interface Anisotropy

Surface anisotropy is a special case of magnetocrystalline anisotropy and comes about due to symmetry breaking at the surface of crystals and at interfaces between different types of magnetic materials. This anisotropy was first described phenomenologically by Néel in 1954 [17], by considering the anisotropy energy per pair of magnetic atoms due to the angle between the bond axis and the magnetisation.

$$\mathcal{H}_i = -\frac{1}{2} \sum_{j \neq i}^{z_i} \mathcal{K}_{N,i} (\mathbf{S}_i \cdot \hat{\mathbf{r}}_{ij})^2, \quad (2.15)$$

where $\mathcal{K}_{N,i}$ is the Néel anisotropy constant (units of energy) which is non-zero for surface and interface atoms, z_i is the number of nearest neighbours for site i , \mathbf{S}_i is the spin vector of the magnetic moment at site i , $\hat{\mathbf{r}}_{ij}$ is the displacement unit vector between site i and site j , and the factor of two is included to prevent double counting. Although Néel's model adequately describes the symmetry of magnetic anisotropies, including surface effects, it is important to note that it does

not provide a physical understanding of magnetic anisotropy. Surface anisotropy is determined by crystal-field interaction and spin-orbit coupling just like magnetocrystalline anisotropy [12]. The loss of symmetry at surfaces and interfaces introduces additional microscopic sources of uniaxial anisotropy which are proportional to m_z^2 . This means we can write an effective total uniaxial anisotropy energy by adding these different sources. Over the last thirty years first principles surface and interface calculations have been performed for a number of systems including those most relevant to this thesis, that is multilayers [18], interfaces [19], nanowires [20; 21], and nanoparticles [22]. Surface anisotropy is the effect that causes the out of plane magnetisation in the samples used in this project.

Perpendicular Magnetic Anisotropy

Perpendicular magnetic anisotropy (PMA) is the term used to describe a magnetic material which has an overall anisotropy which causes the magnetisation of the material to point perpendicular to the plane of the material. This effect is due to the combination of the anisotropies described above. Néel was the first to suggest that the rotation of easy axis from IP to OOP originates in symmetry reduction from interfaces [17]. Shape, magnetocrystalline and interface anisotropies play a role in determining the easy axis of thin films. Considering surface, magnetocrystalline and magnetostatic sources of uniaxial anisotropy one can determine the necessary thickness of a thin film in order for it to have PMA. The total uniaxial anisotropy energy is

$$E_u = - \left(k_s A + K_1 V + \frac{\mu_0 M_S^2}{2} V \right) m_z^2, \quad (2.16)$$

where k_s is the surface anisotropy energy density (in units of energy per area), A is the area of the thin film surface, K_1 is the bulk magnetocrystalline uniaxial anisotropy energy density (units of energy per volume), V is the sample volume. The effective uniaxial anisotropy energy density K_{eff} is then

$$K_{\text{eff}} = \frac{k_s}{t} + K_1 + \frac{\mu_0 M_S^2}{2}, \quad (2.17)$$

where $t = A/V$ is the sample thickness. The surface and magnetocrystalline anisotropy densities have opposite sign with the surface anisotropy being an easy axis. So, as the sample thickness is decreased, the effect of the surface anisotropy is increased. The maximum thickness that a sample can be out-of-plane magnetised is

$$t_{\text{PMA}} = - \frac{k_s}{K_1 + (\mu_0 M_S^2/2)}. \quad (2.18)$$

Ferromagnetic samples grown with thicknesses less than t_{PMA} are expected to be perpendicularly magnetised.

2.3 Dzyaloshinskii-Moriya Interaction (DMI)

The Dzyaloshinskii-Moriya interaction is responsible for the stabilisation of skyrmions in the materials used throughout this project and as such it will be addressed in significant detail here. Anisotropic exchange interactions occur in materials with a crystal structure that lacks inversion symmetry. The Dzyaloshinskii-Moriya Interaction is an example of such an interaction, named for Dzyaloshinskii who proposed the interaction in 1957 [23] and Moriya who calculated the interaction for material systems including α -Fe₂O₃, MnCO₃, and CrFe₃ in 1960 [24]. An important aspect of the DMI is that it occurs when inversion symmetry is broken and as such it was suggested that DMI might be observable at the surface of a magnetic material [25]. This was confirmed analytically in 1998 by Crepieux and Lacroix [26] who used mechanisms suggested by Moriya [24], a microscopic model for localised magnetic systems, and Fert & Levy [27], a three-site mechanism like the one shown in Figure 2.1, to calculate the DMI vector, \mathbf{D}_{ij} . The direction of \mathbf{D}_{ij} was found for nearest neighbour sites at the surface and in the bulk for structures with simple cubic, BCC, and FCC lattices with different crystal planes as the surfaces in question [26]. Nearly ten years later the effect of interfacial DMI on the chirality of magnetic structures was observed experimentally in a Mn monolayer on W(110), which used spin-polarised scanning tunneling microscopy to resolve the chirality of magnetic order within the Mn layer [28]. The DMI has been shown to fix the chirality of domain walls and other structures, including skyrmions, throughout the material in which it acts [29; 30].

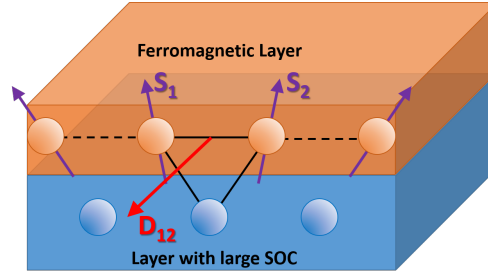


Figure 2.1: The interfacial DMI between a ferromagnetic layer and a layer of a material with a large spin orbit coupling.

Figure 2.1 illustrates the mechanism of the DMI suggested by Fert & Levy, and is described by the Hamiltonian,

$$\hat{\mathcal{H}}_{\text{DMI}} = \mathbf{D}_{12} \cdot \mathbf{s}_1 \times \mathbf{s}_2, \quad (2.19)$$

where \mathbf{D}_{12} is the DMI vector, and \mathbf{s}_1 and \mathbf{s}_2 are the spin vectors of the two ferromagnetic ions. This mechanism is particularly applicable to the samples used throughout this project which are thin multilayers and have an interfacial DMI. This type of DMI acts between ions in a ferromagnetic layer of material and is mediated through spin orbit coupling with atoms in an

adjacent layer. The mediation role of the adjacent layer can be seen more easily in the expression for the DMI vector, \mathbf{D}_{ij} ,

$$\mathbf{D}_{ij} = D_{ij} \sum_n \hat{\mathbf{r}}_{in} \cdot \hat{\mathbf{r}}_{jn} (\hat{\mathbf{r}}_{in} \times \hat{\mathbf{r}}_{jn}), \quad (2.20)$$

where D_{ij} is the DMI strength, n indexes the non-magnetic mediating atoms, $\hat{\mathbf{r}}_{in}$ is the unit displacement vector between the i -th ferromagnetic atom and the n -th non-magnetic mediating atom, and $\hat{\mathbf{r}}_{jn}$ is the unit displacement vector between the j -th ferromagnetic atom and the n -th non-magnetic mediating atom. The DMI strength, D_{ij} , and displacement unit vectors, $\hat{\mathbf{r}}_{in}$ and $\hat{\mathbf{r}}_{jn}$ are material dependent. This means that the size and direction of the DMI is highly dependent on the atomic species at an interface. This is because the type of atomic species affects the DMI strength (where a larger spin-orbit coupling in the non-magnetic mediating atoms increases the strength) and because different atomic species have different crystal structures which affects the direction of the DMI vector. Furthermore, as the direction of the DMI vector is dependent on the unit displacement vectors between the ferromagnetic interface atoms and non-magnetic mediating atoms, the direction of the DMI vector due to an interface with a ferromagnet on top of the non-magnetic layer (e.g. as shown in Figure 2.1) will be opposite to the direction of a DMI vector due to an interface with the same non-magnetic layer grown on top of that same ferromagnetic layer - assuming that the order of growth does not affect the crystallinity of the layers, and perfectly smooth interfaces. Additionally, the roughness of interfaces is expected to affect the DMI strength in multilayers because roughness introduces localised disorder into the interface which changes the directions of the unit displacement vectors in equation 2.20; thus, as the roughness of an interface increases the more disordered the local DMI vectors become. As DMI vectors become disordered the total DMI due to an interface decreases because some local vectors cancel with each other. The layer adjacent to the ferromagnetic layer has the essential property of a large spin orbit coupling, allowing atoms near the interface to mediate the DMI. This interaction acts to try to align the two spin vectors in a plane perpendicular to the DMI vector. In most cases the Heisenberg Hamiltonian is much larger than the DMI and as such the effect of the DMI is to slightly rotate the spins involved away from the collinear ordering that is favoured by the exchange interaction. This form leads to cycloidal magnetisation structures.

Due to its importance in stabilising skyrmions DMI strength in materials hosting skyrmions is an important parameter to characterise. A large number of methods to measure the DMI have been developed and employed over the last decade. The techniques fall into three broad categories: those that employ spin sensitive microscopy techniques to image the period of domain walls; those that exploit non-reciprocal spin wave propagation within materials with DMI; and those that rely on observations of domain wall motion due to currents or external magnetic fields.

The first group of methods, which employ the use of spin-sensitive microscopy techniques, includes: spin-polarised scanning tunnelling microscopy (SP-STM) [31]; spin-polarised low energy electron microscopy (SPLEEM) [32]; and X-ray magnetic circular dichroism photoemission electron micro-

scopy (XMCD-PEEM) [33].

SP-STM uses a tip magnetised in a known direction and a combination of differential conductance measurements and constant tunnelling current imaging to measure DMI[34]. The differential conductance measurements provide magnetic sensitivity while constant tunnelling current imaging provides a measure of the physical topology of the sample by requiring the tip to move up and down whilst scanning over the surface of the sample in order to keep the tunnelling current constant.

SP-LEEM uses spin-polarised illumination electrons with an initial energy range of around 15-20 keV that are emitted from an electron gun. These electrons are focused using condenser optics and deflected towards the sample using a magnetic beam deflector. The sample is held at an electric potential near to that of the electron gun meaning that the electrons decelerate to low energies between 1-100 eV near the surface of the sample and are ‘surface-sensitive’. The incident electrons are elastically scattered from a small area on the surface of the sample and the resultant diffraction pattern is dependent on the periodicity of the sample surface. The spin-polarisation of the incident electrons allows imaging of the magnetic surface structure due to spin-spin coupling which occurs between the incident electrons and those at the surface of the sample.

In XMCD-PEEM X-ray radiation is incident on the sample where the photoelectric effect means that the photons are absorbed by surface electrons and are emitted from the sample if the photon energy is more than the work function of the sample material. Local variations in electron emission, due to materials with different work functions or varying sample topography, are used to produce contrast in the images [33]. Using synchrotron radiation allows the energy of the incident light to be tuned to specific element edges, in particular the L absorption edges of the 3d transition metals are used when XMCD contrast is desired. The difference in absorption of oppositely circularly polarised X-rays in a magnetic material allows the magnetisation of the sample to be imaged using the emitted electrons [35]. The main drawback of these methods is the fact that all three can be expensive to perform as well as highly time consuming.

Brillouin light scattering (BLS) experiments make up the second type of technique and uses non-reciprocal spin wave propagation to measure the DMI [33; 36]. BLS experiments involve the use of a laser to irradiate the sample where the photons scatter inelastically with either thermally generated acoustic vibrations (phonons) or spin-waves which disrupt the magnetic ordering of the sample (magnons). Considering conservation of energy and momentum makes it clear that a magnon created by incident LASER light would create a back-scattered photon with less energy (and longer wavelength) than the incident photon (Stokes scattering), and that a magnon moving toward the applied laser light may be annihilated and a back-scattered photon with more energy (and shorter wavelength) would be created (anti-Stokes scattering). In the case of a symmetric spin-wave dispersion relation the back-scattered photon intensity peaks for Stokes and anti-Stokes scattering occur at the same frequency shift magnitude. The effect of the DMI on magnons is an anti-symmetric spin-wave dispersion relation [36], which manifests as a frequency shift for the

Stokes and anti-Stokes peaks. This is because the spatial chirality is fixed by the sign of the DMI. The DMI strength can then be calculated from the resultant shift in frequency,

$$\Delta f_{\text{DMI}} = \left| \frac{g_{\text{IP}} \mu_{\text{B}}}{h} \right| \text{sgn}(M_z) \frac{2D_{\text{DMI}}}{M_{\text{S}}} k_x, \quad (2.21)$$

where D_{DMI} is the DMI constant that determines the sign and magnitude of the DMI vector, g_{IP} is the in-plane spectroscopic splitting factor, μ_{B} is the Bohr magneton, h is Planck's constant, M_{S} is the saturation magnetisation, k_x is the in-plane component of the spin waves wavevector \mathbf{k} , and M_z is the out-of-plane component of the magnetisation.

The final group of methods relies on the simplification of the DMI to an intrinsic IP-field that enhances or diminishes the domain wall energy, and hence also the motion when driven by an applied current or magnetic field that occurs in the presence of an external IP-field. The interactions governing current-driven domain wall motion in multilayers with PMA have been theoretically [37] and experimentally [38–40] investigated by a number of research groups. This research illuminated some of the difficulties in using current-driven domain wall motion as a method for DMI measurement, most importantly that the use of current to drive the motion complicates the physics involved as the DMI is only one of several effects that are present. Both the Rashba effect and spin Hall effect (SHE) are also involved in producing the resultant motion and in order to untangle the three effects it is necessary to determine the exact strength of the different torques on the domain wall. To know this precisely it is also important to know how the current flows through the material, in particular the current flow through adjacent heavy metal layers in the multilayers needs to be calculated.

Methods that use domain wall observation due to applied magnetic fields have also been developed including asymmetric bubble domain expansion. The use of an in plane (IP) or out of plane (OOP) magnetic field to drive the domain wall motion allows the DMI to be investigated without having to account for spin Hall and Rashba effects. It is important to distinguish between methods which use domain wall motion in different speed regimes, the flow regime (high DW velocity, high applied fields) and the creep regime (low DW velocity, low applied fields). This is because the DW motion follows very different models in each regime and the internal structure of the DW can be deformed by the use of very large IP fields in the flow regime [41].

Asymmetric bubble expansions in the creep regime also rely on the DMI enhancing or diminishing the effect of an applied IP field on DW motion. Bubble expansions have been used by several groups to study the DMI of magnetic multilayers with perpendicular magnetic anisotropy [42; 43], like those used in the devices in this project. Bubble expansions can be a particularly attractive method as the samples do not require any special preparation and the method can be successfully performed using relatively common and inexpensive Kerr microscopes compared to the methods discussed previously which require synchrotron radiation. Many bubble expansions are performed and the difference in the velocity of domain wall motion of the bubble in the directions parallel

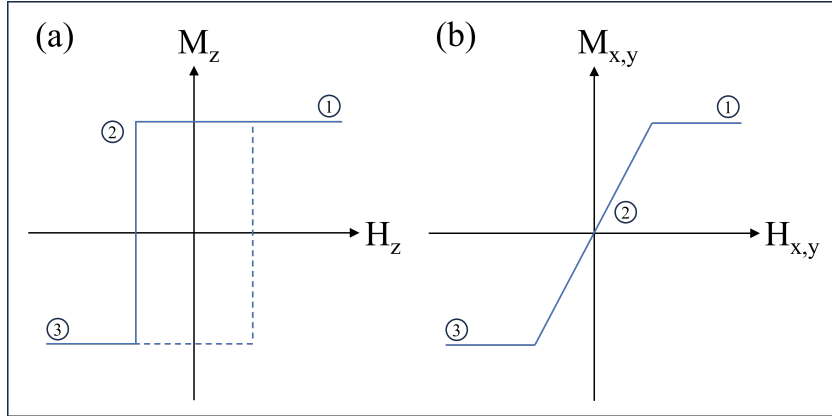


Figure 2.2: Exemplary M-H hysteresis loops for a single-domain particle, modelled by the Stoner-Wohlfarth model, switching magnetisation due to an applied magnetic field where (a) the magnetisation and applied field are along the easy axis; and (b) the magnetisation and applied field are along a hard axis. For consistency with comparison

and anti-parallel to the applied IP field corresponds to the addition or subtraction of the IP-field due to the DMI in the material. This third group all use an IP-field to enhance/oppose the DMI, by finding the balancing point (energy minima) in a material one knows the strength of the DMI field and therefore can calculate the DMI strength.

2.4 Magnetisation Processes in Ferromagnets

Hysteresis loops, or M-H loops, are the result of measuring the magnetisation of a sample as the function of an applied magnetic field. This type of measurement can provide information about the processes of magnetisation switching in magnetic materials which normally include domain formation and movement. By using the Stoner-Wohlfarth model one can begin to understand magnet switching processes. This model considers a single-domain particle in a magnetic field, H , where H is applied at an angle θ to the easy axis of the uniaxial anisotropy of the particle. Figure 2.2 shows the resulting M-H loops for a particle with an easy axis in the z direction, so that in (a) $\theta = 0$ and the magnetic field applied is also in the z direction, and in (b) $\theta = 90^\circ$ and the applied magnetic field is along the hard axis in the x,y plane perpendicular to the easy axis. In the first case, (a), where the magnetic field is applied along the easy axis, at point 1 in the loop the single domain particle has its magnetisation pointing in the same direction as the applied magnetic field. As this field is reduced, the magnetisation stays pointing in the same direction due to the uniaxial anisotropy which means that there is an energy barrier between the energy minima which are promoted by the anisotropy. The minima occur for the magnetisation pointing parallel or antiparallel to the easy axis. As the applied magnetic field begins to point in the opposite direction

along the easy axis, the energy barrier is initially too large for the direction of the magnetisation to flip directions. Eventually, at point 2 in the M-H loop, the energy provided by the applied magnetic field is large enough to overcome the barrier and the magnetisation immediately switches to point in the opposite direction along the easy axis in point 3. The same switching behaviour occurs when the magnetic field is changed from negative to positive - this is shown as a dashed line in Figure 2.2 (a). The field at which the magnetisation flips direction along the easy axis is called the coercive field. This field is related to the energy required to overcome the effective uniaxial anisotropy.

By contrast in 2.2 (b), when a magnetic field is applied along the hard axis of the single domain particle the magnetisation continuously rotates from pointing along the hard axis in region 1, to pointing the opposite direction along the hard axis in region 3. Region 2 is the region where the magnetisation is continuously varying and has an easy axis component and a hard axis component. When there is no applied field the magnetisation is along the easy axis due to the anisotropy of the magnetic particle.

In an idealised ferromagnetic, with very strong exchange coupling, and no local variations in anisotropy magnetisation would be expected to behave very similarly to a single-domain particle where all the magnetic moments in the material switched together. However real materials normally have defects. In real samples, such as the multilayered ferromagnetic thin films used in this project, such physical defects may include grain boundary dislocations or atomic vacancies, mixing of atomic species at interfaces between layers. Defects in real samples produce local variations in the effective anisotropy. This means that, in some areas of a sample, the field required to overcome the local anisotropy may be smaller than the coercive field of the whole sample.

Figure 2.3 (a) shows the expected shape of an M-H loop for a thin ferromagnetic multilayer where the field is applied along the easy axis (out-of-plane of the film). Starting from region 1 where the magnetisation is saturated in the same direction as the applied field, the applied magnetic field is reduced but the effective uniaxial anisotropy keeps the sample magnetisation directed along the easy axis. Then, as the direction of the applied field is reversed, at point 2 domains start to form in the material. This is because the applied field is large enough to switch a small volume of the sample which has a lower local uniaxial anisotropy than the rest of the film. Now at least one domain exists in the sample and it is aligned with the applied magnetic field. As the size of the applied field in the same direction as the domain is increased, this domain is favoured energetically and so it grows by slow domain wall motion in region 3. Additionally, further magnetic domains may also be nucleating around point 3. As the applied field is further increased the speed of domain wall motion increases and the energetically favoured domains expand through the steepest part of the loop which is labelled 4. Finally, these domains merge and a single domain saturated state is reached at point 5 in Figure 2.3 (a). Magnetic skyrmions are special types of magnetic domains that have additional topological characteristics and so one would expect them to be present in the multi-domain regions of a hysteresis loop (between 2 and 4).

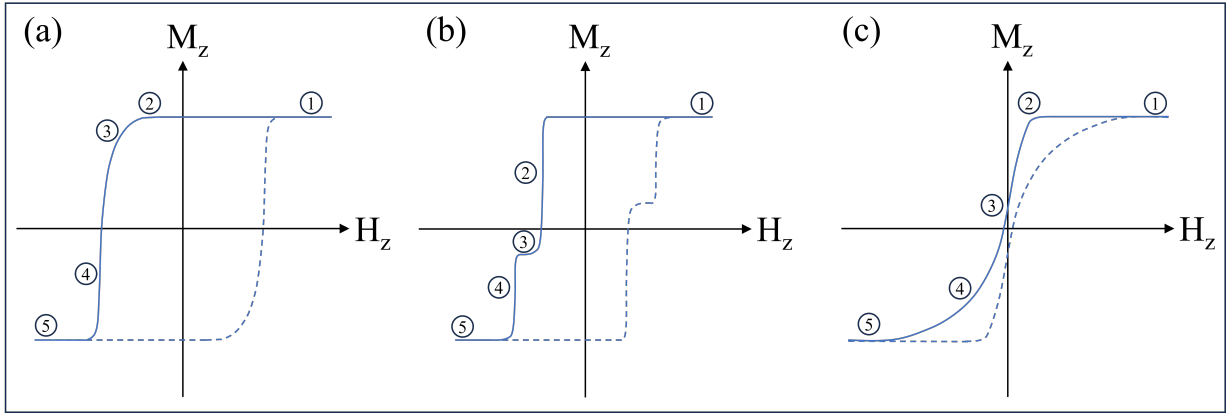


Figure 2.3: Exemplary M-H hysteresis loops for (a) a ferromagnetic multilayered thin film with strong PMA, switching by domain formation; (b) a ferromagnetic multilayered thin film with decoupled ferromagnetic layers where the decoupled layers switch magnetisation by single domain formation; and (c) a ferromagnetic multilayered thin film with a larger number of multilayer repeats which switches via maze domain states.

Figure 2.3 (b) illustrates a stepped hysteresis loop that can occur in magnetic multilayers when there are non-magnetic spacer layers between ferromagnetic layers. If the non-magnetic layers are too thick, and the effective anisotropy of the individual layers is different leading to different coercivities, then the ferromagnetic layers can become decoupled and switch independently. For simplicity, we can imagine a multilayer with two ferromagnetic layers and a non-magnetic spacer layer in between. In this case, the hysteresis loop switching dynamics as like those discussed for M-H loop (a) but instead of steps 2-4 (a) occurring for domains that are stabilised through all of the multilayer at once (in both ferromagnetic layers), steps 2-4 (a) occur twice with domains being nucleated in the layers independently at points 2(b) and 4(b) when the coercive fields of each layer are reached. Point 3 is the state where one layer is still saturated parallel to the easy axis and the other layer is saturated anti-parallel to the easy axis. At point 3 the sample may have a finite magnetisation along the easy axis if the ferromagnetic layers do not have the same magnetisation per layer, for example if the two layers are made of different ferromagnets (e.g. Co and Ni [44]) and/or the layers different thicknesses.

Figure 2.3 (c) shows the expected shape of an M-H loop for a ferromagnetic multilayer with a large number of layers. As the number of layers in a magnetic multilayer increases so does the total thickness of the multilayer. As the total thickness of the ferromagnet increases it becomes more energetically favourable for the sample to break up into magnetic domains to minimise stray fields and the magnetostatic energy cost of the whole sample remaining one domain. At point 1 in the third hysteresis loop the sample is fully saturated, with the applied magnetic field making it energetically favourable for all the moments to be aligned in the direction of the applied field. At

point 2 in the hysteresis loop the applied magnetic field is no longer strong enough to stabilise a single domain state due to the high stray fields produced meaning that a multi-domain state has lower energy. This means that the sample begins to break up into maze-like domains before the applied magnetic field reaches zero. The applied magnetic field favours the domains which point in the same direction as the applied field. At point 3, there is no applied magnetic field and the sample exhibits maze-domains. There is a small remanent magnetisation but the maze domains in the sample nearly cancel each other out as the stray fields are minimised. At point 4 the applied magnetic field points in the opposite direction and favours domains of the opposite magnetisation. This means that the maze-domains favoured expand and the domains with opposite magnetisation contract accordingly. This occurs by domain wall motion, but at the highest magnetic fields coherent rotation of the domains to a direction that is aligned with the applied magnetic field occurs so that the sample is fully saturated at point 5. Again, skyrmion formation would be expected to occur in the multidomain regions 2-4 for samples with this kind of magnetisation loop.

Domain wall motion during hysteresis loops can also be affected by domain wall pinning due to defects in samples. Sometimes very small steps can be seen in magnetisation loops where the magnetisation of a ferromagnet is changing via the Barkhausen effect [11]. In this case the magnetisation changes by discontinuous domain boundary changes that balance the energy costs of being misaligned with the applied field and the magnetostatic energy from stray fields.

2.5 Magnetic Skyrmions

The word skyrmion generally refers to topologically protected defects in continuous non-linear fields which were first considered by Tony Skyrme in 1962 [45]. He considered that these defects, or multidimensional solitons, might behave as particles and that he might be able to thus create a field theory describing mesons and baryons. Despite the origin of skyrmions in particle physics the theory has now been applied to a wide variety of other areas of physics where field theories are essential to explaining phenomena. Most notable is the area of condensed matter physics where skyrmion theory has been applied to various quantum hall and superconductivity theories [46], as well as liquid crystals [47] and Bose-Einstein condensates [48; 49].

Magnetic skyrmions are nano-sized magnetic structures which occur in a variety of different magnetic materials [50]. Their existence in thin films and magnetic multilayers was first predicted in 2001 by Bogdanov and Roßler [51] and subsequently observed in 2011 by Heinze et. al. [52] in a one-atom layer of iron (Fe) on iridium (Ir(111)). The skyrmions present in this material were found to be the magnetic ground state of the monolayer of Fe on Ir, arranged spontaneously in a two-dimensional square lattice. Materials capable of hosting a skyrmion lattice are briefly discussed in section 2.5.4. Individual skyrmions have also been observed in thin multilayers which exhibit an interfacial Dzyaloshinskii-Moriya interaction (DMI) [23; 24] due to interfacial symmetry breaking

at heavy metal/ferromagnet/insulator layers and, importantly, have been shown to form using a driving current which introduces spin transfer torque (STT) [53]. The type of skyrmion present in different materials is highly dependent upon the form and origin of the DMI, this will be discussed in detail in sections 2.5.3 and 2.3.

2.5.1 Skyrmion Definition

Despite the fact that skyrmions are well defined mathematically, by the topology of the magnetisation texture (discussed in Section 2.5.2), their definition and telling them apart in experimental circumstances is slightly more complicated. The complications arise mainly due to ambiguity in experimental methods that are used to observe skyrmions. For example magnetic force microscopy (MFM) is widely used, however it is unknown how much the MFM tip affects the magnetisation texture. X-ray Magnetic Circular Dichroism-Scanning Transmission X-ray Microscopy (XMCD-STXM) allows the out-of plane magnetisation of a sample to be imaged, however as the effect imaged is the overall magnetisation of the whole sample at each point it can be unclear if the skyrmion observed is present throughout all layers in a magnetic multilayer or only in some of them.

In a similar way whether or not the observed textures are ‘true’ skyrmions rather than topologically non-trivial bubble domains seems to be debated in the community and decided by rather arbitrary means such as the size and/or temperature at which they are observed, or by which mechanisms the textures are stabilised. Here a topologically non-trivial bubble domain is considered to be a bubble domain with non zero twists in its magnetisation texture, as defined by the skyrmion winding number, which is given in equation 2.22 in section 2.5.2. These are considered to be distinct from skyrmions due to their much larger size.

Over the last twenty years magnetic skyrmions have been shown to be stable magnetisation structures [54] (as skyrmion crystals [55], skyrmion lattices [56–59], and individually [5; 8; 56; 60]), in a variety of materials (including bulk materials [56–59; 61; 62], thin films [63], and heterogeneous multilayers [5; 8; 60; 64; 65]), and can occur at a range of temperatures from 4.2 K in a PdFe bilayer on an Ir(111) substrate [66], up to room temperature in nanostructures of Pt|Co|MgO [33], Ir|Fe|Co|Pt [67] and Pt|Co|Ir magnetic multilayers [8], and in the β -Mn-type chiral magnet $\text{Co}_9\text{Zn}_9\text{Mn}_2$ [61].

Recent work to extend magnetic skyrmion theory to include the structure and energetics of as many as possible of the types of skyrmions observed has been done by F. Büttner et al. [68]. They concluded that the stabilisation method of different skyrmions could be determined from the radii of the skyrmions at their point of collapse, for room temperature skyrmions DMI stabilised were found to collapse at diameters $\ll 10$ nm whereas skyrmions stabilised by stray fields collapse at diameters $\gg 10$ nm. Büttner et al. also hold the opinion that all the skyrmions observed in the citations in this paragraph are true skyrmions however they may be defined by a combination of

size and the origin of the minima in their energy landscapes into one of three categories: DMI skyrmions, bi-stabilised skyrmions, and stray-field skyrmions.

2.5.2 Topological Considerations

Skyrmions are defined by the mapping of their magnetisation directions onto a sphere. One pole of the sphere represents the outside of the skyrmion and the other its centre, resulting in a sphere with arrows pointing outwards radially at all points in the case of a Néel skyrmion, as shown in Figure 2.4 [69]. The mapping of the Bloch skyrmion magnetisation onto the surface of a sphere is also possible. This topology is defined by the skyrmion winding number, W_{sk} , which indicates the integer number of ‘twists’ in magnetisation texture of a skyrmion, written as

$$W_{sk} = \frac{1}{4\pi} \int \mathbf{M} \cdot \left(\frac{\partial \mathbf{M}}{\partial x} \times \frac{\partial \mathbf{M}}{\partial y} \right) dx dy. \quad (2.22)$$

The fact that the skyrmion winding number cannot be changed by a continuous variation of the local magnetisation of the skyrmion is the cause of its enhanced stability relative to topologically trivial domain walls.

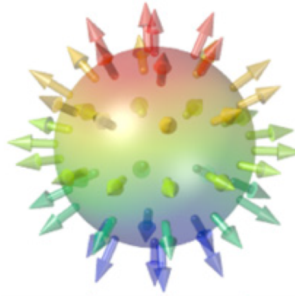


Figure 2.4: The local magnetisation of a Néel skyrmion mapped onto the surface of a sphere in spin space.[69]

The enhanced stability and countability of skyrmions lends itself to applications in high density data storage, which is discussed in detail later in section 2.6.2. Despite their interesting topology and potential for novel spintronics skyrmions are essentially just special magnetic domains and therefore they are subject to all the physics which describes magnetism in general therefore it is essential to understand the interactions responsible for the origins of ferromagnetism as well as the special combinations of anisotropies and interactions that allow skyrmions to be stabilised in certain magnetic materials.

2.5.3 Types of Skyrmions

Bloch Skyrmions are defined by a circular domain wall in which the magnetisation direction rotates from one direction at the perimeter to the opposite in the centre, whilst in plane magnetisation

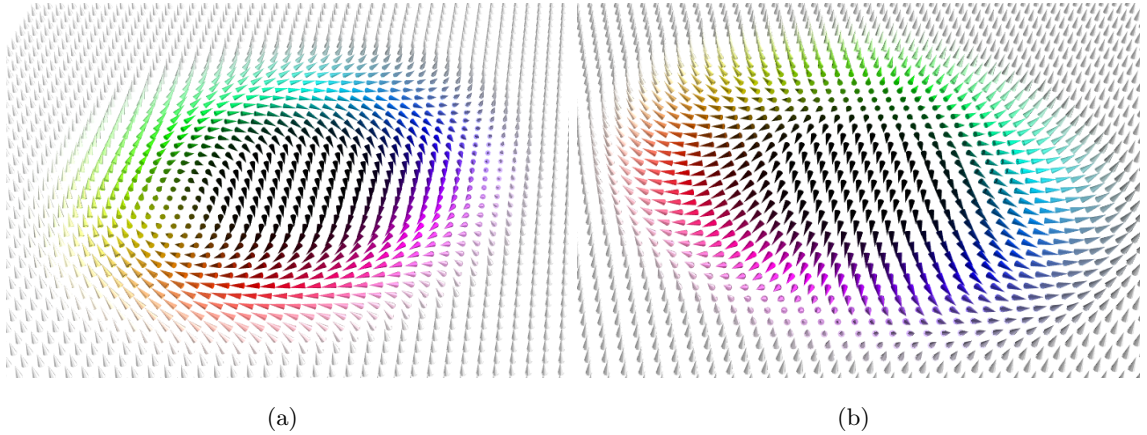


Figure 2.5: Types of Skyrmion: (a) A Bloch type skyrmion; (b) A Néel type skyrmion. Both types of skyrmion have magnetisation pointing upwards along the z axis around their perimeter and downwards along the z axis in their centres. In between the edge of the skyrmion and the centre there exists a finite, circular domain wall which is either (a) Bloch or (b) Néel.

always points tangentially to the domain wall, as shown in figure 2.5 (a). These types of skyrmions are most commonly found as lattices in materials with the bulk DMI including MnSi and other B20 materials which have chiral crystal structure [55; 70].

Néel Skyrmions are defined similarly to Bloch skyrmions however, they differ in that the magnetisation rotates from up to down whilst the in plane component of the magnetisation always points in a direction parallel or antiparallel to the skyrmion radius, as shown in figure 2.5 (b). Néel type skyrmions are most commonly observed in materials formed of magnetic multilayers where there is a large perpendicular magnetic anisotropy (PMA). The PMA draws the magnetisation of the material up out of the plane of the layers and this along with an additive in plane DMI leads to magnetisation that points radially through the skyrmion.

2.5.4 Materials Hosting Skyrmions

Understanding the types of materials which can host different types of skyrmions is very important for any eventual application to industry. It is also an important consideration for this project which involves the design and fabrication of devices which will enable the investigation of electrical transport properties of skyrmions. In particular emphasis on the difference between materials in which 2D skyrmion lattices occur, spontaneously or in the presence of magnetic field, versus materials in which individual skyrmions are both present and stabilised is important. The main difference between these two groups is that skyrmion lattices typically occur in bulk materials and individual skyrmions are observed in various types of multilayer however both types require a DMI to stabilise them. In bulk materials that occur as cubic B20 crystals lacking inversion symmetry, such as MnSi, it was shown that the DMI was responsible for these observed helical magnetic

structures [55; 70; 71].

2.5.5 Magnetic Multilayer Design Strategies

The magnetic interactions discussed in sections 2.2 and 2.3 each play a fundamental role in stabilising magnetic skyrmions in different materials and they need to be balanced correctly in order for skyrmions to appear in the ferromagnetic multilayers used in this project. The exchange interaction and overall anisotropy of thin films promote the formation of domains with out-of-plane magnetisations. The DMI acts to cant the magnetic moments away from the easy axis of the samples (normal to the plane of the sample). Intrinsic material properties have an effect on the DMI strength produced and the DMI can be tailored by modifying the ferromagnet-heavy metal interfaces in a sample. For example, an additive DMI can be produced by putting layers of Pt and Ir on opposite sides of a ferromagnetic layer. This is possible because Pt and Ir have opposite spin-Hall angles which means their DMI vectors point in opposite directions when they exhibit the same relative displacement from ferromagnetic atoms. Thus, careful choice of the materials in magnetic multilayers can change the DMI in a material and make it easier, or harder, to stabilise skyrmions. The DMI discussed here is an interfacial effect and therefore one can increase or decrease the DMI in a multilayer by changing the number of layers (and therefore changing the number of interfaces contributing to the DMI).

The exchange interaction and overall anisotropy are responsible for determining the direction of the magnetisation in the centre of skyrmions and the background magnetisation of the sample. If the sample is grown too thickly then it can exhibit an easy-plane anisotropy rather than perpendicular magnetic anisotropy. This means that there is a limit to how much one can increase the DMI by increasing the number of interfaces in a sample before the exchange and anisotropy overwhelm the DMI making the sample in-plane. Even before the sample exhibits an in-plane anisotropy too many layers can lead to demagnetising and stray field effects that make maze-domains more energetically favourable than skyrmions.

Using heavy-metal layers that are too thick in between ferromagnetic layers can lead to uncoupled ferromagnetic layers that switch magnetisations individually. This could also lead to skyrmions that are only present in some parts of a magnetic multilayer, and domains that are not continuous through all the layers of a sample.

Previous experiments undertaken by members the University of Leeds Condensed Matter group and collaborators at the Paul Scherrer Institut had successfully combined X-Ray Magnetic Circular Dichroism-Scanning Transmission X-ray Microscopy (XMCD-STXM) with electrical transport measurements so that Hall resistivity measurements could be directly connected to the magnetisation textures responsible [60]. This set-up yielded promising measurements of the Hall resistivity due to individual skyrmions in Ta(3.5 nm) | Pt(3.8 nm) | [Co(0.5 nm) | Ir(0.5 nm) | Pt(1.0 nm)]_{×10} | Pt(3.2 nm) multilayers [8]. The use of Co/Ir/Pt multilayers of this structure was partially in-

formed by academic works published in 2014 and 2015 which demonstrated that introducing an Ir layer above the Co layer in Pt/Co/Pt trilayers was capable of inducing a much stronger DMI than in Pt/Co/Pt trilayers [42], and that Co/Pt interfaces and Co/Ir interfaces produced interfacial Dzyaloshinskii-Moriya interactions with opposite signs [72]. As previously discussed in section 2.3, the direction of the DMI vector is dependent on the relative displacement of the ferromagnetic atoms and the non-magnetic mediating atoms. This means that symmetrical multilayers like Pt/Co/Pt are expected to have zero DMI if the interfaces between layers are perfect. In reality, such symmetrical multilayers often have small non-zero DMIs due to interface roughness and defects. In 2016, Moreau-Luchaire et al. exploited the ‘additive’ interfacial DMI created by positioning Pt and Ir on opposite sides of the Co layer such that the opposite DMIs produced by Co/Pt and Co/Ir interfaces instead pointed in the same direction in asymmetric $[\text{Ir}/\text{Co}/\text{Pt}]_{\times 10}$ multilayers [73]. One would expect to see the same additive effect (pointing in the opposite direction) in Pt/Co/Ir multilayers. Moreau-Luchaire et al. also showed that the additive DMI in such multilayers was capable of stabilising individual skyrmions at room temperature.

Extrinsic factors can also affect skyrmion formation. For example, one would expect it to be harder to stabilise skyrmions at higher temperature because thermal fluctuations are more prevalent and so atomic moments are more disordered. All of the interactions discussed are expected to be reduced at higher temperatures because random thermal motion becomes dominant over magnetic ordering.

Finally, defects in real samples can make it easier or harder to nucleate and stabilise skyrmions. This is because defects can change the local energy landscape in a sample, either increasing or decreasing the local anisotropy. Similarly, intermixing and roughness at interfaces can cause local changes in the direction of the DMI such that the overall DMI is reduced due to some cancellation from disordered DMI vectors. If a ferromagnetic-heavy metal interface was extremely rough one would expect the DMI vectors to point randomly and produce a negligible overall DMI. This means that the quality of the interfaces in the ferromagnetic multilayers grown in this project is particularly important if skyrmions are to be stabilised successfully.

2.6 Advances in Skyrmion Research

Initially skyrmions were first observed as lattices in bulk and thin film materials, as discussed in Section 2.5. Individual skyrmions were then observed soon afterwards in a PdFe bilayer by Romming et al. [63]. Despite also showing that they could be manipulated in a controlled manner using spin-polarised tunnel currents this was only possible under quite specific conditions, at very low temperatures (≈ 4 K) and in the presence of an applied magnetic field (≈ 1 T) perpendicular to the surface of the material [63]. Romming et al. also showed that the size and shape of individual magnetic skyrmions was dependent on the magnetic field applied. By combining an

analytical expression describing skyrmions with experimental data they were able to show that careful experimental characterisation of the materials used can provide parameters, like DMI, which are responsible for the stability of individual skyrmions [74]. More recently individual skyrmions have been predicted [73] and observed at room temperature [33; 75], two conditions that are essential if skyrmions are ever to have widespread use in industry.

2.6.1 Skyrmion Dynamics

The effect of pinning and hysteresis on the ability to nucleate skyrmions and move them using currents has been shown by Zeissler et al. [65] where they found that disordering in materials which create pinning sites are, in fact, important in order to nucleate skyrmions. The disorder demonstrated that it is harder to predict the DMI in real materials and the authors attributed the higher than expected currents needed to drive skyrmions to pinning in samples. Skyrmion size also had a large impact on its ability to move, where skyrmions much larger or much smaller than the pinning sites had higher velocities. This was due to larger skyrmions being able to ‘stretch’ around the pinning site and smaller skyrmions being more able to move around them [65].

The Skyrmion Hall Effect (SkHE) is an important effect that has recently been predicted and observed. It sees the deflection of skyrmions during motion due to applied current pulses [32; 76]. The SkHE has been likened to a Magnus effect caused by the topological charge of skyrmions and analogous to the Hall effect that occurs with electrical charges in a magnetic field [69]. The SkHE causes magnetic skyrmions experiencing an applied electrical current to travel in trajectories at an angle to the direction of driving current. A modified Thiele equation, derived from the Landau-Lifshitz-Gilbert equation that describes the time evolution of magnetization, describes the forces acting on moving skyrmions in the presence of an electrical current as

$$\mathcal{D}(\tilde{\beta}\mathbf{v}_s - \tilde{\alpha}\mathbf{v}_d) + \mathbf{G} \times (\mathbf{v}_s - \mathbf{v}_d) + \mathbf{F}_{\text{pin}} = 0, \quad (2.23)$$

wherein \mathcal{D} is the dissipation strength; $\tilde{\beta}$ and $\tilde{\alpha}$ are effective damping parameters; $v_s \approx \frac{j_s}{|\mathbf{M}|}$ is the effective spin velocity; v_d is the drift velocity of the magnetic texture; \mathbf{G} is the gyrocoupling vector which is given directly by the topological winding number, S , in equation 2.22; and \mathbf{F}_{pin} is the phenomenological pinning force [69]. The effective damping parameters are defined by

$$\tilde{\alpha} = \alpha + \alpha' \frac{D'}{D} \text{ and } \tilde{\beta} = \beta + \beta' \frac{D'}{D}, \quad (2.24)$$

where α is the Gilbert damping parameter, α' is a non-linear damping parameter with the same units as Gilbert damping (α), β is the damping parameter for spin transfer torques, β' is a spin transfer torque damping parameter, D is normal dissipation, and D' is the extra dissipation due to the effective field from skyrmion magnetisation. The effective damping parameters in equation 2.23 are dependent on the properties of the material hosting the skyrmion. For a stationary skyrmion with no applied current equation 2.23 has ($v_s = 0$), and as skyrmion does not drift, $v_d = 0$,

due to pinning by impurities in the material. When a current is first applied the pinning force, \mathbf{F}_{pin} compensates for the current induced forces and the skyrmion stays pinned. Once the current density is large enough the first two terms in 2.23 are larger than the pinning force, \mathbf{F}_{pin} , and the skyrmion starts to move. The first term in 2.23 is a dissipative force that moves the skyrmion in the direction of the spin current, and the second term describes a Magnus force acting on the skyrmion. For a skyrmion lattice Jiang et al. [32] used a current-induced spin Hall spin torque to drive skyrmions from the creep-motion regime to the flow-motion regime, observing a resultant skyrmion accumulation at the edge of their device, made of annealed Ta(50 Å)|Co₂₀Fe₆₀B₂₀(11 Å)|TaO_x(30 Å) trilayers grown on 300 nm thermally oxidised silicon. The angle of deflection, the Skyrmion Hall angle (θ_{sk}), is expected to plateau at a constant value when the skyrmions are moving at a large enough velocity. Pinning and disorder within the sample leads the Skyrmion Hall angle to be current-dependent[77].

2.6.2 Potential Applications

The effect of climate change is one of the most pressing issues of the modern day. One month before I began my PhD research in June 2018, Forbes magazine reported that every day we are generating 2.5 quintillion bytes of data [1]. The electricity required to store and recall that data has become a significant proportion of the total used each year with the Independent reporting that in 2016 the electricity used globally for data storage was 1.5 times the total amount used by the UK annually [2]. Application of magnetic skyrmions to magnetic data storage has been proposed as an alternative, lower energy, method of data storage due the potential ease of writing and deleting them compared to conventional magnetic domains. In particular, the ability to nucleate (‘write’) and manipulate skyrmions with small current densities is promising and their potential for use in logic gates has already been demonstrated [3]. The direct writing of room temperature skyrmion lattices was realised in 2018 by Zhang et. al. in Pt/Co/Ta multilayers using Scanning Magnetic Force Microscopy[4]. Racetrack memory devices have been suggested as energy efficient data storage replacements for DRAM and Flash, and a strategy for such a device employing Néel skyrmions was suggested in 2014[7].

Fully realised racetrack memories have been predicted to outperform MRAM and phase-change RAM in terms of storage density. However, because racetrack memory relies upon bits (domains) that are stored in different places along a track, accessing data would take different times to be accessed by read/write sensors by moving the bits along the racetrack using a current. This time is limited by domain wall motion within the racetrack. Additionally, the density of data storage is limited by the maximum density of traditional domains. Skyrmions were suggested are improved magnetisation textures for use as bits in racetrack memories due to several advantageous features that they have over traditional domains. The most important of these is the topological protection afforded to them due to their integer twists in magnetisation. Their topology means that skyrmions

are generally harder to annihilate than domain walls. This means that they are considered to be more robust against accidental annihilation than conventional domains without topological protection. Furthermore, skyrmions can exist in much higher densities than conventional domain walls and be moved at higher speeds using lower current densities than normal domains[78]. The velocity of traditional domain wall motion is also limited by an effect called Walker breakdown [79]. Domain wall velocity increases proportional to the applied current up to a certain point - the Walker breakdown - after which there is a decrease in the net domain wall velocity before it begins to increase again with increased current. The domain wall motion prior to Walker breakdown is smooth whereas after the Walker breakdown the domain wall begins to oscillate, moving with a net velocity in the direction of the applied current but more slowly. By contrast, skyrmions have been predicted to have a universal current-velocity relationship that is less sensitive to Gilbert damping, nonadiabatic effects, and impurity pinning than conventional domain walls [78].

In order to progress towards the realisation of such technologies it is necessary to fully understand the material properties which have an effect on the electrical transport behaviour of skyrmions. The Hall effect is particularly important in this regard because the non-trivial topology of skyrmions has been shown to cause an additional contribution to the Hall effect that could be used to electronically detect the presence of skyrmions. A complete understanding of this topological Hall effect is necessary in order to electrically read any data stored using skyrmions.

2.6.3 The Hall Effect

Despite the original discovery of the Hall effect in 1879 by Edward Hall, first for normal metals[80], and then in 1881 the larger effect which is seen in ferromagnetic materials[81], it has taken well over one hundred years to establish a firm theoretical understanding and description of the latter. Hall observed that when a magnetic field is applied perpendicular to a current flowing within a conducting material, then a voltage is produced across that conductor, transverse to the direction of current flow[80]. It is instructive to consider this effect in terms of the so called Hall resistivity (ρ_{xy}), or Hall conductivity (σ_{xy}), which expresses the ratio between the Hall voltage (V_H) and the current. This has allowed the overall phenomena seen in various types of materials to be broken down into the constituent Hall resistivities:

$$\rho_{xy} = \rho_{xy}^O + \rho_{xy}^A + \rho_{xy}^T, \quad (2.25)$$

where each resistivity term is attributed to separate physical phenomena. The overall Hall resistivity measured during experiments, ρ_{xy} , is given by the sum of the ordinary (ρ_{xy}^O), anomalous (ρ_{xy}^A), and topological (ρ_{xy}^T) Hall effects as shown in equation 2.25.

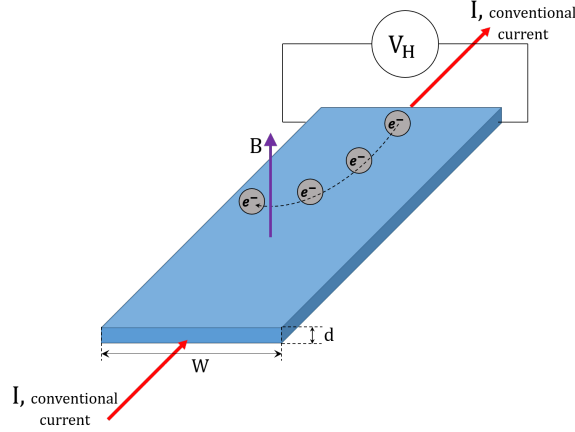


Figure 2.6: Schematic of an experimental arrangement to measure the ordinary Hall effect. The electrons follow a curved path to one side of the metal due to the Lorentz force from the external magnetic field, \mathbf{B} . Note the electrons move with a velocity opposite to the direction of the conventional current.

Ordinary Hall Effect (OHE)

The ordinary Hall effect was the first effect to be observed, in ordinary (non-magnetic) metals. By considering an experimental setup like the one shown in Figure 2.6 the effect can be explained simply by a qualitative understanding of the Lorentz force acting on the current flowing in the metal. Electrical current is the motion of charge carriers within a material, for a simple metal with electrons acting as charge carriers, the force experienced when moving in a magnetic field is given by the second term in

$$\mathbf{F} = \mathbf{F}_E + \mathbf{F}_B = q(\mathbf{E} + \mathbf{v} \times \mathbf{B}), \quad (2.26)$$

where \mathbf{E} is the electric field experienced by the charge carrier, q is the charge of that carrier, \mathbf{v} is the drift velocity of the charge carriers, and \mathbf{B} is the magnetic field experienced by the charge carriers. By virtue of the cross-product in equation 2.26 it is possible to predict the direction of the Lorentz force using a right-hand rule where the thumb (\mathbf{v} - velocity of electrons), first finger (\mathbf{B} - applied magnetic field), and second finger (\mathbf{F}_B) take on the role of the three perpendicular vectors involved in the second term of the Lorentz force. Given this one should now expect the electrons to follow a path which curves towards one side of the material, according to the direction which the Lorentz force acts in, as shown in Figure 2.6. It was shown experimentally that the Hall resistivity for the OHE is proportional to the externally applied field,

$$\rho_{xy}^O = R_O B_z, \quad (2.27)$$

where R_O is the ordinary Hall coefficient. The ordinary Hall coefficient is defined as

$$R_O = \frac{E_y}{j_x B_z} = \frac{V_H d}{I_x B_z}, \quad (2.28)$$

where E_y is the induced electric field, $j_x = \frac{I_x}{d}$ is the current density, and B is the external field. V_H is the Hall voltage which can be found by solving equation 2.26 at equilibrium ($\mathbf{F} = 0$) to yield,

$$V_H = \frac{I_x B_z}{nte}, \quad (2.29)$$

where n is the charge carrier density, t is the sample thickness, and e is the magnitude of the charge of the electron.

Anomalous Hall Effect (AHE)

Ferromagnetic materials were observed to have a much larger Hall signal than normal metals shortly after the discovery of the OHE in 1881[81]. This came to be known as the anomalous Hall effect (AHE) and early on it was shown experimentally that the extra Hall resistivity seen in ferromagnetic materials could be described by

$$\rho_{xy}^A = R_s M_z, \quad (2.30)$$

where R_s is the anomalous Hall coefficient, and M_z is the out-of-plane magnetisation of the sample [82].

Unlike the ordinary Hall coefficient, R_O , which is well explained by existing theory (equation 2.28), the anomalous Hall coefficient is not easily defined. Until recently the physical mechanisms responsible for the AHE have remained unexplained and the subject of much debate. Today the contributions to the AHE are divided based on whether their physical origin is intrinsic (arising from the band structure of the material) or extrinsic (arising from the scattering of charge carriers). In 1954 Karplus and Luttinger showed that it was possible to understand the AHE as the effect of spin-orbit interaction of polarised electrons with an applied electric field [83]. This theory introduced an extra component to electron group velocity called the ‘anomalous velocity’ that is perpendicular to the electric field. In ferromagnets the sum of the anomalous velocity over the occupied band state may be non-zero and therefore contribute to the Hall conductivity [84]. Since then the anomalous velocity has been identified as dependent on the Berry phase curvature of the material. Ye et al. showed that the intrinsic AHE in manganites was due to Berry phase effects from carrier hopping in a non-trivial spin background [85]. This intrinsic effect can be described by the equation

$$\frac{d\langle \vec{r} \rangle}{dt} = \frac{\partial E}{\hbar \partial \mathbf{k}} + \frac{e}{\hbar} \mathcal{E} \times \mathbf{b}_n, \quad (2.31)$$

where E is the energy of a carrier with the wavevector k , \mathcal{E} is the electric field, $\frac{d\langle \vec{r} \rangle}{dt}$ is the expectation value of the electron velocity, the first term on the right hand side is the group velocity of the electrons, and the second term is the anomalous velocity identified by Karplus and Luttinger expressed in terms of \mathbf{b}_n , the Berry curvature [84]. The extrinsic components are commonly divided based on the scattering mechanism responsible for the effect: ‘side-jump’ which occurs when an

electron's velocity is deflected in opposite directions by the opposite electric fields experienced when moving towards and away from an impurity; and 'skew scattering' which is the asymmetric scattering of carriers from impurities due to spin-orbit coupling (SOC) between the two [84]. There have been many attempts to unite the intrinsic and extrinsic components based on the scaling of each contribution with longitudinal resistivity, ρ_{xx} . In 2006, Onoda et al. showed that the contributions due can be calculated from first principles and found that the regions of intrinsic and extrinsic mechanism dominance overlap when the SOC and relaxation time are comparable [86]. They went on to determine which of the intrinsic and extrinsic mechanisms dominates in three different regimes (poorly conducting, moderately dirty, and super clean), as well as the scaling of the anomalous Hall conductivity with longitudinal conductivity in each regime [87]. They found that the intrinsic mechanism dominates, in the poorly conducting region, the anomalous Hall conductivity has been found to follow the longitudinal conductivity with a power law relation of $\sigma_{xy} \propto \sigma_{xx}^{1.6}$ on average. In the moderately dirty regime, where the intrinsic and extrinsic components are both contributing to the anomalous Hall conductivity, it remains relatively constant. In the superclean regime, the extrinsic effects dominate and the anomalous Hall conductivity is proportional to the longitudinal conductivity. Therefore, the empirical relationship seen between the anomalous Hall resistivity and the longitudinal resistivity is highly dependent on the specific balance of intrinsic and extrinsic contributions in each material. The intrinsic contribution is dependent only on the energy band structure of the material. In contrast the intrinsic contribution may be attributed to overall effect of two types of scattering mechanisms, skew-scattering which is proportional to the longitudinal resistivity and side-jump which is proportional to the square of the longitudinal resistivity. Due to the fact that the intrinsic contribution is also proportional to the square of the longitudinal resistivity it can be difficult to separate the different contributions from each other.

Topological Hall Effect (THE)

The Topological Hall Effect is the contribution to the overall Hall effect due to topologically non-trivial magnetic textures, like magnetic skyrmions [88], in addition to the ordinary Hall effect and the anomalous Hall effect. Current theory predicts that the topological Hall resistivity follows the following equation,

$$\rho_{xy}^T = R_O P B_{\text{eff}}^z, \quad (2.32)$$

where P is the spin polarisation in the z direction of the conduction electrons in the material, R_O is the ordinary Hall coefficient, and B_{eff}^z is the effective field which the electrons experience due to the Berry phase they gain whilst traversing the skyrmions [89]. The effective magnetic field is given by the expression,

$$B_{\text{eff}}^z = W_{sk} \cdot \Phi_0, \quad (2.33)$$

where W_{sk} is the total topological charge (normally proportional to the number of skyrmions or skyrmion density) and $\Phi_0 = h/e$ is the magnetic flux quantum, where h is Planck's constant, and $-e$ is the charge on the electron. Considering equation 2.32 one would expect the to be able to detect contributions from individual skyrmions in Hall transport measurements. The topological Hall effect was first distinguished by name from the AHE around fifteen years ago when it was shown by Bruno et al. that the topological Hall effect does not require any spin-orbit coupling contribution and can be explained purely by Berry phase theory of an electron moving through a smoothly varying magnetisation within an adiabatic system [9]. The THE was subsequently described in MnSi as due to the topologically non-trivial magnetisation of itinerant helimagnets in the B20 group [90]. Recent work by Zeissler et. al. has observed a Hall signal with a characteristic dependence on the skyrmion winding number. That is a discrete contribution to the Hall resistivity due to Néel skyrmions present in a Hall disk, however the magnitude of the effect observed is much larger than that predicted by the existing Berry Phase theories for the THE [8].

The topological Hall effect due to magnetic skyrmions has been measured experimentally by multiple research groups and in various types of materials. These include materials hosting individual skyrmions like Ir/Fe/Co/Pt heterostructures [10; 67; 91], Pt/Co/Ir multilayers [8], Pt/Co/Ta multilayers [92], SrRuO₃-SrIrO₃ bilayers [93], BTO/SRO/SrTiO₃ heterostructures [94], and Ca_{1-x}Ce_xMnO₃ thin films, as well as materials hosting skyrmions lattices like FeGe epitaxial films [95; 96], and Fe_{1-y}Co_yGe epitaxial films [97]. The common finding in all of these experiments is that the measured topological Hall contribution per skyrmion is orders of magnitude larger than that found by applying the theory in equation 2.32 to magnetic imaging performed during or after the transport measurements.

2.6.4 Hall Transport Measurements

Considering equations 2.27, 2.30, 2.32 and the exemplary M-H loop for ferromagnetic multilayered thin films with perpendicular magnetic anisotropy shown in Figure 2.3 (a) it is easy to understand what a Hall transport measurements in a ferromagnet without skyrmions would look like. Figure 2.7 (c) shows that one expects to obtain the expected shape of a hysteresis loop for a ferromagnet with a linear contribution that is proportional to the applied magnetic field, from the ordinary Hall effect. In ferromagnetic multilayers capable of hosting skyrmions, one also expects to find a quantised contribution to the Hall resistivity in the region where the magnetisation is switching - i.e. the multidomain state - as described by equation 2.32. However, is unlikely that this extra contribution would be clearly visible in the resistivity hysteresis loop as measured because the contribution due to individual skyrmions is proportional to the number of skyrmions multiplied by the magnetic flux quantum where the magnetic flux quantum is very small. This means that in order to investigate the topological component the other components must first be removed from measure resistivity hysteresis loops.

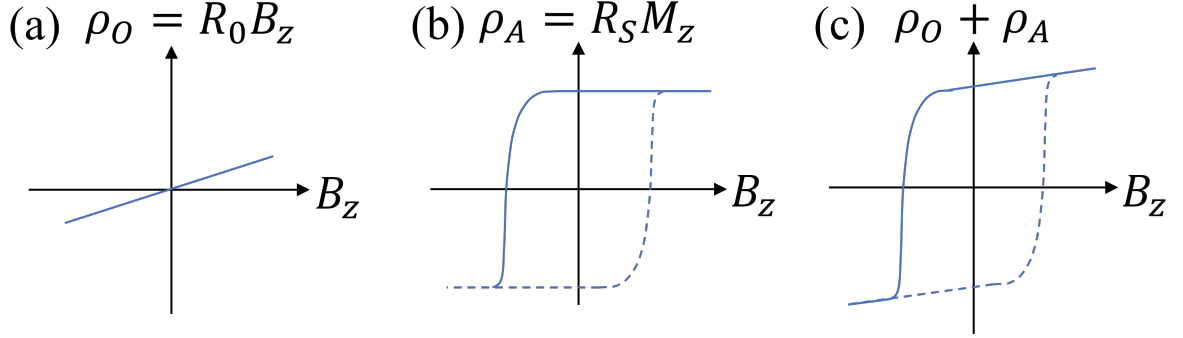


Figure 2.7: (a) The ordinary Hall resistivity measured in a metallic sample in an applied field B where B_z is the component perpendicular to the applied current and measured transverse voltage, like in Figure 2.6. (b) Shows the expected anomalous Hall resistivity in a ferromagnet according to equation 2.30. (c) The expected Hall resistivity measured in a ferromagnetic sample with only topologically trivial magnetisation textures.

2.7 Conclusion

In order to realise the electrical detection of skyrmions, investigation of the mechanisms of the topological Hall effect is essential and is a large component of the research undertaken in this PhD project. In particular, this project aims to improve the understanding of the topological Hall effect by carrying out Hall transport measurements in CoB/Ir/Pt multilayers with differing numbers of repeats, over a wide range of temperatures during magnetisation switching, when one would expect the presence of magnetic skyrmions. The THE has also been suggested as a possible method for skyrmion detection if they are to be used in industry for memory storage [98].

Similarly, the behaviour of the anomalous Hall effect is investigated and the skew-scattering, side-jump, and intrinsic contributions to the anomalous Hall resistivity are determined. The AHE in CoB/Ir/Pt multilayers will also be shown to be well described by the expression $\rho_A M_0/M_S = (\alpha\rho_{xx0} + \beta\rho_{xx0}^2 + b\rho_{xx}^2)$, where ρ_{xx0} is the residual longitudinal resistivity due to impurity scattering, ρ_{xx} is the temperature dependent longitudinal resistivity in accordance with [99].

In order to apply electrical Hall effect measurements to detect the presence of skyrmions in a magnetic data storage device it is necessary to have a complete understanding of not only the THE due to individual skyrmions but also the AHE in the same materials. To this end, the behaviour of the AHE and THE of CoB/Ir/Pt multilayers of various structures have been characterised over a range of temperatures from around 5 K up to room temperature.

CHAPTER 3

Experimental Methods

3.1 Introduction

The flow of experimental work completed for this thesis can be broken down into three main phases: material growth, sample characterisation, and electrical measurement. The magnetic multilayers were grown using DC magnetron sputtering with shadow-mask lithography, as described in section 3.1.1. The magnetic and structural characterisation of the samples was carried out employing a combination of X-ray reflectometry (3.2.1), LASER magneto-optical Kerr effect magnetometry (3.2.3), and superconducting quantum interference device-vibrating sample magnetometry (3.2.4). The methods used to carry out electrical Hall measurements to characterise the behaviour of the anomalous Hall effect and the excess Hall resistivity in CoB/Ir/Pt magnetic multilayers are outlined in section 3.3.

3.1.1 DC Magnetron Sputtering

DC magnetron sputtering is one of many methods of physical vapour deposition (PVD) which involve the material to be deposited changing from a solid (bulk condensed) state, to a vapour phase and then condensing on the substrate back to a solid (thin film condensed) phase. The bulk solids used for deposition are known as targets and in the sputtering system used they are disc shaped. PVD covers various methods of vaporising the target material for deposition, the basic principle of sputtering involves using the ions in a plasma of an inert element, in our case Argon (Ar^+), to knock atoms off of a target [100], this process is shown in Figure 3.1. Figure 3.2(a) shows the positioning of each sputter gun when looking from the top down in the vacuum chamber. Figure 3.2(b) is an example of a material target for sputtering where the direction of the magnetic field is shown with dotted arrows and the lighter racetrack indicates the area eroded by argon ions over time. The atoms which are removed from the target are then free to move through the vacuum system and condense onto the substrate surface (and the rest of the vacuum chamber) forming a thin film of the target material. The sputtering process is conducted in a vacuum system to allow the formation of a low pressure glow discharge plasma environment. A glow discharge plasma is generated by the application of a voltage across a gas at low pressure (in the mTorr region) by two electrodes. A magnet array underneath the material targets is used to confine the argon ions to a circular, doughnut-shaped path. This causes the targets to be worn away in a circular racetrack pattern, shown in Figure 3.2(b). In order to grow the magnetic multilayers required for the devices in this project tantalum (Ta), platinum (Pt), cobalt-boron (CoB), and iridium (Ir) targets are loaded into different magnetron sputter guns in the vacuum chamber. The sample, shadow mask, and shutter wheel, shown in Figure 3.1, are rotated around the chamber by a motor while the relevant guns are lit. By pausing for a finite known time with the sample above each gun layers of material can be grown on the sample. The sputter guns are arranged in a circle within the chamber under the sample and shutter wheels so that the wheels can be rotated between sources

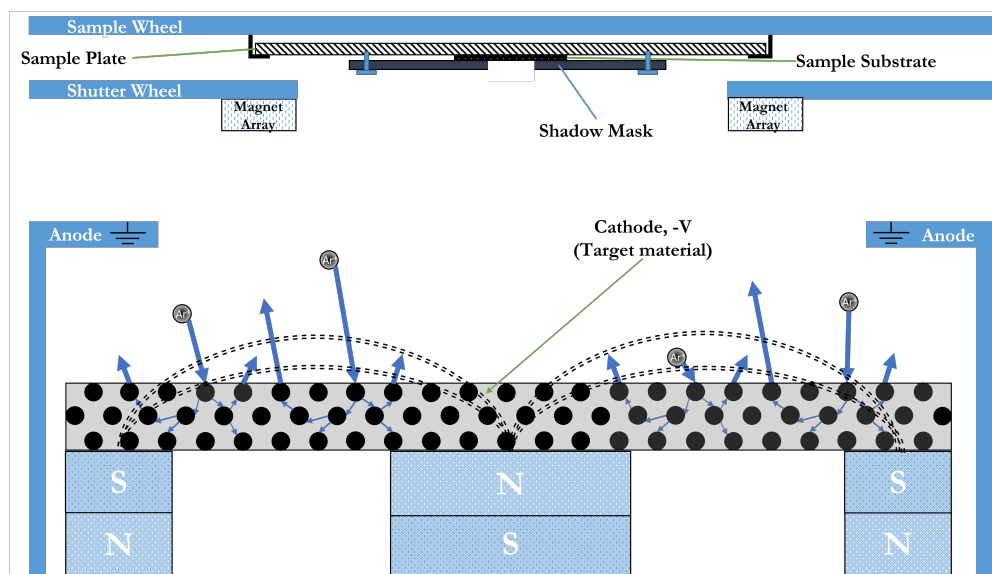


Figure 3.1: A full sectional side view of the arrangement of a material target, magnetron gun, shutter wheel, and sample substrate in the apparatus used for sputtering. The sputtering process, Ar^+ ions knock atoms free from a target by secondary emission. The constituents in this view are not shown to scale.

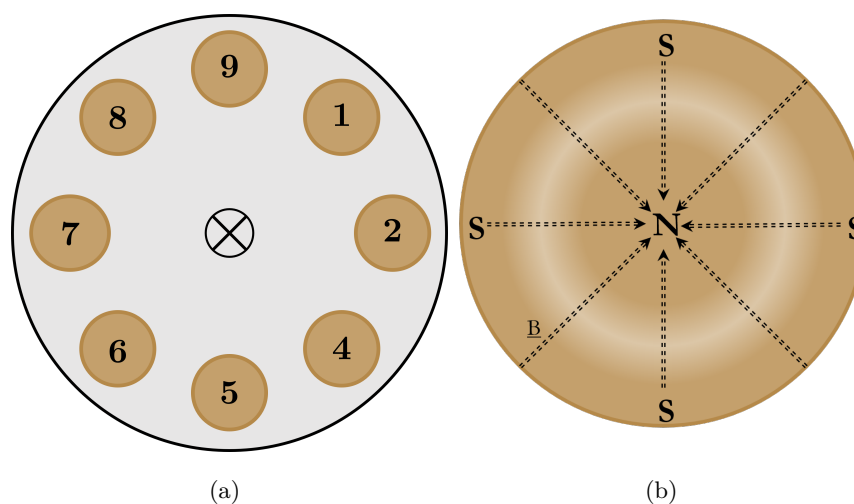


Figure 3.2: **DC Magnetron Sputtering:** (a) A top down view of the arrangement of the sputter guns within the vacuum chamber. (b) An enlarged illustration of a material target for the sputtering system showing the racetrack pattern of erosion which occurs over time. The direction of the magnetic field which confines the Ar^+ ions to the circular racetrack path above the target is indicated by the dotted arrows.

easily during the multilayer growth. The layout of the guns is shown in Figure 3.2(a). Software to drive the motors which rotate the samples and shutter is used to define the order in which the multilayers are grown, and allows automation of the growth such that the reproducibility of samples on different sample plates, but within the same growth, is very high. By controlling the Ar flow, current to the guns, and the time which each sample stops over the guns it is possible to grow consistent samples over multiple growth runs. The shadow mask secured over the top of the sample substrate restricts growth of the multilayer to the shape of the hole in the mask. In this way it is possible to create multilayer films in a desired shape without extensive and complicated lithography processes that require cleanroom access. Typical base pressures for the chamber, Ar pressures during growth, and sputter gun currents and powers are shown in Table 3.1. The flow of Argon used is particularly important for reliable striking of the $\text{Co}_{68}\text{B}_{32}$ target, which can be unreliable at lower Ar pressures than those given in Table 3.1.

Typical Sample Growth Conditions		
<i>Background Gas</i>	<i>Flow</i>	<i>Pressure</i>
Argon	35-40 sccm	3.5-4 mTorr
<i>Target material</i>	<i>Current</i>	<i>Power</i>
Gun 2: $\text{Co}_{68}\text{B}_{32}$	50 mA	18 W
Gun 4: Pt	25 mA	9 W
Gun 6: Ir	25 mA	9 W
Gun 8: Ta	50 mA	15 W

Table 3.1: Standard DC magnetron sputtering conditions used for the growth of $\text{Ta|Pt}[\text{CoB|Ir|Pt}]_{\times n}|\text{Pt}$ multilayers.

The samples grown for the Hall transport experiments used a recipe which produces $[\text{CoB|Ir|Pt}]$ multilayers on a Ta|Pt seed layer, with a Pt capping layer, as illustrated in Figure 3.3. The exact compositions of samples used are detailed in the relevant results sections.

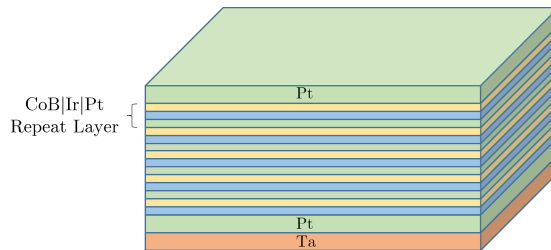


Figure 3.3: A schematic showing an example of a typical $[\text{CoB|Ir|Pt}]$ multilayer.

3.2 Characterisation

A wide variety of material and magnetisation characterisation techniques have been used throughout this project. This section deals with the necessary theory behind the characterisation techniques used, as well as the experimental set up used for each technique. X-Ray Reflectometry (XRR) has been used in order to verify material composition, thicknesses, and roughness of the multilayer samples grown (section 3.2.1). Several methods of magnetometry were employed including: Superconducting Quantum Interference Device Vibrating Sample Magnetometry to determine the saturation magnetisation of the samples (SQUID-VSM, section 3.2.4), and LASER Magneto-optical Kerr Effect Magnetometry (LASER MOKE, section 3.2.3) to find the coercive field of the samples.

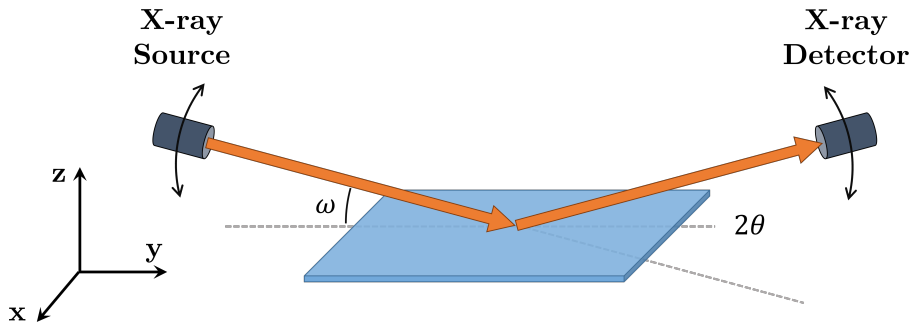


Figure 3.4: A schematic showing the arrangement of the essential components for a working X-ray reflectometry system. The large arrows indicate the x-rays incident on and reflected from the sample. The dotted lines are shown to define the incident angle, ω , and the difference between the incident angle and the reflected angle, 2θ . The double ended arrows indicate general movement of the x-ray source and detector relative to the sample during a scan. In specular XRR measurements ω is kept equal to θ as the scan takes place for a variety of values of 2θ .

3.2.1 X-Ray Reflectometry (XRR)

X-ray diffractometry (XRD) and reflectometry (XRR) exploit the similarity in lengthscale of the wavelength bordering hard and soft x-rays and interatomic spacings (10^{-10} m) in order to gain information about the structure of materials. The x-rays used are normally generated using an x-ray tube which accelerates electrons from a rotating anode through a vacuum towards the cathode. When the accelerated electrons hit the cathode they scatter from core shell electrons (i.e. the 1s or K orbital), ejecting these electrons from the atomic orbital, leaving a vacancy in their place. An outer shell (2s/2p or L orbital) electron then falls into the vacancy left behind, emitting peak radiation at the wavelength of the cathode $K\alpha$ wavelength. In some materials a 3s/3p/3d or M

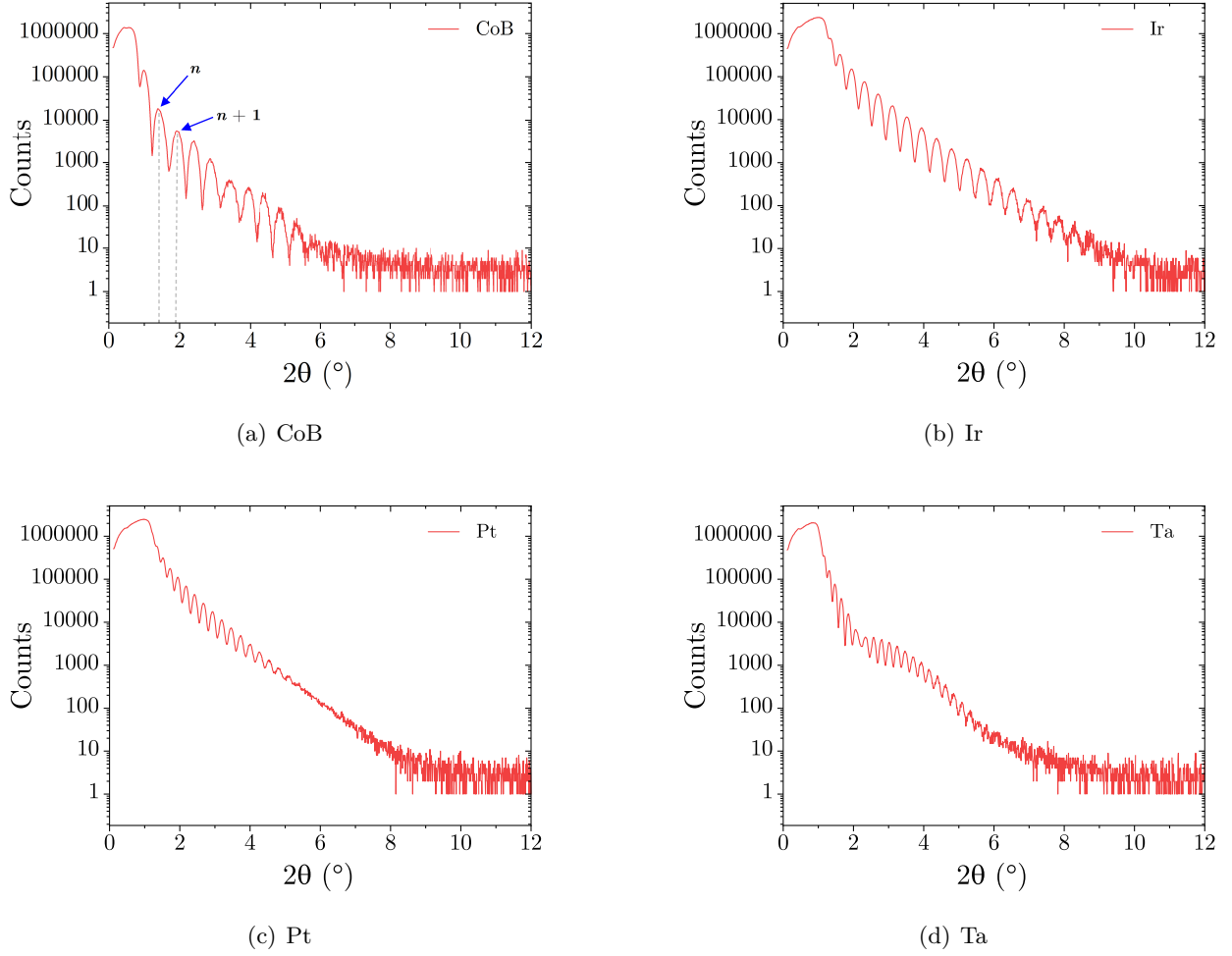


Figure 3.5: $2\theta/\omega$ XRR scans of samples grown to calibrate the rate of growth of materials used during sputtering samples. (a)-(d) show the X-ray intensity vs 2θ for samples of CoB, Ir, Pt, and Ta respectively.

orbital electron may fall into the vacated $1s/K$ orbital to emit a characteristic peak. In this case the x-ray emitted is referred to as a $K\beta$ x-ray. The electrons also lose energy via the Bremsstrahlung mechanism as they decelerate within the material of the cathode emitting a thermal spectrum of x-rays. The cathode in x-ray tubes is often made of copper due to the convenient copper $K\alpha$ emission, which has a wavelength of $\lambda = 1.54 \text{ \AA}$, and copper's low price. The resultant x-rays are then collimated and used in this project to probe thin film samples using low angle scans(LAS). Low angle scans using x-rays, XRR, can provide multiple different types of information about a given sample, however here only the one most relevant for the fabrication of samples in this project, film thickness, is discussed.

Kiessig Fringes as a measure of film thickness

Accurate measurement of the total thickness of a thin film is essential in order to calibrate the growth rate of the materials used during DC magnetron sputtering and can be found from the angular dependence of Kiessig fringes. Kiessig fringes occur due to the interference of x-rays from changes in the refractive index in the sample. The thickness can be estimated from the fringing using

$$t = \frac{(i - j)\lambda}{2(\sin \omega'_i - \sin \omega'_j)} \quad (3.1)$$

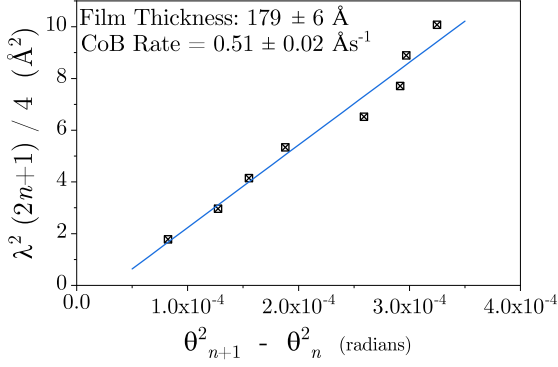
where t is the thickness, i and j are the fringe orders and ω' is half the scattering angle[101]. Equation 3.1 can be derived from Bragg's Law[102] and was used by Kiessig [103] in 1931 to determine sample thickness. Figures 3.5 (a) - (d) are examples of XRR scans in which Kiessig peaks are easily identified. The thicknesses of calibration samples were obtained from the separation between Kiessig peaks in the XRR scans using the relationship described by equation 3.1. When using only adjacent fringes, the relationship required is

$$\frac{\lambda^2(2n + 1)}{4} = t^2(\theta_{n+1}^2 - \theta_n^2), \quad (3.2)$$

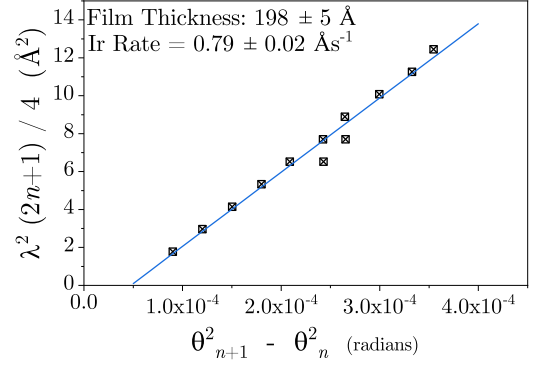
where n is the order of the first of two adjacent fringes, θ is the fringe position, λ is the wavelength of x-rays, and t is the thickness of the film. By producing plots where $\frac{\lambda^2(2n + 1)}{4}$ is plotted vs $(\theta_{n+1}^2 - \theta_n^2)$ the data should produce a straight line with a gradient equal to the square of the film thickness, t^2 , as shown in 3.6. From the obtained thickness for each film the sputtering growth rate of different materials can be found by dividing the thickness by the time taken to grow the measured film.

3.2.2 GenX XRR Fitting & Interface Roughness

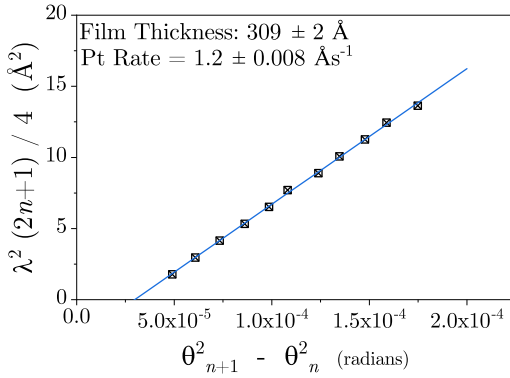
Fitting of XRR scans of growth calibrations and the magnetic multilayers was performed using GenX 3 software by M. Björck [104]. GenX have become a standard program used in the field for fitting XRR and PNR (polarised neutron reflectometry) data since its release in 2007 [105]. Reference [104] describes how GenX 3 (the version used herein) works in detail. In brief, GenX employs a model of the sample in question, broken down into layers, to build a scattering length density (SLD) profile of the sample. The SLD of each layer depends on the elements making up the layer (e.g. CoB vs Pt), the thickness of the layer, and the roughness of the layer. These parameters are varied to find a depth-dependent SLD for the measured sample that fits the experimental XRR (or PNR) data provided. The GenX model is able to handle magnetic multilayers with relative ease, including the ability to model repeating groups of layers rather than fitting each trilayer individually. The GenX simulated XRR results for the growth calibration samples and Ta/Pt/[CoB/Ir/Pt]_n/Pt multilayers with $n = 1, 4, 6,$ and $8,$ are shown in Figures 3.7 (a)-(d) and



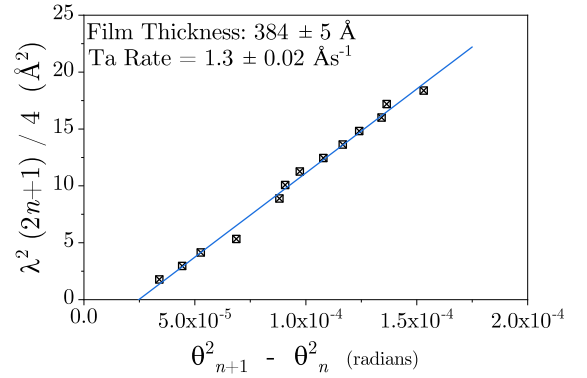
(a) CoB



(b) Ir

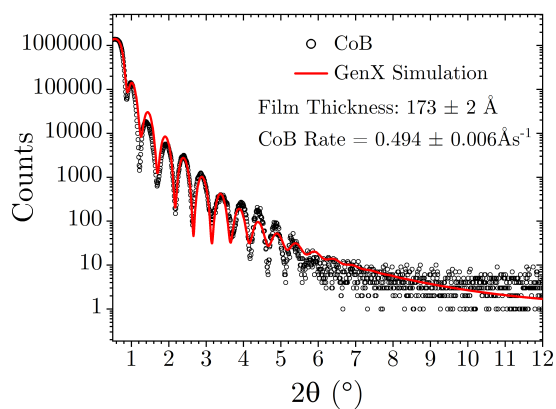


(c) Pt

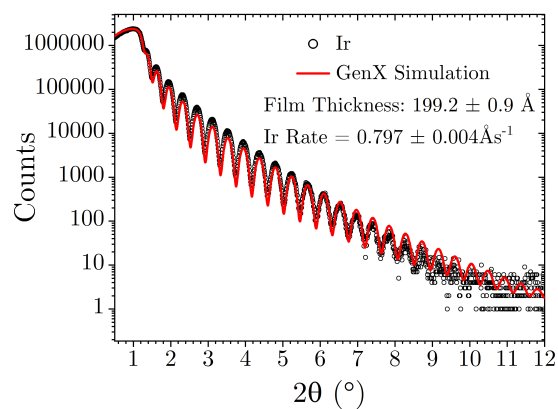


(d) Ta

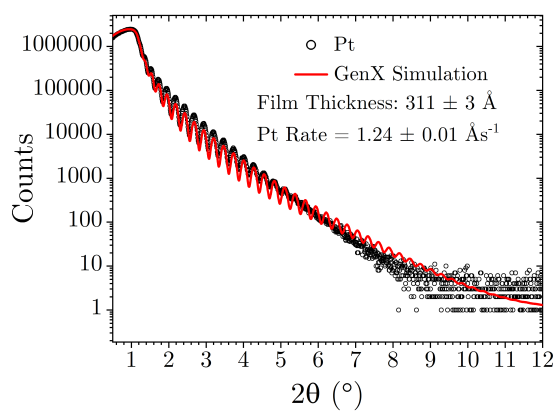
Figure 3.6: $\frac{\lambda^2(2n+1)}{4}$ vs $(\theta_{n+1}^2 - \theta_n^2)$ for samples grown to calibrate the rate of growth of materials used during sputtering samples. (a)-(d) show the relationship between $\frac{\lambda^2(2n+1)}{4}$ vs $(\theta_{n+1}^2 - \theta_n^2)$ for Kiessig peaks in XRR measurements of samples of CoB, Ir, Pt, and Ta respectively. The gradient of each of the linear data sets is equal to the thickness of the thin film sample squared.



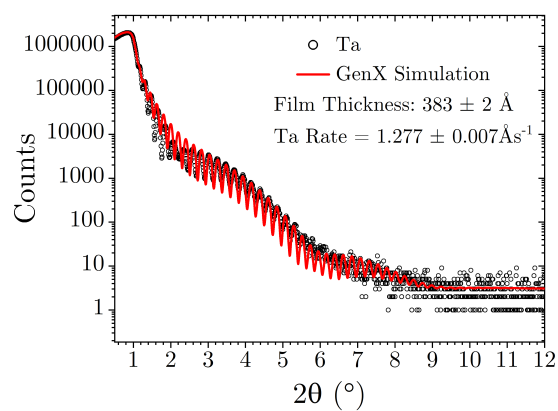
(a) CoB



(b) Ir



(c) Pt



(d) Ta

Figure 3.7: $2\theta/\omega$ XRR scans of calibration samples with GenX simulations shown as lines on top of the experimental data. (a)-(d) show the X-ray intensity vs 2θ for samples of CoB, Ir, Pt, and Ta respectively.

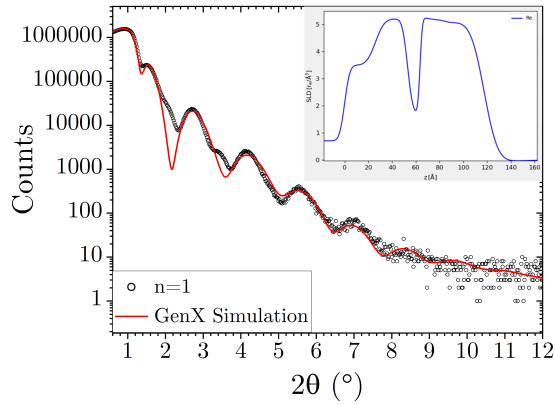
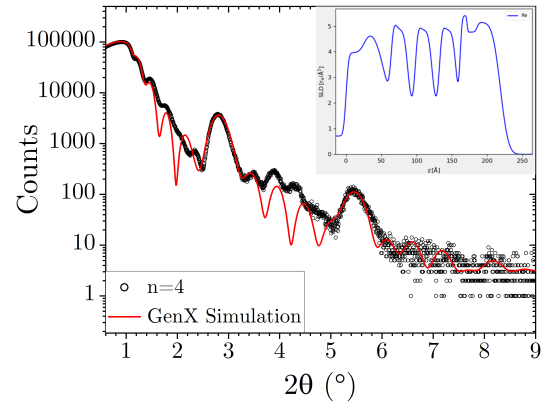
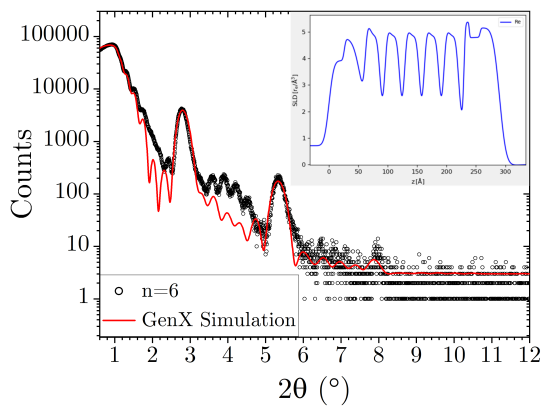
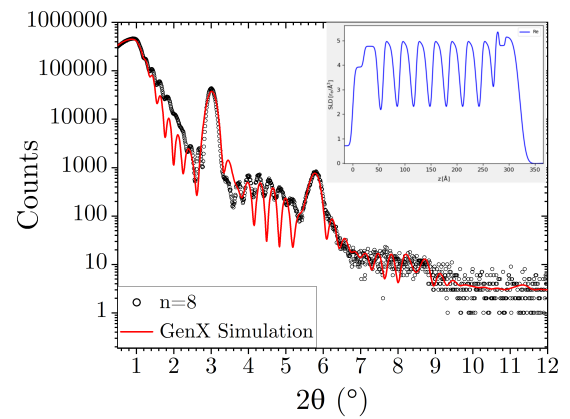
(a) $n=1$ (b) $n=4$ (c) $n=6$ (d) $n=8$

Figure 3.8: $2\theta/\omega$ XRR scans of magnetic multilayer samples with GenX simulations shown as lines on top of the experimental data. (a)-(d) show the X-ray intensity vs 2θ for Ta/Pt/[CoB/Ir/Pt] $_{\times n}$ /Pt samples where $n = 1, 4, 6,$ and 8 respectively. The simulated scattering length density (SLD) model is shown in the insets in the top right corner of each subfigure.

3.8 (a)-(d) respectively. The thicknesses of the calibration samples found from the GenX fit, and growth rates calculated from these, are also shown in subfigures 3.7 (a)-(d). The thicknesses and growth rates are consistent with the values obtained using Keissig peak analysis as discussed in the previous section and shown in Figures 3.6 (a)-(d). The thickness and growth rates obtained by both methods are provided for the calibrations samples in Table 3.2 for easy comparison. The

Keissig Analysis (K) vs GenX Simulation (G)				
Calibration	K: Thickness/Å	K: Growth Rate/Å/s	G: Thickness/Å	G: Growth Rate/Å/s
CoB	179 ± 6	0.51 ± 0.02	173 ± 2	0.494 ± 0.006
Ir	198 ± 5	0.79 ± 0.02	199.2 ± 0.9	0.797 ± 0.004
Pt	309 ± 2	1.20 ± 0.008	311 ± 3	1.24 ± 0.01
Ta	384 ± 5	1.3 ± 0.02	383 ± 2	1.277 ± 0.007

Table 3.2: Calibration film thicknesses, and sputtering growth rates, found using Keissig peak analysis and GenX fitting.

nominal multilayer structure of the samples measured for this thesis can be found from the growth rates in Table 3.2 and the times for which the sample was kept over the sputter guns during the growth:

$$\text{Ta}(19 \text{ s})|\text{Pt}(18 \text{ s})|[\text{CoB}(15 \text{ s})|\text{Ir}(5 \text{ s})|\text{Pt}(9 \text{ s})]_{\times n}|\text{Pt}(20 \text{ s}). \quad (3.3)$$

This gives a nominal multilayer structure of

$$\text{Ta}(2.47 \text{ nm})|\text{Pt}(2.16 \text{ nm})|[\text{CoB}(0.77 \text{ nm})|\text{Ir}(0.40 \text{ nm})|\text{Pt}(1.08 \text{ nm})]_{\times n}|\text{Pt}(2.4 \text{ nm}). \quad (3.4)$$

Interface Roughness in CoB/Ir/Pt Multilayers

The roughness of the Pt/CoB and CoB/Ir interfaces was also obtained from GenX fits of the XRR scans for multilayers with the nominal structure given by 3.4 for $n = 1, 4, 6,$ and 8 . Figure 3.9 shows the interface roughness for Pt/CoB (black squares) and CoB/Ir (blue circles) interfaces in these magnetic multilayers. There does not appear to be a clear trend in either interface roughness with the number of repeats in the magnetic multilayer. Additionally, the interface roughness values generated from the GenX simulations are very low. For reference, the rough diameter of an atom of Co - around 3 \AA - is shown as a dashed line in Figure 3.9. The estimated roughness of the interfaces responsible for production of the DMI in magnetic multilayers is shown to be between 2 \AA and 4 \AA , indicating high quality interfaces and smooth magnetic multilayer growth. GenX is not able to distinguish between intermixing at an atomic scale at an interface and roughness on the same order due to nanometre scale crystal grain structures. Either way, the interface roughness is shown to be very low and that there is little variation in the roughness with the number of repeats in the multilayer. There may be a slight increase in the roughness in the CoB/Ir interfaces with the

number of repeats in the samples but I do not think that the trend is significant given the small number of samples for which it was possible to carry out GenX fitting. The impact of interface roughness on DMI was discussed briefly in section 2.3 of chapter 2. Given that the DMI is essential for stabilising skyrmions in Pt/CoB/Ir multilayers it is possible that varying interface roughness in multilayers with different numbers of repeats could produce trends in excess Hall resistivity. It is unlikely that the roughness plays a significant role in these samples given that the variation is on the order of the diameter of Co atoms and that neither the Pt/CoB nor CoB/Ir interfaces appear to exhibit a clear dependence on the number of repeats in the multilayers.

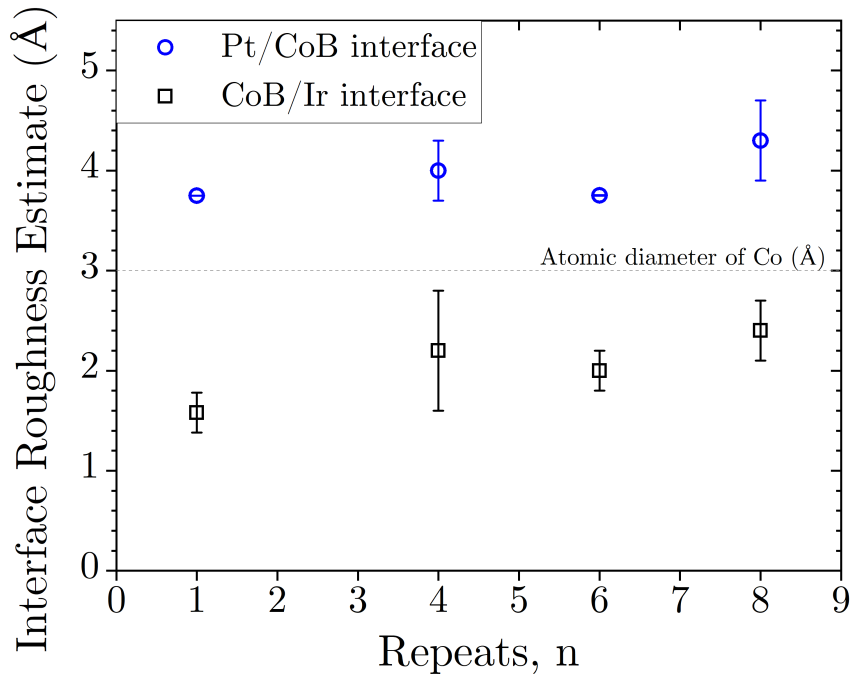


Figure 3.9: Interface roughness for Pt/CoB and CoB/Ir interfaces in Ta/Pt/[CoB/Ir/Pt]_n/Pt multilayers from GenX simulation of XRR scans shown in Figures 3.8 (a)-(d).

3.2.3 LASER MOKE Magnetometry

Laser MOKE magnetometry is used during this project in order to check if the samples made have a magnetisation perpendicular to the plane of the sample and obtain hysteresis loops from which the coercive field, H_C , of the sample can be calculated. The essential experimental apparatus of which the laser MOKE comprises a laser, a large electromagnet, a polariser, and an analyser. These components are arranged in a configuration similar to the one shown in Figure 3.10, such that the sample can be placed between the pole pieces of the electromagnet and the laser light is reflected off the surface of the sample, passes through the analyser, and then enters the photodetector. The polariser ensures that all the light incident on the magnetic sample is of one known polarisation. The

analyser allows only the components of light with a polarisation different to the original direction to reach the photodetector. In this way, the magnitude of the photocurrent detected is proportional to the amount by which the light's polarisation has been rotated by the magnetisation of the sample. The photocurrent detected is then recorded as the magnetic field is varied across a range, starting at one saturation magnetisation and moving in steps towards the opposite saturation field and back again. The normalised photocurrent can be used as a proxy for the magnetisation of the sample when the field is varied. This produces a hysteresis loop which can be used to calculate the coercive field, H_C , of the sample from the points where the loop crosses the magnetic field axis. Due to the use of normalised photocurrent, the magnitude of the saturation magnetisation, M_S , cannot be found from a laser MOKE hysteresis loop. This method for measuring hysteresis loops is highly surface sensitive as it relies on the interaction of laser light reflecting from the surface of the sample. The light only penetrates the skin depth of the sample (dependent on the wavelength of the laser used and the sample material) and the rotation of polarisation only occurs due to the magnetisation in the area where the beam is incident. Due to the locality of this method it cannot be used to find the bulk magnetic moment and the coercive field value may vary with the position of the incident light in large or non-uniform samples. In this project, knowledge of the expected coercive and saturated fields makes more precise or time consuming measurement methods easier and more efficient to perform, like SQUID magnetometry (3.2.4), and Hall transport cryostat measurements (3.3.1).

3.2.4 Superconducting Quantum Interference Device (SQUID) Magnetometry

The ability to precisely and accurately characterise the magnetic properties of samples used in experiments is very important and various magnetometry methods have been developed for this purpose. Faraday's law of induction states that temporal variations in magnetic flux through a circuit will induce a voltage, and therefore a current in an adjacent pick-up coil. This is described by equation 3.5,

$$V_{\text{ind}} = -N \frac{d\Phi}{dt} \quad (3.5)$$

where V_{ind} is the induced voltage, N is the number of turns in the pick-up coil, and Φ is the magnetic flux. This law is the fundamental basis of many magnetometry methods. The most basic type of magnetometer detects a change in magnetic flux from the changing proximity of a magnetic material relative to the inductive coil by the induced voltage across the circuit. This principle is the basis for the vibrating coil magnetometer, suggested by D. O. Smith in 1956 [106], which lead to vibrating sample magnetometry (VSM), developed by S. Foner in 1959 [107], where a magnetic sample is vibrated inside an inductive pick-up coil. A current is induced by the voltage due to the magnetic dipole field of the oscillating sample and is measured in an experimental set-up similar to that shown in Figure 3.11 (a) and (b). The voltage in the circuit can then be measured by a lock-in

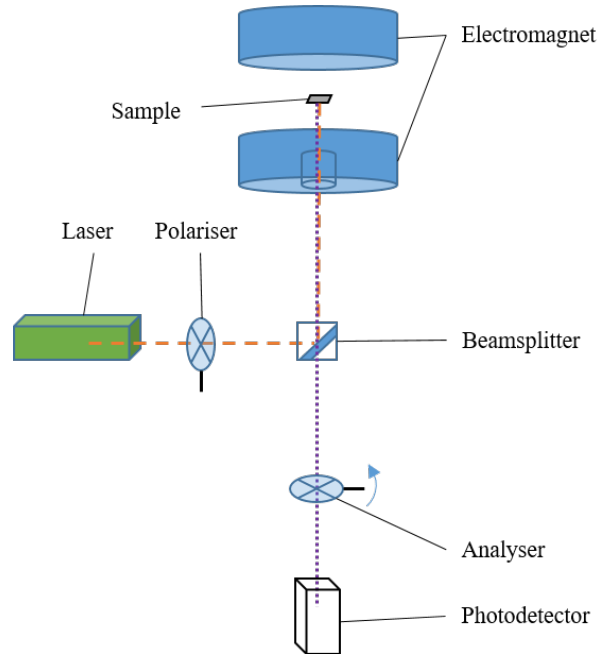


Figure 3.10: Schematic showing the essential components for a working LASER MOKE system. The dashed line is the laser light before reflection from the sample between the electromagnet and the dotted line depicts the path of the light after reflection from the sample.

amplifier which uses the sample oscillation frequency as a reference signal. By situating the pick-up coils between the pole pieces of an electromagnet it is possible to measure the induced voltage, and therefore changing magnetic flux due to the sample, over a range of constant externally applied magnetic fields. The induced voltage measured is converted to a magnetic moment via the relation in equation 3.5 and the specific calibration of the instrument which is completed using materials with known magnetic moment. Due to the fact that the induced voltage is only proportional to the rate of change of magnetic flux experienced by the pick-up coils, not simply the presence of an external field, the constant external field has no bearing on the validity of calculating the magnetic moment responsible. In this way hysteresis loops of the sample, such as those shown in Section 3.2.4, can be obtained. Following the prediction of supercurrents, which flow indefinitely in the absence of an applied voltage, by Josephson in 1962 [108] and the subsequent experimental observation by Anderson and Rowell in 1963 [109], the so-called Josephson effect has been used in many different applications including but not limited to the pursuit of high precision magnetometers. Superconducting quantum interference devices take advantage of the quantum interference effect between two Josephson junctions (JJ) connected in parallel which was first observed in 1954 [110]. Figure 3.2.4 shows the effect of Meissner screening which acts to expel flux in the centre of the superconducting loop formed by the parallel JJs. The flux is expelled by the formation of a screening current. By applying a known current through the SQUID, when any screening current is produced

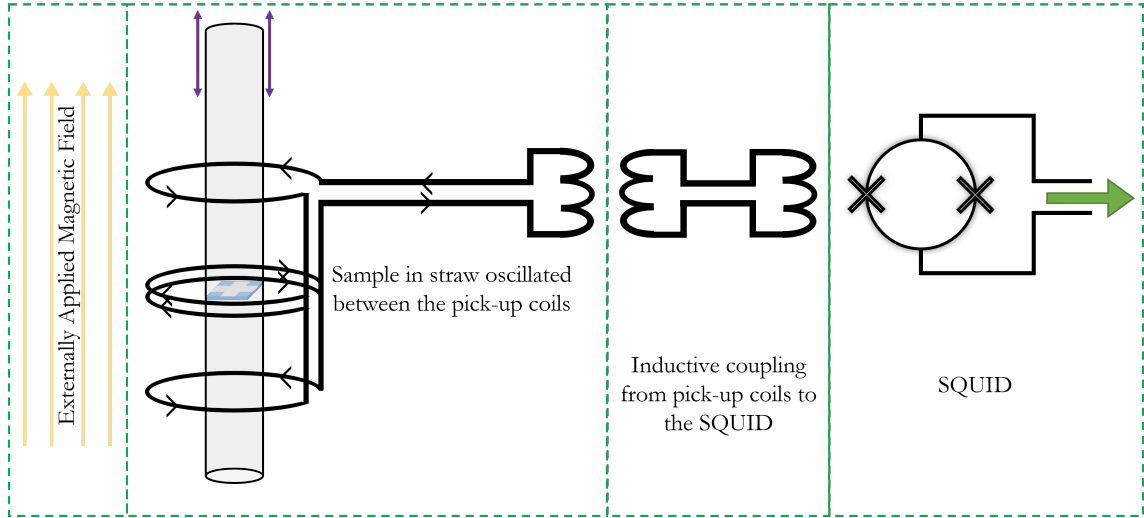


Figure 3.11: Schematic showing the most essential components for a working SQUID VSM system, used to measure very small magnetic moments. (a) An externally applied magnetic field, kept constant during each measurement of the moment of the sample; (b) the VSM, which oscillates the sample within pick-up coils which are inductively coupled via (c), the inductive circuit, to (d) the SQUID.

this will produce a voltage, V_{SQUID} which oscillates with a period Φ_0 . Essentially the SQUID acts as a highly sensitive flux to voltage converter. By combining the existing VSM methods with a SQUID it is possible to measure fields with a noise level of only $10^{-6}\Phi_0 \text{ Hz}^{1/2}$ [111].

In this project SQUID-VSM measurements are used to characterise the magnetic properties of the different materials used. Accurate measurement of the magnetic moment, m , vs applied field, H , is used to find the saturation magnetisation, M_S ; coercive field, $H_C = H(m = 0)$; and the saturation field, $H_S = H$. These properties can be found for OOP and IP hysteresis loops, where these orientations are the easy and hard axes for CoB|Ir|Pt multilayers respectively.

In particular, careful measurement of the OOP magnetisation in the sample, $M_z(B)$, is essential in order to be able to predict the magnitude of the expected anomalous Hall effect. $M_z(B, T)$ was measured for each sample and this was then used to estimate the anomalous Hall component of the sample resistivity and determine any excess Hall signal measured using the cryostat electrical transport set up discussed in Section 3.3.1. To obtain $M_z(B)$ the samples used in cryostat transport measurements were mounted inside plastic straws such that the field inside the SQUID-VSM is aligned OOP to the sample as shown in Figure 3.11. It is possible to write a script of instructions for the SQUID-VSM used during this project such that hysteresis loops with the same field sweep are performed at multiple temperatures. Automation of this process allows the measurements to be made in a repeatable manner, where the same script is used for each sample and the temperatures the measurements are performed at are changed. An example of the raw moment vs OOP field

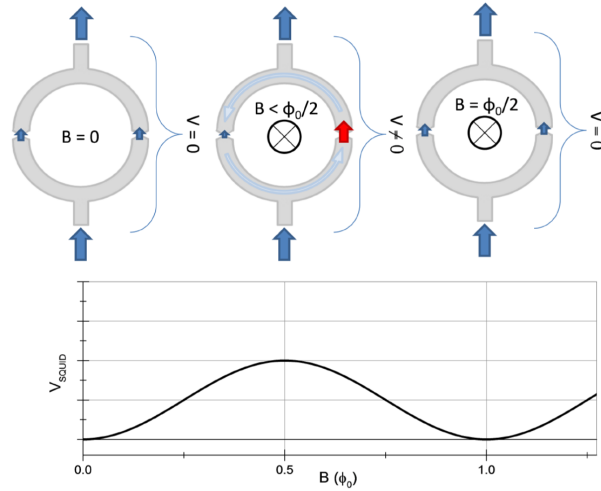


Figure 3.12: A schematic of the SQUID showing the current flowing through the parallel Josephson junctions and how the magnetic flux through the loop relates to V_{SQUID} [112].

measurement of a multilayer with six repeats is shown in Figure 3.13 where (a) shows the whole range of magnetic fields applied and (b) shows a zoomed in view. The measurement was performed at a variety of temperatures for each sample, in Figure 3.13 $T = 250$ K. During SQUID-VSM measurements a superconducting magnet is used to apply the external magnetic field and as such it is necessary to correct for trapped flux within the magnet. The physical origins of this necessary correction are discussed in detail in Chapter 5, the methods used to calibrate the correction to the superconducting magnet are also described. Chapter 5, section 5.2.3 illustrates all the steps taken to find the true field experienced by the sample during SQUID-VSM measurements. Similarly, a linear diamagnetic background can be seen easily in Figure 3.13 (a). This background is most likely due to the silicon substrate on which the samples are grown. This linear background is corrected for during the analysis processes in Chapter 5.

3.2.5 Instrument Precision, Systematic Errors, and Random Errors

The most important source of systematic error in the SQUID-VSM measurements arises due to the trapped flux in the superconducting magnet which is used to apply the magnetic field. As previously mentioned this is discussed in detail in Chapter 5. The SQUID-VSM system used to carry out moment vs OOP magnetic field hysteresis loop measurements is a Quantum Design MPMS3 which is capable of measuring magnetic moments with a sensitivity of $0.08 \mu\text{emu}$ with an applied magnetic field of more than 250 mT, or $0.01 \mu\text{emu}$ with an applied magnetic field of less than 250 mT [113].

Another source of systematic error in SQUID magnetometry measurements arises from the geometry of the sample being measured. SQUID gradiometers measure the flux lines penetrating the plane of

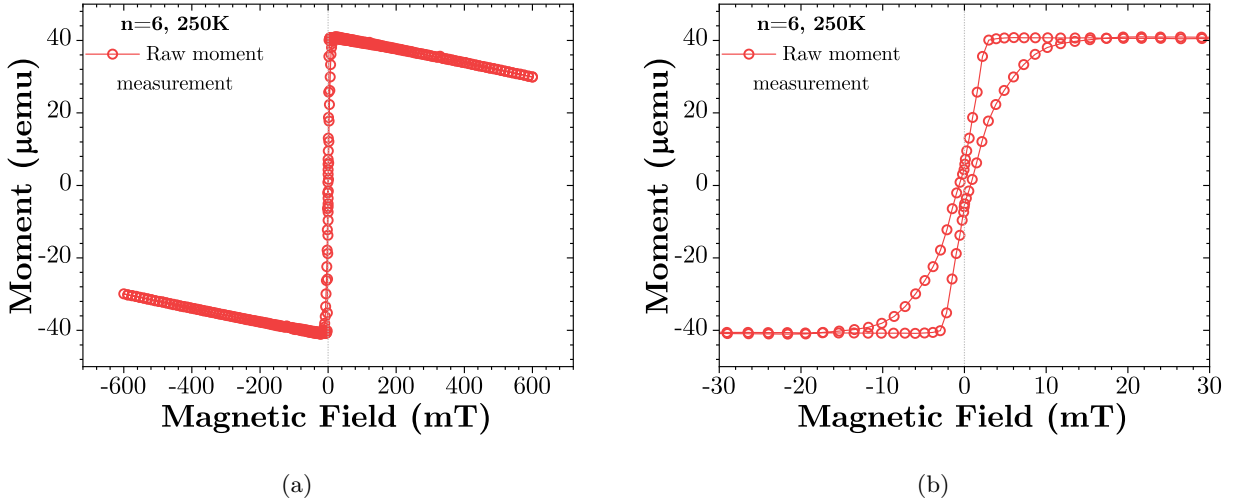


Figure 3.13: A raw moment vs field SQUID-VSM measurement (in $[\text{CoB}|\text{Ir}|\text{Pt}]_{n=6}$, at 250 K) shown over the full field range in (a) and a zoomed perspective in (b). This moment data has not been corrected to show the true field experienced by the sample or to remove the linear background present.

the pick-up coils (see Figure 3.11). In small samples the flux lines can close within the pick-up coils and not be measured by the SQUID. On the other hand, a larger sample which nearly completely fills the detection coils would have all of its moment detected. This means that two samples with the same moment may be reported as having different moments due only to differences in their size. Additionally, the magnetic field gradients detected by the pick up coils are predominantly present at the ends of samples. This means that samples that are too large (vertically within the pick-up coils shown in Figure 3.11) may have their moments under-reported because the amplitude of the oscillation during measurement is not large enough to bring the ends between the pick-up coils. The MPMS3 SQUID is calibrated using a cylindrical palladium reference sample. The samples measured do not have the same geometry as the Pd reference sample and therefore this can affect the reported moments. The systematic errors which occur due to sample geometry discussed here can be corrected for by something known as the fill factor [114]. The fill factor is a multiplicative factor which depends on the geometry of the sample compared to the geometry of the calibration sample (in this case the cylinder of Pd). This correction is important if the measurements performed are for the purpose of quantitatively accurate moment measurement and magnetisation calculation. Due to the fact that the magnetisation measurements performed in this project are to determine the shape of the out-of-plane hysteresis loops and are normalised and then scaled to produce an estimate of the AHE as a function of applied magnetic field it was not necessary to apply the multiplicative fill factor to the measurements.

Other sources of random error include misalignment of the sample in the applied magnetic field.

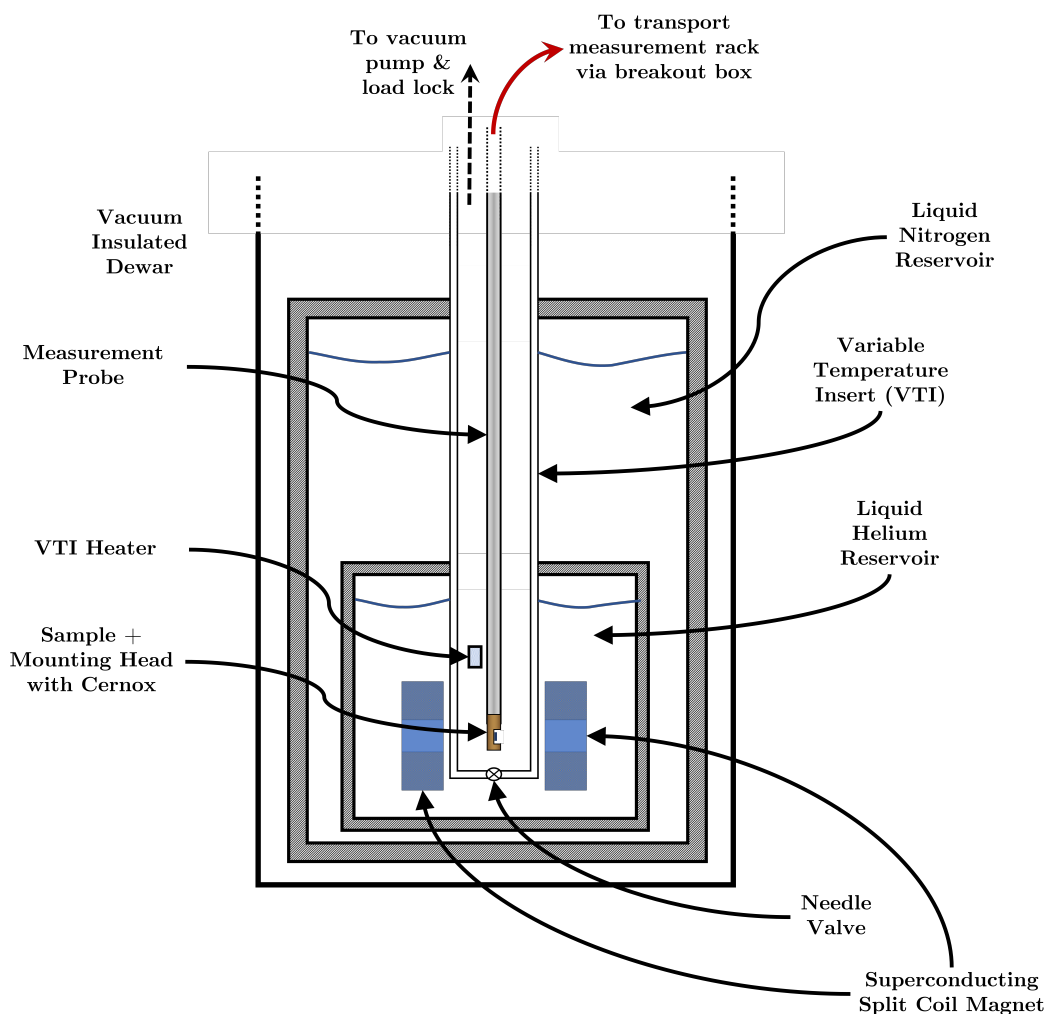


Figure 3.14: Schematic showing a sectional view of inside of the cryostat.

Figure 3.11 shows the ideal mounting of a sample within a straw but this is extremely difficult to achieve because the sample is placed in this location manually, with the help of a wooden stick (like a bamboo skewer). It is impossible to make sure that the sample is aligned so that it is perpendicular to the magnetic field applied by the MPMS3 system. This error is reduced as much as possible by careful placement of the sample. The stick used to align the sample is wooden so that magnetic impurities are not introduced to the sample during mounting.

3.3 Electrical Transport Measurements

This project aims to investigate the topological contribution to the Hall resistance in materials where skyrmions are expected to be present. Therefore it was essential that reliable and accurate electrical transport measurements were carried out in order to investigate the effect of the number

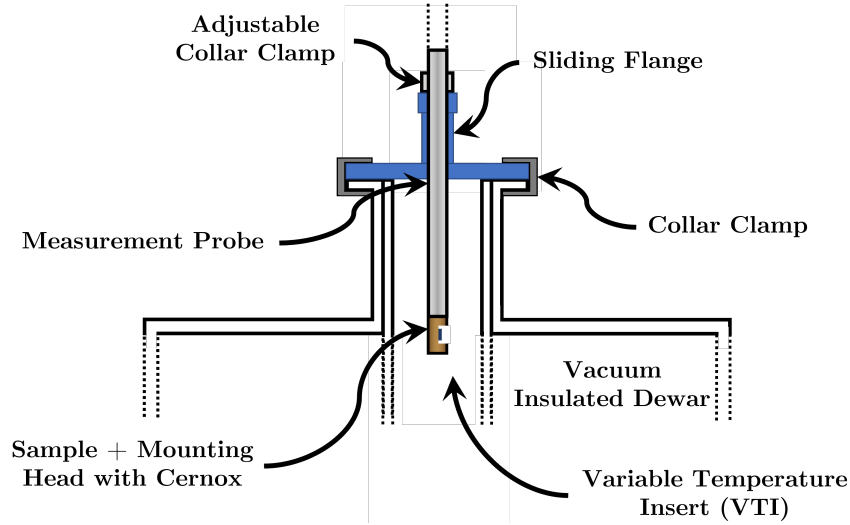


Figure 3.15: Schematic showing a sectional view of inside of the neck of the cryostat.

of multilayer repeats in the sample and the effect of temperature on any excess Hall resistivity observed.

Section 3.3.1 discusses the method used for transport measurements carried out in cryostats at the University of Leeds. This setup was used to control the temperature of the sample (290 K - 2 K) and the Hall resistance was measured during a major hysteresis loop. Multilayers with repeats ranging from one to fifteen were investigated. All measurements were intended to be combined with imaging methods either during or after the electrical measurements in order to be able to definitively link effects seen in the transport measurements with magnetic textures present in the samples.

3.3.1 Cryostat Hall Resistance Measurements

In order to investigate any topological Hall signal from skyrmions that may occur during a major hysteresis loop, a cryostat with electrical transport capabilities was used to measure the total Hall resistance, R_{xy} , of multilayers with different numbers of repeats, over a range of temperatures from 290 K to 1.5 K. A specific combination of experimental apparatus is required to be able to perform Hall resistance measurements at the same time as applying a magnetic field and keeping the sample at a stable temperature. Therefore, the experimental setup used in this project consisted of three main parts, the cryostat and magnet setup (Figure 3.14), the sample mounting head (Figure 3.16), and the transport measurement rack and breakout box (Figure 3.18). A hollow metal stick, henceforth referred to as a measurement probe, electrically connects the sample head to the instruments in the transport measurement rack and holds the sample in the correct place inside of the cryostat. The cryostat and magnet arrangement allows cooling and thermal regulation of the sample, while the magnet was used to sweep the magnetic field over a range larger than the saturation fields of the major hysteresis loop for each sample.

Figure 3.14 shows a full section diagram of the cryostat and superconducting magnet configuration and includes the measurement probe and sample located in the position used during measurement. The temperature in the variable temperature insert (VTI) is controlled by varying the degree to which the needle valve is opened and throttling the vacuum pump to create a steady flow of cold He gas around the sample. The VTI heater controls the temperature by varying the power used based on temperature measurement from a Cernox temperature probe in the VTI and a Cernox on the sample head. The sample can be cooled faster by opening the needle valve more or by turning off the VTI heater, this can be done automatically by setting a target temperature for the VTI and/or sample and a limit on the rate of change of temperature in different ranges. By limiting the speed of warming and cooling at the lowest temperatures it is possible to access temperatures around or below the boiling point of helium safely. In particular, it is important not to heat the VTI too fast if the system has been measuring at very low temperatures for a long time, in case there is a buildup of liquid helium at the bottom of the VTI. Heating too fast can cause the helium to boil very quickly causing an extremely sharp rise in pressure within the cryostat. This is avoided by including limits on the rate of change of temperature in the software that is used to control the VTI heater and read temperature information from the two Cernox temperature probes.

A pair of superconducting split coils submerged in the helium reservoir are used to produce a uniform magnetic field through the VTI in the area where the sample is located. It is ensured that the sample is placed in the correct position within the VTI by measuring the distance between the sample head and the bottom of an adjustable ring clamp near the top of the measurement probe. The adjustable collar clamp rests on top of a sliding flange that is clamped to the neck of the cryostat using another collar clamp, as shown in Figure 3.15. The distance from the neck of the cryostat to the centre of the superconducting magnets is known and therefore the position of the adjustable collar clamp can be changed to ensure that the sample is aligned correctly in the vertical direction.

The sample is also aligned to ensure that the magnetic field from the superconducting magnet is perpendicular to the sample by aligning the measurement probe with markers on the neck of the cryostat indicating the direction of the magnetic field. It is possible to fine tune the rotational alignment of the sample by measuring the Hall resistance in a saturated field while rotating the sample to find the orientation with maximum Hall resistance which occurs when the magnetic field perpendicular to the sample is largest (i.e. sample is totally perpendicular and the field has no in-plane field contribution).

The sample is connected electrically to the measurement apparatus via a sample head and measurement probe. The sample is shown in place on the sample head attached to the measurement probe in Figure 3.14, and wirebonded to the sample head in Figure 3.16. The wirebonding pads on the sample head correspond to the wiring within the measurement probe and the corresponding

To breakout box
via cryostat stick

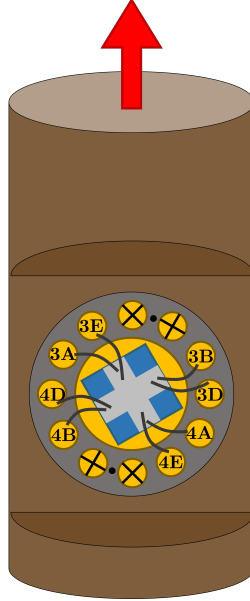


Figure 3.16: Schematic showing the sample mounted to the measurement head that attaches to the end of the cryostat measurement probe.

contact pins that are connected to a breakout box using a circular 12 or 24 pin cable. The breakout box is used to contact the different pins (and therefore wirebonding pads) to specific instruments used for the transport measurements. The breakout box is shown in Figure 3.18.

The parameters for the measurements, including temperature, magnetic field range, field step size, and applied current, were decided by the author and executed using the measurement apparatus shown in Figure 3.18. The measurement apparatus is controlled by a NI LabVIEW™ code developed in-house by Dr G Burnell. The author benefited from the guidance and support of Dr G Burnell during the initial set-up of the apparatus and Dr N Satchell while performing out-of-hours measurements.

Once the sample is wirebonded to the head, as shown in Figure 3.16, it is connected to the measurement probe and the contact resistance of the wirebonds is measured with the sample outside of the cryostat (at room temperature). Four point measurements (in the absence of magnetic field) are performed to check that the values of R_{xx} and R_{xy} are of the order of magnitude that is expected and therefore that the contacts are good. Generally for R_{xy} this is $\mathcal{O}(10 - 100 \text{ m}\Omega)$, whilst for R_{xx} this is $\mathcal{O}(10 - 100 \text{ }\Omega)$. These measurements are carried out using the same configuration of applied current and relative voltage measurements as used for all the measurements inside the cryostat with field applied, for example a current applied from contact 3A to 4A and a longitudinal voltage measurement across contacts 3E and 4E is used to measure R_{xx} , whereas the same current

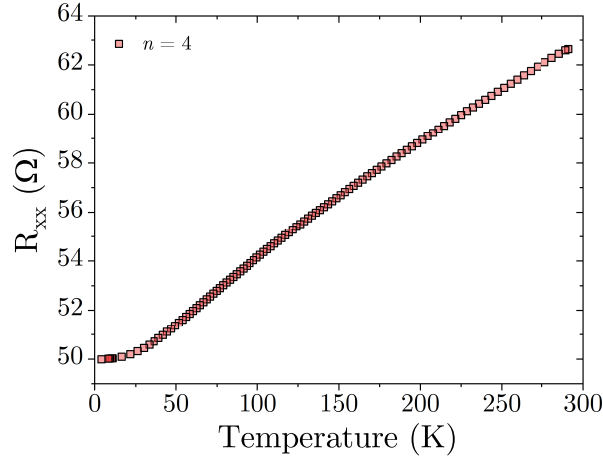


Figure 3.17: Longitudinal resistance measured as a function of decreasing temperature, from room temperature down to base temperature (around 4 K)

contacts and a transverse voltage measurement across contacts 4B and 3B, or equivalently 4D and 3D, can be used to measure R_{xy} . All contacts are tested in this manner so that initially extraneous wirebonds can be used as backups if a wirebond becomes disconnected while the sample is in the cryostat due to helium flow or constriction due to cooling of the sample.

The sample and measurement probe are then loaded into the cryostat, which is kept at 300K during this process. First, the dependence of R_{xx} and R_{xy} on temperature, in the absence of a magnetic field, is measured. After making sure that the needle valve is open, to allow He to enter the VTI, the temperature controller is used to change the temperature set point to the desired value (e.g. 10 K), this turns off the heater that is used to warm the cryostat VTI and the sample begins to cool. At this point a measurement controlled by NI LabVIEW™ code developed in-house by Dr G Burnell, is started and used to measure both voltages and calculate the resistances every ten seconds. This produces plots like the one shown in Figure 3.17. Once the sample has reached the lowest temperature that it will be measured at (around 4 K) the resistance versus temperature measurement is stopped.

In order to perform resistance versus field measurements at multiple temperatures a measurement, controlled by NI LabVIEW™ code developed in-house by Dr G Burnell, is reconfigured to perform multi-parameter measurements. This allows the measurement of R_{xx} and R_{xy} versus applied out-of-plane magnetic field, producing hysteresis loops in resistance, at a variety of different temperatures. A list of temperatures is specified by the user, as well as the range of the magnetic field for the hysteresis loops, and then the measurements can be started. The software changes both parameters, temperature and field, such that the sample is cooled or warmed to the desired temperature using the heater (see Figure 3.18) in zone mode, the software then waits until the specified temperature stability condition is met, and then the magnetic field is swept and R_{xx}

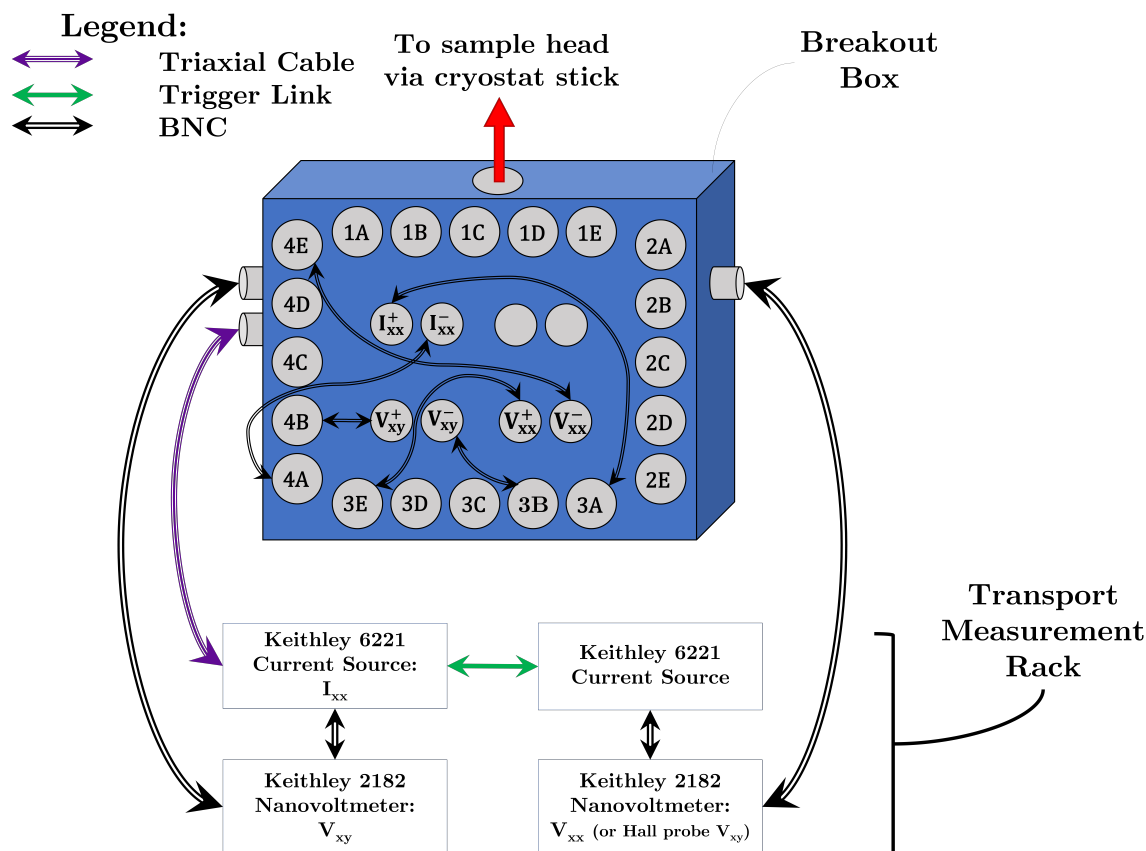


Figure 3.18: Schematic showing the arrangement and connections between the electronic measurement instruments and breakout box that make up the transport measurement rack.

and R_{xy} measurements are taken every 1-2 mT using one Keithley 6221 current source to apply a longitudinal current in the sample and communicate with a Keithley 2182 nanovoltmeter triggering a transverse voltage measurement. A second 6221 is connected to the first using a triggerlink cable and used to communicate with a second 2182 nanovoltmeter to trigger a longitudinal voltage measurement or Hall probe transverse voltage measurement concurrent with the transverse voltage measurement of the sample. The same preset longitudinal current is used for every measurement meaning that the transverse and longitudinal resistance of the sample can be calculated easily, and in fact is output in addition to the raw voltage data by the NI LabVIEW™ code developed in-house by Dr G Burnell. Following completion of the major hysteresis loop the sample is then cooled or warmed to the next chosen temperature, the software again waits until the temperature has stabilised, and then measurements are repeated as described previously. These measurements produce loops in Hall resistivity. The methods for evaluating and finding the ‘true’ field experienced by the sample in the cryostat during the transport measurements are discussed in Chapter 5.

3.3.2 Instrument Precision, Systematic Errors, and Random Errors

As mentioned above the electrical transport measurements were carried out using two Keithley 2182 nanovoltmeters trigger-linked to a Keithley 6221 DC and AC current source. Keithley 2182 nanovoltmeters have a maximum analog output of $\pm 1.2\text{V}$, an accuracy of $\pm(0.1\%$ of output + 1mV), an output resistance of $1\text{ k}\Omega \pm 5\%$, and a gain which is adjustable from 10^{-9} to 10^6 (with gain set to 1, a full range input produces a 1V output) [115]. The full specification for Keithley 6221 DC and AC current sources can be found in the manual [116]. For the measurements in this project, the current source was set up to perform a DC sweep with a 1 mA range level for the 6221 current source and the 2182 nanovoltmeters measured when triggered off the current source with a 10 nV range and fixed 10 V compliance. Keithley 2182 nanovoltmeters and 6221 DC/AC current sources require 2.5 hours and 1 hour to warm up to rated accuracy respectively. Therefore, they are left on when not in use (except for extended periods when the university labs are closed). This increases efficiency for lab users and ensures that the transport measurement equipment is always warm and capable of high accuracy measurements.

Systematic errors in the transport measurements include zero errors in the V_{xy} and V_{xx} measurements due to misalignment of the wirebonds which introduces crosstalk between the transverse and longitudinal measurements proportional to the misalignment of the wirebonds on the samples. This zero error was removed for each transverse measurement by centring the hysteresis loops such that the saturated values are of equal magnitude (but opposite sign) - this step is discussed in detail in chapter 5, section 5.3.1. Errors between sample measurements may also have occurred due to varying wirebond misalignment in cases where the wirebonds broke during measurement or sample loading and had to be redone. However, these should be minimal as the systematic error in each hysteresis loop is corrected individually using the method given in section 5.3.1.

Other systematic errors in transport measurements can occur due to imperfections in the measuring instruments or cables and connectors used in the testing arrangement. Sources of these include signal leaks, reflections in the measurement system, and the frequency response of receivers in the measurement systems used. Errors due to signal leaks can be minimised by using well isolated and shielded cables in all parts of the measurement set-up so that cross-talk is minimised. The cabling used was in good condition and the electronics in the cryostat stick have been isolated as well as possible. Errors due to reflections can be minimised by impedance matching the samples and cables used for the measurements. In this project, it was not really possible to impedance match the samples to the equipment used because the only method available for electrically contacting the samples was to wirebond them to the cryostat head for measurement. Similarly, thermal EMFs can occur at interfaces between different metals; these can be reduced by using clean, single metal connections but this is not always possible. It is possible to minimise offsets due to thermal EMFs by using the ‘Relative’ feature on 2182 nanovoltmeters or by using the DC current-reversal technique

which was employed here. Voltage measurements were performed on the positive and negative alternations of the 6221 current source and then the 2182 nanvoltmeters can remove the thermal EMF components by taking the averaged difference of the positive and negative current polarity measurements.

An important possible source of error during transport measurements arises due to magnetic fields. This is particularly the case in this project where magnetic field are being applied to the sample which is being measured, but it is also possible for very small magnetic fields like that of the Earth to cause a noticeable effect. Errors in transport measurements due to magnetic fields occur because currents are generated in the test cables when a conductor loop (the cable) cuts through magnetic field lines. It is clearly not possible to completely eliminate such errors as transport measurements necessarily require cables with finite lengths which therefore cut through at least the Earth's magnetic field. In this project, there is also the magnetic field applied to the sample in the cryostat to be concerned with. To minimise effects due to magnetic fields the shortest connecting cables possible were used and the instruments and cables were kept as far as practical from the cryostat magnet. Additionally the instruments and cables are kept in a rack as far above the height of the magnet in the cryostat as possible.

CHAPTER 4

Preliminary Work

4.1 Introduction

The main aim of this project is to better understand the topological Hall effect that can occur in the presence of skyrmions. Previous experiments undertaken by members the University of Leeds Condensed Matter group and collaborators at the Paul Scherrer Institut had successfully combined X-Ray Magnetic Circular Dichroism-Scanning Transmission X-ray Microscopy (XMCD-STXM) with electrical transport measurements so that Hall resistivity measurements could be directly connected to the magnetisation textures responsible [60]. This set-up yielded promising measurements of the Hall resistivity due to individual skyrmions in Ta(3.5 nm)| Pt(3.8 nm)| [Co(0.5 nm)| Ir(0.5 nm) | Pt(1.0 nm)]_{×10} | Pt(3.2 nm) multilayers [8]; however, as discussed in previous chapters, the topological Hall effect due to individual skyrmions found in this work, 22 ± 2 nΩcm, was orders of magnitude larger than that predicted by Berry phase THE theory, 0.01 nΩcm. Additionally, a successful beamtime investigating skyrmion motion was performed in 2018 using samples fabricated by Zeissler [117]. I was involved in the XMCD-STXM imaging for this experiment. For the devices in that experiment a multilayer structure of Ta(3.2 nm)| Pt(2.7 nm)| [CoB(0.8 nm)| Ir(0.4 nm) | Pt(0.6 nm)]_{×5} | Pt(2.2 nm) was used. The Co used in [8] was swapped for CoB in [117] because the amorphous nature of CoB results in less pinning of skyrmions in the samples which was important for investigation of skyrmion motion and the skyrmion Hall angle in the latter.

One of the original aims of this project was to be able to nucleate skyrmions on demand, and then to measure the THE due to individual skyrmions while carrying out magnetic imaging such that it would be possible to better measure and understand the individual contribution of skyrmions to the Hall effect. Combination of transport measurements and XMCD-STXM imaging, as used in reference [8], was planned. In order to do this, nano-scale Hall discs were fabricated on x-ray transparent silicon nitride membranes. During fabrication (section 4.2) a variety of thin film growth and lithography techniques were used to construct nano-scale devices in which skyrmions could be observed and measured. Magnetic multilayers were grown onto silicon wafers scribed into 5 mm × 5 mm squares with 0.5 mm × 0.5 mm square holes in the middle. These ‘holes’ have 200 nm thick Si₃N₄ membranes across the top of them. The fabricated devices are positioned on the membranes over the holes in the silicon wafer so that XMCD-STXM imaging can be performed. Similarly, the devices are made to be nanoscale so that all of the magnetic multilayer, where skyrmions may be found, can be imaged efficiently using XMCD-STXM. In order to employ the same analysis techniques as Zeissler et al. in [8], the XMCD-STXM images of the Hall devices need to provide the out-of-plane magnetisation of the whole device so that the anomalous Hall effect can be accounted for using the percentage of the magnetic device that is saturated in each image.

4.2 Device Fabrication & Lithography Design Evolution

The combination of techniques discussed here was chosen such that the resultant devices are optimised for the XMCD-STXM transport experiments in which the devices were used. In order to explore the topological Hall effect a combination of Hall transport measurements and scanning transmission x-ray microscopy measurements are used. There are several standard Hall transport geometries including Hall bars, and Hall discs which are used in this project (see Figure 4.1). These geometries allow Hall transport measurements to be performed without requiring complicated post-measurement analysis like that required by Van der Pauw measurements. In order to

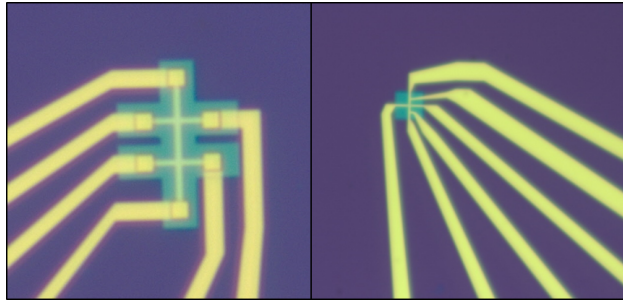


Figure 4.1: The nano Hall devices after contact deposition. **Left:** Nano Hall bar; **Right:** Nano Hall disc

combine transport measurements with x-ray microscopy the devices used are fabricated on 200 nm thick silicon nitride (SiN_x) membranes which have a 0.5×0.5 mm window where x-rays can penetrate the sample and are transmitted all the way through to a detector on the other side of the sample from the x-ray source. The fragility of the membranes, final size of the devices, and properties of the magnetic stack chosen to host the skyrmions dictate the final lithography recipe used, both in terms of methods and regarding their order.

4.2.1 Lithography Process Summary

In order to create magnetic multilayer devices of the required size (disks with diameters of 400 nm, 800 nm, and 1000 nm) on top of the silicon nitride membranes multiple lithography steps are necessary, there are three lithography steps in total, shown in Figure 4.2, each of which is a separate lithography ‘layer’.

The first layer, Figure 4.2(a), is necessary to prevent the silicon nitride membrane breaking the sputtering or buckling due to strain after sputtering. Two layers of positive photoresists, MMA and PMMA, are spun onto the substrate and baked at 180°C after each spin. The sample is then exposed to an electron beam in a pattern which, after developing in a solution of IPA and water (7:3), creates small holes in the photoresist through which the multilayer is sputtered, as explained in section 3.1.1. The extra multilayer is then removed by a lift off process where the photoresists

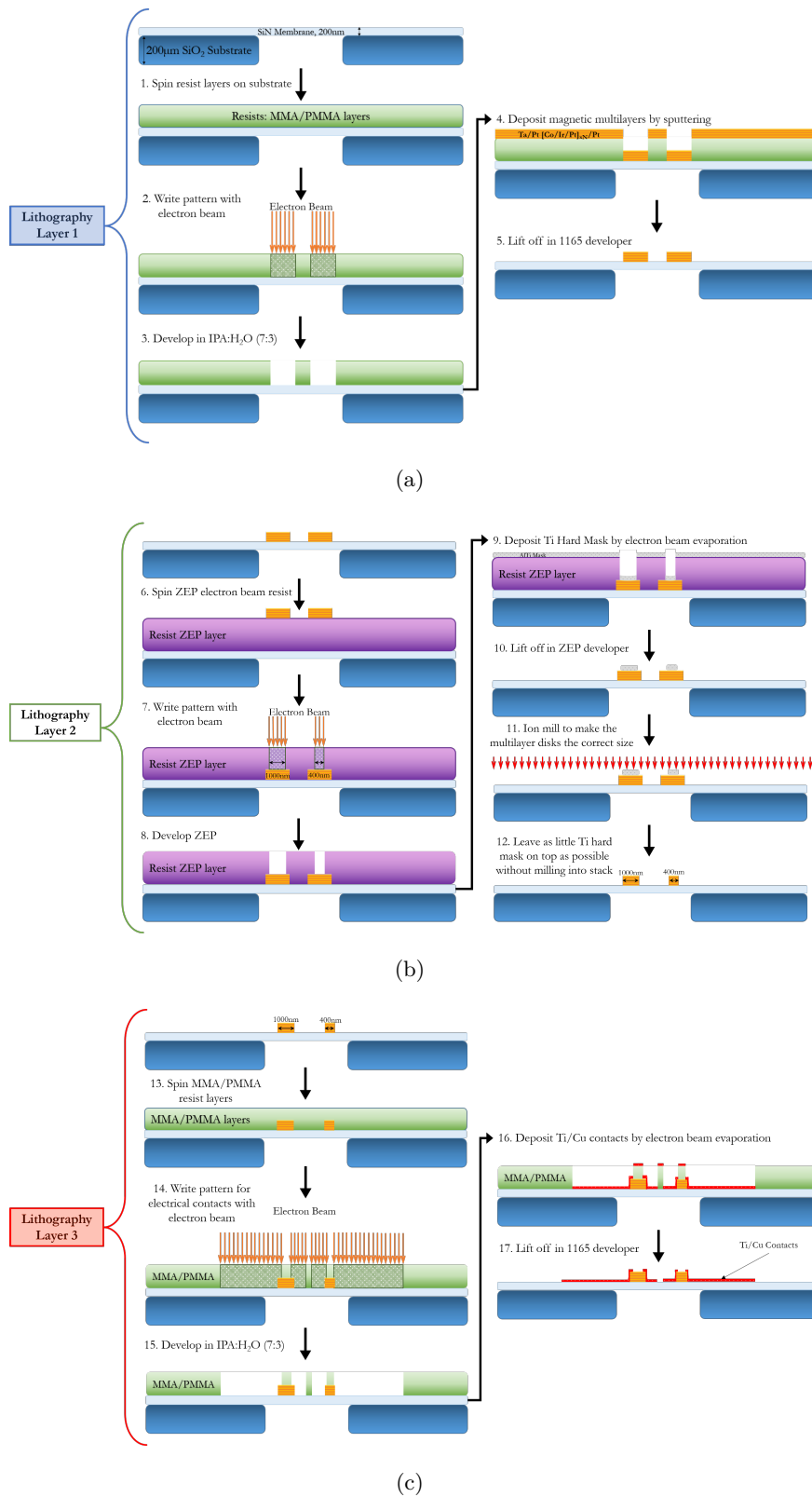


Figure 4.2: Lithography Blueprint: (a) Lithography layer one steps; (b) Lithography layer two steps; (c) Lithography layer three steps.

are dissolved in 1165 developer at 70°C. After 10 minutes, when the resists have dissolved, the multilayer can be carefully removed using a flow of developer from a pipette to lift it off the substrate. This leaves only the multilayer which sits directly on the membrane surface. The second lithography layer, Figure 4.2(b), is necessary in order to create nanoscale devices of the desired size and shape from the magnetic multilayer squares deposited during the first step. This layer starts with the spinning of a positive photoresist ZEP layer. Following this the sample is once again exposed to an electron beam. After development, small areas on top of the multilayer stacks are no longer covered by the photoresist. This allows the deposition of a Ti hard mask by electron beam evaporation, as explained in section 4.2.4. Following the Ti deposition the ZEP is removed using 1165 at 70°C to lift off the extra Ti film with the same method described in the previous paragraph. With a hard mask in place, it is possible to use an ion miller to carve the stacks into the shape of the devices to be fabricated. Ideally, no Ti remains on top of the multilayer stacks after ion milling. The third lithography layer, Figure 4.2(c), is used to create contacts on the nanoscale devices that can be wirebonded to a holder which can then be electrically connected to the experimental equipment for measurement. First MMA, PMMA layers are spun and baked onto the samples, using the same method as in the first lithography layer. Following this the samples are once again exposed to an electron beam, this time in the shape of the electrical contacts which are wanted. The photoresists are then developed in IPA:water, 7:3, and then Ti/Au* is deposited onto the samples using electron beam evaporation. Finally, the resists are dissolved to lift off the extra Ti/Au* leaving contacts of the correct shape.

4.2.2 Optical Lithography (OL) and Electron Beam Lithography (EBL)

Lithography methods are used extensively in the electronics manufacturing industry to produce integrated circuits (IC). There are three groups of processes that take place to make an IC in industry: film deposition; patterning; and semi-conductor doping. The first two of these were also essential for the fabrication of Hall measurement devices in this project and they were designed and fabricated by hand in the University of Leeds cleanroom and physics laboratories. These devices are designed specifically to measure the topological Hall effect due to magnetic skyrmions. The term lithography is used for the patterning process which involves the formation of a three dimensional relief image over the top of the material that the image is to be transferred to. There are two main types of lithography, optical lithography and electron beam lithography, that are separated by the method of image exposure and the scale of the images that can be produced due by each of the methods. In both types of lithography patterns are written into resists that are developed to expose the material under the resist in the desired shape. Once there is a defined pattern, material is either added to (additive patterning) or removed from (subtractive patterning) the exposed layer, the left over resist is finally removed to leave material in the shapes required for the devices. Resists are energy-sensitive polymers which become more or less soluble after exposure to energy from a

suitable source, which may be optical light or a beam of electrons with a well defined energy. The minimum size of the features which can be defined by optical lithography is limited by diffraction to the scales on the same order as the wavelength of light that is used. Given this limitation smaller wavelengths tend to be favoured and sources such as UV mercury lamps ($\lambda = 365 \text{ nm}$) or ArF lasers ($\lambda = 193 \text{ nm}$) can be used to produce line widths of around 250 nm and 150 nm respectively. In order to make devices which are smaller than these scales shorter wavelength beams are needed. To achieve this ion beams like electron beams with appropriate energies are used. An electron beam with 10 keV has electrons with a wavelength of $\lambda \approx 0.1 \text{ \AA}$. In principle this allows definition of linewidths which are $< 100 \text{ nm}$, but the final linewidth is determined by the interaction with the resist layer which depends on the type and thickness of the resist used. In photolithography the final linewidth also depends on the dose and defocus of the laser beam during exposure. The dose controls the energy delivered to the resist and the defocus controls the height at which the light is focused. The combination of dose and defocus which will create a sharp design of the desired scale is different for each combination of design and resist, this means that for each new design there needs to be a dose and defocus test performed.

Device Fabrication - Lithography

For the devices used in this project a combination of optical and electron lithography steps were used as discussed in Section 4.2.1. In the first electron beam step, to define the nanodiscs, a 1:1 ZEP:Anisole 4 resist is spun onto the samples at 4 krpm for 40s. This is then baked and the design is then exposed to an electron beam using a Jeol JBX 6300FS electron beam lithography system. The devices are then developed to remove the resist in the area which will become the nanodiscs. This process is illustrated in Figure 4.2. A second electron beam step, to define the inner contacts of the devices, uses an MMA/PMMA bilayer. These layers are spun and baked individually. The design for the inner contacts is the written by the Jeol. The design is then developed removing the resist where the inner contacts will be deposited. This process was shown in Figure 4.2. The Jeol JBX 6300FS electron beam lithography system used in this project is capable of writing areas of $150 \text{ mm} \times 150 \text{ mm}$, with a minimum feature size of around 8 nm, and an overlay accuracy of around 25 nm. Using electron beam lithography for this step was particularly important for defining the current injectors in later devices. The outer contacts and alignment markers for the devices are defined using optical lithography, as it is quicker and cheaper than EBL, and the features are large enough to use this method. A LOR7B-S1805 bilayer resist is used for all OL steps in this project. The two resist layers are spun and baked individually, LOR7B: spun at 6 krpm for 40s, and baked at 180°C for 5-10 minutes, S1805: spun at 4 krpm for 40s, and baked at 115°C for 2 minutes. A maskless aligner (MLA) is used to expose the resists, where the features are written by a 375 nm laser at up to $1\mu\text{m}$ precision. Following the exposure the samples are developed in a solution of 4:1 MF351:IPA for around 50s, or until the layers of resist have cleared in the design, and a visible

undercut in the LOR7B is observed. The undercut in LOR7B allows an easier and cleaner lift off of extraneous material after electron beam evaporation. The lift offs are performed in 40°C SVC-14 photoresist stripper, or warmed acetone. Both chemicals can have a corrosive effect on the thin, Ti/Cu inner contacts used in the devices, and this is one possible reason for the contact resistance issues faced in the more complicated and smaller featured injector devices. The MLA used for the OL is capable of writing areas up to 150 mm × 150 mm per hour on substrates between 5 mm × 5 mm and 150 mm × 150 mm in area. To use the MLA safely on membranes it is necessary to place an additional wafer coated in PDMS, a silicon-based organic polymer, underneath the membrane to be patterned between it and the MLA stage. This protects the membrane from the vacuum used to hold the sample to the stage during laser writing, while the PDMS coating provides enough friction with the small, light membrane on top that the sample remains stationary relative to the PDMS coated wafer and the MLA stage during writing.

4.2.3 Ion Mill Etching

Ion mill etching is a dry physical etching process which is used to remove unwanted magnetic material during nanofabrication of Hall devices used in this project. In terms of the physical process which occurs ion mill etching is equivalent to reverse sputtering, where the sample could be considered to be like the magnetron targets from which material is removed by incident Ar ions striking the target in a ring shape. In ion mill etching material is removed from the sample using the same process, but without a magnetic field present the ions strike the sample isotropically. A Ti hard mask is deposited over the areas of magnetic multilayer which are to be protected. The thickness of the hard mask deposited is decided based on the ion etch time to remove the extraneous magnetic multilayer and the corresponding etch time of the materials used in the hard mask.

The thickness of Ti chosen to be deposited during electron beam evaporation is calculated from the expected time to mill through the multilayer stacks and the known mill rate of Ti; however, the exact thickness deposited during electron beam evaporation is not known to a high level of accuracy and so calibration samples are also made, on silicon oxide wafer, during the same deposition. The thickness of these calibration samples can be measured using XRR to find an estimated milling time which is then checked by milling them to check. The calibrations are milled starting from the estimated time to clear the Ti mask, and then in 10 second increments either side of this time. Clearance of the Ti mask is verified using a two-point contact resistance measurement after each milling increment to check when the film is no longer conductive. Once an optimum mill time has been established, a sister sample from the sputtering growth is milled to check that the magnetic multilayer stack also clears within the optimum mill time. Ideally, no Ti mask is left on top of the multilayer stack. If continuous Ti remained on top of the multilayer stack then it would be possible for the current used during Hall measurements to go through the Ti rather than the multilayer stack which is undesirable.

For the later injector devices, the hard mask was chosen to be Ti/Pt/Ti because Ti a very slow etch rate compared to the metals which need to be etched, this means that one can be confident that the multilayer stack will etch away faster than the chosen thickness of Ti. The thickness of the Pt layer in the hard mask is chosen so that the point when all of the extra multilayer is removed occurs before or just after the etch reaches the Pt layer in the mask. This allows one to stop the etch confident that all the extra multilayer is removed and that the remaining multilayer is not damaged due to the ion beam. A very thin Ti layer is at the bottom of the hard mask in contact with the magnetic multilayer to help with adhesion of the Pt and as back up protection in the case that the Pt is etched through too quickly.

Inclusion of the platinum layer in the hard mask also made it possible to keep the ion beam further from the multilayer at the end of the etch process, and therefore cooler. Heating the samples for a prolonged period has the potential to begin an annealing process, which mixes the elements at the layer boundaries. Given the thinness of the layers in the multilayer used any mixing could easily make very thin layers into an amorphous mix at each boundary which is not desirable for producing a high interfacial DMI in the samples to promote skyrmion formation and stabilisation. The platinum layer included as a buffer could be detected by the secondary ion mass spectrometer (SIMS) in the miller. The SIMS produces a real time graph of the ions that are removed from the sample allowing the progress of the etch to be tracked. This means that it is possible to tell when the magnetic multilayer has been totally removed (a dip in the Co signal from the multilayer, and a rise in the Si signal from the substrate), and when the platinum layer in the hard mask is reached (a rise in the platinum signal).

The samples are also capped with a thick layer of Pt such that if the previously discussed fail-safes did not succeed there is still time to stop the etch before it reaches the important part of the magnetic multilayer stack (the CoB/Ir/Pt repeats). A piece of silicon with only the Ti hard mask is also milled at the same time as each sample, to provide a larger Si signal when the etch has removed all of the hard mask. This is needed so that it is easier to detect the Si rise in the SIMS graph, and thermally oxidised silicon creates a stronger signal than silicon nitride membranes. Crucially, it is not possible to track the Ti being milled using SIMS because components of the ion miller are made out of Ti due to its extremely low mill rate so there is always a high background of Ti ions.

Throughout this project a Scia Mill 150 was used to perform the ion mill etch. This miller has a 218mm, 2kW, circular microwave electron resonance (ECR) plasma source. The miller has the capacity for Ar etching, as well as Cl₂ and BCl₃ chemically assisted etching, however Ar etching is the only process used during this project. In addition to water cooling the Scia Mill 150 has helium backside cooling for the substrate/sample holder, to keep the sample cool during the ion mill, this is particularly important for the magnetic multilayers used in this project as we require them to stay as deposited - in thin, clearly defined layers. During the etch process argon ions are directed onto the sample in an isotropic beam. The sample plate is tilted such that it is at a 45 ° angle to

the incoming ion beam. The samples are rotated at between three and five revolutions per minute throughout the process so that the etch occurs in the most uniform way possible.

4.2.4 Electron Beam Evaporation

The electron beam evaporator was also used as a method of material deposition. The process is somewhat similar to the sputtering process, both techniques use physical vapour deposition however the energies of the atoms in evaporation techniques are thermal whereas in sputtering the energies are much higher. In electron beam evaporation a beam of electrons is incident on the material to be deposited, which is held in a crucible at the bottom of the vacuum chamber. During deposition the vacuum chamber is kept at a pressure less than 2×10^{-6} mbar allowing the material evaporated from the crucible by the incident electrons to disperse through the chamber and condense onto the sample surface. Electron beam evaporation was used to deposit the Ti/Pt/Ti hard mask in lithography layer 2, Figure 4.2(b) and the Ti/Cu electrical contacts for the devices in lithography layer 3, Figure 4.2(c). Electron beam evaporation was used to deposit the Ti/Pt/Ti hard mask for the ion milling step and the Ti/Cu inner electrical contacts because the features in the patterns are too small to be able to sputter into directly. In addition, electron beam evaporation produces better step coverage than sputtering, and can be done at a much higher rate, both of these features are important for the deposition of the electrical contacts. Similarly, both the hard mask and contacts are made of fewer layers than the magnetic multilayers which are sputtered, and the deposition is the same for each sample whereas different numbers of repeats of the multilayers are grown by sputtering.

4.2.5 Device Fabrication Challenges

Fabrication of functional nanodevices has proved to be challenging for a number of reasons. The main difficulties have arisen from an attempt to incorporate current injectors in the design in order to nucleate skyrmions whenever it is desired. Similarly, adjustments to the materials used for the measurement contacts, in order that they may be X-ray transparent, may have also contributed to contact resistance problems that have prevented measurement of many devices. In the next section motivation for the design changes is provided along with some of the systematic tests which were performed to troubleshoot and eliminate the causes of problems.

Changes to Fabrication Process

After the measurement of a first set of devices with Ti/Au* contacts it was decided that future devices should be made with Ti/Cu contacts to allow for magnetic imaging of the areas of the disc which are underneath the contacts. In the initial measurements of devices with Ti/Au, the contacts hide a significant portion of the disc meaning that later analysis may not be accurate as there may

be skyrmions present in the obscured areas and the percentage of the device that is magnetised OOP cannot be estimated accurately. In 2019 our collaborator at PSI, Simone Finizio, successfully

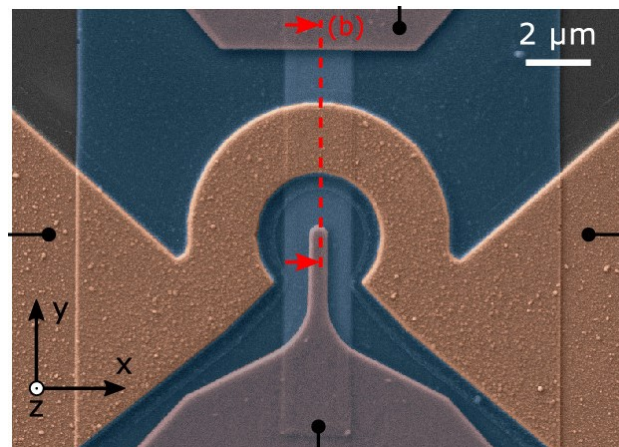


Figure 4.3: False color scanning electron micrograph of the injector structure employed for the skyrmion nucleation by Finizio et al., reproduced from reference [5].

created current injectors that can nucleate skyrmions on demand using multilayers that had been grown using DC sputtering in Leeds [5]. Growth of these multilayers included a run of samples with varying Co thicknesses and one with varying platinum thicknesses. The test multilayers were imaged at the beamline at PSI to determine the samples that provided the best environment in which to nucleate skyrmions. The results of the imaging was reported to us by our collaborator and these thicknesses determined the structure of the multilayers grown for all of the samples used in this project. The subsequent design changes were made to try to incorporate the current injector design used in Finizio’s experiment into the Hall discs so that skyrmions could be nucleated in the discs on demand using current pulses. Incorporating injectors required scaling the design down by an order of magnitude - Finizio’s devices were micron scale not nano-scale - and keeping separate Hall measurement contacts that would be able to withstand the measurement currents required. This is also the point at which Co was switched for CoB in the Hall devices made for this project. The hope was that following successful skyrmion nucleation it would be possible to use current pulses to move the skyrmion into the centre of the device away from the injectors, contacts, and disc edge. Additionally, multiple skyrmions could be added in this manner.

4.2.6 Testing the Effects of Lithography Techniques on Contact Resistance

One of the first methods used to try to overcome the contact resistance issues was an oxygen plasma ashing step that was introduced before final contact deposition to clear any CuO or resist residue that could exist between the inner and outer contacts. This did not produce any noticeable improvements. A different order of contact placement was used for some nanodisc fabrications

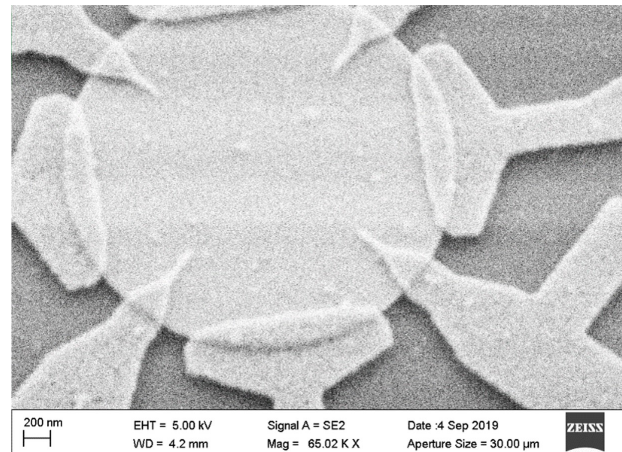


Figure 4.4: A scanning electron microscope (SEM) image of a device which was fabricated for a September 2019 beamtime. The device includes eight contacts, four current injectors and four grounding contacts.

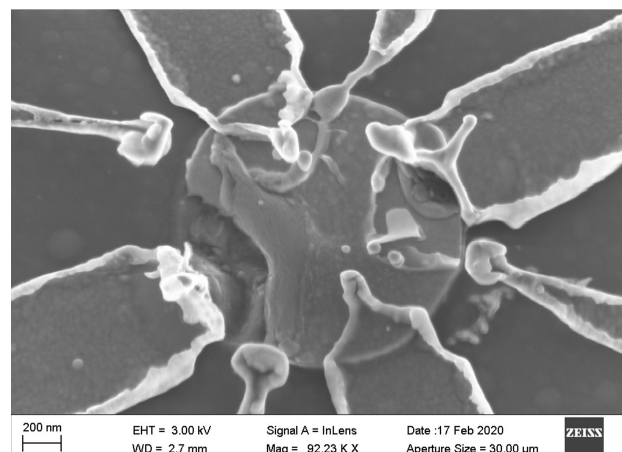


Figure 4.5: A scanning electron microscope (SEM) image of a blown up device.

in order to limit contact erosion due to these chemicals. For these devices the outer contacts (Ti/Au and corrosion resistant) were deposited before the inner Ti/Cu contacts. This also had no noticeable effect on the contact resistance and the devices remained either poorly electrically contacted or extremely sensitive and liable to ‘blow up’ from static discharge before it was possible to measure the devices, or early in measurement. This resulted in many devices with damage like that shown in Figure 4.5 and very little useable data.

This is the point in my PhD project when the COVID-19 pandemic started and the university labs and cleanroom closed down. When the labs were opened again six months later the first thing that I did was fabricate wires and devices on which to measure the contact resistance. The aim was to try to see if particular steps in the fabrication process were affecting the contact resistance to the nano-scale devices. Examples of overlapping wires and a multilayer disc with contacts

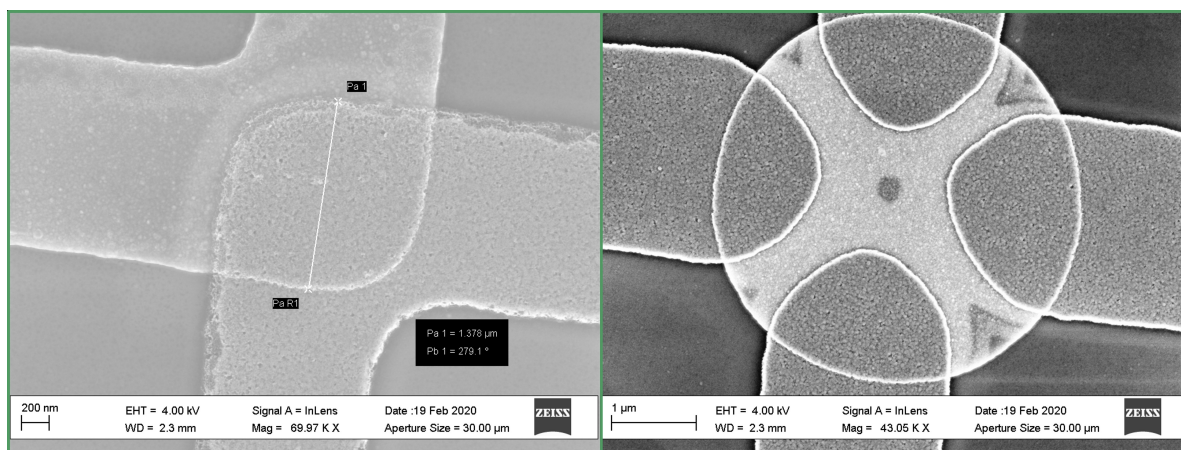


Figure 4.6: A scanning electron microscope (SEM) image of devices used for contact resistance tests.

deposited are shown in Figure 4.6. These images were taken in order to measure the area of the contact-multilayer overlap. The results of resistance measurements on these, and other devices with different overlap areas are shown in Figures 4.7(a) and 4.7(b). Figure 4.7(a) is an exemplary non-linear I-V curve from one such contact resistance test device. This type of I-V relationship could be indicative of resist residue left between the magnetic multilayer and the contacting metals. The resistance-area products calculated, and plotted in figure 4.7(b) show a high variation in R.A even for samples with the same contact area. Additionally, the RAs are on the order of $\text{m}\Omega \mu\text{m}^2$ which suggests pretty low contact resistances. Unfortunately, due to reduced cleanroom access (from social distancing precautions) followed by the cleanroom closure for university building work I was unable to carry out further tests to try to troubleshoot the problems with the nano-Hall devices. As such the samples measured to produce the results that are presented in Chapters 6 and 7 were grown without access to lithography techniques.

4.2.7 X-Ray Magnetic Circular Dichroism - Scanning Transmission X-Ray Microscopy (XMCD-STXM)

Scanning transmission x-ray microscopy (STXM) is a technique which is based on the varying levels of absorption of x-rays by different elements. By fabricating the devices used in this project on thin (200 nm) silicon nitride membranes, which transmit high levels of x-rays it is possible to image the hall disks by scanning across the area of the disk and measuring the intensity of the transmitted x-rays. X-ray magnetic circular dichroism relies on similar theory to that of the magneto-optical Kerr effect which was discussed in section 3.2.3 where the main differences are: the wavelength of light incident on the sample; that the x-rays are transmitted through the sample in XMCD versus reflected from the surface in MOKE; and that MOKE uses polarised optical wavelength laser light

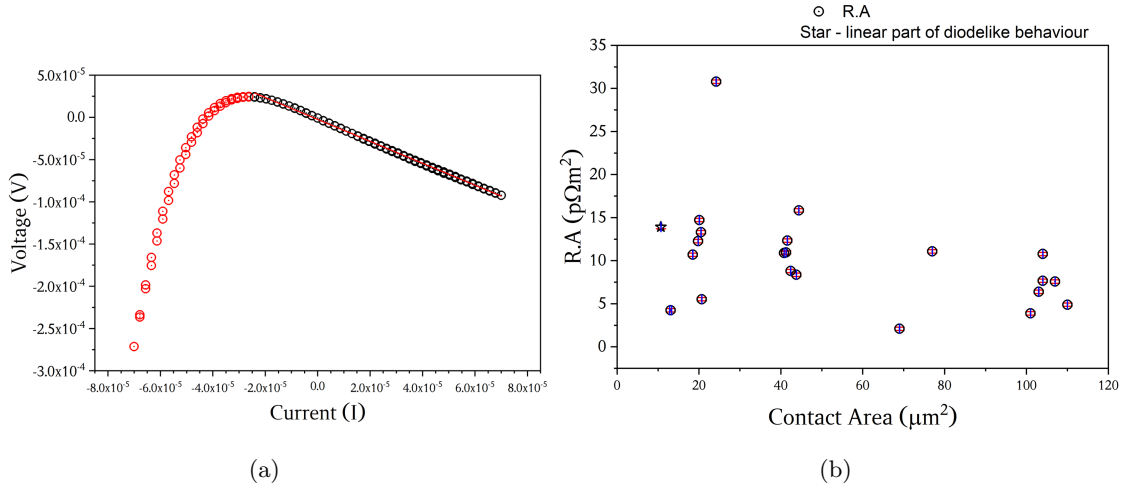


Figure 4.7: (a) A non-linear I-V curve from a contact resistance test wire. (b) Resistance-Area products for the contact resistance test devices.

whereas XMCD uses circularly polarised x-rays. In this project both polar laser MOKE and XMCD imaging are used due to their sensitivity to the out of plane magnetisation of the sample, M_z . In order to produce an XMCD picture of the Hall disk a STXM picture is taken with each x-ray helicity, as shown in Figures 4.8(a) and 4.8(b).

The two helicities are oppositely affected by the M_z experienced as they are transmitted through the sample, therefore by taking the normalised difference of the intensity of the two images,

$$\frac{I_+ - I_-}{I_+ + I_-}, \quad (4.1)$$

where I is the intensity of the array of pixels making up the image and $+/-$ denote the helicity of the x-ray polarisation used in the image, it is possible to resolve the differences between the two clearly, which is the perpendicular component of a magnetic structure in the Hall disk, as shown in Figure 4.8(c).

4.3 XMCD-STXM Room Temperature Transport Measurements

In-situ Hall transport measurements which occur at the same time as XMCD-STXM imaging have been made possible at the PolLux endstation at the Swiss Light Source (SLS) at the Paul Scherrer Institut (PSI)[60]. A simple schematic of the wiring used to perform the Hall transport measurements is given in figure 4.9, and the sample is placed in a vacuum chamber, on a piezoelectric stage which is moved in the x-y plane such that the stationary x-ray beam, which is pointing along the z-axis, scans across the sample in order to image the disk. The transport measurement uses a nanovoltmeter measure the Hall voltage in the y direction due to the alternating current (AC) which is applied in the x direction using a Keithley 6221 current source. A lock-in amplifier, locked

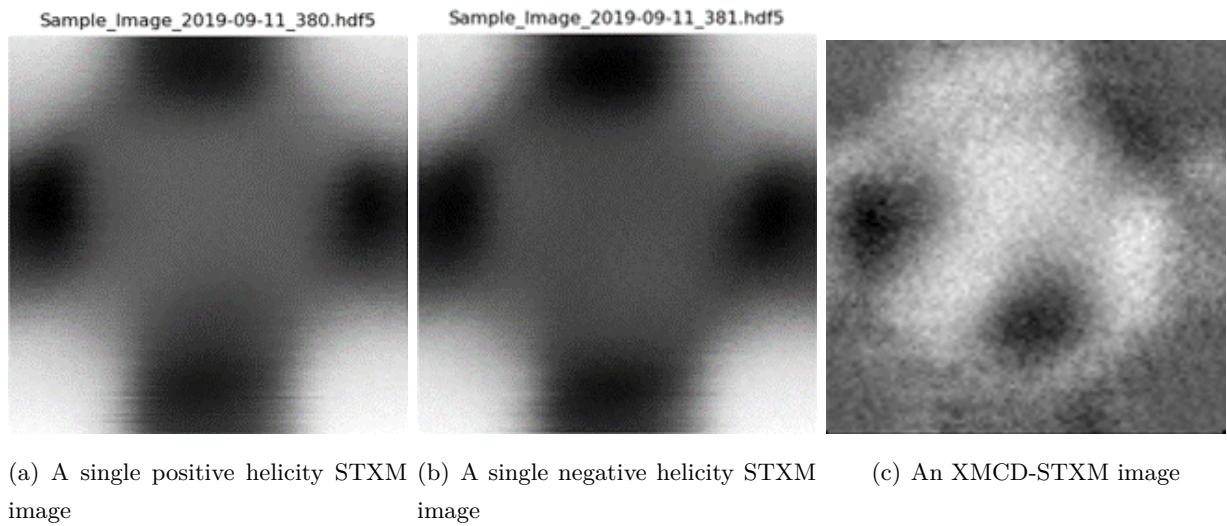


Figure 4.8: Example of an XMCD-STXM image (c) generated from two opposite helicity STXM images (a) and (b).

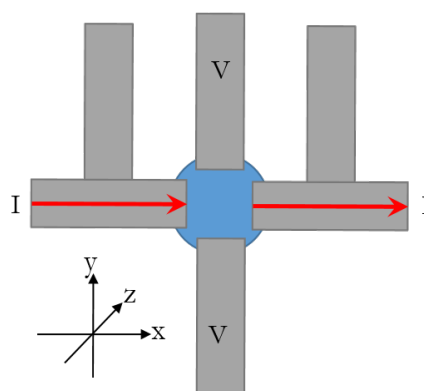


Figure 4.9: The wiring of the 800nm nanodevice in order to carry out in-situ Hall transport measurements.

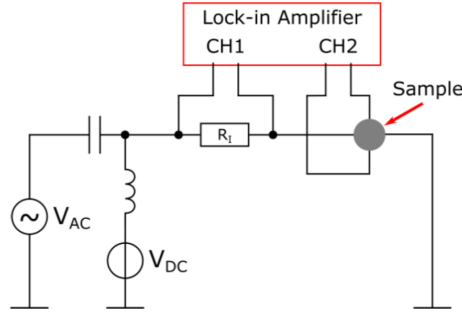


Figure 4.10: Transport measurement schematic, the first lock-in amplifier channel is used to measure the current passed through the device (using a reference resistor, R_I), and the second channel is used to measure the Hall voltage generated across the sample. [60]

to the frequency of the AC from the current source, is used to trigger the voltage measurement. This setup and method for transport measurements has been successfully implemented by Finizio et al. in combination with XMCD-STXM described in the previous section[60]. This makes the analysis and interpretation of the transport data much easier, as each data point taken will have an image of the associated out of plane magnetisation in the sample.

Preliminary XMCD-STXM and transport results

Presented here are the limited preliminary results that were obtained during XMCD-STXM beam-times in the first year and a half of my PhD from Hall discs with a nominal multilayer structure of Ta(2.9 nm) | Pt(3.0 nm) | [Co(0.6 nm) | Ir(0.4 nm) | Pt(0.8 nm)] \times_6 | Pt(2.2 nm) and four Ti/Au contacts for transport measurements, as shown in the right of Figure 4.1. Figure 4.11 shows XMCD-STXM images of a nano-Hall device and a major hysteresis loop measured in Hall resistivities. The labelled points on the hysteresis loop relate to the images with the same letter. It is easy to see the effect of the anomalous Hall resistivity (which is proportional to the OOP magnetisation of the Hall discs) in both the hysteresis loop and then images. In the images, black and white indicate magnetisation point into or out of the images and grey indicates diminished or zero OOP component of magnetisation. In particular, images (a), (b), (h), and (i) relate to a positively saturated OOP magnetisation at the top of the hysteresis loop, (d)-(f) relate to a negatively saturated OOP magnetisation at the bottom of the hysteresis loop, and (c) and (g) relate to the sides of the hysteresis loop where the disc is switching from positive to negative OOP magnetisation and vice versa, as shown by the intermediate grey of the disc in those images. Figure 4.12 shows the results of transport measurements during a minor hysteresis loop, starting from a magnetisation texture with three skyrmions present and ending with annihilation and a saturated magnetisation. Some of the images corresponding to the transport measurements are shown in Figure 4.13. The transport data

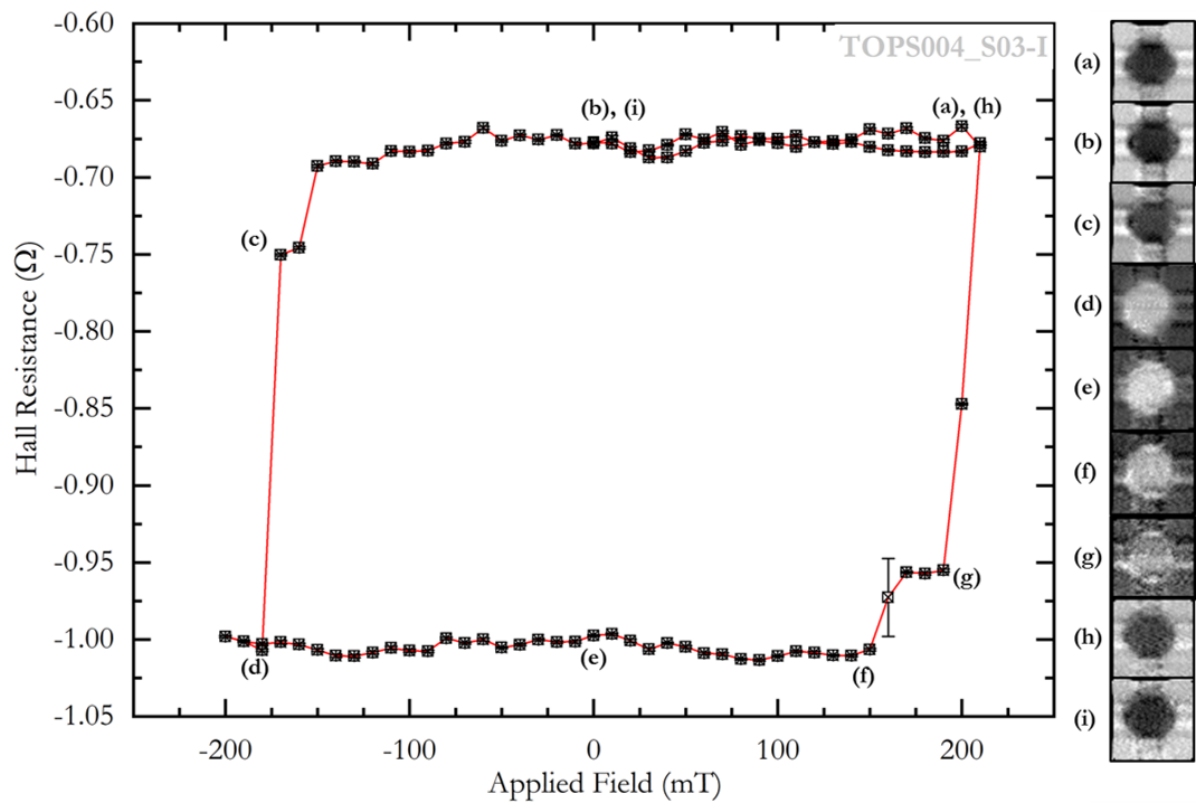


Figure 4.11: A hysteresis loop in Hall resistivity measured during XMCD-STXM imaging where the XMCD-STXM images relate to the labelled points on the hysteresis loop.

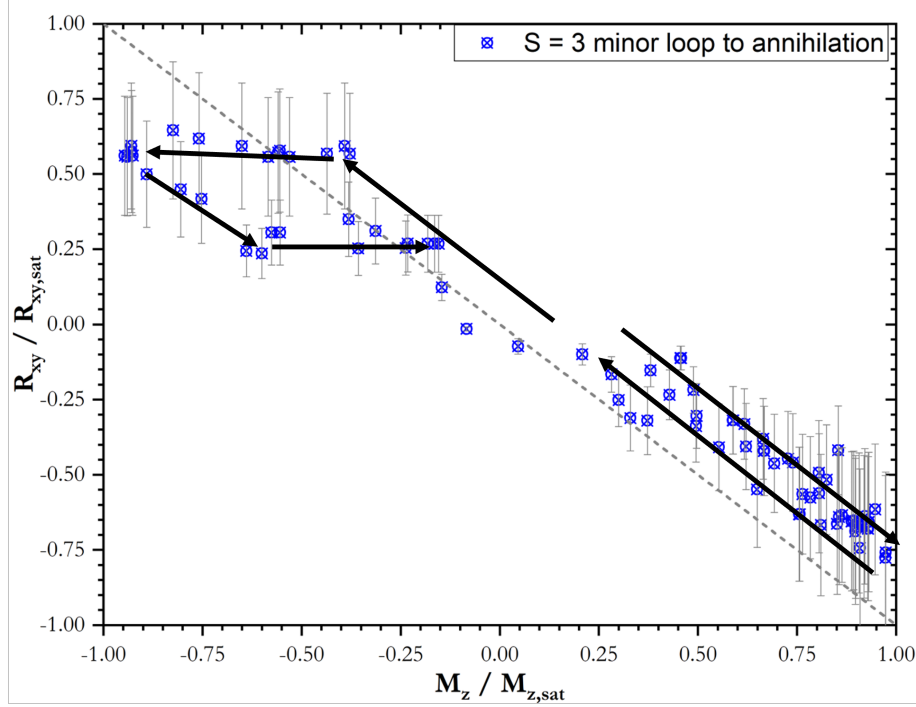


Figure 4.12: Normalised OOP magnetisation in a Hall disc vs normalised Hall resistivity for a minor hysteresis loop with a Hall disc with magnetisation texture with $S=3$ (three skyrmions) until annihilation. The dotted line included indicates the line upon which all the points are expected to fall when there are no topological textures present.

in Figure 4.12 was processed following the same methods as used by Zeissler et al. in reference [8]. The data in the top left of figure 4.12 does not clearly correspond to the imaged magnetisation textures and it is likely that the data here contains drift related to varying background x-ray intensity in the XMCD-STXM images which were used to find $\frac{M_z}{M_{z,sat}}$. In any future work this could be corrected by normalising the XMCD-STXM images using the x-ray intensity from part of the image without a device on it. Most importantly, the images presented in Figure 4.13 and the work done on skyrmion motion by Zeissler et al. presented in reference [117] provides good evidence for skyrmion presence at room temperature in samples with structures similar to Ta(2.9 nm) | Pt(3.0 nm) | [Co(0.6 nm) | Ir(0.4 nm) | Pt(0.8 nm)] \times_6 | Pt(2.2 nm) and Ta(3.2 nm) | Pt(2.7 nm) | [CoB(0.8 nm) | Ir(0.4 nm) | Pt(0.6 nm)] \times_5 | Pt(2.2 nm) respectively which justifies the choice of sample structure used in the rest of this project.

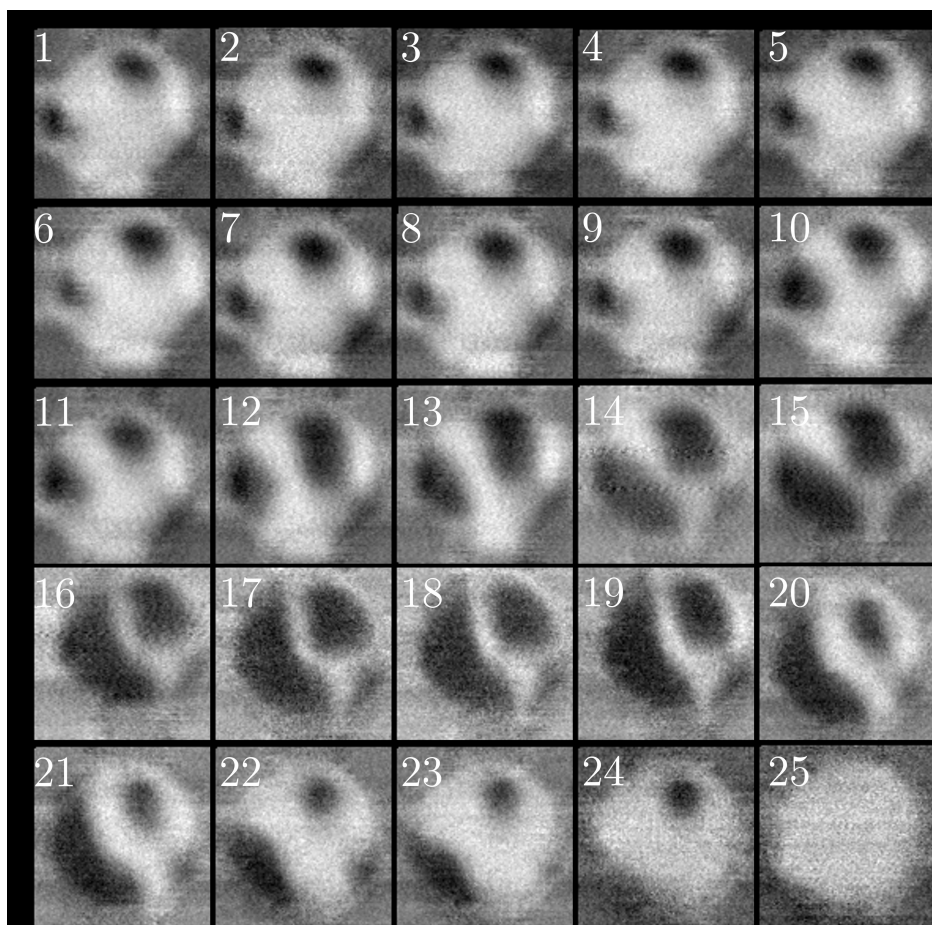


Figure 4.13: XMCD-STXM images relating to the transport data presented in Figure 4.12 where the arrows show the order that the transport data was collected and correspond to images 1-25.

CHAPTER 5

Field Corrections and Data Analysis

5.1 Introduction

In section 2.6.3 three known contributions to the Hall effect were identified, the ordinary (Eq. 2.27), anomalous (Eq. 2.30), and topological (Eq. 2.32) resistivities. In order to investigate the topological contribution to the Hall resistivity electrical transport measurements of the overall Hall resistance (R_{xy}) were performed in a cryostat as described in section 3.3.1, and magnetometry measurements were conducted using a SQUID-VSM as described in section 3.2.4, to allow the anomalous Hall contribution ($\propto M_z$) to be estimated. Equation 2.25 expresses the overall Hall resistivity as the sum of each component. In this thesis the excess Hall resistivity, often identified in published works as the topological Hall resistivity, is calculated by subtracting the ordinary and anomalous resistivity components from the overall Hall resistivity that was measured. This required coordinated evaluation of hysteresis loops measured in Hall resistance and magnetisation. By necessity these data sets were collected using equipment with different superconducting magnets. In this chapter the methods used for magnet calibration (5.2), field corrections (5.2.3), and data analysis (5.3) are explained in detail. Potential pit-falls, limitations, and assumptions in experimental (5.2.1, 5.2.2) and analytical (5.3.4, 5.4) procedures are identified.

5.2 Calibration of Superconducting Magnets

Superconducting magnets are electrical coils (often a single solenoid or pair of coils) made of superconducting materials. The zero-resistance state of superconductors that occurs below the critical temperature of the superconductor is exploited to create large magnetic fields, overcoming the limitations of high currents in resistive materials (over-heating and the need for extremely high voltages). Unfortunately, in addition to properties that make superconducting magnets highly efficient and capable of very strong magnetic field production there is also an effect that makes it difficult to know the field at the position of the sample - trapped flux. When zero current is applied to the superconducting magnet (i.e. attempting to apply zero field) flux vortices persist within the superconducting material due to pinning in the material. These vortices each contribute a very small persistent current that produces a non-zero magnetic field known as the ‘trapped flux’. In order to reach zero current in a superconducting magnet a small current that produces a field equal and opposite to the trapped flux from the pinned vortices must be applied. This means that all measurements where a superconducting magnet is used have a non-zero offset in the magnetic field. The offset correction to be applied differs depending on: the geometry of the coils in the magnet, the direction the magnetic field is being swept in, and the history of the superconducting magnet. The dependence of trapped flux on the geometry of the coils and the relative location of the sample to the magnet both contribute to the sign and magnitude of the field correction required. The dependence on direction of field sweep means that hysteresis loops must be corrected in two parts,

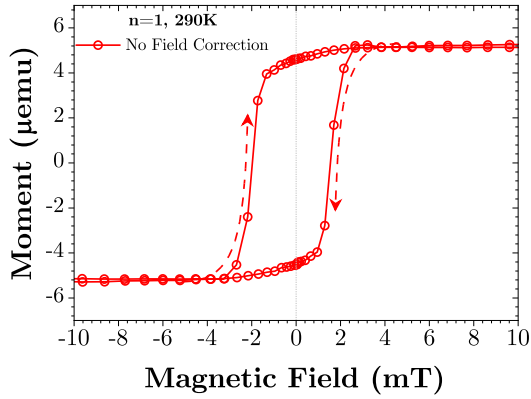


Figure 5.1: A raw moment vs field hysteresis loop, measured at 290 K, in a $[\text{CoB}|\text{Ir}|\text{Pt}]_{n=1}$ sample. The raw data suggests that the sample changes magnetisation *before* the external magnetic field has changed direction.

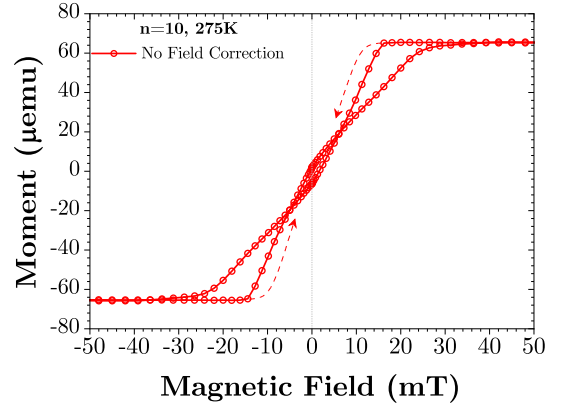


Figure 5.2: The raw moment vs field hysteresis loop, measured at 275 K, in a $[\text{CoB}|\text{Ir}|\text{Pt}]_{n=10}$ sample. The two branches of the hysteresis loop cross in the centre near $H = 0$.

by adding or subtracting the field correction depending on the direction of field sweep. The history dependence of the magnet means that the amount of trapped flux may change if the measurements are performed over a different field range, or if a different field sweep rate or settle time is used.

When samples have a high enough coercive field (are magnetically ‘hard’ enough) the size of the zero-error in field can be negligible compared to the coercive field. It can be easy to overlook these issues when working with very ‘soft’ materials with perpendicular magnetic anisotropy where the hysteresis loops can be extremely square. This is because, at first glance, it can be difficult to tell which half of the hysteresis loop is collected during the positive to negative field sweep versus the negative to positive field sweep. An example of this kind of hysteresis loop is shown in figure 5.1, measured in the single repeat $[\text{CoB}|\text{Ir}|\text{Pt}]$ sample used in this thesis. By contrast, in multilayer samples with larger numbers of repeats the shape of the hysteresis loop becomes wasp-waisted while maintaining a very low coercivity. The change in shape from square to wasp-waisted highlights the crossing points of the hysteresis loop and the unphysicality of data if presented without applying field corrections. Figure 5.2 was measured in a $[\text{CoB}|\text{Ir}|\text{Pt}]_{\times n}$ sample with $n = 10$ repeats in the multilayer and is illustrative of a typical wasp-waisted hysteresis loop prior to applying a field correction.

As demonstrated in figures 5.1 and 5.2 the $[\text{CoB}|\text{Ir}|\text{Pt}]$ samples used in this work clearly have coercive fields that are of a similar order of magnitude to the field offset caused by trapped flux. Similarly, the excess resistivity due to skyrmions is expected to occur when the samples are switching magnetisation within the field range close to the coercive of the samples. Due to this it is important to calibrate the trapped flux for the specific measurement sequences used.

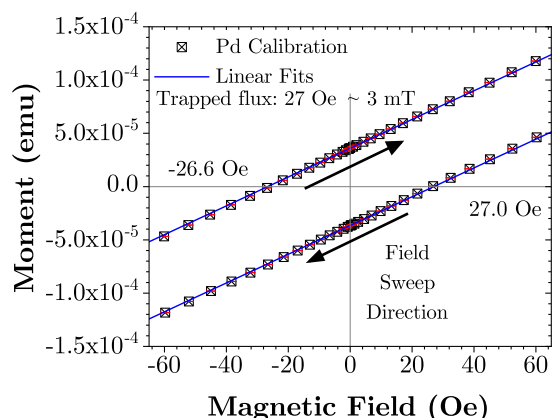


Figure 5.3: Magnetic moment vs applied field for paramagnetic calibration sample made of Pd. Arrows indicate the direction of field sweep and the trapped flux is found from the magnetic field intercepts of a linear fit of the data.

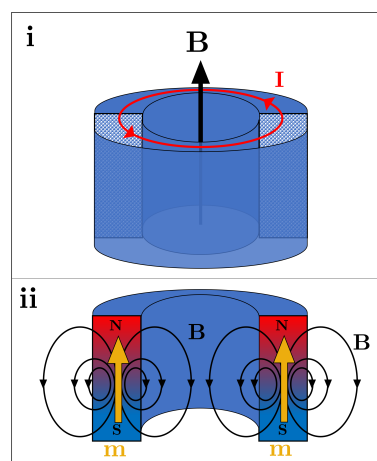


Figure 5.4: Schematic of a superconducting solenoid showing (i) the resultant magnetic field when the magnet is on, and (ii) the magnetic field due to the trapped flux within the coils of the solenoid that remains when the current is zero.

5.2.1 SQUID-VSM Magnet

The superconducting magnet in the SQUID-VSM (Quantum Design MPMS 3) was calibrated by measuring a Pd reference sample. Pd is paramagnetic so its magnetic moment aligns with the applied magnetic field producing a line with a positive gradient as shown in Figure 5.3. The magnetic field axis intercepts indicate the trapped flux in the magnet due to the measurement sequence used. The trapped flux points in opposite directions for each side of the hysteresis loop measured. One can understand the direction of the correction by considering the geometry of the superconducting solenoid employed in the QD MPMS 3, shown in figure 5.4. When applying a magnetic field, the current through the superconducting solenoid induces a magnetic field through the centre of the coils, in figure 5.4 (i) this is shown in the upwards direction. Applying a large enough field (> 1000 Oe) creates trapped flux within the solenoid coils that points in the same direction. This trapped flux may be thought of as a ring of small bar magnets with their poles pointing upwards (figure 5.4 (ii)). This means that the resultant field, in the centre of the solenoid coils where the sample is located, is the sum of the field generated by the current in the solenoid, and the field pointing in the opposite direction due to the trapped flux. This causes the field felt by the sample to reach zero *before* the current through the solenoid is zero. Therefore, when no current is applied the sample is in fact already experiencing a field pointing downwards (for the example discussed and shown in figure 5.4 (ii)). In this situation the correction for trapped flux is constant near zero field and negligible at large fields. For the measurements in this thesis it is

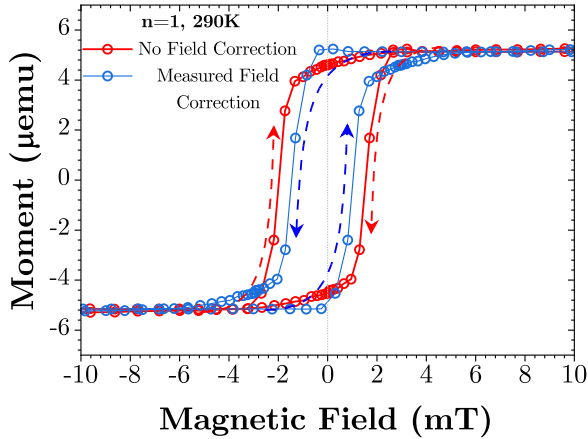


Figure 5.5: Moment vs corrected field hysteresis loop, measured at 290 K, in a $[\text{CoB}|\text{Ir}|\text{Pt}]_{n=1}$ sample.

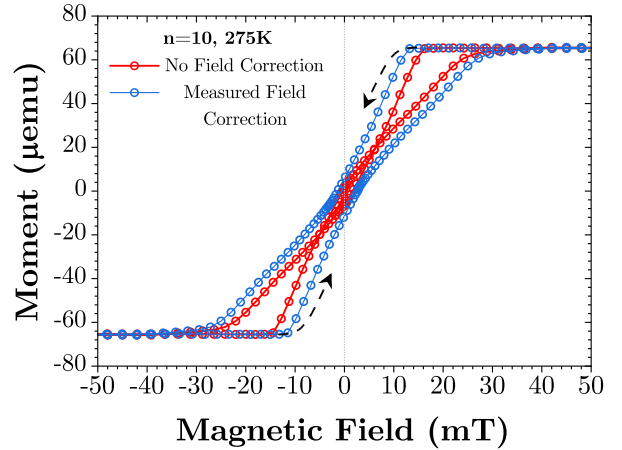


Figure 5.6: Moment vs corrected field hysteresis loop, measured at 275 K, in a $[\text{CoB}|\text{Ir}|\text{Pt}]_{n=10}$ sample.

sufficient to use a constant correction for the trapped flux by adding or subtracting the magnitude of the trapped flux from the applied field, depending on if the field is sweeping positive to negative or vice versa. This adjusts the loops so that the data reflect that zero field occurs when the sample experiences zero field rather than when the instrument is not applying a current to the magnet. Confirmation of the validity of this method of field correction can be seen in figures 5.5 and 5.6 which show the moment vs field measurements from figures 5.1 and 5.2 (in red) with the same data when the correction for the trapped flux is applied (in blue). It is clear in figures 5.5 and 5.6 that the field correction produces hysteresis loops with sensible behaviours and no crossings.

5.2.2 Cryostat Transport Magnet

In order to calibrate the magnetic field applied by the superconducting magnet used during transport measurements a sample holder with a Hall bar was used. The Hall resistance of the semiconductor Hall sensor was measured at the same time as the magnetic multilayers allowing the trapped flux of the magnet to be defined. In figure 5.7 the data from the calibration sweep of the measurement regime used is presented. This measurement sequence used a sweep rate of 500 mT/min and had no waits or settle time for the magnet included. It is clear from the size of the trapped flux that this is an important effect that must be taken into consideration during the data analysis stage, particularly in my samples which have very low coercive fields at room temperature (< 10 mT) and still low coercive fields at low temperatures (< 10 K \rightarrow 50 – 80 mT) where a trapped flux on the order of 10 mT is a significant percentage of the coercive field. The calibration measurement was performed over the whole range of temperatures that the samples were measured over in order to evaluate the repeatability of the measurements and establish if the trapped flux has

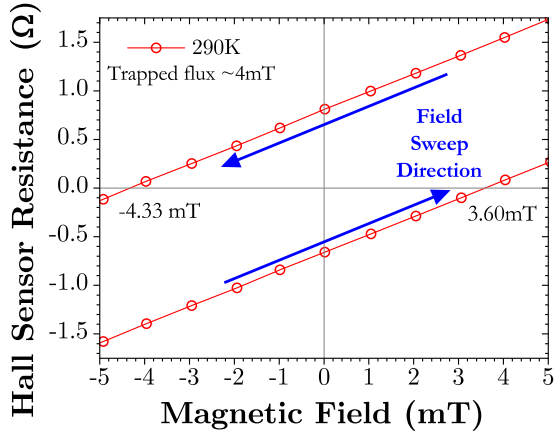


Figure 5.7: Hall resistance vs applied magnetic field in the cryostat transport measurement setup using a Hall sensor with linear magnetic field dependence. The magnetic field intercepts indicate the points when the magnetic field at the sample position is zero.

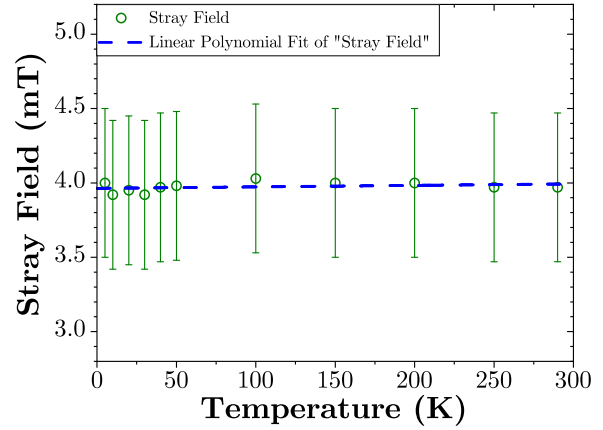


Figure 5.8: Trapped flux correction for the cryostat superconducting magnet vs temperature. The correction is independent of temperature and is a repeatable 4 mT. The error in stray field is taken to be half the step size of the magnetic field (i.e. the precision with which the magnetic field was varied) in Figure 5.7.

any temperature dependence. An example of the calibration data collected at 290K is presented in figure 5.7. The direction of field sweep is indicated by blue arrows. The trapped flux is defined as the average of the absolute values of magnetic field when the Hall resistance is zero (magnetic field axis intercepts). This is possible because the Hall resistance from field sweeps in opposite directions are parallel to each other: they have the same gradient. Taking the average of the absolute values of the field intercepts allows the trapped flux correction to be found, despite the small non-zero Hall sensor resistance when no magnetic field applied. Looking at figure (5.7) one can see that the direction of the field correction to be applied is opposite to that needed for the SQUID data. This is because the superconducting magnet in the cryostat has split coils that the sample sits between rather than being in the centre of a superconducting solenoid. Figure 5.8 shows the field correction was found to be 4 mT and independent of temperature.

5.2.3 Additive Effect of the Field Corrections

The trapped flux in each superconducting magnet has now been determined, and it is possible to apply a constant offset correction to the magnetic field, dependent on the direction of field sweep. As shown in figures 5.3 and 5.7 the field corrections to be applied to the magnetometry and transport measurements have opposite effects on the measured hysteresis loops. The cumulative effect on the zero-error in field is best illustrated in figure 5.9 where the Hall resistivity (red circles)

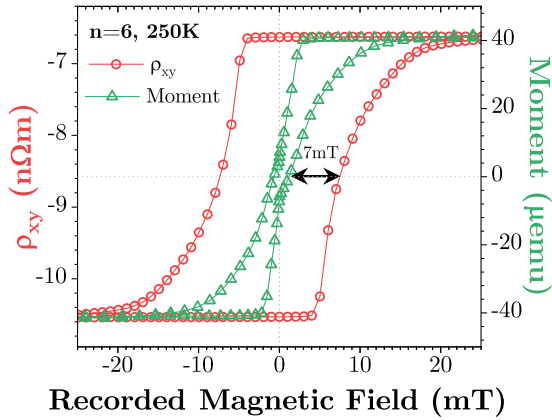


Figure 5.9: Magnetic moment and Hall resistivity vs recorded field, measured in $[\text{CoB}|\text{Ir}|\text{Pt}]_{n=6}$ at 250 K. The additive effect of trapped flux produces a discrepancy of 7 mT between the two hysteresis loops measured.

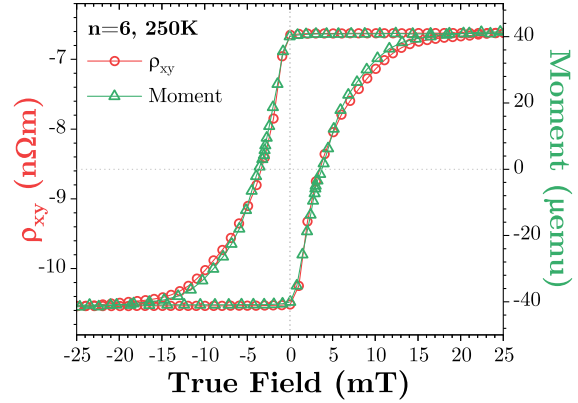


Figure 5.10: Magnetic moment and Hall resistivity vs true field, in $[\text{CoB}|\text{Ir}|\text{Pt}]_{n=6}$ at 250 K. The hysteresis loops lie nearly on top of each other after the calibrated corrections are applied.

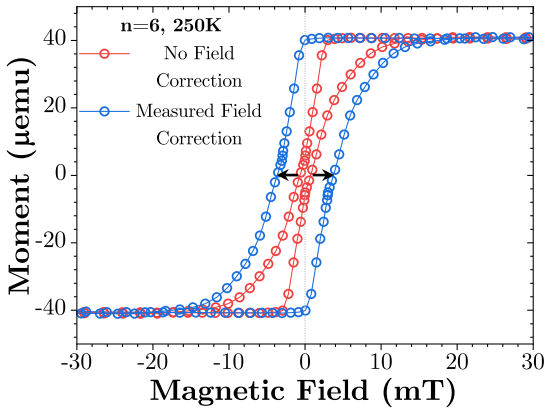


Figure 5.11: Magnetic moment vs field in $[\text{CoB}|\text{Ir}|\text{Pt}]_{n=6}$ at 250 K for recorded field (red) and true field (blue) showing the widening effect of the field correction for the SQUID-VSM measurements.

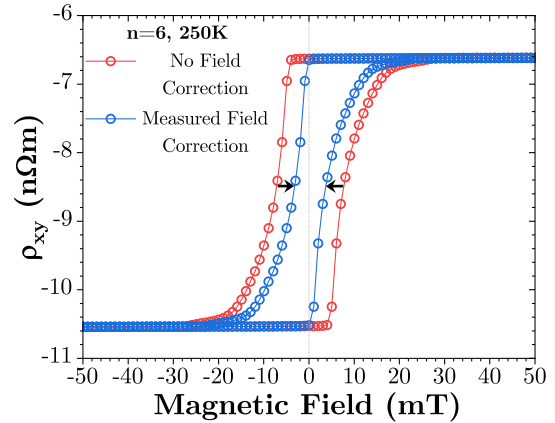


Figure 5.12: Hall resistivity vs field in $[\text{CoB}|\text{Ir}|\text{Pt}]_{n=6}$ at 250 K for recorded field (red) and true field (blue) showing the narrowing effect of the field correction for the cryostat transport measurements.

and the out of plane moment (green triangles) of the $[\text{CoB}|\text{Ir}|\text{Pt}]_{n=6}$ sample are plotted on the same field axis. The additive effect of the trapped flux in the different superconducting magnets causes a 7 mT difference between the two hysteresis loops. Applying the field correction to the moment vs field hysteresis loop has the effect of widening the loop in field, as shown in figure 5.11. Conversely, the resistivity data is narrowed by the field correction as shown in figure 5.12. Plotting the corrected data on the same field axis, as shown in figure 5.10, illustrates the effectiveness of the correction. Following the correction, the hysteresis loops are now very close to being aligned in field, they exhibit the same coercivity and general shape.

However, there are several more steps that must be taken before the hysteresis loops can be subtracted from each other to find any excess Hall resistivity. These are detailed in section 5.3.

5.3 Data Analysis

Before the loops are ready to be subtracted from each other there are a number of other steps that must be taken. This includes removing background effects such as the OHE in the transport data and para/diamagnetic signals from the sample substrate in the magnetometry data. The moment must also be normalised and converted into an estimate of the anomalous Hall resistivity. The analysis method used for each step is shown in this section with all figures showing data collected from measurement of $[\text{CoB}|\text{Ir}|\text{Pt}]_{n=6}$ at 270 K as an example presented in detail, but the same analysis is applied to all data presented in this thesis.

5.3.1 Transport Measurements

The raw transport measurements collected for each sample are in the form of Hall resistance hysteresis loops which need to be converted to resistivities. The Hall voltage is given by

$$V_{\text{H}} = V_y = \frac{I_x B_z}{net}, \quad (5.1)$$

where I_x is the current applied in-plane, V_y is the in-plane voltage perpendicular to the applied current, B_z is the magnetic field perpendicular to the sample, n is the carrier density, e is the charge on the electron, and t is the thickness of the multilayer. Resistivity is defined as

$$\rho_{\text{xy}} = \frac{R_{\text{xy}} A}{l}, \quad (5.2)$$

where R_{xy} is the measured Hall resistance, A is the area of the ‘wire’, and l is the length of the wire. Due to the geometry of the samples (crosses, figure 6.1), in the case of the samples used here

$$A = wt, \quad (5.3)$$

where w is the width of the arm of the Hall cross and t is the thickness of the multilayer. The Hall resistance measured applies only to the square area in the centre of the cross, where the contacts of

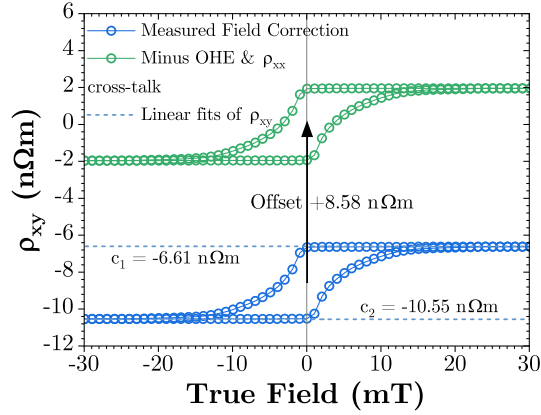


Figure 5.13: Removal of OHE and ρ_{xx} cross-talk from resistivity hysteresis loops. Dashed lines show linear fits to the data in the saturated regions.

the perpendicular current and voltage leads meet, and as such $l = w$, the width of the cross arm. This means that the Hall resistivity may be found simply by multiplying the Hall resistance by the sample thickness. The sample thicknesses were determined using sputtering rate calibrations which were measured using XRR, as discussed in section 3.2.1.

Removing Constant Offset & OHE gradient

Each sample was wirebonded to a sample head in order to be able to measure the transport properties while inserting the sample into a cryostat. Each wirebond was made manually using a wirebonder with Al wire. This means that the contacts to the sample are never perfectly aligned and there will always be some cross-talk between the longitudinal and transverse resistances measured. This means that the resistivity hysteresis loops will have an offset (due to imperfect cross geometry and misalignment of the wirebonds) that must be removed. Similarly the ordinary Hall effect contributes a small, but finite, transverse resistivity that is proportional to the applied magnetic field. In order to remove these two effects, the hysteresis loops were fitted using a standard linear fit of the form

$$\rho_{xy,fit} = m_i H_T + c_i, \quad (5.4)$$

where H_T is the True Field applied to the sample, c_i are the ρ_{xy} axis intercepts, and m_i is the gradient. The linear fit is performed in the saturated regions of the hysteresis loops (at high applied magnetic fields, ie $H_T \gg H_c$), and i is an iterator starting from 1 which counts the saturated regions in the hysteresis loop. The average of the gradients of the fits

$$\bar{m} = \sum_{i=1}^N \frac{m_i}{N} \quad (5.5)$$

is the ordinary Hall coefficient, where N is the total number of fits - here $N = 2$ because there are two linear ranges in the hysteresis loops where the sample is saturated either in the positive or negative direction - and the average of the ρ_{xy} axis intercepts

$$\bar{c} = \sum_{i=1}^N \frac{c_i}{N} \quad (5.6)$$

is the offset in resistivity. This allows linear correction of the data where each corrected data point is found using

$$\rho_{xy,corr} = \rho_{xy,raw} - \bar{m}H_T - \bar{c}. \quad (5.7)$$

This correction is shown in figure 5.13 where the uncorrected data is in blue, the linear fits are shown as dashed lines, and the corrected data is shown in green. The corrected resistivity when the sample is saturated should now be entirely due to the anomalous Hall effect since the OHE has been removed and at saturation the sample should be uniformly magnetised meaning the THE is expected to be zero. Therefore, the resistivity at saturation provides a scaling factor to convert the normalised moments into an estimate of the anomalous Hall resistivity. The same method of applying a linear fit to the saturated regions of the loop and finding the $\rho_{xy,corr}$ intercepts is used to determine the correct scaling factor for each sample and temperature.

5.3.2 SQUID Magnetometry

The out-of-plane moment dependence on applied magnetic field will be used to estimate the anomalous Hall resistivity. Before this is possible it is necessary to remove any background signal in the measurements. The data must then be normalised and then scaled by the anomalous Hall resistivity at saturation.

Removal of Para/Diamagnetic Backgrounds

Moment vs field hysteresis loops can contain linear paramagnetic and diamagnetic background signals. These signals can arise from the substrate of the sample (silicon) and the material with which the sample is mounted (e.g. inside a plastic straw). Fortunately diamagnetic and paramagnetic materials behave linearly with field, with paramagnetic contributions being proportional to the applied field and diamagnetic contributions being inversely proportional to the applied field. An example of a moment vs field measurement, in $[\text{CoB|Ir|Pt}]_{n=6}$ at 250 K, containing a diamagnetic background signal is shown in blue in figure 5.14. The gradient of the saturated region (fitted with a straight line) is used to subtract the background signal from the data producing the corrected hysteresis loop shown in green in figure 5.14. The intercept of the linear fit is used to normalise the moment vs field data in the next step.

Normalisation & Scaling of Data

Dividing all the moment vs field data by the moment at saturation (the y-intercepts of the linear fits in figure 5.14) allows for normalisation of the data. Following this step the normalised data is multiplied by the anomalous Hall resistivity at saturation, as found from the corrected Hall resistivity data shown in figure 5.13 (green). This produces an estimate of the anomalous Hall resistivity loop, shown in purple in figure 5.15.

5.3.3 Subtraction of Hysteresis Loops

Now that the data has been corrected it is nearly ready to be subtracted to try to find any excess resistivity that cannot be explained by the anomalous Hall resistivity. The difference between the hysteresis loops must be found by subtracting the anomalous Hall resistivity from the Hall resistivity (minus the OHE) at each field. This is complicated somewhat due to the fact that the data is collected at different magnetic field intervals which means that first it is necessary to interpolate both hysteresis loops.

Linear Interpolation & Subtraction of Corrected Data

The corrected data for both the Hall resistivity (minus OHE), ρ_{xy} , and the anomalous Hall resistivity, ρ_{xy}^A , are interpolated using linear interpolation between ± 500 mT, with a field step size of 1 mT. This step size was chosen as it is the same as the step in field used to collect the ρ_{xy} data in the cryostat, minimising the introduction of errors due to the interpolation process, shown in figure 5.16. The anomalous Hall resistivity and its linear interpolation are shown in figure 5.17. The interpolated data for both ρ_{xy} (black circles) and ρ_{xy}^A (red triangles) are shown in figure 5.18. The curves lie very close to each other however there is a noticeable difference between the two in the range of the magnetic field where the samples switch magnetisation. This difference is what we wish to investigate in more detail, and is found by subtracting ρ_{xy}^A from ρ_{xy} at each magnetic field. This produces an excess resistivity signal, $\rho_{xy,excess}$, which is shown in figure 5.19.

5.3.4 Critical Analysis of Subtraction Result

It is very easy to introduce a difference between the ρ_{xy} and ρ_{xy}^A due to the necessary field corrections and linear interpolation steps. This means that it is important to critically analyse the resulting excess resistivity found. The results of the analysis procedure described previously for all temperatures in $[\text{CoB|Ir|Pt}]_{n=6}$ are shown in figure 5.20. The excess resistivity at low temperatures has features that span more than 50 mT as well as some odd, sharp features that occur when the sample is starting to change magnetisation for the first time. We can be confident that the smooth features containing many data points are real, however the features in the curves that have only two or three data points could be artefacts of the analysis process. This section will investigate

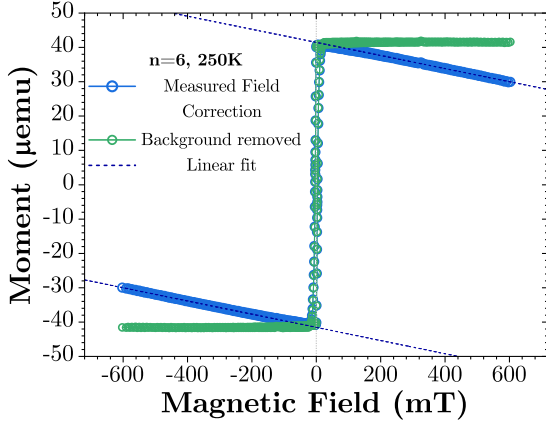


Figure 5.14: Moment vs field in $[\text{CoB|Ir|Pt}]_{n=6}$ at 250K for data with a diamagnetic background signal (blue) and after removal of the background signal (green). The diamagnetic background is identifiable because the regions of the hysteresis loop which are saturated exhibit a negative gradient, shown by the dashed lines.

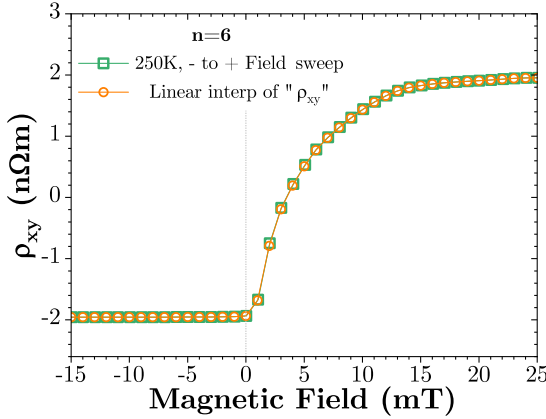


Figure 5.16: The negative to positive field sweep of ρ_{xy} (green squares), and the linear interpolation of ρ_{xy} (orange circles) for $[\text{CoB|Ir|Pt}]_{n=6}$ at 250 K.

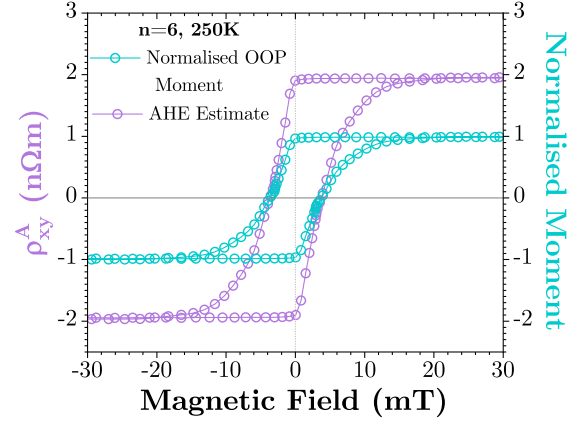


Figure 5.15: Normalised moment vs field (turquoise) in $[\text{CoB|Ir|Pt}]_{n=6}$ at 250 K, and the scaled data (purple) as an estimate of the anomalous Hall resistivity, ρ_{xy}^A .

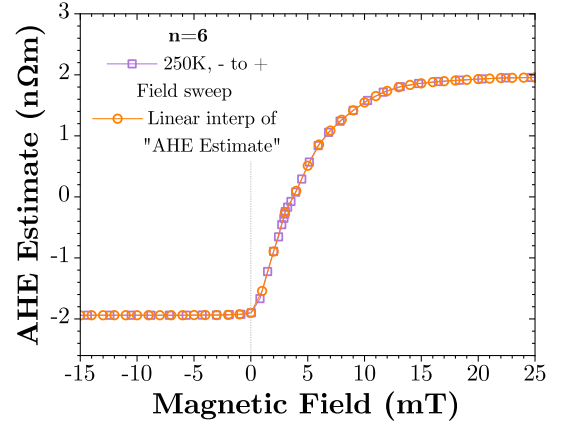


Figure 5.17: The negative to positive field sweep of ρ_{xy}^A (purple squares), and the linear interpolation of ρ_{xy}^A (orange circles) for $[\text{CoB|Ir|Pt}]_{n=6}$ at 250 K.

the origin of potential artefacts in the data and justify an extra field correction step to align the interpolated data as well as possible.

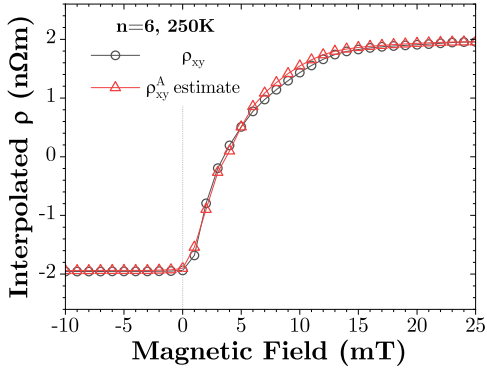


Figure 5.18: The interpolated data for ρ_{xy} (black circles) and ρ_{xy}^A (red triangles). This is the negative to positive field sweep in $[\text{CoB}|\text{Ir}|\text{Pt}]_{n=6}$ at 250 K.

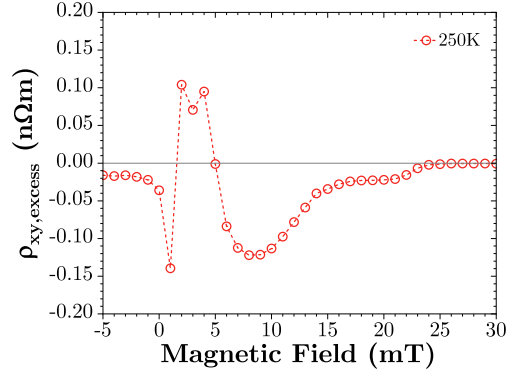


Figure 5.19: The excess Hall resistivity, $\rho_{xy,\text{excess}}$, in $[\text{CoB}|\text{Ir}|\text{Pt}]_{n=6}$ at 250 K.

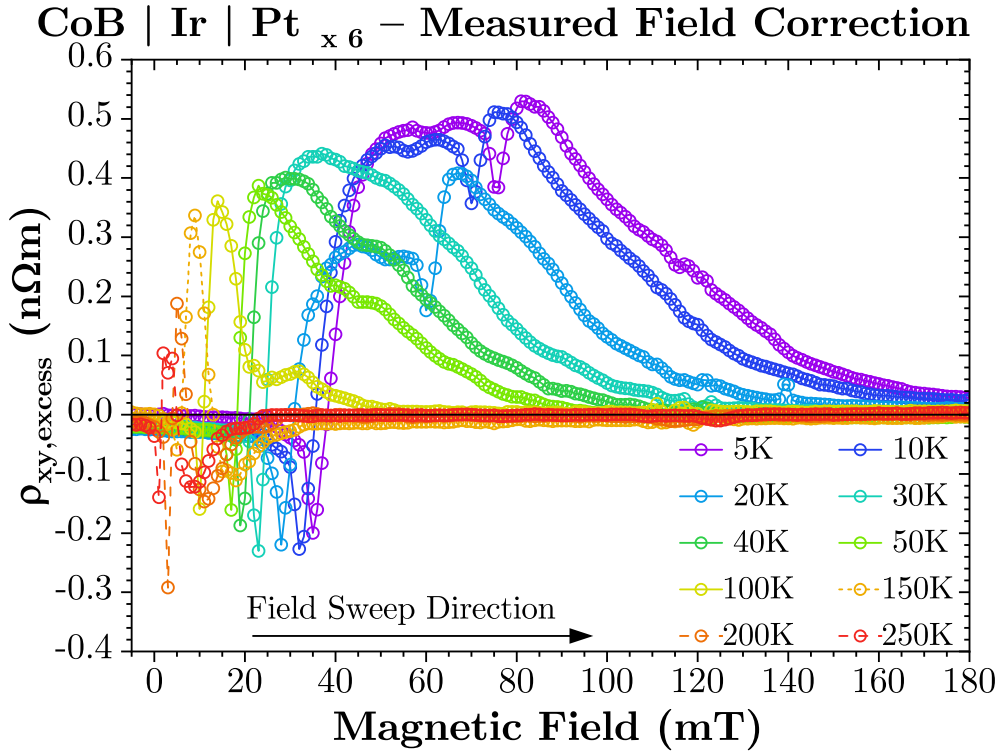


Figure 5.20: The excess Hall resistivity in $[\text{CoB}|\text{Ir}|\text{Pt}]_{n=6}$ when the magnetic field is swept from negative to positive. There are clear features that exist over a large field range as well as sharp features consisting of only a few data points.

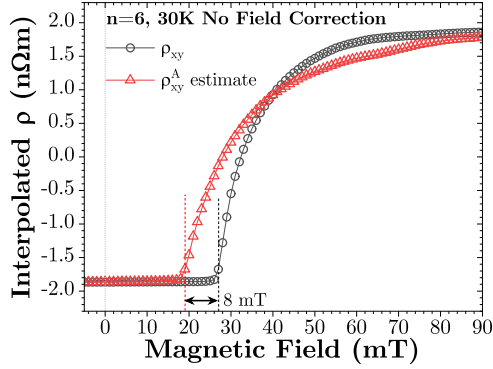


Figure 5.21: Interpolated resistivities for $[\text{CoB}|\text{Ir}|\text{Pt}]_{n=6}$ at 30 K with no field corrections applied. The dashed lines indicate the first point exhibiting a significant change from the saturated resistivity in each dataset.

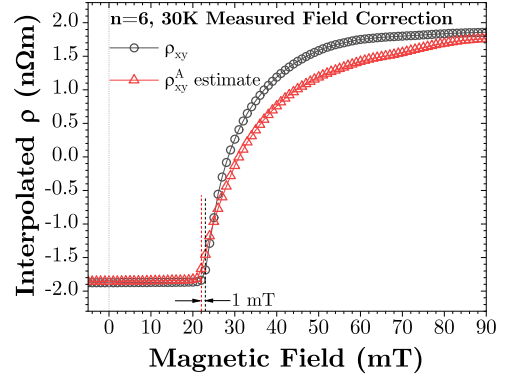


Figure 5.22: Interpolated resistivities for $[\text{CoB}|\text{Ir}|\text{Pt}]_{n=6}$ at 30 K with field corrections of +3 mT applied to the ρ_{xy}^A data and -4 mT applied to the ρ_{xy} data. The dashed lines indicate the first point exhibiting a significant change from the saturated resistivity in each dataset.

Comparison of Interpolated Data

To understand the origin of the sharp features in the excess resistivity the interpolated data at 30 K, 100 K, and 250 K will be looked at in more detail with and without the measured field corrections that were found in section 5.2.3. By considering the differences before application of the measured field correction and afterwards it should be possible to determine if the sharp features are enhanced or reduced by the measured field correction. The $[\text{CoB}|\text{Ir}|\text{Pt}]_{n=6}$ data at 30 K, after the linear interpolation step, is shown without the field correction in figure 5.21 and with the corrections in figure 5.22. In each figure the first data point that changes significantly from the saturated resistivity is marked with a dashed line, coloured black or red for the ρ_{xy} and ρ_{xy}^A interpolated data respectively. It is clear to see that the measured field corrections for the two superconducting magnets are necessary and also quite accurate as the difference between the first non-saturated resistivity is reduced to only 1 mT after application of the field corrections (figure 5.22) compared to 8 mT when the corrections are omitted (figure 5.21). In order to confirm that the small misalignment in field may be the cause of the sharp artefacts the excess resistivity signal for $n = 6$ at 30 K, 100 K, and 250 K was found prior to and following field correction. Figures 5.23 (a), (b), and (c) show the excess resistivity at 30 K, 100 K, and 250 K respectively; the corrected results are shown as squares whereas the results prior to correction are shown by circles. In each subfigure one can see that the measured field correction has reduced the large negative features. This suggests that they may be attributed to uncorrected misalignment of the two loops in field. By taking another look at figure 5.22 it is possible to make an attempt to remove any

small remaining artefacts. This is done by shifting one of the loops by 1 mT such that the data points indicated by dashed lines are lined up. The excess resistivity following this shift in field is shown for $[\text{CoB|Ir|Pt}]_{n=6}$ at 30 K, 100 K, and 250 K in figure 5.23 (d). This custom correction is henceforth referred to as an ‘extra’ field correction and is determined manually for each temperature and sample combination by comparing the interpolated data. It is my belief that the need for small extra corrections is due to a combination of an error introduced by the linear interpolation step, unknown errors in the measured field corrections, and the limitations in measuring ρ_{xy} accurately at higher temperatures when using a 1 mT step size. The third contribution is most likely the largest because the coercive field of all the samples studied is very small at higher temperatures. This means that for a small change in field the change in ρ_{xy} is very large and the sample switches between saturated states over a very small field range, i.e. the field resolution is not good enough. The effect of small shifts in field on the magnitude of the excess resistivity can be readily observed in figure 5.23, and the same effect is seen for samples with different numbers of repeats as seen in figure 5.24. Wherever an extra field correction has been applied it will be shown in the legend of the results figures presented. In some cases the extra adjustment required is larger at lower temperatures. This may be attributed to the fact that at lower temperatures the field resolution during switching is comparatively better than at higher temperatures.

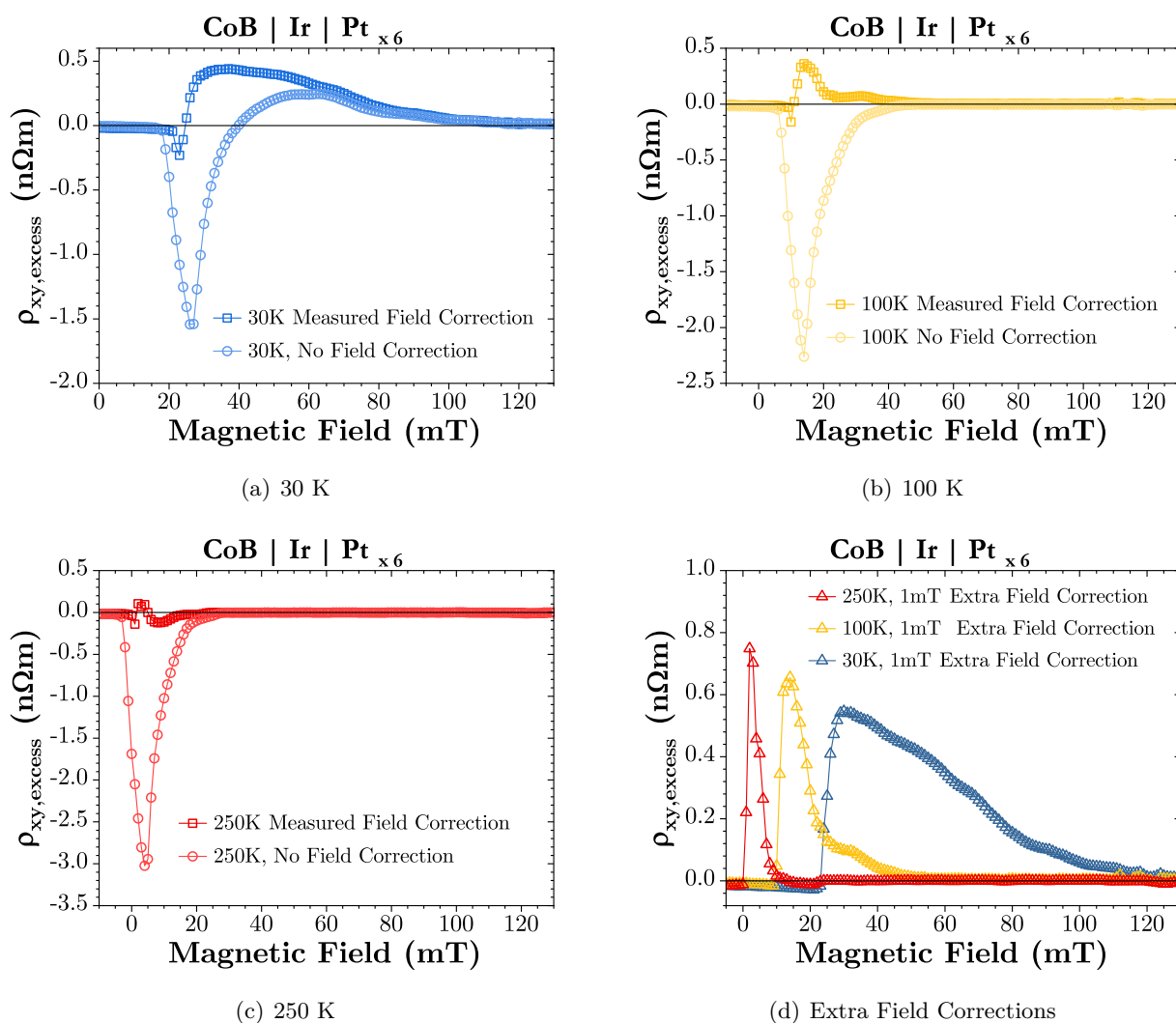


Figure 5.23: Excess ρ_{xy} prior to (circles) and following (squares) field corrections are applied for $[CoB|Ir|Pt]_{n=6}$ at (a) 30 K, (b) 100 K, and (c) 250 K. The measured field correction clearly reduces the large negative features in excess ρ_{xy} .

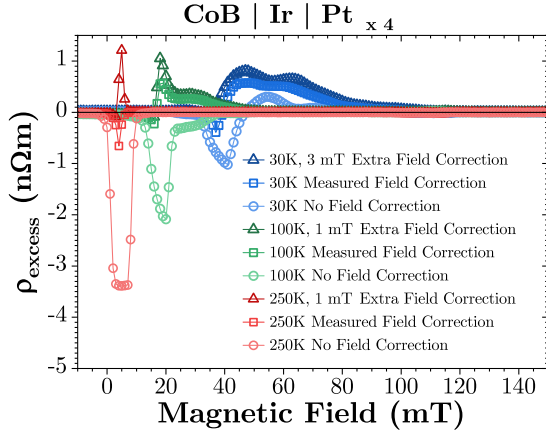


Figure 5.24: Excess ρ_{xy} prior to (circles) and following the measured (squares) and extra (triangles) field corrections are applied for $[\text{CoB}|\text{Ir}|\text{Pt}]_{n=4}$ at 30 K (blue), 100 K (green), and 250 K (red).

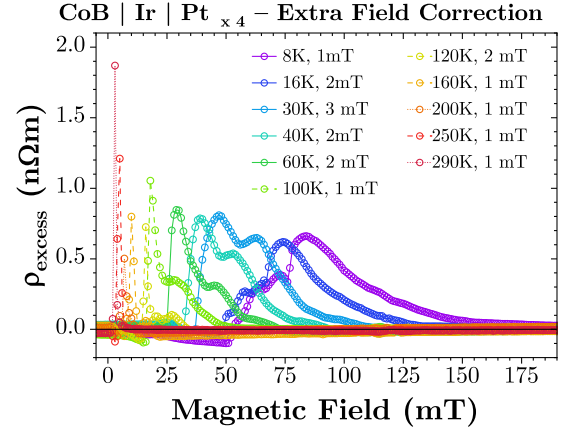


Figure 5.25: Excess ρ_{xy} in $[\text{CoB}|\text{Ir}|\text{Pt}]_{n=4}$ for a range of temperatures from 8 K-290 K. The highest temperatures show features arising from the only a few data points.

5.4 Features or artefacts?

Following the analysis steps outlined above it is desirable to investigate trends in the excess ρ_{xy} with temperature and number of magnetic multilayer repeats. In order to do this it is important to be able to distinguish between artefacts that occur when the field resolution is too poor, or perhaps due to residual misalignment in field. Figure 5.25 provides good examples of $\rho_{xy,excess}$ where it is difficult to distinguish between parts of the curves that are real features and sections that may be artefacts, for example at temperatures between 290 K and 100 K. These temperatures all have large spiky sections that occur at the onset of magnetisation switching. Some of these (100 K and 120 K) also have smaller features that occur at a higher field and over a larger range in field. In order to be able to decide which temperatures in each sample produce results that may be considered real it is desirable to define a method for measuring the width of the different features in the curves.

5.4.1 FWHM as a Measure of Feature Size

The full-width half-maximum (FWHM) of a peak is a well defined property that is most simply defined as the width of a curve at the y-value equal to half of the maximum of the peak. The $\rho_{xy,excess}$ curves contain multiple peaks that are not expected to follow any particular shape. Given this each curve was fitted individually, for multiple peaks where necessary, with various peak functions including gaussian, exponentially modulated gaussian, and bigaussian functions. There is no physical justification for the use of any of these functions over others, and each were chosen to produce the best fit to the individual $\rho_{xy,excess}$ curves. These functions are used purely as a

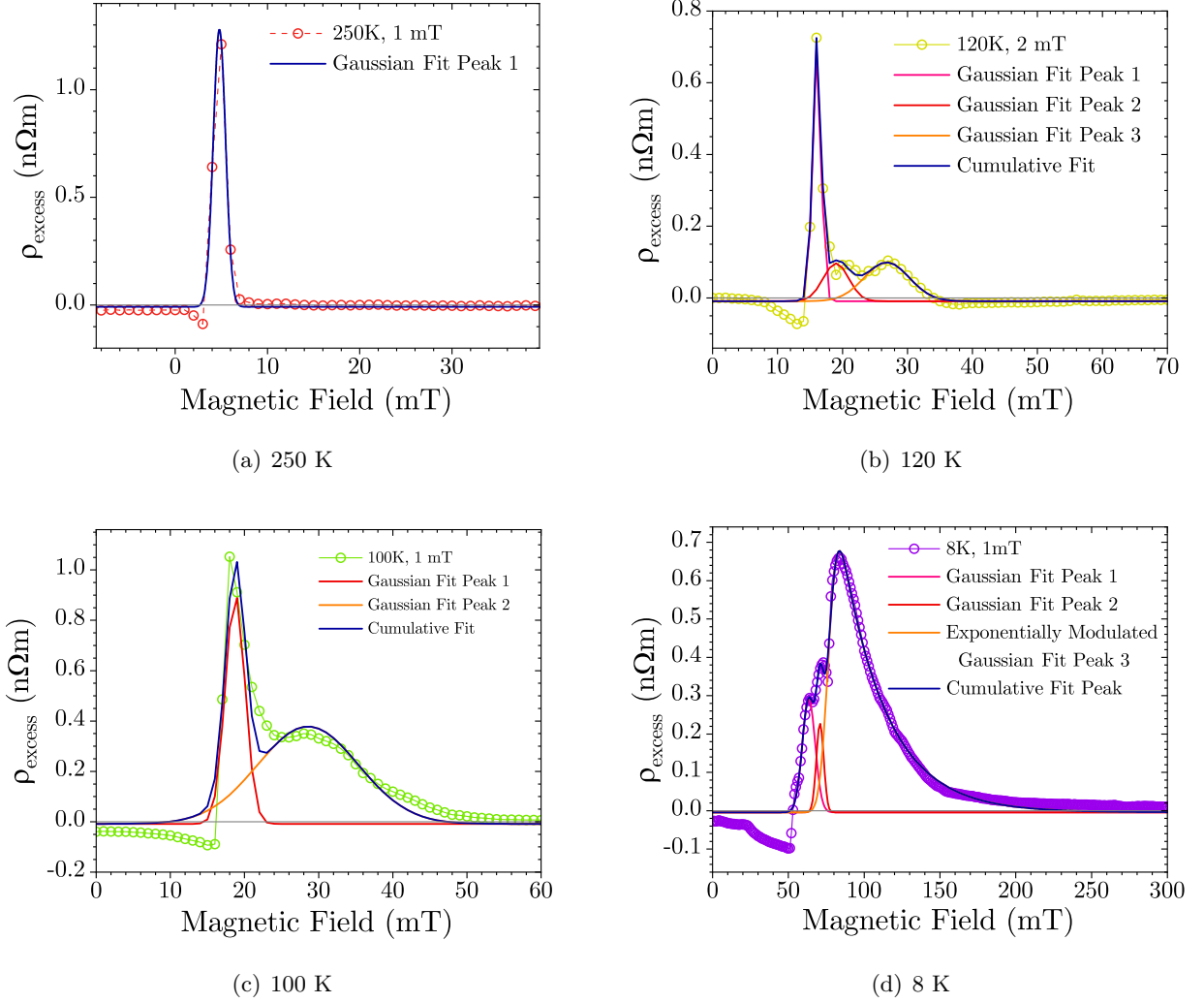


Figure 5.26: Examples of $\rho_{xy,excess}$ curves (in $[\text{CoB|Ir|Pt}]_{n=4}$) that have been fitted to estimate the width of the peaks within each curve. The cumulative fits for each curve are also shown.

mathematical method of measurement of the FWHM of the peaks in the data. Several examples of fitted $\rho_{xy,excess}$ curves in $[\text{CoB|Ir|Pt}]_{n=4}$ are presented in figure 5.26. The individual curves fitted to features within the overall $\rho_{xy,excess}$ curves are shown, as well as the cumulative fits. For the most part the features can be fit well with a Gaussian function but in some circumstances such as at 8K (figure 5.26 (d)) an exponentially modulated Gaussian function produces a better cumulative fit. All the fitting performed during this stage was carried out using Origin(Pro) software [118].

5.4.2 Defining the Size of a ‘Real’ Feature

Following successful fitting of each curve the FWHM of the individual features can be used to compare the significance of the signal with the field resolution used to collect the data and the size of the extra field corrections that were needed to align the hysteresis loops. The FWHM of each peak in $\rho_{xy,excess}$ was then plotted vs temperature for each sample, shown in figure 5.27 (b) for $[\text{CoB}|\text{Ir}|\text{Pt}]_{n=4}$. The light red region of the plot indicates FWHM that are lower than the field step used to collect the data (1 mT). The light orange region of the graph indicates FWHM that are larger than the field step used but smaller than the largest extra field correction applied to data from the same sample (i.e. same number of repeats). Features with data points that fall into these highlighted regions may be considered more suspect as their size and shape would change drastically based on any errors in experimental measurement or the following analysis. By contrast the features that correspond to data points that are not within these regions are considered more robust signals that are likely to be reliable and real. Figure 5.27 presents the FWHM as a function of temperature for all the samples measured during this project. In each sample it is clear to see that the FWHM of the features decreases as the temperature is increased. This is unsurprising as the FWHM of the overall $\rho_{xy,excess}$ curve is dependent on the coercive field of the sample and the saturation field of the sample, i.e. a $\rho_{xy,excess}$ signal is only expected while the multilayers are in a multidomain state switching from one single domain saturated state to the other. As the number of multilayer repeats increases so does the coercive field explaining the increase in FWHM with increased n. The extra field correction required - discussed previously in section 5.3.4 - decreases as the coercivity, saturation field, and number of repeats in the samples increases. The extra field correction is illustrated by the orange shaded areas narrowing in Figures 5.27(a) to 5.27(d) with increasing multilayer repeats (n). The results shown in figure 5.27 are used in the following chapter to identify less reliable data points when the temperature and multilayer dependence of the maximum $\rho_{xy,excess}$ are investigated.

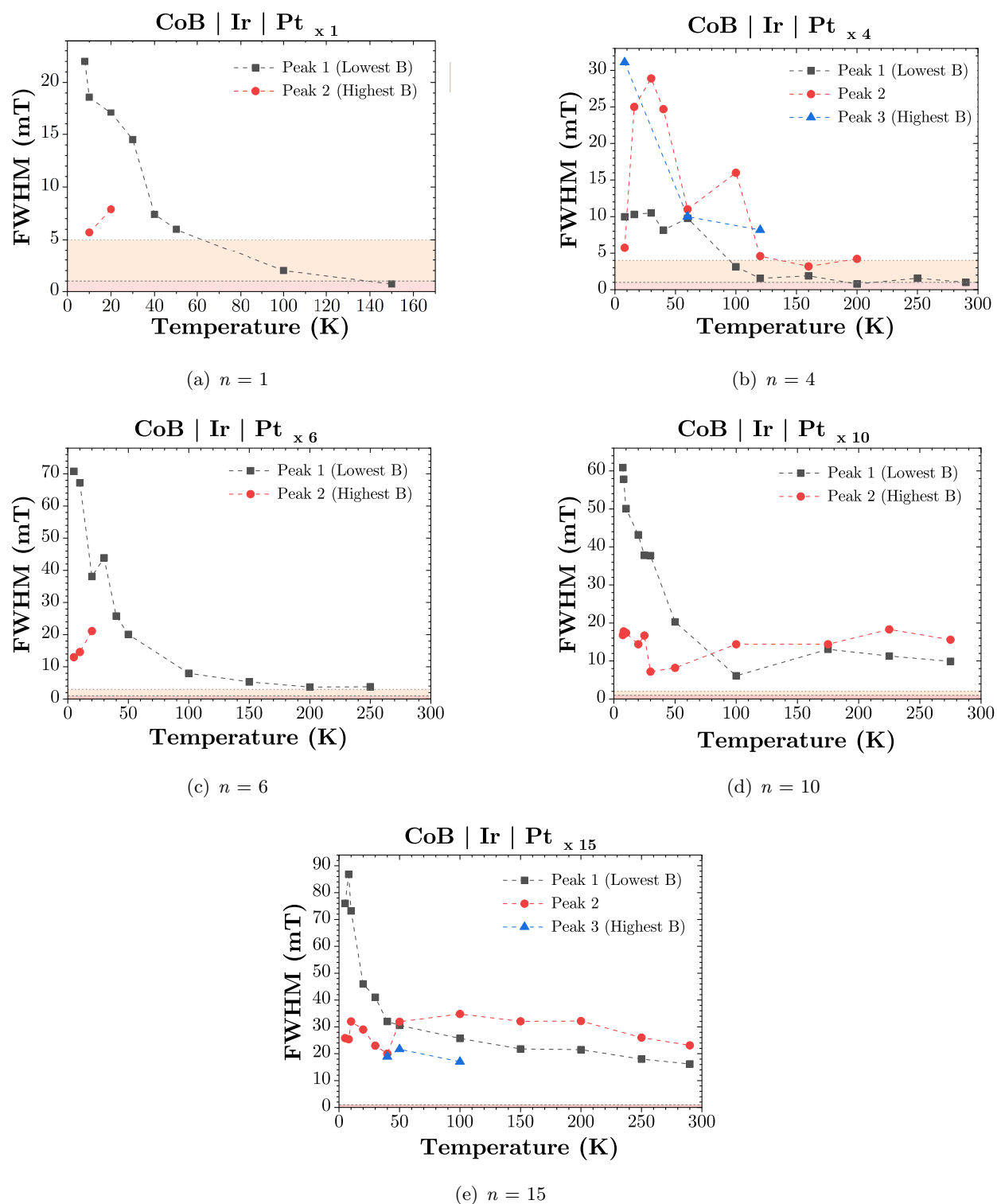


Figure 5.27: Full-width half-maximum of the peaks found within a $\rho_{xy,excess}$ curve vs temperature for each sample, where n represents the number of repeats of [CoB|Ir|Pt]. The coloured areas on each plot represent the field resolution used to collect the data (1 mT), shown in red, and the maximum extra field correction used to align the hysteresis loops for each sample, shown in orange.

5.5 Error Estimation and Propagation

The anomalous Hall resistivity is found by using the following expression,

$$\rho_A = \frac{\rho_{A,\text{sat,avg}}}{m_{\text{sat,avg}}} m, \quad (5.8)$$

where ρ_A is the anomalous Hall resistivity at an applied OOP magnetic field B , $\rho_{xy,\text{sat,avg}}$ is the average Hall resistivity after the ordinary Hall resistivity, and any systematic offset, is removed, $m_{\text{sat,avg}}$ is the average moment measured when the sample is saturated, after any background signal has been removed, and m is the OOP moment in the sample in the same applied magnetic field B . To find the error in the anomalous Hall resistivity the percentage errors must be added in quadrature (because the variables in the previous equation are multiplied and/or divided together) to obtain an estimated fractional uncertainty in the anomalous Hall resistivity according to

$$\frac{\Delta\rho_A}{\rho_A} = \times \sqrt{\left(\frac{\Delta\rho_{A,\text{sat,avg}}}{\rho_{A,\text{sat,avg}}}\right)^2 + \left(\frac{\Delta m_{\text{sat,avg}}}{m_{\text{sat,avg}}}\right)^2 + \left(\frac{\Delta m}{m}\right)^2}, \quad (5.9)$$

where $\rho_{A,\text{sat,avg}}$, $m_{\text{sat,avg}}$, and m are the same variables as in the previous equation and Δ denotes the absolute error in a parameter. To obtain an estimated fractional uncertainty the largest fractional uncertainties for each parameter were used from the sample with $n = 6$ repeats. This yielded an estimated fractional uncertainty for ρ_A of 0.002, or 0.2% of ρ_A , with this value being dominated by the fractional errors in moment which are ten times larger than the largest fractional error in the transport measurements. The largest value of ρ_A occurs when the sample is saturated so the maximum possible error can be estimated to be 0.2% of the anomalous Hall resistivity at sample saturation. To simplify analysis and plotting, the absolute error in anomalous Hall resistivity at all fields is taken to be the same and equal to the maximum possible absolute error which is calculated using the anomalous Hall resistivity at sample saturation for each sample.

The excess resistivity is found by subtracting the anomalous Hall resistivity from the corrected Hall resistivity (after removal of the ordinary Hall resistivity). This means that to find the error in the excess resistivity the absolute errors in the anomalous Hall resistivity and corrected Hall resistivity should be added in quadrature according to

$$\Delta\rho_{\text{excess}} = \sqrt{\Delta\rho_A^2 + \Delta\rho_{xy,\text{corr-OHE}}^2}, \quad (5.10)$$

where $\Delta\rho_{\text{excess}}$ is the absolute error in the excess Hall resistivity, $\Delta\rho_A$ is the absolute error in the anomalous Hall resistivity, and $\Delta\rho_{xy,\text{corr-OHE}}$ is the absolute error in the corrected Hall resistivity after removal of the ordinal Hall effect. The absolute error in the corrected Hall resistivity is taken to be the noise in the transport signal at saturation and is the same for all the measurements, $\Delta\rho_{xy} \approx 1 \times 10^{-3}$ n Ω m. Again, for ease, the absolute uncertainty for the excess Hall resistivity will be estimated using the maximum possible result from equation 5.10 by using the largest absolute

uncertainty in the anomalous Hall resistivity. This occurs in the sample with $n = 28$ repeats which has a maximum anomalous Hall resistivity of $5.24 \text{ n}\Omega\text{m}$ at 10 K . This results in a maximum absolute error in anomalous Hall resistivity of $0.01 \text{ n}\Omega\text{m}$ which renders the error contribution from the noise in the transport measurements negligible. As such, the maximum error in the excess Hall resistivity can be estimated to be the same as the maximum error in the anomalous Hall resistivity, that is $\pm 0.01 \text{ n}\Omega\text{m}$ to one significant figure. This error overestimates the error in the samples with $n < 28$ for all applied magnetic fields, and even for the $n = 28$ sample for magnetic fields where the sample is not fully saturated. Figure 5.28 shows the excess Hall resistivity signal at 200K for the $n = 6$ (orange circles) and $n = 28$ (green circles) samples, including y-error bars of $\pm 0.01 \text{ n}\Omega\text{m}$. In this figure, only every third data point is plotted in order to increase visibility of the error bars which are the same size as the data points. Given that the maximum possible absolute uncertainty in excess resistivity is not able to be seen easily due to the size of the data points, the y-error is not included in the rest of the results figures in chapter 6, and elsewhere in this thesis. The y-errors for the AHE results in chapter 7 are also too small to be seen in the figures.

5.6 Conclusion

This chapter has served to explain the analysis steps performed on the raw transport and moment measurements made that yield the results presented in the following chapters. The importance of field calibration when using multiple superconducting magnets has been observed and the steps taken to mitigate trapped flux zero errors were detailed. It has been shown that finding a $\rho_{xy,\text{excess}}$ signal can be easy if any misalignment in field remains between the transport and moment hysteresis loops, and that ensuring the $\rho_{xy,\text{excess}}$ signal is real is a difficult task. By performing field calibration measurements in the magnets used, investigating the effect of the resulting field correction, and defining a threshold FWHM for features in $\rho_{xy,\text{excess}}$, I have ensured, to the best of my ability, that the results presented in the rest of this thesis are real.

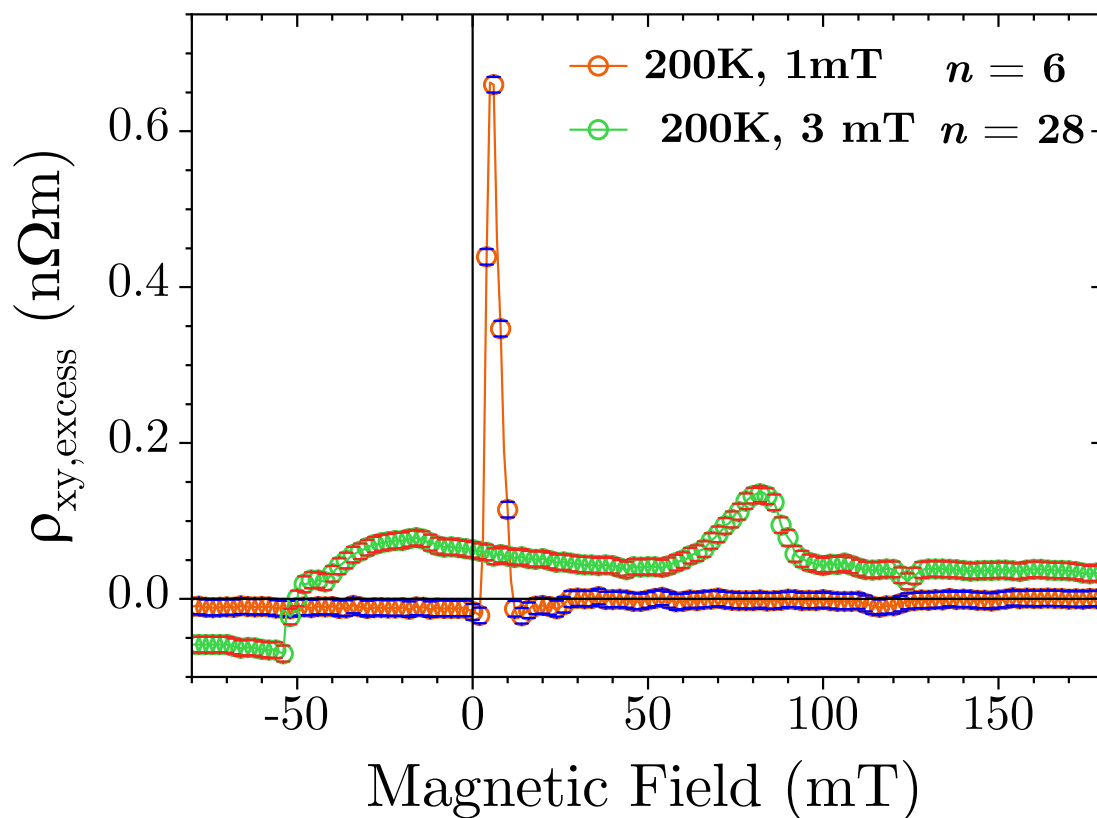


Figure 5.28: The excess Hall resistivity in samples with $n = 6$ and $n = 28$ repeats, at 200K, including an extra field correction and with y error bars = ± 0.01 $n\Omega m$, where this is the maximum absolute error in excess resistivity, due to known and quantifiable uncertainties, for all samples and temperatures as explained in section 5.5.

CHAPTER 6

Topological Hall Effect in CoB|Ir|Pt
Multilayers

6.1 Introduction

In chapter 3 section 2.6.2 the potential use of magnetic skyrmions to store data in more energy efficient ways was discussed. In particular, in order to read data stored by skyrmions using electrical measurement rather than magnetic tunnel junctions it is essential that the relationship between the number of skyrmions present and their individual contribution to the Hall effect is understood. So far, attempts to measure the magnitude of the topological Hall effect due to magnetic skyrmions has yielded results that are inconsistent with each other [8; 10; 58; 70; 119] and with those predicted by Berry phase theory [9; 120]. Therefore, in this chapter, the results of experimental work investigating the behaviour of the excess Hall resistivity in CoB|Ir|Pt \times n multilayers, that exists after accounting for the ordinary and anomalous Hall, as a function of temperature and multilayer repeat number, n , are presented.

An overview of the growth conditions of the samples is given in section 6.2.1. This is followed by the characterisation parameters including the multilayer structure and magnetic properties in section 6.2.2. The overall Hall resistivity measurements are presented in section 6.2.3, followed by the temperature dependence of the excess Hall resistivity in section 6.3, and repeat dependence in section 6.4. The $\rho_{xy,excess}$ signal measured in CoB|Ir|Pt \times n multilayers is shown to change in shape depending on the temperature of measurement and with the number of repeats in multilayer, where lowering temperature appears to increase the number of peak or trough like features present in the signal and lowering the number of multilayer repeats appears to increase the variation in the number of features present at different temperatures.

6.2 Sample Growth and Characterisation

The samples measured to obtain the results in this chapter are magnetic multilayers with a nominal structure Ta(2.43 nm)|Pt(2.23 nm)|[CoB(0.74 nm)|Ir(0.40 nm)|Pt(1.12 nm)] \times n |Pt(2.48 nm), where n is the number of repeats of the multilayer. The Hall transport properties of samples with $n = 1, 4, 6, 10$, and 15 were measured at room temperature in order to determine the effect of the number of repeat layers on R_{xy} . Samples that have been shown to host Néel skyrmions in similar multilayers in the past [5; 8; 65; 117; 121] tend to have a number of repeats in the range of around $3 \leq n \leq 8$. For the measurements as a function of temperature, the samples were chosen to span the number of repeat layers where skyrmions would be expected. The magnetic multilayer was deposited as a thin film, through a metal mask, using DC magnetron sputtering as described in section 3.1.1. This method created samples with cross-shaped geometry to make measurement of Hall transport properties easier. The area that is measured in these samples is a 2×2 mm square in the centre of the cross, i.e. bulk multilayer film. An image of a typical sample from this batch is shown in Figure 6.1.



Figure 6.1: A typical sample with cross-shaped geometry, wirebonded for measurement of the longitudinal and transverse resistance of the sample.

6.2.1 Growth Conditions

During the growth process the vacuum chamber was kept at a base pressure on the order of $10^{-7} - 10^{-8}$ mBar, and an argon flow of 35 sccm ≈ 3.2 -3.7 mTorr was used during sputtering. Tantalum, platinum, cobalt-68 boron-32, and iridium were each sputtered using a recipe to produce the following magnetic multilayers:

$$\text{Ta}(19 \text{ s})|\text{Pt}(18 \text{ s})|[\text{CoB}(15 \text{ s})|\text{Ir}(5 \text{ s})|\text{Pt}(9 \text{ s})]_{\times n}|\text{Pt}(20 \text{ s}), \quad (6.1)$$

where the magnetron guns, supply current, and power used during growth are given in Table 6.1. The growth rate for each material shown in table 6.1 was found from bulk films grown during the same growth. XRR measurements were used to determine the thickness of the film, using the dependence of Kiessig peaks on reflection angle (eq. 3.1). The thickness found was then divided by the growth time in seconds for each material (typically chosen to be around 300s).

Material	Source Current (mA)	Power (W)	Growth Rate ($\text{\AA}/\text{s}$)
Tantalum	50	15	1.4
Platinum	25	9	1.4
Cobalt-68 Boron-32	50	18	0.8
Iridium	25	9	0.9

Table 6.1: Growth conditions used to grow the multilayered samples used in this thesis. DC magnetron sputtering was used with the source current and power for each material shown in this table. The subsequent growth rate is found from XRR of the thickness of the calibration samples as explained in section 3.2.1.

6.2.2 Characterisation Parameters

The structure of the whole multilayer and thickness of individual layers within the multilayer were determined by measuring the sister samples using X-ray Reflectometry (XRR), as discussed in section 3.2.1, and then fitting the resultant curves using GenX. The multilayers grown for the devices in this chapter were found to have a nominal structure of

$$\text{Ta}(2.47 \text{ nm})|\text{Pt}(2.16 \text{ nm})|[\text{CoB}(0.77 \text{ nm})|\text{Ir}(0.40 \text{ nm})|\text{Pt}(1.08 \text{ nm})]_{\times n}|\text{Pt}(2.4 \text{ nm}). \quad (6.2)$$

The laser magneto-optical Kerr effect (LASER-MOKE) and Superconducting Quantum Interference Device-Vibrating Sample Magnetometry (SQUID-VSM) were also used to characterise the samples as described in sections 3.2.3 and 3.2.4 in chapter 3. The coercive field of the films at room temperature was measured using LASER-MOKE and was found to be $H_{C,RT \approx 290K} = 2.0 \pm 0.6$ mT. The coercive field, found from Hall resistance loops when $T \leq$ room temperature, of all the samples increases as the temperature is decreased and ranges from 20 mT in high repeat samples ($n = 28$) to nearly 100 mT in low repeat samples ($n = 1$). An average saturation magnetisation at $T = 0$ K of $M_{S,0} = 1460 \pm 70$ kA/m was found from SQUID-VSM measurements. This value was calculated using only the volume of Co in each sample and does not take into account any proximity magnetisation that occurs within the Pt layers that are adjacent to the CoB layers. The value found is consistent with the expected saturation magnetisation for Co of $1.7 \mu_B$ per atom ≈ 1400 kA/m [122], however it is also likely that the M_S was found to be above the magnetisation of pure Co due to Pt proximity magnetisation effects that have not been accounted for and that make the volume contributing to the total moment larger than used in the calculation of magnetisation here.

6.2.3 Excess Hall Resistivity

The experimental set-up used to perform the temperature dependent Hall transport measurements that are presented in this chapter consists of a cryostat capable of producing temperatures between 5 K and 300 K and electrical wiring between the sample and the external transport equipment (nanovoltmeter and current source). This is provided through a stick to which the sample is wirebonded. The stick also contains a Cernox chip for measuring the temperature inside the cryostat. Full details of the experimental set-up and measurement protocols can be found in section 3.3.1.

The data collection method, described in detail in section 3.3.1, was used to measure the Hall resistance for both the repeat layer, n , and temperature, T , dependence investigations. To collect the repeat layer dependence it was necessary to measure samples with the same geometry but grown with different numbers of repeat layers, the sample growth was discussed in section 3.1.1. Temperature dependent data was collected for each sample and some common temperature values were chosen to be measured for all samples to allow comparison of the effect of repeat

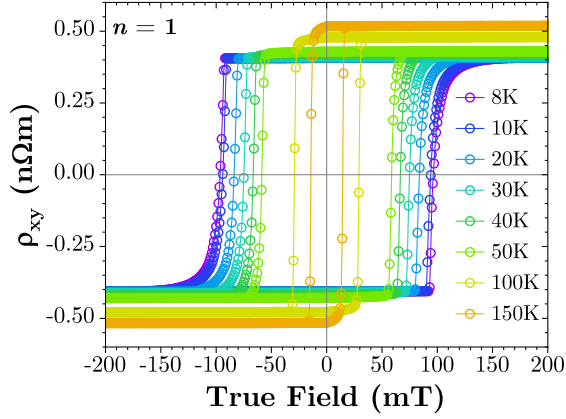
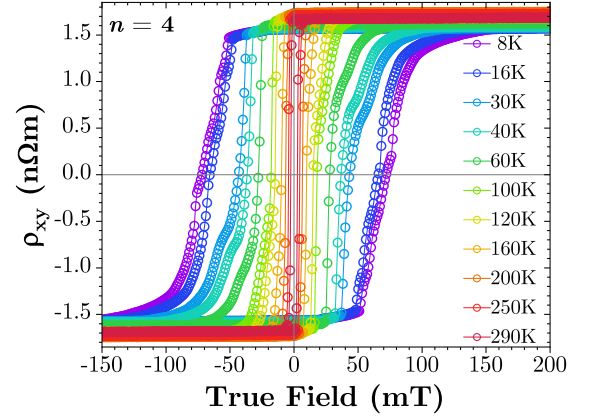
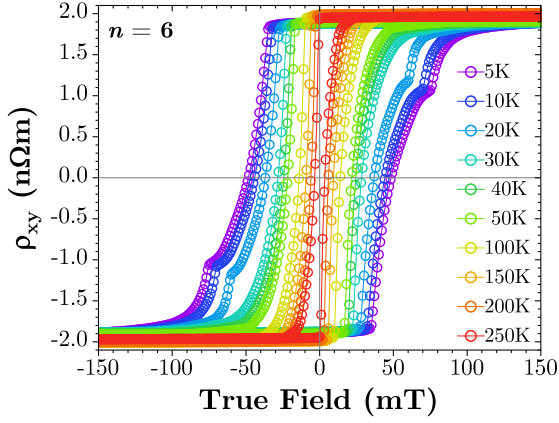
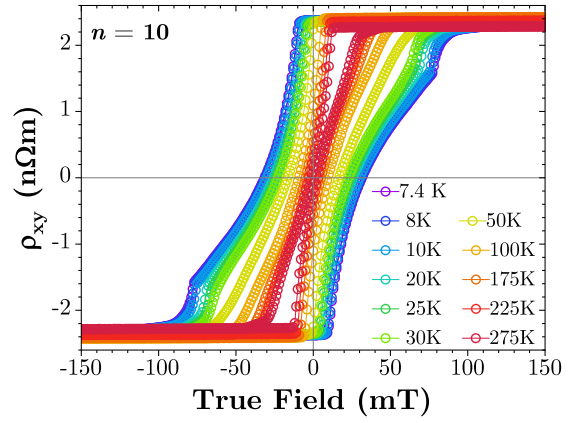
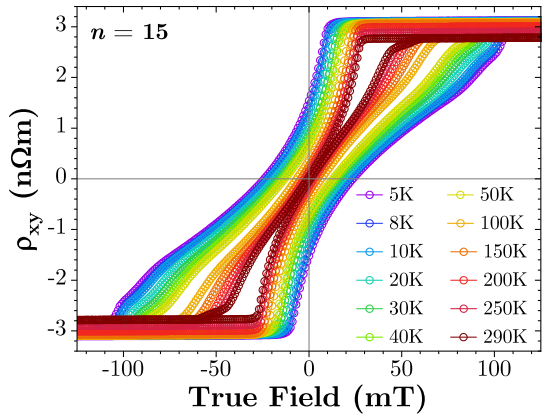
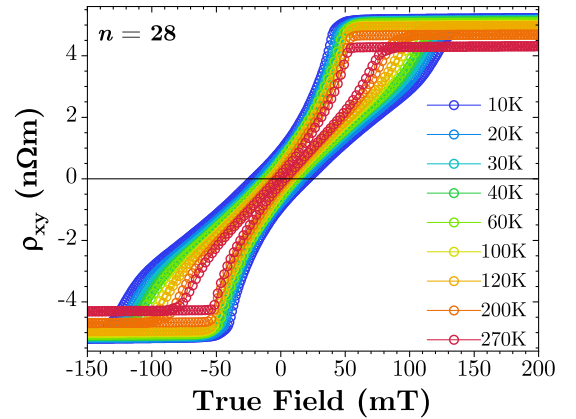
(a) $n = 1$ (b) $n = 4$ (c) $n = 6$ (d) $n = 10$ (e) $n = 15$ (f) $n = 28$

Figure 6.2: Hysteresis loops in the Hall resistivity signal, ρ_{xy} , for multilayer repeats $n = 1, 4, 6, 10, 15,$ and 28 shown in subfigures (a)-(f) respectively. The temperature of each measurement is indicated by the colour of the data, where purple is the coldest at ~ 5 K and red is the warmest at ~ 290 K. Bumps in the loops are evident at temperatures below ~ 50 K in (b)-(d).

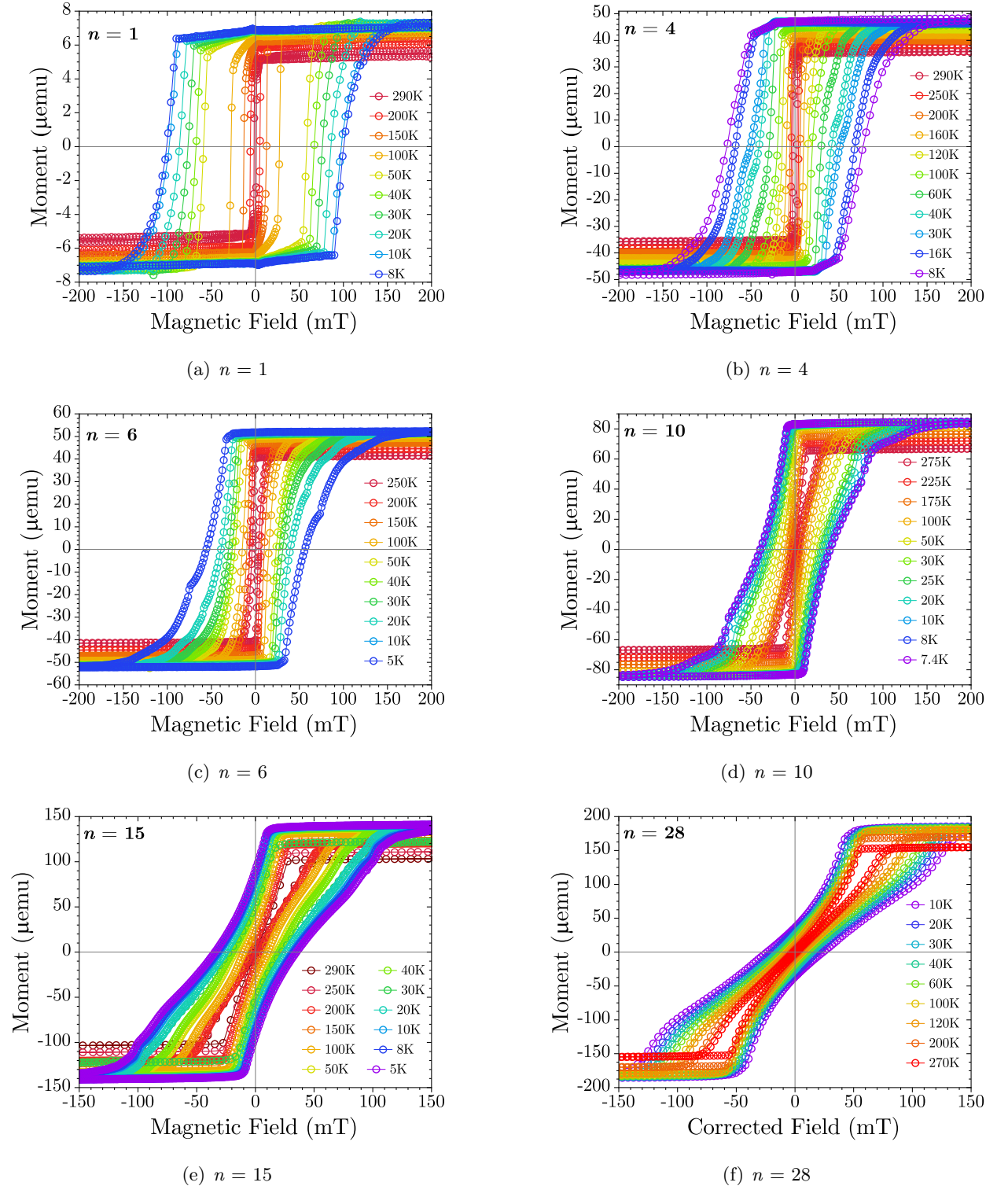
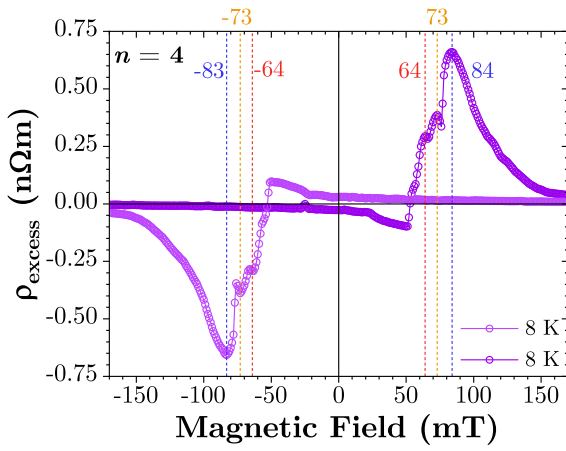


Figure 6.3: Out-of-plane magnetic moment vs applied magnetic field (easy axis hysteresis loops) for multilayer repeats $n = 1, 4, 6, 10, 15,$ and 28 shown in subfigures (a)-(f) respectively. The temperature of each measurement is indicated by the colour of the data, where purple is the coldest at ~ 5 K and red is the warmest at ~ 290 K.

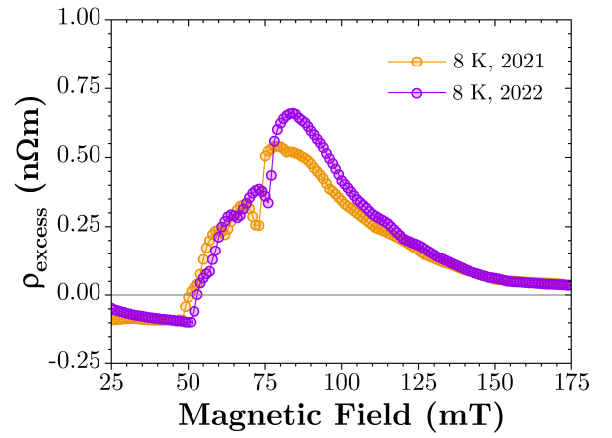
layer at multiple different temperatures. In a similar way, samples with numbers of repeats that are expected to span the range in which one might expect skyrmions to be present were selected to be measured over a wide range of temperatures, with more measurements being performed in temperature ranges ($T < 30$ K) where unexpected features in the transport hysteresis loops were observed, figure 6.2.

Chapter 5 provided an in depth discussion of the methods used for calibration of the superconducting magnets used (section 5.2 and the analysis steps taken to extract the excess Hall resistivity from the raw Hall resistivity data that is shown in figure 6.2 by using SQUID magnetometry measurements (shown in Figure 6.3) to estimate the anomalous Hall effect (section 5.3). Figure 6.4 shows the $\rho_{xy,excess}$ signal at 8K in the sample with $n = 4$ for the whole hysteresis loop. No symmetrisation of the data has been performed, $\rho_{xy,excess}$ is antisymmetric with magnetic field with all features in the signal occurring within 1 mT of their opposite field counterparts. This is highlighted in figure 6.4 (a) by dashed, coloured lines at each peak in the signal. In the rest of this thesis the $\rho_{xy,excess}$ signal will be presented only for the negative to positive field sweep direction in order to improve visibility in figures. The negative to positive sweep was chosen for presentation to ensure that the cryostat VTI and the sample were in thermal equilibrium for the entirety of the magnetic field sweep. In some data files the sample temperature was still several degrees from the VTI chamber when the positive to negative field sweep was started. This occurs when the stability criterion for the temperature has been met (i.e. the change in temperature is small enough over a set period of time) but there is still a significant difference between the VTI and sample temperature. This introduces a small artifact at the beginning of the measurement until thermal equilibrium is reached. Data collected prior to thermal equilibrium are excluded and don't occur within the region of interest in the hysteresis loop.

Some samples were measured multiple times with a large time period in between in order to check the robustness of the sample with time and if the features observed in $\rho_{xy,excess}$ were repeatable. The $\rho_{xy,excess}$ signal at 8 K in the sample with $n = 4$ measured in the summer of 2021 (orange) and spring of 2022 (purple) is shown in figure 6.4 (b). While there is clearly some variation in $\rho_{xy,excess}$ between the two measurements all the features within the signal are present in both measurements and the magnitude of the excess Hall resistivity is comparable. The small differences between the two signal are not surprising as the magnetic domains formed during hysteresis loops when materials switch magnetisation are never identical, there are imperfections in all materials that change the energy landscape affecting domain nucleation and the spread of domains during switching. In a similar way, any topological textures present during switching will be dependent on the specific defects and local properties of the multilayer, and as such are not necessarily produced at exactly the same applied field during each measurement. It is also possible that the temperature of the sample was slightly different in the two measurements changing the coercivity of the material, shifting the position of $\rho_{xy,excess}$ in field and changing the magnitude of the signal. Now that the



(a) $\rho_{xy,excess}$ for both magnetic field sweep directions. Reference lines of different colours indicate the magnetic field at which features in $\rho_{xy,excess}$ occur in each sweep. The signal is antisymmetrical in field, as one would expect, and only one of the features occurs at a different place during the magnetic field sweep in the opposite direction.



(b) Repeatability of measurements: The $\rho_{xy,excess}$ signal is extremely similar with only slight variations in magnitude and magnetic field position. This validates the use of longitudinal resistance measurements from 2021 combined with the $\rho_{xy,excess}$ signals measured in 2022 in chapter 7.

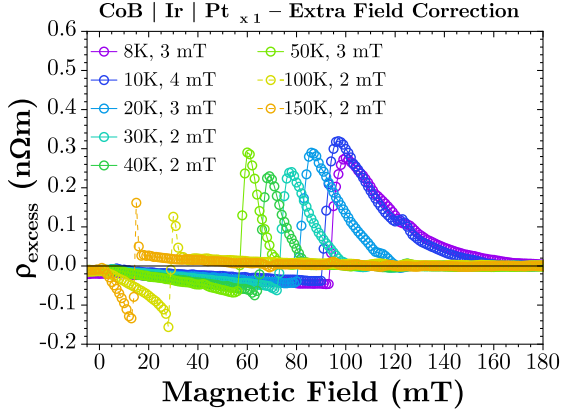
Figure 6.4: The $\rho_{xy,excess}$ signal vs magnetic field for the sample with $n = 4$ multilayer repeats. (a) $\rho_{xy,excess}$ while the magnetic field is swept in both directions. (b) $\rho_{xy,excess}$ in the same sample measured ~ 10 months apart.

robustness of the $\rho_{xy,excess}$ signal has been established the temperature dependence of $\rho_{xy,excess}$ will be discussed.

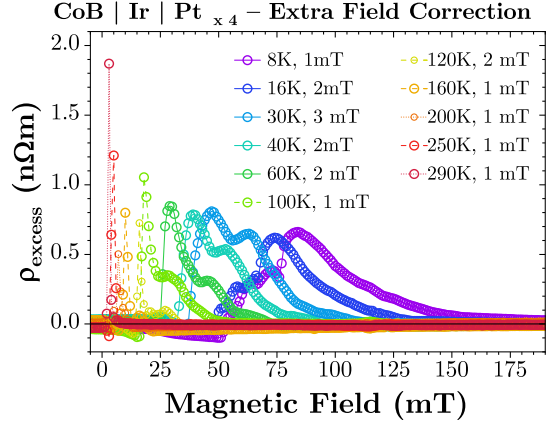
6.3 Temperature Dependence

The temperature dependence of the excess Hall resistivity, $\rho_{xy,excess}$, measured when sweeping from negative to positive field is presented in figure 6.5, with each subfigure (a) - (f) showing the data for different numbers of multilayer repeats, where n increases from 1 in (a) to a maximum of 28 in (f). The temperature of each $\rho_{xy,excess}$ curve is shown by the colour of the data where the lowest temperatures are shown in purple and move through the colour spectrum to the highest temperatures that are shown in red. As discussed in sections 5.4.1 and 5.4.2 the FWHM of the features within $\rho_{xy,excess}$ was used to determine the reliability of the features (figure 5.27). The $\rho_{xy,excess}$ in samples with $n=1$ and $n=4$ were identified as having features that may be unreliable and as such the relevant $\rho_{xy,excess}$ curves in figures 6.5 (a) and 6.5 (b) are shown with dashed or dotted lines joining the data points rather than solid lines. The lines in all figures should be considered as guides to the eye unless explicitly stated otherwise. In existing literature $\rho_{xy,excess}$ is attributed to topological spin textures within the material, as discussed in section 2.6.3, and often referred to as ρ_{xy}^T - a topological Hall effect. Despite numerous reports of skyrmion presence in samples grown with the same structure as those measured for this thesis [5; 8; 60; 65], I have chosen to label the resulting signal presented in results as $\rho_{xy,excess}$. This is partially due to lack of corroborating evidence (such as magnetic imaging e.g. MFM or XMCD-STXM) for skyrmion presence in the specific samples measured, as well as some unexpected results that serve to prove that the theory explaining the overall Hall effect is incomplete when describing magnetic materials with complicated multilayer structures and/or topologically non-trivial spin textures present.

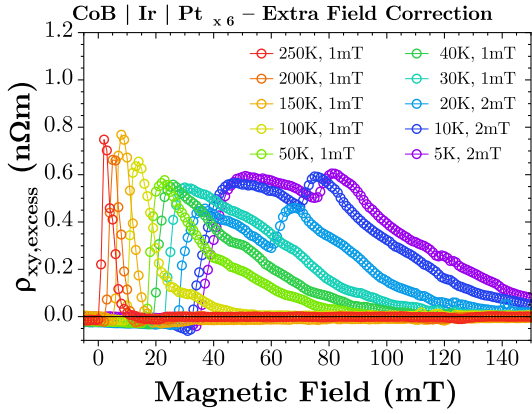
Comparing figures 6.2, 6.3, and 6.5 it is clear to see that the $\rho_{xy,excess}$ signal is concurrent with the field range where each sample exhibits multidomain states while it switches between opposite OOP magnetisation directions, which is to be expected. The general shapes of the raw transport hysteresis loops in Figure 6.2 (a)-(f) and the raw moment hysteresis loops in Figure 6.3 are very similar. As mentioned in section 2.6.4 this is to be expected because the topological Hall contribution from skyrmions is very small and dependent on the number of skyrmions present as well as the size of the magnetic flux quantum. Similarly, R_0 , the ordinary Hall coefficient is very small and so the dominant component in the transport hysteresis loops comes from the anomalous Hall contribution which is proportional to the out-of-plane magnetisation. The shape of the magnetisation loops is generally what is expected in ferromagnetic multilayers with perpendicular magnetic anisotropy, as was discussed in section 2.4. Generally, Figure 6.3 (a)-(f) suggests that the multilayers are switching via domain nucleation and domain wall motion where the domains are continuous through the whole multilayer stack because there are no obvious steps in the moment loops. It is



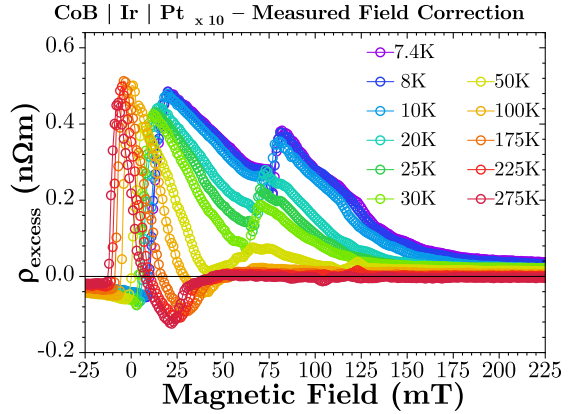
(a) $n = 1$



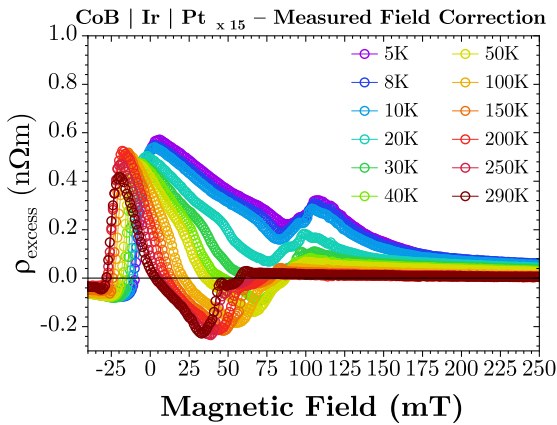
(b) $n = 4$



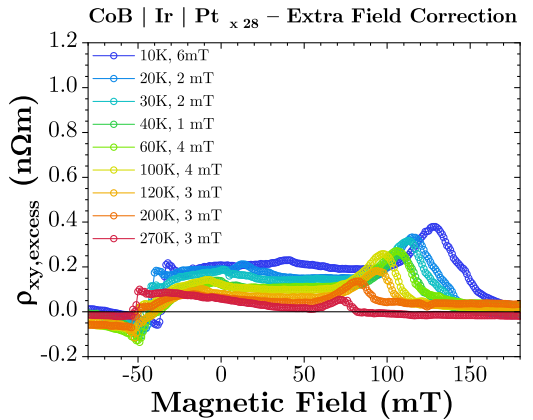
(c) $n = 6$



(d) $n = 10$



(e) $n = 15$



(f) $n = 28$

Figure 6.5: The $\rho_{xy,excess}$ signal vs magnetic field for all samples, where the multilayer repeats $n = 1, 4, 6, 10, 15,$ and 28 are shown in subfigures (a)-(f) respectively. The temperature of each measurement is indicated by the colour of the data, where purple is the coldest at ~ 5 K and red is the warmest at ~ 290 K.

possible that the bumps in the hysteresis loops for the samples with $n = 6, 10$ at low temperatures are due to some ferromagnetic layers switching independently but I think this is unlikely because the bumps are much less prominent in the magnetisation loops than in the transport loops. The change in magnetisation hysteresis loop shape from square to more wasp-shaped with increasing n can be easily understood by considering the fact that as the total thickness of the multilayer increases the samples are more inclined to form maze-domain patterns in order to decrease the stray fields associated with the domains. The field dependence of the $\rho_{xy,excess}$ signal with temperature follows the temperature dependence of the coercive field in each sample, and as the temperature is increased the signal in $\rho_{xy,excess}$ occurs at lower temperatures and vice versa as one would expect.

There are several other qualitative observations that can be made about the dependences of $\rho_{xy,excess}$ from figures 6.5 (a)-(f). The amplitude and number of peaks within the $\rho_{xy,excess}$ signal appear to vary with the temperature in each sample. In samples with $n = 1, 4$ and 6 the number of features within the $\rho_{xy,excess}$ signal increases at lower temperatures, whereas in the samples with $n = 10$ and 15 the number of features does not appear to be dependent on temperature. Instead, in these samples, temperature variation produces changes in the shape and sign of the signal; lower temperatures produce peaks with only positive $\rho_{xy,excess}$ and higher temperatures produce one positive feature and one negative feature. The topological contribution to the Hall effect is given by

$$\rho_{xy}^T = R_O P B_{\text{eff}}^z, \quad (6.3)$$

where R_O is the ordinary Hall coefficient, P is the spin polarization of the charge carriers, and B_{eff}^z is the effective field felt by charge carriers traversing a topologically non-trivial magnetisation texture. B_{eff}^z is proportional to the skyrmion winding number, S (eq 2.22), or number of skyrmions present. Given that R_O and P are not known to change with either applied magnetic field or temperature, interpreting $\rho_{xy,excess}$ as topological implies a change in the sign of the sum of the skyrmion winding number in the sample and therefore the presence of skyrmions with opposite magnetisation. This is unexpected and counter-intuitive when one considers that applying an external magnetic field should favour the creation of skyrmions with the same magnetisation direction of the applied field. It is tempting to suggest that the samples were perhaps not fully saturated before the direction of the magnetic field sweep was reversed. However, looking at figure 6.5 (d) and (e), one can see that this is an unsatisfactory explanation as in all $\rho_{xy,excess}$ signals the positive features occur first (on the left) as the magnetic field is swept from negative to positive (left to right). If skyrmions that contribute a negative $\rho_{xy,excess}$ were not destroyed by the maximum negative magnetic field applied then one would expect that the first feature apparent in $\rho_{xy,excess}$ would be negative not positive. Similarly, a positive applied field is expected to promote positive $\rho_{xy,excess}$ as seen in all the other samples. This logic is supported by the fact that a positive to negative field sweep produces a negative $\rho_{xy,excess}$ signal as shown previously in figure 6.4 (a).

The observation of multiple features within the $\rho_{xy,excess}$ signal is also somewhat unexpected as

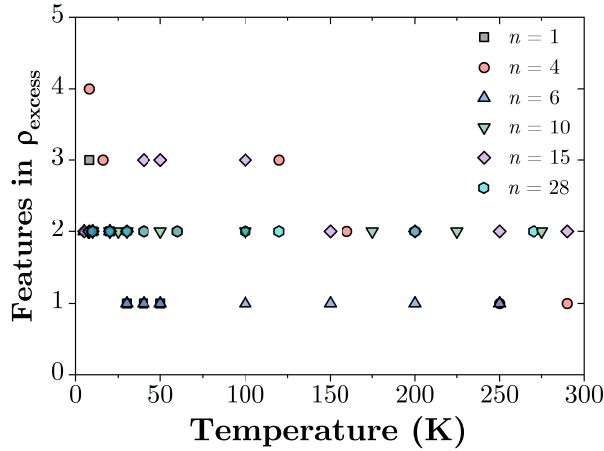


Figure 6.6: The number of features vs temperature. The different samples are differentiated by different symbols and colours as given in the legend. The variation in the number of features present, when comparing between samples, is largest at lower temperatures.

one would expect the number of skyrmions nucleated during switching to increase until a maximum density is reached at which point a higher magnetic field ceases to favour the production of more skyrmions and instead topologically trivial domains are favoured and spread until the sample is entirely saturated and $\rho_{xy,excess}$ is zero. Figure 6.6 shows the number of features in the $\rho_{xy,excess}$ signal vs temperature for all the samples measured. This figure supports the conclusion that the number of features within $\rho_{xy,excess}$ signals has a temperature dependence in some of the samples but not others. The most obvious temperature dependence is exhibited by the sample with 6 repeats which appears to have a critical dependence on temperature, exhibiting multiple features at 20 K and below but not above. The 4 repeat sample has a similar dependence where the signals at 8 K and 16 K show at least three peaks that increase in amplitude with field position but the signals at higher temperatures have fewer features that decrease in amplitude as the field position increases. The single repeat sample also has very small bumps in the signal at 8 K and 10 K, in addition to the main peak, although this is much harder to distinguish from the overall signal. The other three samples appear to have less dependence on temperature when considering the number of features within the $\rho_{xy,excess}$ signal with each keeping a relatively constant two features present, however it is only at the highest temperatures that one of these features changes sign in the 10 and 15 repeat samples. The existing theory for the topological Hall effect cannot explain the presence of multiple features within the $\rho_{xy,excess}$ signals presented here, nor the unexpected change in sign. Combined temperature and field dependent MFM (or other magnetic imaging method) is likely to be necessary in determining if the origin of these features is due to topological magnetic textures.

In order to try to understand the temperature dependence of the $\rho_{xy,excess}$ signals better the magnitude of each of the features (maxima or minima) has been plotted vs temperature, as shown

in figure 6.7. For each temperature the features in $\rho_{xy,excess}$ are identified by counting them from left to right such that 1 always refers to the feature that occurs at the lowest field (sweeping from negative to positive). In all subfigures the first feature is represented by black squares, the second by red circles, and the third by blue triangles. Although there does not appear to be a universal $\rho_{xy,excess}$ temperature dependence that applies to all the samples, it is clear to see that there is some variation in the size of the $\rho_{xy,excess}$ signal with temperature for most of the samples. The variations in temperature are most obvious in the sample with $n = 4$ multilayer repeats, which has large variations (~ 0.5 n Ω m) in $\rho_{xy,excess}$ in all features, and in the secondary features in the samples with $n = 10$ and 15 multilayer repeats. In both the $n = 10$ and 15 multilayer repeat samples there is a decrease in the magnitude of the first $\rho_{xy,excess}$ feature as the temperature increases from ~ 5 K to 50 K followed by a gradual increase and plateau ~ 150 K followed by a decrease in size as the temperature reaches ~ 270 K. These samples also both exhibit secondary features that decrease in amplitude as the temperature is increased, before changing sign completely. The negative $\rho_{xy,excess}$ signal increases slowly with temperature in the $n = 10$ sample whereas in the $n = 15$ sample the negative feature appears to reach a maximum amplitude that stays constant for temperatures above 150 K. The sample with $n = 4$ appears to have the most complicated temperature dependence because the feature with maximum $\rho_{xy,excess}$ at each temperature initially occurs at the highest magnetic field (for the lowest T) and then swaps such that the largest $\rho_{xy,excess}$ occurs first during the field sweep, shown previously in figure 6.5 (b). It appears that the size of the first and second peak (in field) increases at 30 K, the first peak then stays around the same magnitude up to 60 K before decreasing whereas the second peak decreases in size immediately. The clearest trend in $\rho_{xy,excess}$ with temperature is exhibited in the sample with $n = 28$ repeats where all the features decrease in magnitude as the temperature is increased. The second feature in these signals (peak) is initially ~ 1.5 times the size of the first feature (plateau-like) at the lowest temperatures measured but by ~ 270 K the features are the same size as each other. To make it easier to identify trends due to temperature, the maximum $\rho_{xy,excess}$ vs temperature for all samples is shown in figure 6.8. The unfilled circles indicate temperatures where the amplitude of a smaller feature has been used because the largest feature is not wide enough to be confident that it is not an artefact of field correction or analysis. As previously noted most of the samples have a non-linear temperature dependence that is not easily described. Between 5 K and 60 K all the samples (except $n = 4$) have $\rho_{xy,excess}$ that decreases as the temperature is increased, whereas $n = 4$ increases is proportional to temperature in this range. The shape of the maximum $\rho_{xy,excess}$ in the samples with $n = 10$ and 15 above 60 K appears to have a similar dependence on temperature to saturation magnetisation. As previously noted the AHE, ρ_{xy}^A , is proportional to the OOP magnetisation of the sample and therefore the maximum AHE in each sample will occur at saturation and be proportional to the saturation magnetisation at each temperature. The maximum ρ_{xy}^A vs temperature for all the samples is shown in figure 6.9. Comparing figures 6.8 and

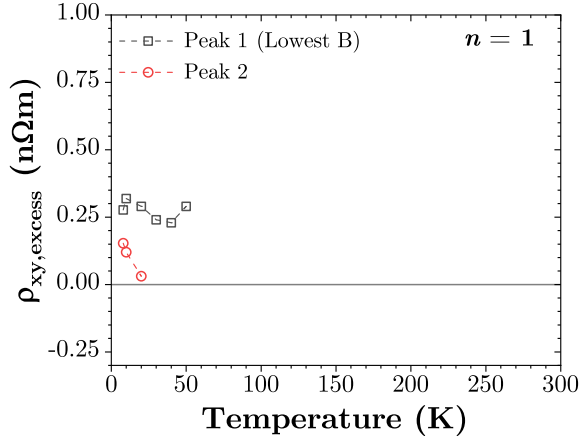
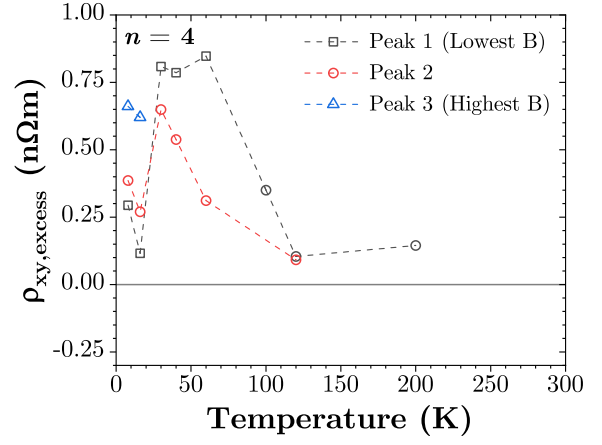
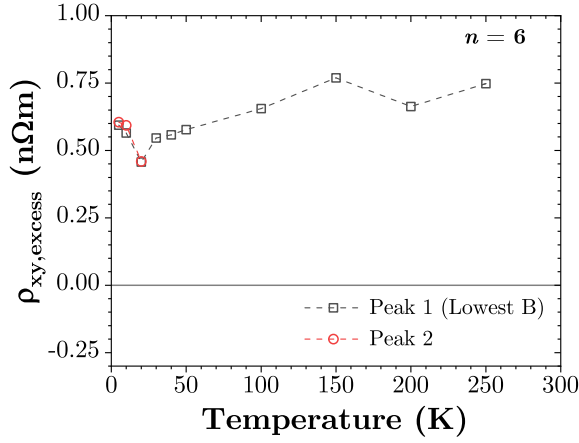
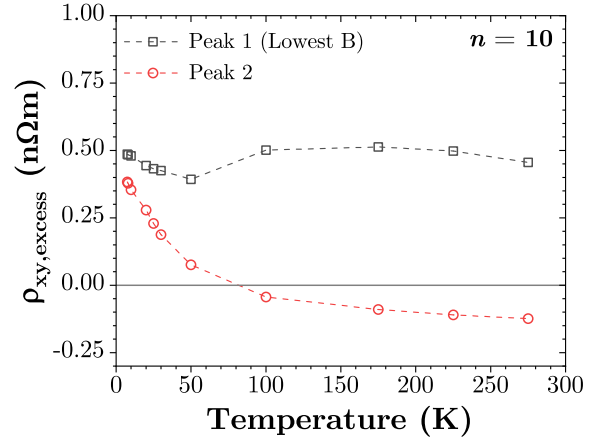
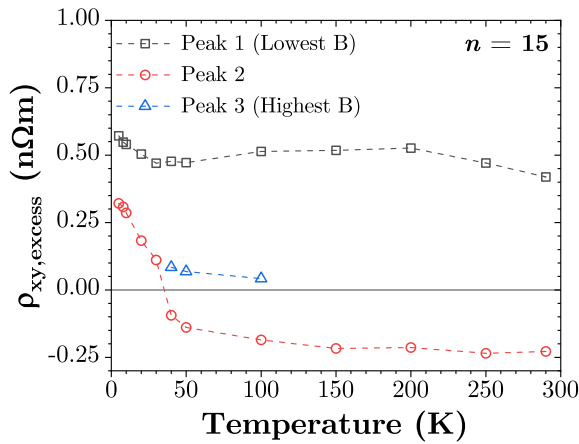
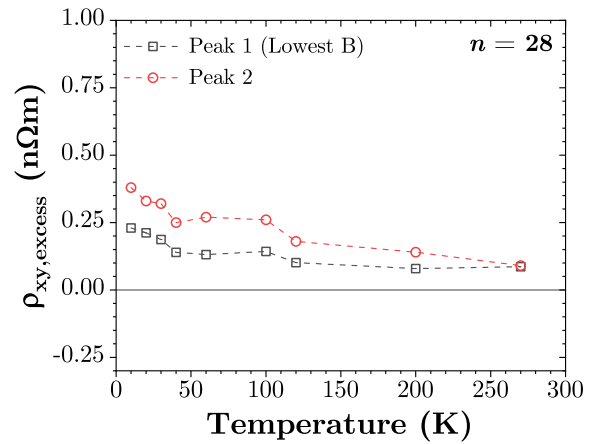
(a) $n = 1$ (b) $n = 4$ (c) $n = 6$ (d) $n = 10$ (e) $n = 15$ (f) $n = 28$

Figure 6.7: The amplitude of $\rho_{xy,excess}$ features vs temperature for multilayer repeats $n = 1, 4, 6, 10, 15,$ and 28 shown in subfigures (a)-(f) respectively.

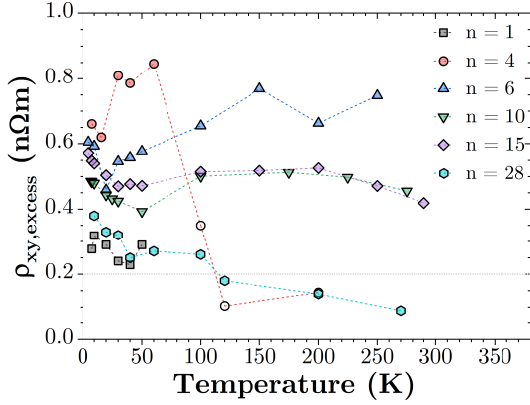


Figure 6.8: Maximum $\rho_{xy,excess}$ vs temperature for all samples. Here open symbols indicate features that are the largest when those that are too narrow are discounted - based on their FWHM as compared to the field and analysis resolution.

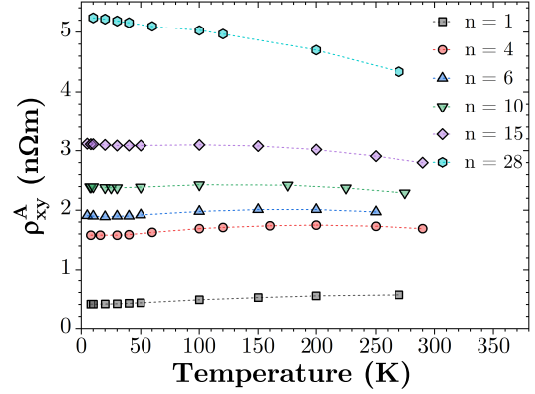


Figure 6.9: Maximum $\rho_{xy,A}$ vs temperature for all samples.

6.9 it is clear to see that the maximum AHE does not follow the same multilayer dependence as the maximum $\rho_{xy,excess}$. At all temperatures the AHE increases with the number of multilayer repeats, n , in the sample whereas in $\rho_{xy,excess}$ this is not the case. The temperature dependence of $\rho_{xy,excess}$ in the samples with $n = 6, 10, 15,$ and 28 repeats is very similar to the temperature dependence of the AHE, this can be seen even more clearly in figures 6.10 (a) - (f) where $\rho_{xy,excess}$ and AHE have been plotted with the same temperature axis for each sample. The vertical ranges of $\rho_{xy,excess}$ and ρ_{xy}^A have been adjusted, such that the maxima and minima in $\rho_{xy,excess}$ and ρ_{xy}^A occur at roughly the same height, so that the variation of each with temperature can be more clearly seen. Figures 6.10 (a) and (b) clearly have different $\rho_{xy,excess}$ temperature dependence than ρ_{xy}^A (over the range in temperature for which data exists). Conversely, the $\rho_{xy,excess}$ and ρ_{xy}^A signals in figures (c)-(f) have similar shapes, despite some having a $\rho_{xy,excess}$ signal that deviates somewhat from the shape of the maximum ρ_{xy}^A temperature dependence. Given these observations: that the samples with $n = 1$ and 4 do not appear to follow the same trends as ρ_{xy}^A , that three out of four of the other samples have some deviation from the shape of the ρ_{xy}^A temperature dependence, and that the maximum $\rho_{xy,excess}$ for each temperature occurs at different magnetic fields whereas all the maximum ρ_{xy}^A always occur at saturation (i.e. $H \neq H(\rho_{xy,excess})$ for all measurements), it seems reasonable to conclude that the $\rho_{xy,excess}$ temperature dependence is probably not due to ρ_{xy}^A remaining within the $\rho_{xy,excess}$ signal following analysis. Some different explanations may be that $\rho_{xy,excess}$ cannot be explained solely by equation 6.3 or that another contribution may exist that shares some or all of the physical mechanisms responsible for the AHE. The first of these is supported by multiple

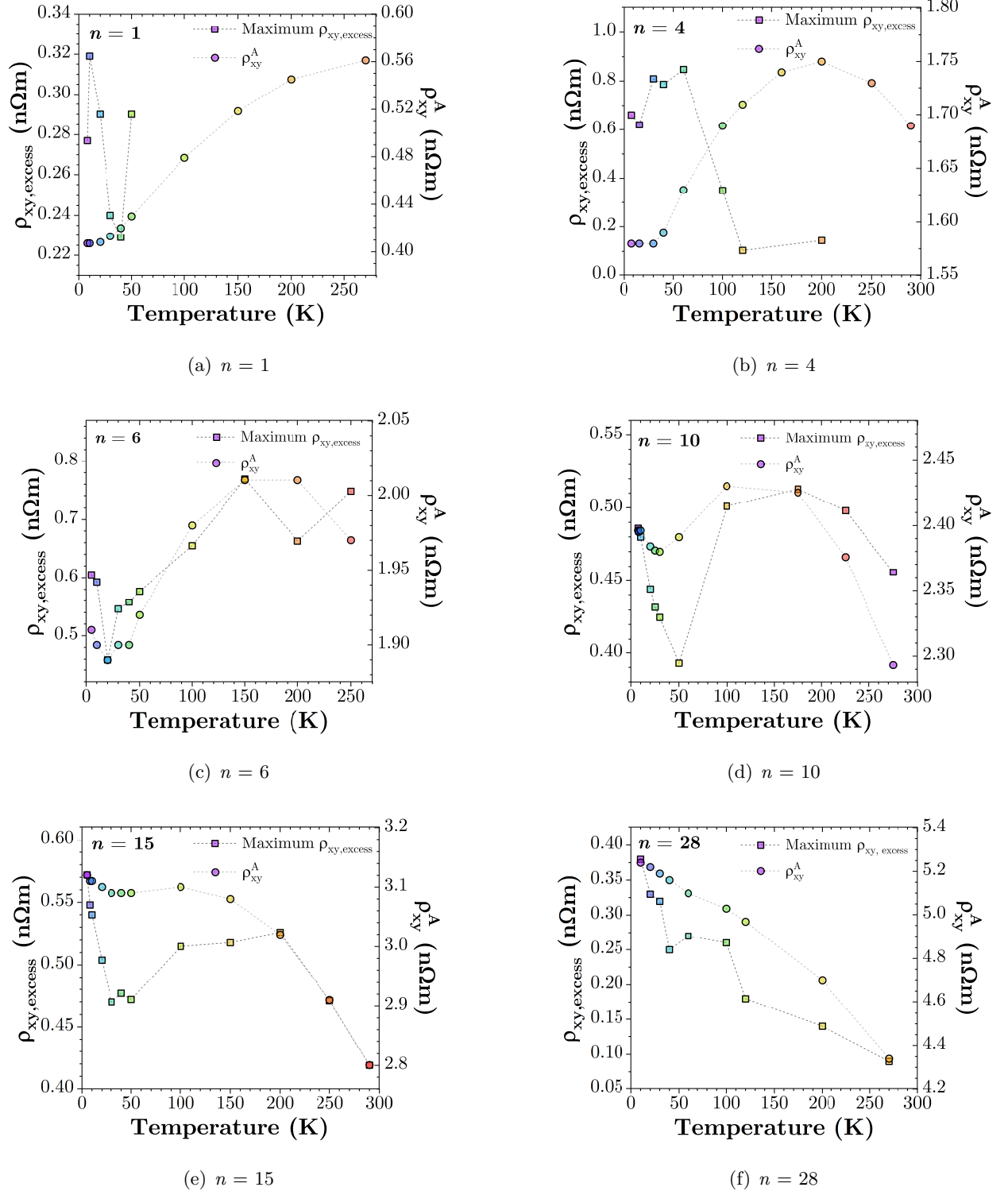


Figure 6.10: The maximum $\rho_{xy,excess}$ signal and ρ_A vs temperature for samples with $n = 1, 4, 6, 10, 15,$ and 28 shown in subfigures (a)-(f) respectively. The temperature dependence of the maximum $\rho_{xy,excess}$ signal appears to have some similarities to the temperature dependence of ρ_A in (c)-(f) ($n = 6$ to 28). Conversely for (a) and (b) ($n = 1$ and 4) the temperature dependence of maximum $\rho_{xy,excess}$ and ρ_A have no similarity.

reports of ρ_T of unexpected magnitudes in the literature [8; 10]. It is worth noting that many of the maxima in $\rho_{xy,excess}$ have much larger values than those reported by Raju et al. of around 20 n Ω cm (0.2 n Ω m, shown by the horizontal dotted line in figure 6.8) in Fe/Co multilayers that they dubbed a ‘colossal’ effect [10]. The largest $\rho_{xy,excess}$ shown here is four times larger than the maximum ρ_T reported in the Fe/Co multilayers. They found that the maxima in ρ_T corresponded to conditions when their samples were in the transition region between individual skyrmions and a skyrmion lattice by combining the transport measurements with temperature and field dependent MFM imaging. Despite this, the largest excess resistivity reported here, which is on the order of 80 n Ω cm ($n = 4$, $T \approx 50$ K), is of the same order as the topological Hall signal per skyrmion reported by Zeissler et al., 22 ± 2 n Ω cm, in reference [8], in multilayers with a very similar material composition measured at room temperature. Furthermore, a topological resistivity of around 100 n Ω cm has been reported previously in Hall resistivity measurements of Pt/Co/Ta multilayers [92]. Even larger topological resistivity signals have been reported in other materials, including: ~ 200 n Ω cm in SrRuO₃-SrIrO₃ bilayers [93]; ~ 300 n Ω cm in BTO/SRO/SrTi₃ heterostructures [94]; ~ 900 -1000 n Ω cm in FeGe epitaxial films [95; 96]; and ~ 1000 n Ω cm in FeCoGe epitaxial films. As such, the order of magnitude of the excess resistivity presented here seems to be consistent with magnitude of the signal reported by other experiments in the literature.

Future work in the Co/Ir/Pt multilayers measured here would benefit from using imaging techniques (MFM, Kerr microscopy, or XMCD-STXM) to investigate the magnetic textures responsible for the $\rho_{xy,excess}$ signal. Similarly, calculation of the stability parameter used by Raju et al., $\kappa \equiv \pi D/4\sqrt{AK_{eff}}$, for the samples measured here would allow more direct comparison to their results [10]. This would require more measurements of the samples including measurements of the DMI strength, D ; the exchange coupling, A ; and the magnetic anisotropy, K_{eff} ; of the samples.

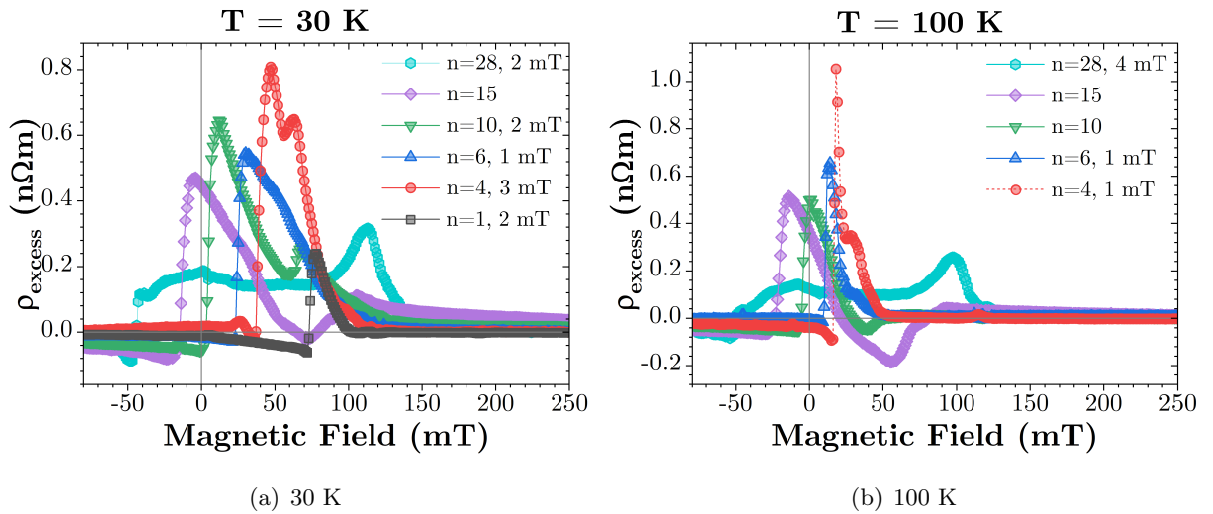


Figure 6.11: $\rho_{xy,excess}$ vs magnetic field for $n = 1, 4, 6, 10, 15, 28$ at (a) $T = 30$ K, and (b) $T = 100$ K.

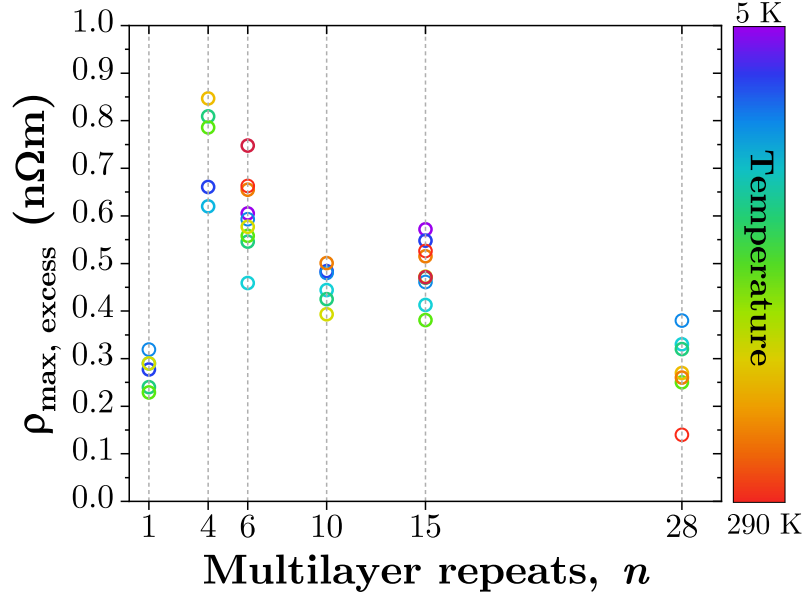


Figure 6.12: Maximum $\rho_{xy,excess}$ vs number of multilayer repeats, n . Values of $\rho_{xy,excess}$ at various temperatures are included, indicated by the colour of the data points with a rainbow spectrum between purple, the lowest temperature ~ 5 K, through green to red, the highest temperature ~ 290 K.

6.4 Multilayer Repeat, n , Dependence

The dependence of $\rho_{xy,excess}$ on the number of multilayer repeats, n , at constant temperature is shown in figures 6.11 (a), at $T = 30$ K, and (b), at $T = 100$ K. There are clear differences in both the shape and size of the $\rho_{xy,excess}$ signal in the samples with different n . The shape of the $\rho_{xy,excess}$ signal broadens as the number of multilayer repeats increases. This is related to the increased range in field within which the sample exhibits multidomain states while switching magnetisation. Similarly, the onset of $\rho_{xy,excess}$ occurs at lower fields as the number of repeats is increased due to the lowering coercivity as repeats are increased. However, it is hard to identify trends in the magnitude of $\rho_{xy,excess}$ when the data is presented like this. Therefore, the maximum $\rho_{xy,excess}$ signal vs multilayer repeat number is presented in figure 6.12 for a variety of temperatures. For this figure data points that correspond to $\rho_{xy,excess}$ signals with any features narrower than the limits defined for each sample in section 5.4.2, figure 5.27 are not included. Figure 6.12 shows an initial increase in $\rho_{xy,excess}$ for multilayer repeat numbers higher than one followed by a decrease, and possible plateau, in maximum $\rho_{xy,excess}$ for $n = 10$ and 15 . This is followed by another decrease for $n = 28$ which has similar maximum $\rho_{xy,excess}$ signal as the sample with $n = 1$. This is consistent with the reports of skyrmion presence in similar Co/Ir/Pt and CoB/Ir/Pt multilayer samples with $2 \leq n \leq 10$ used in previous research by the condensed matter group at the University of Leeds

and collaborators where various magnetic imaging methods were used including XMCD-STXM and LTEM [8; 117; 121; 123; 124]. However, this is the first time that the relationship between $\rho_{xy,excess}$ and n has been investigated in CoB/Ir/Pt multilayers using transport measurements at various temperatures. It appears that this behaviour is consistent for at individual temperatures despite the very different temperature dependences for the different numbers of repeats, shown previously in figures 6.5. Assuming that $\rho_{xy,excess}$ is at least partially topological in nature, figure 6.12 indicates that multilayers with $4 \leq n \leq 6$ are the most likely to host skyrmions. This would make sense considering the competing interactions that change as the number of multilayer repeats increases. The interfacial DMI interaction is known to contribute to the stabilisation of skyrmion magnetisation textures due to the canting effect that it has on the magnetic moments of interfacial ferromagnetic atoms, as discussed in section 2.3. Considering solely the DMI, one would expect that increasing the number of interfaces contributing to the DMI strength would result in a larger overall DMI in the sample, and thus easier skyrmion stabilisation. This is in agreement with the initial increase in excess resistivity seen from $n = 1$ to $n = 6$. In order to understand the subsequent decrease in excess resistivity, when interpreted as due to skyrmions, it is necessary to consider other interactions at play in the multilayers. In addition to increasing the interfaces, and therefore the DMI, increasing the number of multilayers also increases the total thickness of the sample. As previously mentioned in section 2.4, as the thickness of a sample increases so do the stray fields associated with the sample. This means that it becomes energetically more favourable to form maze-domains within samples with larger numbers of repeats. It is possible that these maze-domains have a lower energy than skyrmions or topologically non-trivial domains when the number of repeat layers is higher and so it may be more favourable to create maze-domains than skyrmions, even with increased DMI. Another factor that could affect this is if the interface roughness was increasing with the number of repeat layers because this would reduce the DMI in the samples with larger numbers of repeats vs lower numbers of repeats. However, it is not possible to conclude if this is the case in these samples as there was no observed increase in interface roughness in the samples with $n = 2, 4, 6, 8$ as shown in figure 3.9 in section 3.2.2. Samples with higher numbers of repeat layers would need to be scanned using XRR and fitted with GenX in order to determine if changing interface roughness is a reason for the decreasing excess resistivity seen here.

If $\rho_{xy,excess}$ is not taken to be topological in nature then this figure implies that samples with $4 \leq n \leq 6$ are the best candidates for further investigation into the origin of the $\rho_{xy,excess}$. Comparison of the ordinary Hall coefficient and charge carrier polarisation for samples with n corresponding to high and low measurements of $\rho_{xy,excess}$ could determine if the large $\rho_{xy,excess}$ found is due to multilayer band structure changes with repeat number, topological charge density, or some as yet unknown contribution to the Hall effect.

6.5 Conclusion

The $\rho_{xy,excess}$ signal measured in Pt/CoB/Ir multilayers has been shown to change in shape depending on the temperature of measurement and with the number of repeats in multilayer, where lowering temperature appears to increase the number of peak or trough like features present in the signal and lowering the number of multilayer repeats appears to increase the variation in the number of features present at different temperatures. The different multilayers have been shown to have maximum $\rho_{xy,excess}$ with different temperatures dependences from one another and that in four out of six samples ($6 \leq n \leq 28$) there are some similarities between the temperature dependence of the maximum $\rho_{xy,excess}$ and the anomalous Hall resistivity. This could mean that there are commonalities in the physical origins of $\rho_{xy,excess}$ and ρ_A .

Completely different maximum $\rho_{xy,excess}$ and ρ_A temperature dependences are seen in the samples with fewest multilayer repeats, $n = 1$ and 4, combined with the fact that the other four samples are not identical to the ρ_A measured suggests that the $\rho_{xy,excess}$ signal is, at least partially, topological in nature. This is supported by the dependence of maximum $\rho_{xy,excess}$ on the number of multilayer repeats which is in agreement with reports of skyrmion presence in similar Co/Ir/Pt and CoB/Ir/Pt multilayer samples with $2 \leq n \leq 10$ [8; 117; 121; 123; 124], including samples imaged during preliminary work and images presented in chapter 4.

It has been shown that the $\rho_{xy,excess}$ signal initially increases as the multilayer repeat number increases between $n = 1$ and 4 and then decreases with increasing repeat number until, when $n = 28$, a magnitude comparable to the initial $\rho_{xy,excess}$, when $n = 1$, is seen. It is not possible to definitively say $\rho_{xy,excess}$ is topological in nature due to an inability to link $\rho_{xy,excess}$ measurements with the magnetic textures present during measurement, due to time and equipment limitations (no access to variable temperature and field MFM). Suggestions for further work in these multilayers include variable temperature and field MFM, and/or Kerr microscopy with in-situ transport measurements. A preliminary experimental set-up was constructed and proof of concept measurements were carried out for room temperature Kerr microscopy with in-situ resistivity measurements towards the end of the experimental work carried out for this thesis. The dependence of maximum $\rho_{xy,excess}$ on multilayer repeat could prove useful for future skyrmion research in these multilayers as it indicates multilayers with $4 \leq n \leq 15$ have high $\rho_{xy,excess}$ (most likely corresponding to a high probability of skyrmion presence) at all temperatures. In particular samples with $4 \leq n \leq 6$ have the highest $\rho_{xy,excess}$ out of those measured here and therefore have the most promise for use in further investigations into contributions to the Hall effect in these multilayers.

CHAPTER 7

Anomalous Hall Effect in $[\text{CoB}|\text{Ir}|\text{Pt}]_{\times n}$
Multilayers

7.1 Introduction

While attempting to understand the origin of $\rho_{xy,excess}(T, n)$ by comparing it to $\rho_A(T, n)$ in the previous chapter a possible link between the physical origin of the temperature and multilayer repeat number dependencies of both resistivities was noted. In order to investigate this further, in this chapter the extrinsic and intrinsic contributions to ρ_A are found by exploitation of the manner in which different contributions scale with the longitudinal resistivity, ρ_{xx} . All of the contributions to the AHE arise from spin-orbit coupling phenomena, however the extrinsic contributions are due to two different types of scattering mechanisms, skew scattering and side-jump, whereas the intrinsic contribution arises only from the underlying band-structure of the material. Contributions to ρ_A in the CoB/Ir/Pt multilayers measured here are found to be $\alpha = -0.02$, $\beta = 1720$ S/cm, and $b = 520$ S/cm, where α , β , and b are from skew scattering, side-jump, and the intrinsic contributions respectively. The observed correlation between $\rho_{xy,excess}(T, n)$ and $\rho_A(T, n)$ in the previous chapter may be due to the relatively large value of side-jump scattering, $\beta = 1720$ S/cm, when compared to the other contributions to the AHE and to the side-jump contributions reported in other ferromagnetic materials (table 7.1). The measurements that yielded the results presented in this chapter were performed by the author with guidance and support from Dr G Burnell and Dr N Satchell.

7.2 Temperature Dependence of the AHE

The AHE at saturation has long been known to follow the empirical relationship,

$$\rho_A = R_S M_S, \quad (7.1)$$

where R_S is the anomalous Hall coefficient and M_S is the OOP magnetisation of the sample at saturation. In the experimental results presented here ρ_A is found from the Hall resistivity when the sample is saturated following the subtraction of the OHE,

$$\rho_A = \rho_{xy,S} - \rho_O, \quad (7.2)$$

where $\rho_{xy,S}$ is the Hall resistivity at saturation and ρ_O is the ordinary Hall resistivity subtracted as a linear background from the experimental data. This is possible because when a sample is saturated it is expected to be in a single domain state, without topologically non-trivial textures like skyrmions present. As such $M = M_S$, the saturation magnetisation, in these samples. The temperature dependence of the AHE is presented in figure 7.1 where the number of multilayer repeats in each sample is $n = 1, 4, 6, 10, 15$, and 28 in subfigures (a)-(f) respectively. The temperature dependence of the saturation magnetisation in each sample is shown in figure 7.2.

The saturation magnetisation was calculated using only the volume of Co in each sample, assuming that the composition of CoB in each thin layer is the same as the target that was used

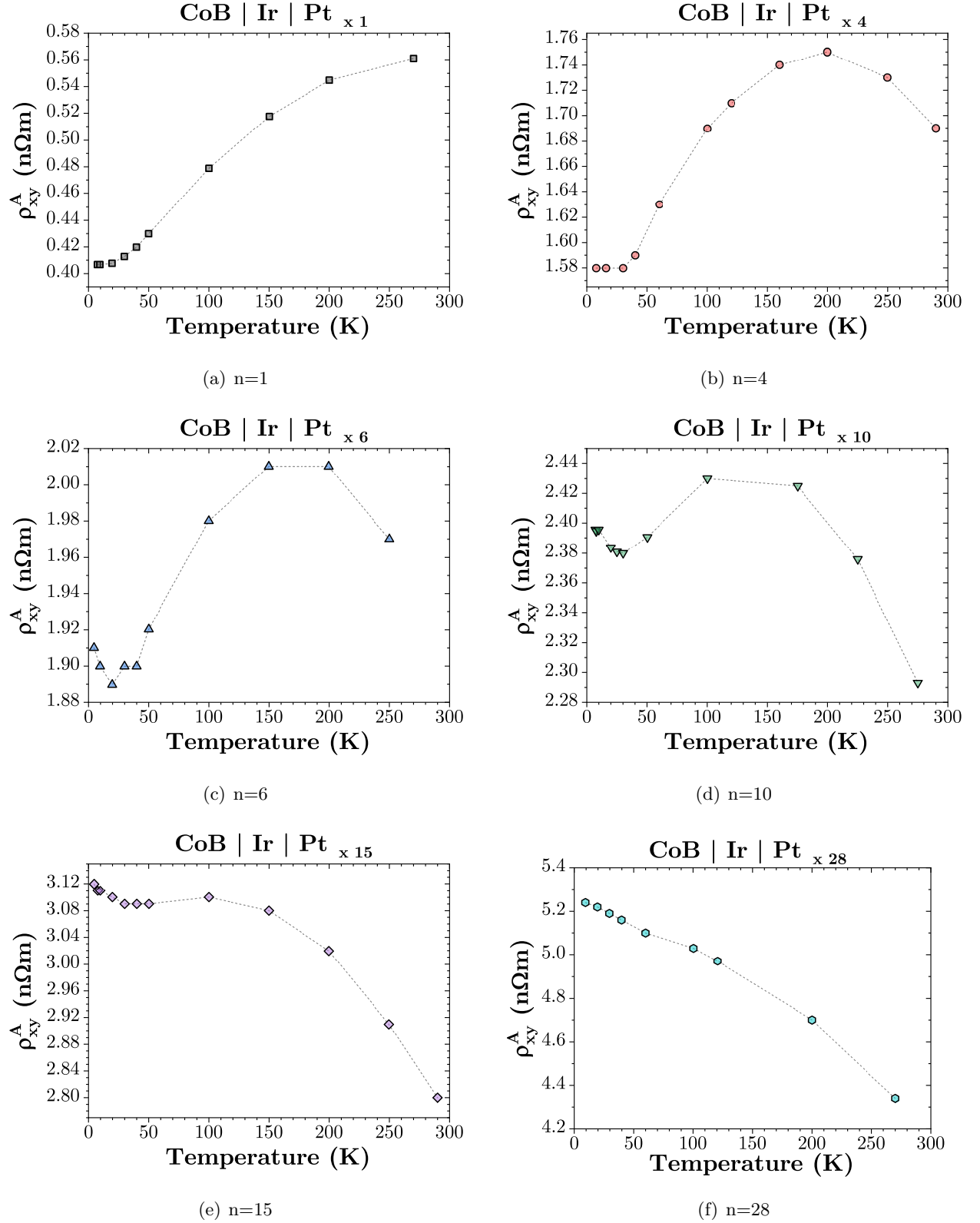


Figure 7.1: The anomalous Hall resistivity vs temperature in $[\text{CoB}|\text{Ir}|\text{Pt}]_n$ multilayers where $n = 1, 4, 6, 10, 15, \text{ and } 28$ in subfigures (a)-(f) respectively. By comparing the different samples it is clear to see that there is a gradual change in the variation of $\rho_A(T)$ from a positive gradient to a negative gradient.

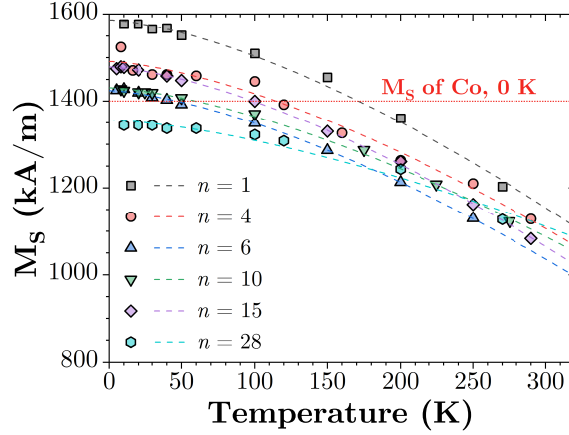


Figure 7.2: $M_S(T)$ for the Co volume in $[\text{CoB}|\text{Ir}|\text{Pt}]_{\times n}$ multilayers, where $n = 1, 4, 6, 10, 15,$ and 28 . Each set of $M_S(T)$ data is fit using Bloch's law and the accepted value of M_0 for Co is indicated by a red dotted line.

to grow the samples: $\text{Co}_{68}\text{B}_{32}$. The accepted value of the saturation magnetisation in Co at 0 K is indicated on figure 7.2 by a red dotted line. The dashed lines indicate a Bloch law fit using

$$M_S = M_0(1 - (T/T_c)^{3/2}), \quad (7.3)$$

Comparing the shape of $\rho_A(T)$ and $M_S(T)$ for each sample, at first glance it does not appear to be possible to attribute all of the temperature dependence in $\rho_A(T)$ to the temperature dependence from the changing saturation magnetisation.

7.3 AHE and Longitudinal Resistivity

As discussed previously in section 2.6.3, the anomalous Hall resistivity is known to follow the empirical relationship given in equation 7.1, and to be made up of contributions from intrinsic and extrinsic effects. The anomalous Hall coefficient, R_S , was not understood well for a long time but has been found to depend on various material properties including the longitudinal resistivity, ρ_{xx} . R_S is now normally broken down into two parts, one that is proportional to ρ_{xx} from skew-scattering and one that is proportional to ρ_{xx}^2 from the combined effect of side-jump and the intrinsic energy band properties of the material. In light of this, it is possible to reform equation 7.1 as

$$\rho_A = [\alpha\rho_{xx} + \beta\rho_{xx}^2 + b\rho_{xx}^2]M_S, \quad (7.4)$$

where α is the skew scattering coefficient, β is the side-jump coefficient, and b is the intrinsic coefficient. It is possible to test if this provides an accurate description of the anomalous Hall effect in the $[\text{CoB}|\text{Ir}|\text{Pt}]_{\times n}$ multilayers measured here by using

$$\frac{\rho_A}{\mu_0 M_S \rho_{xx}} = \frac{\alpha}{\mu_0} + \frac{(\beta + b)}{\mu_0} \rho_{xx}, \quad (7.5)$$

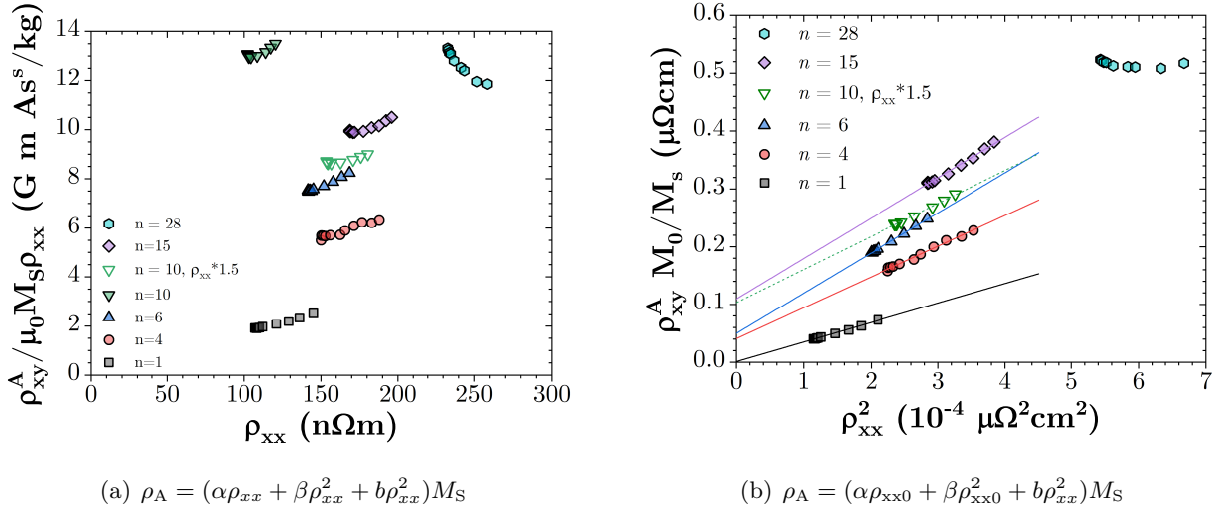
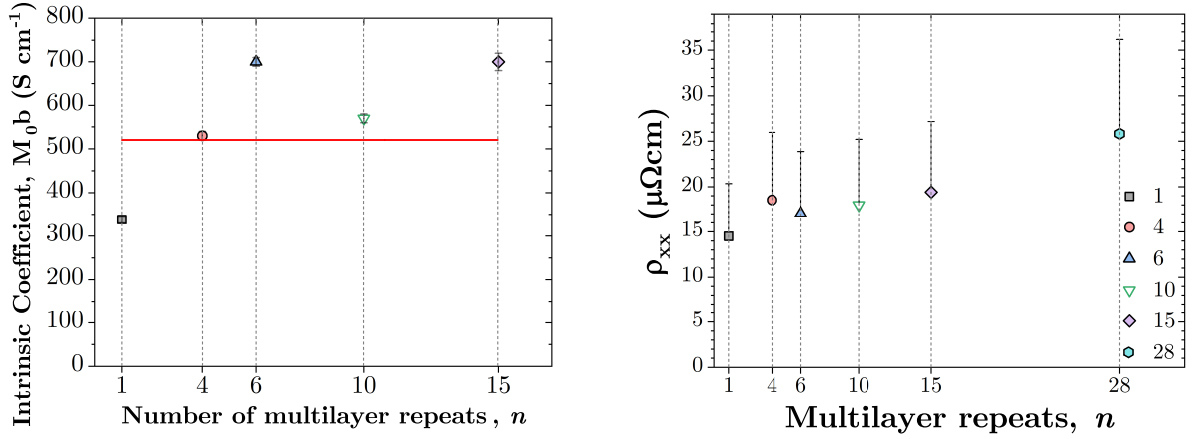


Figure 7.3: Correlation of (a) anomalous Hall resistivity scaled by $\mu_0 M_S \rho_{xx}$ with ρ_{xx} , and (b) anomalous Hall resistivity scaled by M_0/M_S with ρ_{xx}^2 . In each subfigure the relationship is expected to be linear if the expressions in equations 7.4 and 7.6 are correct for (a) and (b) respectively.

and plotting $\rho_A/\mu_0 M_S \rho_{xx}$ vs ρ_{xx} to check if the result is a straight line for each sample. The result of this process is shown in figure 7.3 (a), however the samples with $n \geq 6$ are still curved in this figure.

The longitudinal resistance was measured for each sample and converted to a resistivity using the same distance between the voltage contacts for each sample because the exact distance was unknown. The maximum possible distance between the wirebonds was used. It is clear in figure 7.3 (a) that the sample with $n = 10$ is an outlier. This is most likely due to the contacts being placed differently in this sample and so a second data set was included where the ρ_{xx} was scaled to represent the minimum possible distance between the contacts for $n = 10$, this is shown by the unfilled green triangles. The adjusted data for $n = 10$ is included in all the following figures, however it was excluded from all fitting and was not used to calculate the values of α, β , and b . From equation 7.5 it is clear that α and $(\beta + b)$ could be found from the intercept of a linear fit with the ordinate axis and the gradient of said fit respectively. Figure 7.3 (a) therefore implies that α and $(\beta + b)$ are dependent on the number of repeats in the sample. This does not seem to be intuitively true and combined with the non-linear relationships of multiple samples appears to be evidence that another approach to understanding the scaling of ρ_A with ρ_{xx} should be tried.

A similar method separates the resistivity into contributions from elastic and inelastic scattering by applying Matthiessen's rule. This is an empirical approximation that allows the combination of effects from impurities and lattice phonons to carrier mobility (or resistivity) by summation of independent terms from impurity scattering and lattice phonon scattering. In this case, it means using the residual longitudinal resistivity, ρ_{xx0} , for the extrinsic terms from scattering and the



(a) Intrinsic coefficient vs multilayer repeat number, n . (b) ρ_{xx} vs multilayer repeat number, n , at $T = 290$ K.

Figure 7.4: (a) The intrinsic coefficient vs n , with linear fit that assumes no dependence on n . (b) Dependence of ρ_{xx} on n at 290 K. The large error bars are due to uncertainty in the distance between contacts during measurement of ρ_{xx} .

temperature dependent resistivity ρ_{xx} for the intrinsic contribution. This results in the following expression for the anomalous Hall resistivity:

$$\rho_A = [\alpha\rho_{xx0} + \beta\rho_{xx0}^2 + b\rho_{xx}^2]M_S. \quad (7.6)$$

Figure 7.3 (b) shows $\rho_A M_0/M_S$ vs ρ_{xx}^2 , where

$$\rho_A \frac{M_0}{M_S} = M_0[(\alpha\rho_{xx0} + \beta\rho_{xx0}^2) + b\rho_{xx}^2], \quad (7.7)$$

and thus one would expect straight lines for each sample (because ρ_{xx0} is a constant). The gradient of each data set then provides a value of the intrinsic anomalous Hall contribution multiplied by M_0 . Comparing figures 7.3 (a) and (b) it appears that the data for all the samples except $n = 28$ is more linear in 7.3 (b) than 7.3 (a) and therefore equation 7.6 is seems to be a more appropriate description of the AHE in these multilayers. The fact that $n = 28$ has such a different gradient to the other samples in both figure 7.3 (a) and (b) suggests that at very large numbers of repeats neither equation 7.4 nor equation 7.6 are good descriptions of the contributions to the anomalous Hall resistivity. It is likely that interfacial scattering becomes increasingly important as the number of multilayer repeats increases. For this reason the data from $n = 28$ is not used when extracting α , β , and b .

The intrinsic coefficient, b , can be found from the gradient of linear fits to the data presented in figure 7.3 (b). The value of b found for each sample is plotted vs the number of multilayer repeats, n , in figure 7.4 (a). The weighted average of the values of b for $n = 1, 4, 6$, and 15 is indicated by a horizontal red line and b_{avg} found to be 520 S/cm. b is generally assumed to be independent

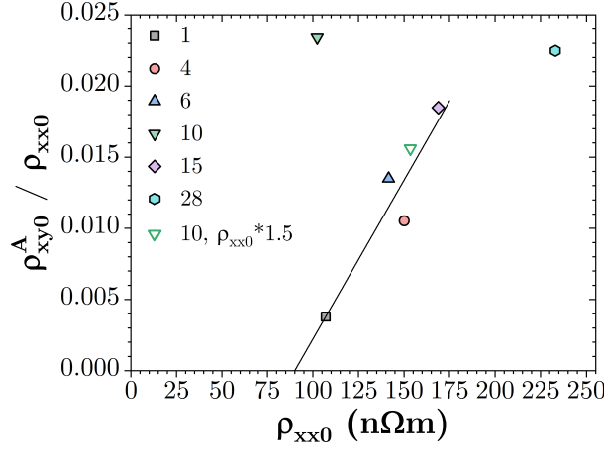


Figure 7.5: $\rho_{xy0}^A / \rho_{xx0}$ vs ρ_{xx0} for all samples. Using equation 7.8 allows the linear fit shown here to be used to identify the scattering parameters α , β and b .

of sample thickness because it is supposed to be independent of scattering, however this is not immediately obvious looking at figure 7.4 (a).

In these samples, one should also consider the fact that increasing the number of magnetic multilayers is not analogous to increasing the thickness of a single layer thin film as is commonly done in the literature [99; 125]. Doubling the number of repeats increases the number of interfaces, and therefore may increase any interfacial scattering. Similarly the seed and capping layers in these samples stay the same thickness when the number of multilayer repeats in between is increased. The easiest way to check if samples with different n have the same basic properties is to check if ρ_{xx} is independent of n at constant temperature. ρ_{xx} vs n is shown in figure 7.4 (b) for $T = 290$ K. This figure appears to indicate that the longitudinal resistivity may increase as the number of multilayer repeats is increased, although it is also possible to fit a horizontal line through all the error bars for $n = 1, 4, 6,$ and 15 , which will be used to calculate the different coefficients. It therefore appears plausible that the intrinsic properties of the samples do not change drastically with different numbers of repeats. It is also possible that the increased interfacial scattering in samples with larger n is the cause of any variation in ρ_{xx} with multilayer repeat number. If this is the case, one would expect that this would alter extrinsic coefficients that are scattering dependent rather than the intrinsic coefficient, b . In light of these points, and that it is necessary to assume constant b in order to be able to extract α and β from the data available, the average intrinsic coefficient shown in figure 7.4 (a) will be used going forward to find the extrinsic coefficients.

However, at this point I would like to highlight that there remains some uncertainty regarding whether or not b is truly independent of n . If b is in fact dependent on n this would indicate some changes in the band structure of the multilayers as n is varied. The intrinsic coefficient of the AHE is linked to the Berry curvature of the band structure and changes in this with n could explain

Material	α , skew scattering	β , side-jump	b , intrinsic
[CoB Ir Pt] $_{\times n}$	-0.02	1710 S/cm	520 S/cm
CoFeB (amorphous) [125]	-230	190 S/cm	-130 S/cm
Epitaxial Fe(001) [99]	-0.0037	700 S/cm	1100 S/cm
Epitaxial Fe(111) [126]	-0.013	305 S/cm	821 S/cm
Epitaxial FCC Co (001) [127]	0.0015	-311 S/cm	730 S/cm

Table 7.1: The AHE coefficients from skew scattering, side-jump, and intrinsic contributions found experimentally in [CoB|Ir|Pt] $_{\times n}$ multilayers, amorphous CoFeB [125], Fe (001) [99], Fe(111) [126], and FCC Co (001) [127].

the similarity between $\rho_{xy,excess}(T, n)$ and $\rho_A(T, n)$ observed in the previous chapter in figures 6.10 (a)-(f).

In order to find the extrinsic coefficients it is necessary to consider equation 7.6 at the lowest temperature when $\rho_{xx} = \rho_{xx0}$ by definition. Dividing through by ρ_{xx0} results in the following relationship,

$$\frac{\rho_{xy0}^A}{\rho_{xx0}} = [\alpha + (\beta + b)\rho_{xx0}]M_0, \quad (7.8)$$

where ρ_{xy0}^A is the anomalous Hall resistivity at the same temperature as ρ_{xx0} in each sample (typically $T = 5 - 10$ K), M_0 is the saturation magnetisation at 0 K, and all other parameters are as defined previously. Plotting ρ_{xy0}^A/ρ_{xx0} vs ρ_{xx0} , as shown in figure 7.5, and a linear fit of the data points from $n = 1, 4, 6$, and 15 allows identification of $M_0\alpha$ from the ordinate intercept, and $M_0(\beta + b)$ from the gradient of the fit. $M_0\alpha$ is found to be -0.02, and $M_0(\beta + b)$ is 2230 S/cm. Given that $M_0b = 520$ S/cm, then $M_0\beta = 1710$ S/cm.

At this point, note that in existing literature when these coefficients are found the saturation magnetisation of the measured materials is normally more or less constant over the range of temperatures used and therefore M_S is generally absorbed into the different coefficients whenever it is reported. Due to the significant temperature dependence in AHE, which becomes negligible in samples $n = 1, 4, 6$, and 15 following appropriate scaling with $M_S(T)$, the magnetisation has been kept separate from the coefficients until this point. From this point M_0 will be absorbed into each coefficient such that the results found here have consistent units (none for α , and S/cm for β and b as expected for the ordinate intercept and gradient from figure 7.5) with the results reported in existing literature. This also allows for more appropriate comparison as the coefficients are of the same order as those reported elsewhere, rather than one thousand times smaller. The values for the different AHE coefficients are displayed in table 7.1, along with the values that have been found using the same analysis method by different research groups for comparison.

Comparing the different values for α , β , and b found for several different ferromagnetic materials one can see that there is a wide range of reported values. The results for [CoB|Ir|Pt] $_{\times n}$ multilayers

reported for the first time here have signs that are in agreement with three out of four of the literature values included in table 7.1. Similarly the magnitudes of α and b are comparable to those reported in the other materials. In contrast to this the value of β found is a lot larger than those reported in CoFeB, Fe(111), and Co (001). This indicates a larger contribution to the AHE from side-jump scattering in $[\text{CoB|Ir|Pt}]_{\times n}$ multilayers than in any other single-layered ferromagnetic thin films.

This could indicate that the interfacial scattering inherently present in multilayers may be contributing to the AHE by increasing the amount of side-jump scattering compared to in single layered films. The values of α , β , and b found here indicate that the origin of the largest contribution to the AHE in $[\text{CoB|Ir|Pt}]_{\times n}$ multilayers is from side-jump scattering. To confirm if this mechanism occurs more due to the interfaces present in the multilayers, new samples where the thicknesses of the individual CoB, Ir, and Pt layers are tuned would need to be measured. Sets of samples where all the layers are scaled to be thicker or thinner, such that the ratio of CoB:Ir:Pt in each repeat stays constant, as well as sets where the thickness of CoB, Ir, or Pt are varied from 0 to a maximum while the other two are kept constant, would be useful to understand more about the effect of the multilayer structure on the different contributions to the AHE. Similarly, measurements in more samples with n between 15 and 28 would be useful to determine if the behaviour of the AHE in the multilayers is dependent on n or if the $n = 28$ dataset shown in figures 7.3 (a) and (b) is an anomaly.

7.4 Conclusion

The temperature dependence of the AHE in $[\text{CoB|Ir|Pt}]_{\times n}$ multilayers has been investigated, and it has been shown that this can be accounted for by the temperature dependence of $M_S(T)$. The AHE has been shown to be described well, in the samples with $n = 1, 4, 6,$ and 15 , by the expression $\rho_A M_0/M_S = (\alpha\rho_{xx0} + \beta\rho_{xx0}^2 + b\rho_{xx}^2)$, where ρ_{xx0} is the residual longitudinal resistivity due to impurity scattering, ρ_{xx} is the temperature dependent longitudinal resistivity from phonon-lattice interactions, $\alpha = -0.02$ is the skew scattering coefficient, $\beta = 1710 \text{ S/cm}$ is the side-jump coefficient, and $b = 520 \text{ S/cm}$ is the intrinsic coefficient from the band structure of the multilayers. These values of α , β , and b are of the same order as those found in the literature for single layered ferromagnetic materials, shown in table 7.1. In general there are still few examples of experimental measurements of the AHE where the extra time has been taken to disentangle all three contributions, despite Nagaosa et al. suggesting separation of the resistivity into elastic and inelastic contributions via Matthiessen's rule in 2010 [84]. Further experimental measurements of the AHE in other materials where the same analysis method is applied would prove useful in mapping the behaviour of the different coefficients and understanding the material characteristics that promote skew scattering vs side-jump type scattering. Similarly, further measurements in multilayers would be useful to identify

if the relatively large side-jump contribution observed here is impacted by interfacial scattering in multilayers. Measurements and analysis of the AHE in $[\text{CoB}(t_{\text{CoB}})|\text{Ir}(t_{\text{Ir}})|\text{Pt}(t_{\text{Pt}})]_{\times n}$ multilayers, where the thicknesses of the individual layers, t_{material} , are scaled such that $t_{\text{CoB}} : t_{\text{Ir}} : t_{\text{Pt}}$ remains the same, could be used to investigate the intrinsic dependence of the AHE further by eliminating the potential for coefficient dependence on the number of multilayer repeats in figure 7.4 (a). Similarly tuning the multilayer by varying the individual layer thicknesses one at a time (keeping the others constant) and measuring samples with n between 15 and 28 could provide more insight into the dependence of the AHE, and individual contributions to the AHE, on the multilayer structure. In particular, further measurements in samples with larger n could indicate if $n = 28$ is an anomaly or if the AHE has a real dependence on the number of multilayer repeats.

CHAPTER 8

Conclusion

8.1 Conclusion

This thesis aimed to measure the topological Hall effect due to magnetic skyrmions in $[\text{CoB|Ir|Pt}]_{\times n}$ multilayers, and determine any temperature or n dependent behaviour exhibited. The motivation for this research topic, relevant background condensed matter theory, and pertinent existing literature was discussed in detail in chapter 2.

As a reminder, the motivational context of this project is presented briefly here in three main points. Skyrmions have been suggested as topologically stable magnetic textures that could be applied to low-energy data storage in racetrack memory devices or similar. Their topological properties may provide better stability and reliability compared to typical magnetic domains, as well as causing an additional contribution to the Hall effect that is predicted to be proportional to the number of skyrmions present. Previous measurements and reports of the magnitude of the topological Hall effect in materials hosting skyrmions have been inconsistent, both with each other and with the magnitude predicted by existing Berry phase theory.

Understanding the relationship between the number of skyrmions present and their individual contribution to the Hall effect is essential to their application in magnetic data storage devices. To this end, hysteresis loops in Hall resistivity were measured in $[\text{CoB|Ir|Pt}]_{\times n}$ samples, with $n = 1, 4, 6, 10, 15,$ and 18 ; at temperatures ranging from ~ 290 K down to ~ 5 K. The experimental equipment and methods used to perform these measurements were presented in chapter 3.

The analysis methods used to apply field corrections and remove the ordinary and anomalous Hall effects from the Hall measurements to determine the excess resistivity, $\rho_{xy,\text{excess}}$, were outlined in detail in chapter 5.

The results of this analysis were presented in chapter 6, and the behaviour of $\rho_{xy,\text{excess}}$ in relation to the temperature, sample structure, and corresponding anomalous Hall contribution are summarised in section 8.1.1 of this chapter.

The behaviour of the anomalous Hall resistivity in the same samples, and at the same temperatures, was also investigated. In particular, the different extrinsic (skew scattering and side-jump) and intrinsic contributions to the anomalous Hall effect were determined from the scaling of the anomalous Hall resistivity, ρ_A , with the longitudinal resistivity, ρ_{xx} , in chapter 7, and are summarised in section 8.1.2 of this chapter.

Following a summary of the results presented in this thesis, several suggestions for areas of further work are laid out in section 8.2. Suggestions for further investigation into the origins of the AHE in $[\text{CoB|Ir|Pt}]_{\times n}$ multilayers and short summary of some experimental work that was hindered by the COVID-19 pandemic and subsequent university building work is presented in section 8.2.

8.1.1 Excess Hall Resistivity

The $\rho_{xy,excess}$ signal measured in Pt/CoB/Ir multilayers was shown to change shape depending on the temperature and number of repeats in the multilayer. Lowering the temperature increased the number of peak or trough like features present in the signal and lowering the number of multilayer repeats increased the variation in the number of features present at different temperatures.

The maximum $\rho_{xy,excess}$ in different multilayers was shown to have different temperature dependencies from one another and in four out of six samples ($6 \leq n \leq 28$) some similarities between the temperature dependence of the maximum $\rho_{xy,excess}$ and the anomalous Hall resistivity were identified. This could be indicative of commonalities in the physical origins of $\rho_{xy,excess}$ and ρ_A , and was investigated in chapter 7. A summary of the results from the investigation into the different contributions to the AHE are presented in section 8.1.2 of this chapter.

It was shown that the $\rho_{xy,excess}$ signal initially increases as the multilayer repeat number increases between $n = 1$ and 4 and then decreases with increasing repeat number until it reached a magnitude comparable to the initial $\rho_{xy,excess}$, when $n = 1$.

It has not been possible to definitively say that $\rho_{xy,excess}$ is topological in nature due to the lack of magnetic imaging concurrent with the $\rho_{xy,excess}$ measurements performed in this project. The fact that completely different maximum $\rho_{xy,excess}$ and ρ_A temperature dependencies were seen in the samples with fewest multilayer repeats, $n = 1$ and 4, combined with the $\rho_{xy,excess}$ of the other four samples having differences from the ρ_A measured suggested that the $\rho_{xy,excess}$ signal is, at least partially, topological in nature. This is supported by the observed dependence of maximum $\rho_{xy,excess}$ on the number of multilayer repeats which is in agreement with reports of skyrmion presence in similar Co/Ir/Pt and CoB/Ir/Pt multilayer samples with $2 \leq n \leq 10$ [8; 117; 121; 123; 124]. Similarly, XMCD-STXM images and Hall transport measurements would provide evidence that skyrmions may be easily found within samples with marginally different multilayer thicknesses and the same multilayer structure as those measured in this thesis.

Suggestions for further work to definitively determine the origin of the $\rho_{xy,excess}$ signal in $[\text{CoB}|\text{Ir}|\text{Pt}]_{\times n}$ multilayers are presented in section 8.2.

8.1.2 Anomalous Hall Effect

The temperature dependence of the AHE in $[\text{CoB}|\text{Ir}|\text{Pt}]_{\times n}$ multilayers was investigated, and it was shown that the temperature dependence can be accounted for by the temperature dependence of the saturation magnetisation of the samples, $M_S(T)$. The AHE in $[\text{CoB}|\text{Ir}|\text{Pt}]_{\times n}$ samples with $n = 1, 4, 6,$ and 15 , was demonstrated to be well described by the expression $\rho_A M_0/M_S = (\alpha\rho_{xx0} + \beta\rho_{xx0}^2 + b\rho_{xx}^2)$, where ρ_{xx0} is the residual longitudinal resistivity due to impurity scattering, ρ_{xx} is the temperature dependent longitudinal resistivity from phonon-lattice interactions. $\alpha = -0.02$ is the skew scattering coefficient, $\beta = 1710 \text{ S/cm}$ is the side-jump coefficient, and $b = 520 \text{ S/cm}$ is

the intrinsic coefficient from the band structure of the multilayers. These values of α , β , and b were shown to be of the same order as those found in the literature for single layered ferromagnetic materials.

The side-jump scattering coefficient was identified to be the largest contribution to the anomalous Hall resistivity in the multilayers measured. If the topological and anomalous Hall resistivities share a physical origin that explains the correlation between the temperature dependence of $\rho_{xy,excess}$ and ρ_A , it is possible that this could be attributed to the large side-jump coefficient relative to the other coefficients and the side-jump contribution reported in other ferromagnetic single thin films.

8.2 Further Work

Further research into the origin of the excess Hall resistivity, $\rho_{xy,excess}$, reported in this thesis is required to determine if it is caused by the presence of magnetic skyrmions. There is strong circumstantial evidence that there is some topological component to the effects observed but without combined transport measurements and magnetic imaging it is not possible to say this definitively. The dependence of maximum $\rho_{xy,excess}$ on multilayer repeat could prove useful for future skyrmion research in these multilayers as it indicates samples with $4 \leq n \leq 15$ have high $\rho_{xy,excess}$ (most likely corresponding to a high probability of skyrmion presence) at all temperatures. In particular samples with $4 \leq n \leq 6$ have the highest $\rho_{xy,excess}$ out of those measured here and therefore have the most promise for use in further investigations into contributions to the Hall effect in these multilayers.

In light of this, suggestions for further work in these multilayers include variable temperature and field MFM (or other magnetic imaging techniques e.g. XMCD-STXM), and Kerr microscopy with in-situ transport measurements. Ideally one would be able to create individual skyrmions and measure the Hall contribution when the number of skyrmions present is known. XMCD-STXM is one of the best methods for magnetic imaging in this case as the X-rays incident on the sample do not affect the magnetic textures present whereas the use of a tip very close to the sample in MFM imaging has the potential to disturb the magnetic textures present. In other words, the textures imaged may not be the same as when transport measurements are performed. Significant effort was spent early in my PhD studentship on the design and fabrication of Hall devices on silicon nitride membranes for imaging using XMCD-STXM while carrying out Hall transport measurements. These devices, discussed briefly in chapter 4, attempted to incorporate contacts, for Hall transport measurements, and current injectors, for controllable nucleation of skyrmions within the devices, inspired by work with collaborators in 2019 [5]. The devices produced aimed to combine multilayers like those used in the rest of this project with injectors for on-demand skyrmion nucleation. The main steps that I would take in order to get devices like these working would be to increase the

dimensions of the discs and contacts. It is likely that the fragility and contact resistance issues were mainly due to the extremely small dimensions that I was trying to achieve. Making the devices micron scale rather than nano scale is likely to increase the yield of samples for which transport measurements can be performed. If this was unsuccessful, I would also consider including an insulating layer over the top of the magnetic multilayer with gaps at point where skyrmions would be injected. The injector could then be deposited over the top of the insulating layer and into the gaps to make contact. This could stop current from entering the magnetic multilayers from the sides of the discs as the contacts or current injectors are in contact with the sidewalls of the magnetic discs when using the fabrication method of this project. Alternatively, previous members of the University of Leeds Condensed Matter Group have had success in fabricating bridges to inject currents down into magnetic materials. This type of lithography may also be advantageous for skyrmion nucleating current injectors.

Similarly, a preliminary experimental set-up was constructed and proof of concept measurements were carried out for room temperature Kerr microscopy with in-situ resistivity measurements in $[\text{CoB}|\text{Ir}|\text{Pt}]_{\times n}$ samples with focused ion beam (FIB) irradiation for skyrmion nucleation. This may provide a cheaper and more easily accessible method of combining magnetic imaging with transport measurements. This could be extremely valuable in providing proof of working devices prior to application for beamtime at facilities with XMCD-STXM capabilities.

Further experimental measurements of the AHE in thinfilm, multilayer, and magnetically interesting materials could prove useful in mapping the behaviour of the different coefficients and understanding the material characteristics that promote skew scattering vs side-jump type scattering. Similarly, measurements in multilayers with large numbers of repeats would be useful to identify if the relatively large side-jump contribution observed in chapter 7 is impacted by interfacial scattering in multilayers. Measurements and analysis of the AHE in $[\text{CoB}(t_{\text{CoB}})|\text{Ir}(t_{\text{Ir}})|\text{Pt}(t_{\text{Pt}})]_{\times n}$ multilayers, where the thicknesses of the individual layers, t_{material} , are scaled such that $t_{\text{CoB}} : t_{\text{Ir}} : t_{\text{Pt}}$ remains the same, could be used to investigate the intrinsic dependence of the AHE further by eliminating the potential for coefficient dependence on the number of multilayer repeats. Similarly tuning the multilayer by varying the individual layer thicknesses one at a time (keeping the others constant) and measuring samples with n between 15 and 28 could provide more insight into the dependence of the AHE, and individual contributions to the AHE, on the multilayer structure. In particular, further measurements in samples with larger n could indicate if $n = 28$ is an anomaly or if the AHE has a real dependence on the number of multilayer repeats in $[\text{CoB}(t_{\text{CoB}})|\text{Ir}(t_{\text{Ir}})|\text{Pt}(t_{\text{Pt}})]_{\times n}$ multilayers.

REFERENCES

- [1] B. Marr, “How much data do we create every day? The mind-blowing stats everyone should read.” forbes.com: <https://bit.ly/ForbesArticle3gZvk2V>, 2018.
- [2] T. Bawden, “Global warming: Data centres to consume three times as much energy in next decade, experts warn.” Independent.co.uk: <https://bit.ly/IndependentArticle3sMXzVo>, 2016.
- [3] X. Zhang, M. Ezawa, and Y. Zhou, “Magnetic skyrmion logic gates: Conversion, duplication and merging of skyrmions,” *Scientific Reports*, vol. 5, no. 9400, 2015.
- [4] S. Zhang, J. Zhang, Q. Zhang, C. Barton, V. Neu, Y. Zhao, Z. Hou, Y. Wen, C. Gong, O. Kazakova, W. Wang, Y. Peng, D. A. Garanin, E. M. Chudnovsky, and X. Zhang, “Direct writing of room temperature and zero field skyrmion lattices by a scanning local magnetic field,” *Applied Physics Letters*, vol. 112, no. 13, 2018.
- [5] S. Finizio, K. Zeissler, S. Wintz, S. Mayr, T. Weßels, A. J. Huxtable, G. Burnell, C. H. Marrows, and J. Raabe, “Deterministic field-free skyrmion nucleation at a nano-engineered injector device,” *Nano Lett*, vol. 19, p. 13, 2019.
- [6] S. S. P. Parkin, M. Hayashi, and L. Thomas, “Magnetic domain-wall racetrack memory,” *Science*, vol. 320, no. 5873, pp. 190–194, 2008.
- [7] R. Tomasello, G. Finocchio, L. Torres, M. Carpentieri, R. Zivieri, and E. Martinez, “A strategy for the design of skyrmion racetrack memories,” *Scientific Reports*, vol. 4, no. 1, p. 6784, 2014.
- [8] K. Zeissler, S. Finizio, K. Shahbazi, J. Massey, F. A. Ma’Mari, D. M. Bracher, A. Kleibert, M. C. Rosamond, E. H. Linfield, T. A. Moore, J. Raabe, G. Burnell, and C. H. Marrows, “Discrete Hall resistivity contribution from Néel skyrmions in multilayer nanodiscs,” *Nat. Nanotechnol.*, vol. 13, pp. 1161–1166, 10 2018.
- [9] P. Bruno, V. K. Dugaev, and M. Taillefumier, “Topological Hall effect and Berry phase in magnetic nanostructures,” *Physical Review Letters*, vol. 93, no. 9, 2004.

- [10] M. Raju, A. P. Petrović, A. Yagil, K. S. Denisov, N. K. Duong, B. Göbel, E. Şaşıoğlu, O. M. Auslaender, I. Mertig, I. V. Rozhansky, and C. Panagopoulos, “Colossal topological Hall effect at the transition between isolated and lattice-phase interfacial skyrmions,” *Nature Commun.*, vol. 12, no. 2758, 2021.
- [11] S. Blundell, *Magnetism in Condensed Matter*. Oxford University Press, 2001.
- [12] R. Skomski, *Simple Models of Magnetism*. Oxford University Press, 2008.
- [13] Y. Yang, P. Guo, and Y. Luo, “Strain modulated ferromagnetic phase transitions in monolayer FeCl₂ through exchange competitions: the first-principle and Monte Carlo simulations,” *Phys. Chem. Chem. Phys.*, vol. 22, pp. 17291–17298, 2020.
- [14] K. Fallon, S. Hughes, K. Zeissler, W. Legrand, F. Ajejas, D. Maccariello, S. McFadzean, W. Smith, D. McGrouther, S. Collin, N. Reyren, V. Cros, C. H. Marrows, and S. McVitie, “Controlled individual skyrmion nucleation at artificial defects formed by ion irradiation,” *Small*, vol. 16, 4 2020.
- [15] C. Kittel, *Ferromagnetism and Antiferromagnetism*. Wiley, 7th ed., 2005.
- [16] J. Coey, *Magnetism and Magnetic Materials*. Cambridge University Press, 2009.
- [17] L. Néel, “Surface magnetic anisotropy and orientation superstructures,” *J. Phys. Radium*, vol. 15, no. 4, pp. 225–239, 1954.
- [18] M. T. Johnson, P. J. H. Bloemen, F. J. A. den Broeder, and J. J. de Vries, “Magnetic anisotropy in metallic multilayers,” *Rep. Prog. Phys.*, vol. 59, no. 11, pp. 1409–1458, 1996.
- [19] R. H. Victora and J. M. MacLaren, “Theory of magnetic interface anisotropy,” *Phys. Rev. B*, vol. 47, no. 17, pp. 11583–11586, 1993.
- [20] M. Komelj and M. Fähnle, “On the magnetoelastic contribution to the magnetic anisotropy of thin epitaxial permalloy films: an ab initio study,” *Journal of Magnetism and Magnetic Materials*, vol. 238, pp. 125–128, 2002.
- [21] M. Eisenbach, B. L. Györfy, G. M. Stocks, and B. Újfalussy, “Magnetic anisotropy of monoatomic iron chains embedded in copper,” *Phys. Rev. B*, vol. 65, p. 144424, Mar 2002.
- [22] B. Radhakrishnan, D. Nicholson, M. Eisenbach, C. Parish, G. Ludtka, and O. Rios, “Alignment of iron nanoparticles in a magnetic field due to shape anisotropy,” *Journal of Magnetism and Magnetic Materials*, vol. 394, pp. 481–490, 2015.
- [23] I. Dzyaloshinskii, “A thermodynamic theory of ‘weak’ ferromagnetism of antiferromagnetics,” *J. Phys. and Chem. Solids*, vol. 4, 1958.

- [24] T. Moriya, “Anisotropic superexchange interaction and weak ferromagnetism,” *Physical Review*, vol. 120, no. 1, 1960.
- [25] A. Fert, “Magnetic and Transport Properties of Metallic Multilayers,” *Mater. Sci. Forum*, vol. 59-60, pp. 439–480, 1 1991.
- [26] A. Crèpieux and C. Lacroix, “Dzyaloshinskii-Moriya interactions induced by symmetry breaking at a surface,” *Journal of Magnetism and Magnetic Materials*, vol. 182, no. 3, pp. 341–349, 1998.
- [27] P. M. Levy and A. Fert, “Anisotropy induced by nonmagnetic impurities in cu mn spin-glass alloys,” *Physical Review B*, vol. 23, pp. 4667–4690, 5 1981.
- [28] M. Bode, M. Heide, K. von Bergmann, P. Ferriani, S. Heinze, G. Bihlmayer, A. Kubetzka, O. Pietzsch, S. Blügel, and R. Wiesendanger, “Chiral magnetic order at surfaces driven by inversion asymmetry,” *Nature*, vol. 447, pp. 190–193, 5 2007.
- [29] M. Heide, G. Bihlmayer, and S. Blügel, “Dzyaloshinskii-Moriya interaction accounting for the orientation of magnetic domains in ultrathin films: Fe/W(110),” *Phys. Rev. B*, vol. 78, p. 140403, 10 2008.
- [30] M. J. Benitez, A. Hrabec, A. P. Mihai, T. A. Moore, G. Burnell, D. McGrouther, C. H. Marrows, and S. McVitie, “Magnetic microscopy and topological stability of homochiral Néel domain walls in a Pt/Co/AlOx trilayer,” *Nat. Commun.*, vol. 6, p. 8957, 12 2015.
- [31] S. Meckler, N. Mikuszeit, A. Preßler, E. Y. Vedmedenko, O. Pietzsch, and R. Wiesendanger, “Real-Space Observation of a Right-Rotating Inhomogeneous Cycloidal Spin Spiral by Spin-Polarized Scanning Tunneling Microscopy in a Triple Axes Vector Magnet,” *Phys. Rev. Lett.*, vol. 103, p. 157201, 10 2009.
- [32] W. Jiang, G. Chen, K. Liu, J. Zang, S. G. te Velthuis, and A. Hoffmann, “Skyrmions in magnetic multilayers,” *Physics Reports*, vol. 704, pp. 1–49, 2017.
- [33] O. Boulle, J. Vogel, H. Yang, S. Pizzini, D. de Souza Chaves, A. Locatelli, T. O. Menteş, A. Sala, L. D. Buda-Prejbeanu, O. Klein, M. Belmeguenai, Y. Roussigné, A. Stashkevich, S. M. Chérif, L. Aballe, M. Foerster, M. Chshiev, S. Auffret, I. M. Miron, and G. Gaudin, “Room-temperature chiral magnetic skyrmions in ultrathin magnetic nanostructures,” *Nat. Nanotechnol.*, vol. 11, pp. 449–454, 1 2016.
- [34] A. Kubetzka, O. Pietzsch, M. Bode, and R. Wiesendanger, “Spin-polarized scanning tunneling microscopy study of 360 degree walls in an external magnetic field,” *Phys. Rev. B*, vol. 67, no. 2, 2003.

- [35] ALSHub and R. Chopdekar, “Tutorial - contrast using PEEM.” <http://xraysweb.lbl.gov/peem2/webpage/Project/TutorialContrast.shtml>, 2020.
- [36] H. T. Nembach, J. M. Shaw, M. Weiler, E. Jué, and T. J. Silva, “Linear relation between Heisenberg exchange and interfacial Dzyaloshinskii–Moriya interaction in metal films,” *Nat. Phys.*, vol. 11, pp. 825–829, 8 2015.
- [37] E. Martinez, M. Kläui, J.-S. Kim, G. V. Karnad, K. Lee, C.-Y. You, H. J. M. Swagten, T. Schulz, R. L. Conte, N.-H. Kim, S. Prenzel, and D.-S. Han, “Ferromagnetic layer thickness dependence of the Dzyaloshinskii-Moriya interaction and spin-orbit torques in Pt/Co/AlO_x,” *AIP Advances*, vol. 7, p. 065317, 6 2017.
- [38] K. S. Ryu, S. H. Yang, L. Thomas, and S. S. Parkin, “Chiral spin torque arising from proximity-induced magnetization,” *Nature Communications*, vol. 5, no. 3910, pp. 1–8, 2014.
- [39] J. Torrejon, E. Martinez, and M. Hayashi, “Tunable inertia of chiral magnetic domain walls,” *Nature Communications*, vol. 7, no. 13533, 2016.
- [40] S. Emori, U. Bauer, S.-M. Ahn, E. Martinez, and G. S. D. Beach, “Current-driven dynamics of chiral ferromagnetic domain walls,” *Nature Materials*, vol. 12, pp. 611–616, 2013.
- [41] K. Yamada, J.-P. Jamet, Y. Nakatani, A. Mougin, A. Thiaville, T. Ono, and J. Ferré, “Influence of Instabilities on High-Field Magnetic Domain Wall Velocity in (Co/Ni) Nanostrips,” *Appl. Phys. Express*, vol. 4, p. 113001, 10 2011.
- [42] A. Hrabec, N. A. Porter, A. Wells, M. J. Benitez, G. Burnell, S. Mcvitie, D. Mcgrouter, T. A. Moore, and C. H. Marrows, “Measuring and tailoring the Dzyaloshinskii-Moriya interaction in perpendicularly magnetized thin films,” *Rapid Comms. Phys. Rev. B*, vol. 90, p. 20402, 2014.
- [43] S.-G. Je, D.-H. Kim, S.-C. Yoo, B.-C. Min, K.-J. Lee, and S.-B. Choe, “Asymmetric magnetic domain-wall motion by the Dzyaloshinskii-Moriya interaction,” *Phys. Rev. B*, vol. 88, p. 214401, 12 2013.
- [44] K. Y. Aktaş, B. Kocaman, and A. C. Basaran, “Magnetic and electrical (GMR) properties of Rh(IrMn)/Co/Cu/Ni(Py) multilayered thin films,” *Journal of Superconductivity and Novel Magnetism*, vol. 33, pp. 2093–2100, Mar. 2020.
- [45] T. Skyrme, “A unified field theory of mesons and baryons,” *Nucl. Phys.*, vol. 31, pp. 556–569, 3 1962.
- [46] G. E. Brown and M. Rho, *The Multifaceted Skyrmion*. World Scientific Publishing Co., 2nd ed., 2009.

- [47] D. C. Wright and N. D. Mermin, “Crystalline liquids: the blue phases,” *Rev. Mod. Phys.*, vol. 61, pp. 385–432, 4 1989.
- [48] U. Al Khawaja and H. Stoof, “Skyrmions in a ferromagnetic Bose-Einstein condensate,” *Nature*, vol. 411, pp. 918–920, 2001.
- [49] L. Brey, H. A. Fertig, R. Côté, and A. H. MacDonald, “Skyrme Crystal in a Two-Dimensional Electron Gas,” *Phys. Rev. Lett.*, vol. 75, pp. 2562–2565, 9 1995.
- [50] A. Fert, N. Reyren, and V. Cros, “Magnetic skyrmions: advances in physics and potential applications,” *Nat. Rev. Mater.*, vol. 2, p. 17031, 6 2017.
- [51] A. N. Bogdanov and U. K. Röbner, “Chiral Symmetry Breaking in Magnetic Thin Films and Multilayers,” *Phys. Rev. Lett.*, vol. 87, p. 037203, 6 2001.
- [52] S. Heinze, K. von Bergmann, M. Menzel, J. Brede, A. Kubetzka, R. Wiesendanger, G. Bihlmayer, and S. Blügel, “Spontaneous atomic-scale magnetic skyrmion lattice in two dimensions,” *Nat. Phys.*, vol. 7, pp. 713–718, 7 2011.
- [53] A. Hoffmann, O. Heinonen, M. B. Jungfleisch, W. Jiang, S. G. E. te Velthuis, J. E. Pearson, P. Upadhyaya, F. Y. Fradin, G. Yu, Y. Tserkovnyak, K. L. Wang, and W. Zhang, “Blowing magnetic skyrmion bubbles,” *Science*, vol. 349, no. 6245, pp. 283–286, 2015.
- [54] C. Back, V. Cros, H. Ebert, K. Everschor-Sitte, A. Fert, M. Garst, T. Ma, S. Mankovsky, T. L. Monchesky, M. Mostovoy, N. Nagaosa, S. S. P. Parkin, C. Pfleiderer, N. Reyren, A. Rosch, Y. Taguchi, Y. Tokura, K. V. Bergmann, and J. Zang, “The 2020 skyrmionics roadmap,” *J. Phys. D: Appl. Phys.*, vol. 53, no. 36, 2020.
- [55] S. Mühlbauer, B. Binz, F. Jonietz, C. Pfleiderer, A. Rosch, A. Neubauer, R. Georgii, and P. Böni, “Skyrmion lattice in a chiral magnet,” *Science*, vol. 323, pp. 915–919, 2 2009.
- [56] X. Z. Yu, Y. Onose, N. Kanazawa, J. H. Park, J. H. Han, Y. Matsui, N. Nagaosa, and Y. Tokura, “Real-space observation of a two-dimensional skyrmion crystal,” *Nature*, vol. 465, pp. 901–904, 6 2010.
- [57] W. Münzer, A. Neubauer, T. Adams, S. Mühlbauer, C. Franz, F. Jonietz, R. Georgii, P. Böni, B. Pedersen, M. Schmidt, A. Rosch, and C. Pfleiderer, “Skyrmion lattice in the doped semiconductor $\text{Fe}_{1-x}\text{Co}_x\text{Si}$,” *Phys. Rev. B*, vol. 81, p. 041203, Jan 2010.
- [58] R. Ritz, M. Halder, C. Franz, A. Bauer, M. Wagner, R. Bamler, A. Rosch, and C. Pfleiderer, “Giant generic topological hall resistivity of MnSi under pressure,” *Phys. Rev. B*, vol. 87, p. 134424, Apr 2013.

- [59] K. Karube, J. S. White, N. Reynolds, J. L. Gavilano, H. Oike, A. Kikkawa, F. Kagawa, Y. Tokunaga, H. M. Rønnow, Y. Tokura, and Y. Taguchi, “Robust metastable skyrmions and their triangular-square lattice structural transition in a high-temperature chiral magnet,” *Nature Materials*, vol. 15, no. 12, pp. 1237–1242, 2016.
- [60] S. Finizio, K. Zeissler, G. Burnell, C. Marrows, and J. Raabe, “In-situ electrical transport measurements combined with scanning transmission x-ray microscopy,” *Microscopy and Microanalysis*, vol. 24, pp. 78–79, 8 2018.
- [61] K. Karube, J. S. White, D. Morikawa, M. Bartkowiak, A. Kikkawa, Y. Tokunaga, T. Arima, H. M. Rønnow, Y. Tokura, and Y. Taguchi, “Skyrmion formation in a bulk chiral magnet at zero magnetic field and above room temperature,” *Phys. Rev. Materials*, vol. 1, p. 074405, Dec 2017.
- [62] I. Kezsmarki, S. Bordacs, P. Milde, E. Neuber, L. M. Eng, J. S. White, H. M. Rønnow, C. D. Dewhurst, M. Mochizuki, K. Yanai, H. Nakamura, D. Ehlers, V. Tsurkan, and A. Loidl, “Néel-type skyrmion lattice with confined orientation in the polar magnetic semiconductor GaV_4S_8 ,” *Nature Materials*, vol. 14, no. 11, pp. 1116–1122, 2015.
- [63] N. Romming, C. Hanneken, M. Menzel, J. E. Bickel, B. Wolter, K. von Bergmann, A. Kubetzka, and R. Wiesendanger, “Writing and Deleting Single Magnetic Skyrmions,” *Science*, vol. 341, pp. 636–639, 8 2013.
- [64] J. Sampaio, V. Cros, S. Rohart, A. Thiaville, and A. Fert, “Nucleation, stability and current-induced motion of isolated magnetic skyrmions in nanostructures,” *Nature Nanotechnology*, vol. 8, pp. 839–844, 11 2013.
- [65] K. Zeissler, M. Mruczkiewicz, S. Finizio, J. Raabe, P. M. Shepley, A. V. Sadovnikov, S. A. Nikitov, K. Fallon, S. McFadzean, S. McVitie, T. A. Moore, G. Burnell, and C. H. Marrows, “Pinning and hysteresis in the field dependent diameter evolution of skyrmions in Pt/Co/Ir superlattice stacks,” *Scientific Reports*, vol. 7, p. 15125, 12 2017.
- [66] R. Wiesendanger, “Nanoscale magnetic skyrmions in metallic films and multilayers: a new twist for spintronics,” *Nat. Rev. Mater.*, vol. 1, p. 16044, 6 2016.
- [67] A. Soumyanarayanan, M. Raju, A. L. Gonzalez Oyarce, A. K. C. Tan, M.-Y. Im, A. P. Petrović, P. Ho, K. H. Khoo, M. Tran, C. K. Gan, F. Ernult, and C. Panagopoulos, “Tunable room-temperature magnetic skyrmions in Ir/Fe/Co/Pt multilayers,” *Nat. Mater.*, vol. 16, pp. 898–904, 7 2017.
- [68] F. Büttner, I. Lemesh, and G. S. Beach, “Theory of isolated magnetic skyrmions: From fundamentals to room temperature applications,” *Scientific Reports*, vol. 8, p. 4464, 12 2018.

- [69] K. Everschor-Sitte and M. Sitte, “Real-space Berry phases: Skyrmion soccer (invited),” *J. Appl. Phys.*, vol. 115, p. 172602, 5 2014.
- [70] T. Schulz, R. Ritz, A. Bauer, M. Halder, M. Wagner, C. Franz, C. Pfleiderer, K. Everschor, M. Garst, and A. Rosch, “Emergent electrodynamics of skyrmions in a chiral magnet,” *Nat. Phys.*, vol. 8, pp. 301–304, 2 2012.
- [71] P. Bak and M. H. Jensen, “Theory of helical magnetic structures and phase transitions in MnSi and FeGe,” *J. Phys. C: Solid State Phys.*, vol. 13, pp. 881–885, 11 1980.
- [72] H. Yang, A. Thiaville, S. Rohart, A. Fert, and M. Chshiev, “Anatomy of Dzyaloshinskii-Moriya interaction at Co/Pt interfaces,” *Physical Review Letters*, 2015.
- [73] C. Moreau-Luchaire, C. Moutafis, N. Reyren, J. Sampaio, C. A. F. Vaz, N. Van Horne, K. Bouzehouane, K. Garcia, C. Deranlot, P. Warnicke, P. Wohlhüter, J.-M. George, M. Weigand, J. Raabe, V. Cros, and A. Fert, “Additive interfacial chiral interaction in multilayers for stabilization of small individual skyrmions at room temperature,” *Nat. Nanotechnol.*, vol. 11, no. 5, pp. 444–448, 2016.
- [74] N. Romming, A. Kubetzka, C. Hanneken, K. von Bergmann, and R. Wiesendanger, “Field-Dependent Size and Shape of Single Magnetic Skyrmions,” *Phys. Rev. Lett.*, vol. 114, p. 177203, 5 2015.
- [75] S. Woo, K. Litzius, B. Krüger, M. Y. Im, L. Caretta, K. Richter, M. Mann, A. Krone, R. M. Reeve, M. Weigand, P. Agrawal, I. Lemesch, M. A. Mawass, P. Fischer, M. Kläui, and G. S. Beach, “Observation of room-temperature magnetic skyrmions and their current-driven dynamics in ultrathin metallic ferromagnets,” *Nature Materials*, vol. 15, pp. 501–506, 2016.
- [76] K. Litzius, I. Lemesch, B. Krüger, P. Bassirian, L. Caretta, K. Richter, F. Büttner, K. Sato, O. A. Tretiakov, J. Förster, R. M. Reeve, M. Weigand, I. Bykova, H. Stoll, G. Schütz, G. S. Beach, and M. Kläui, “Skyrmion Hall effect revealed by direct time-resolved x-ray microscopy,” *Nature Physics*, vol. 13, pp. 170–175, 2017.
- [77] J.-V. Kim and M.-W. Yoo, “Current-driven skyrmion dynamics in disordered films,” *Appl. Phys. Lett.*, vol. 110, p. 132404, 2017.
- [78] J. Iwasaki, M. Mochizuki, and N. Nagaosa, “Current-induced skyrmion dynamics in constricted geometries,” *Nature Nanotechnology*, vol. 8, pp. 742–747, 10 2013.
- [79] A. Mougin, M. Cormier, J. P. Adam, P. J. Metaxas, and J. Ferré, “Domain wall mobility, stability and walker breakdown in magnetic nanowires,” *Europhysics Letters (EPL)*, vol. 78, p. 57007, May 2007.

- [80] E. H. Hall, “On a new action of the magnet on electric currents,” *American Journal of Mathematics*, vol. 2, no. 3, pp. 287–292, 1879.
- [81] E. H. Hall, “XVIII. on the rotational coefficient in nickel and cobalt,” *Philos. Mag.*, vol. 12, no. 74, pp. 157–172, 1881.
- [82] E. Pugh and N. Rostoker, “Hall effect in ferromagnetic materials,” *Reviews of Modern Physics*, vol. 25, no. 1, pp. 151–157, 1953.
- [83] R. Karplus and J. M. Luttinger, “Hall effect in ferromagnetics,” *Physical Review*, vol. 95, no. 5, 1954.
- [84] N. Nagaosa, J. Sinova, S. Onoda, A. H. MacDonald, and N. P. Ong, “Anomalous Hall effect,” *Reviews of Modern Physics*, vol. 82, no. 2, pp. 1539–1592, 2010.
- [85] J. Ye, Y. B. Kim, A. J. Millis, B. I. Shraiman, P. Majumdar, and Z. Teanovic, “Berry phase theory of the anomalous Hall effect: Application to colossal magnetoresistance manganites,” *Physical Review Letters*, vol. 83, no. 18, pp. 3737–3740, 1999.
- [86] S. Onoda, N. Sugimoto, and N. Nagaosa, “Intrinsic versus extrinsic anomalous Hall effect in ferromagnets,” *Physical Review Letters*, vol. 97, p. 126602, 2006.
- [87] S. Onoda, N. Sugimoto, and N. Nagaosa, “Quantum transport theory of anomalous electric, thermoelectric, and thermal Hall effects in ferromagnets,” *Phys Rev B*, vol. 77, p. 165103, 2008.
- [88] N. Nagaosa and Y. Tokura, “Topological properties and dynamics of magnetic skyrmions,” *Nature Nanotechnology*, vol. 8, no. 12, pp. 899–911, 2013.
- [89] K. Tanabe and K. Yamada, “Electrical detection of magnetic states in crossed nanowires using the topological Hall effect,” *Applied Physics Letters*, vol. 110, no. 13, p. 132405, 2017.
- [90] B. Binz and A. Vishwanath, “Chirality induced anomalous-Hall effect in helical spin crystals,” *Physica B: Condensed Matter*, vol. 403, no. 5-9, pp. 1336–1340, 2008.
- [91] M. Raju, A. Yagil, A. Soumyanarayanan, A. K. C. Tan, A. Almoalem, F. Ma, O. M. Auslaender, and . C. Panagopoulos, “The evolution of skyrmions in Ir/Fe/Co/Pt multilayers and their topological Hall signature,” *Nature Communications*, vol. 10, no. 696, 2019.
- [92] M. He, G. Li, Z. Zhu, Y. Zhang, L. Peng, R. Li, J. Li, H. Wei, T. Zhao, X.-G. Zhang, S. Wang, S.-Z. Lin, L. Gu, G. Yu, J. W. Cai, and B.-g. Shen, “Evolution of topological skyrmions across the spin reorientation transition in Pt/Co/Ta multilayers,” *Phys. Rev. B*, vol. 97, p. 174419, May 2018.

- [93] J. Matsuno, N. Ogawa, K. Yasuda, F. Kagawa, W. Koshihara, N. Nagaosa, Y. Tokura, and M. Kawasaki, "Interface-driven topological hall effect in SrRuO₃-SrIrO₃ bilayer," *Science Advances*, vol. 2, July 2016.
- [94] L. Wang, Q. Feng, Y. Kim, R. Kim, K. H. Lee, S. D. Pollard, Y. J. Shin, H. Zhou, W. Peng, D. Lee, W. Meng, H. Yang, J. H. Han, M. Kim, Q. Lu, and T. W. Noh, "Ferroelectrically tunable magnetic skyrmions in ultrathin oxide heterostructures," *Nature Materials*, vol. 17, pp. 1087–1094, Nov. 2018.
- [95] N. A. Porter, J. C. Gartside, and C. H. Marrows, "Scattering mechanisms in textured FeGe thin films: Magnetoresistance and the anomalous Hall effect," *Physical Review B - Condensed Matter and Materials Physics*, vol. 90, no. 2, p. 24403, 2014.
- [96] J. C. Gallagher, K. Y. Meng, J. T. Brangham, H. L. Wang, B. D. Esser, D. W. McComb, and F. Y. Yang, "Robust zero-field skyrmion formation in FeGe epitaxial thin films," *Phys. Rev. Lett.*, vol. 118, p. 027201, Jan 2017.
- [97] C. S. Spencer, J. Gayles, N. A. Porter, S. Sugimoto, Z. Aslam, C. J. Kinane, T. R. Charlton, F. Freimuth, S. Chadov, S. Langridge, J. Sinova, C. Felser, S. Blügel, Y. Mokrousov, and C. H. Marrows, "Helical magnetic structure and the anomalous and topological hall effects in epitaxial B20 Fe_{1-y}Co_yGe films," *Phys. Rev. B*, vol. 97, p. 214406, Jun 2018.
- [98] K. Hamamoto, M. Ezawa, and N. Nagaosa, "Purely electrical detection of a skyrmion in a constricted geometry," *Appl. Phys. Lett.*, vol. 108, p. 112401, 2016.
- [99] Y. Tian, L. Ye, and X. Jin, "Proper scaling of the anomalous hall effect," *Physical Review Letters*, vol. 103, no. 087206, 2009.
- [100] S. Krishna, *Handbook of Thin-Film Deposition Processes and Techniques*. William Andrew Publishing/Noyes, 2nd ed., 2002.
- [101] P. F. Fewster, "X-ray analysis of thin films and multilayers," *Reports on Progress in Physics*, vol. 59, no. 11, pp. 1339–1407, 1996.
- [102] W. H. Bragg and W. L. B. Apr, "The reflection of x-rays by crystals," *Proceedings of the Royal Society A: Mathematical, Physical and Engineering Sciences*, vol. 88, no. 605, pp. 428–438, 1913.
- [103] H. Kiessig, "Untersuchungen zur totalreflexion von röntgenstrahlen," *Annalen der Physik*, vol. 402, pp. 715–768, 1931.
- [104] A. Glavic and M. Björck, "GenX 3: the latest generation of an established tool," *Journal of Applied Crystallography*, vol. 55, pp. 1063–1071, Aug 2022.

- [105] M. Björck and G. Andersson, “GenX: an extensible X-ray reflectivity refinement program utilizing differential evolution,” *Journal of Applied Crystallography*, vol. 40, pp. 1174–1178, Dec 2007.
- [106] D. O. Smith, “Development of a vibrating-coil magnetometer,” *Review of Scientific Instruments*, vol. 27, no. 5, pp. 261–268, 1956.
- [107] S. Foner, “Versatile and sensitive vibrating-sample magnetometer,” *Review of Scientific Instruments*, vol. 30, no. 7, pp. 548–557, 1959.
- [108] B. D. Josephson, “Possible new effects in superconductive tunnelling,” *Physics Letters*, vol. 1, no. 7, pp. 251–253, 1962.
- [109] P. W. Anderson and J. M. Rowell, “Probable observation of the Josephson superconducting tunneling effect,” *Physical Review Letters*, vol. 10, no. 6, pp. 230–232, 1963.
- [110] R. C. Jaklevic, J. Lambe, A. H. Silver, and J. E. Mercereau, “Quantum interference effects in Josephson tunneling,” *Physical Review Letters*, vol. 12, no. 7, pp. 159–160, 1964.
- [111] R. Kleiner, D. Koelle, F. Ludwig, and J. Clarke, “Superconducting quantum interference devices: State of the art and applications,” *Proceedings of the IEEE*, vol. 92, no. 10, pp. 1534–1548, 2004.
- [112] T. Moorsom, *Electron transfer and spin injection in C60-ferromagnetic composites*. PhD thesis, University of Leeds, 2016.
- [113] Q. D. Inc, *Magnetic Property Measurement System SQUID VSM User’s Manual*. Quantum Design, Inc, San Diego, CA, U.S.A., 2009.
- [114] <https://qdusa.com/siteDocs/appNotes/1500-015.pdf>, *SQUID VSM Application Note 1500-015, Accuracy of the Reported Moment: Sample Shape Effects*. Quantum Design, Inc, San Diego, CA, U.S.A., 2010.
- [115] K. I. Team, *Model 2182 and 2182A Nanovoltmeter User’s Manual*. Keithley Instruments, Inc., Cleveland, Ohio, U.S.A., 2004.
- [116] K. I. Team, *Model 6220 DC Current Source, Model 6221 AC and DC Current Source User’s Manual*. Keithley Instruments, Inc., Cleveland, Ohio, U.S.A., 2004.
- [117] K. Zeissler, S. Finizio, C. Barton, A. J. Huxtable, J. Massey, J. Raabe, A. V. Sadovnikov, S. A. Nikitov, R. Brearton, T. Hesjedal, G. van der Laan, M. C. Rosamond, E. H. Linfield, G. Burnell, and C. H. Marrows, “Diameter-independent skyrmion hall angle observed in chiral magnetic multilayers,” *Nature Commun*, vol. 11, no. 428, 2020.

- [118] OriginLab Corporation, Northampton, MA, USA., “Origin(Pro),” Version 2022.
- [119] A. Neubauer, P. G. Niklowitz, R. Ritz, B. Binz, A. Rosch, P. Böni, and C. Pfleiderer, “Topological Hall effect in the A phase of MnSi,” *Physical Review Letters*, vol. 102, no. 18, 2009.
- [120] M. B. A. Jalil and S. G. Tan, “Robustness of topological hall effect of nontrivial spin textures,” *Scientific Reports*, vol. 4, no. 5123, 2014.
- [121] S. McVitie, S. Hughes, K. Fallon, S. McFadzean, D. McGrouther, M. Krajenak, W. Legrand, D. Maccariello, S. Collin, K. Garcia, N. Reyren, V. Cros, A. Fert, K. Zeissler, and C. H. Marrows, “A transmission electron microscope study of Néel skyrmion magnetic textures in multilayer thin film systems with large interfacial chiral interaction,” *Scientific Reports*, vol. 8, p. 5703, 2018.
- [122] S. Chikazumi, *Physics of Ferromagnetism*. Oxford University Press, 1997.
- [123] J. F. Pulecio, A. Hrabec, K. Zeissler, Y. Zhu, and C. H. Marrows, “Phase transitions of chiral spin textures via dipolar coupling in multilayered films with interfacial DMI,” *arXiv* : <https://doi.org/10.48550/arXiv.1611.00209>, 2016.
- [124] M. Cubukcu, S. Pollath, S. Tacchi, A. Stacey, E. Darwin, C. W. F. Freeman, C. Barton, B. J. Hickey, C. H. Marrows, G. Carlotti, C. H. Back, and O. Kazakova, “Manipulation of magnetic skyrmions in continuous Ir/Co/Pt multilayers,” *arXiv*: <https://doi.org/10.48550/arXiv.2111.12634>, 2021.
- [125] G. Su, Y. Li, D. Hou, X. Jin, H. Liu, and S. Wang, “Anomalous Hall effect in amorphous $\text{Co}_{40}\text{Fe}_{40}\text{B}_{20}$,” *Physical Review B*, vol. 90, no. 214410, 2014.
- [126] L. Wu, Y. Li, J. Xu, D. Hou, and X. Jin, “Anisotropic intrinsic anomalous Hall effect in epitaxial Fe films on GaAs(111),” *Physical Review B*, vol. 87, no. 155307, 2013.
- [127] D. Hou, Y. Li, D. Wei, D. Tian, L. Wu, and X. Jin, “The anomalous Hall effect in epitaxial face-centered-cubic cobalt films,” *J. Phys.: Condens. Matter*, vol. 24, no. 482001, 2012.